

Journal of Medical Physics

ISSN 0971 - 6203

Journal *of* Medical Physics

Volume 45 | Issue 2 | April-June 2020

Full text at www.jmp.org.in



Journal of Medical Physics • Volume 45 • Issue 2 • April-June 2020 • Pages 59-142



Association of Medical Physicists of India

An affiliate of Indian National Science Academy
and
International Organization for medical Physics

www.ampi.org.in

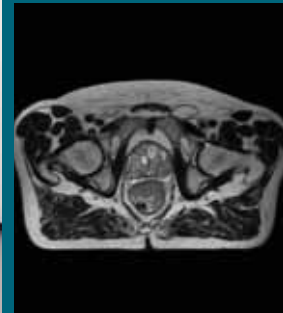


 Wolters Kluwer

Medknow

Elekta Unity Uncompromised.

See clearly during treatment to attack
the tumor and protect the patient.
Two worlds, one future.



Captured on Elekta Unity during
2018 imaging studies

[elekta.com/unity](https://www.elekta.com/unity)

Elekta Unity has CE-mark and 510(k) clearance
but not commercially available in all markets.

LADMRL180216 v4.0 © 2018 Elekta AB (publ.)

 **Elekta**



positioning
patients for life.®

Qfix Medical India Pvt. Ltd.

+91 98335 65139

Sunil.Paradkar@Qfix.com

www.Qfix.com

 **Encompass™**
SRS Immobilization System

Patent(s) Pending

**U-frame
Masks**



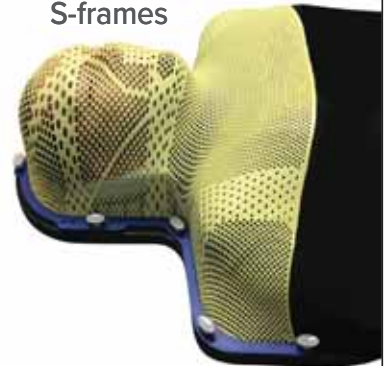
 **Access™**
Supine™



**Carbon Fiber
Pelvis System**



Portrait™
S-frames



RPL

Test and
Measurement
Solutions

Radiological Precision Labs (India) Pvt. Ltd.



Newly Launched
**RaySafe 452
Radiation Survey Meter
& Contamination Monitor**

Newly launched RaySafe 452 Radiation survey meter and contamination monitor measures radiation in a wide variety of applications including these:

- X-ray tube leakage
- X-ray wall leakage
- Scattered room radiation
- Contamination measurements
- Environmental radiation
- Non-destructive testing

ONE DEVICE
ENDLESS POSSIBILITIES

Compliant with
IEC 60846-1

Flat Energy
Response

No Corrections or
Manual Settings
required

Built for Indoor &
Outdoor Applications

Key Features

Alarm Threshold
Setting

USB Charging:
Long battery life

Automatic
Data Storage

PC Software
Connectivity

Measurements

Measures: Alpha, Beta, Gamma & X-ray

Measures: Dose rate, peak dose rate, accumulated dose and mean energy

Units: R, Gy, Sv, cpm, cps.

Radiological Precision Labs (India) Pvt. Ltd.

We are authorized distributors in India for Fluke Biomedical, USA and Unfors Raysafe AB, Sweden

For demo contact us on: sales@rplqa.com | +917030948874



APPLICATIONS

- Absolute dosimetry in radiation therapy
- Photons and High Energy Electrons.
- Traditional chamber construction for absolute dosimetry in x-rays
- Standard reference detector for reference dosimetry and scientific applications

FEATURES

- Air ionisation chamber
- Chamber with graphite wall, for all applicable radiation conditions
- Non waterproof
- Vented through waterproof sleeve
- Guarded upto 15 mm from base
- Supplied with individual factory calibration certificate and user's guide (Provisional)

MATERIAL

- Outer electrode Graphite (1.82 g/cm³)
- Inner electrode Aluminium (2.70 g/cm³)
- Build-up cap for ⁶⁰Co Delrin (1.42 g/cm³)

ACTIVE DIMENSIONS

- Volume (nominal) 0.65 cm³
- Total active length 23.1 mm
- Inner diameter of cylinder 6.2 mm
- Wall thickness 0.4 mm
- Diameter of inner electrode 1.0 mm
- Wall thickness of build-up cap for ⁶⁰Co 3.9 mm

CABLE AND CONNECTOR

- Connector type TNC triaxial
- Cable length 1.40 m

OPERATIONAL DATA

- Leakage current $\leq \pm 10 \times 10^{-15}$ A
- Sensitivity 21×10^9 C/Gy
- Radiation quality (e⁻) 1.3 Mev - 50 MV
- Polarising voltage + 300 V
- Reference point w/o build-up cap 13 mm from the distal end of the chamber
- Reference point with build-up cap 17 mm from the distal end of the build-up cap

127, Bussa Udyog Bhavan,
T.J Road, Sewri (W)
Mumbai - 400 015.
India

91 22 24166630
support@rosalina.in
www.rosalina.in



RETRANT WELL CHAMBER

BDS 1000 BRACHYTHERAPY DOSIMETRY SYSTEM



BRACHYTHERAPY SOURCE CALIBRATION

The BDS 1000 Well Chamber is air vented chamber, Highly accurate for low dose rate and high dose rate brachytherapy. Source holders are available for most existing sources as well as custom made source holders.

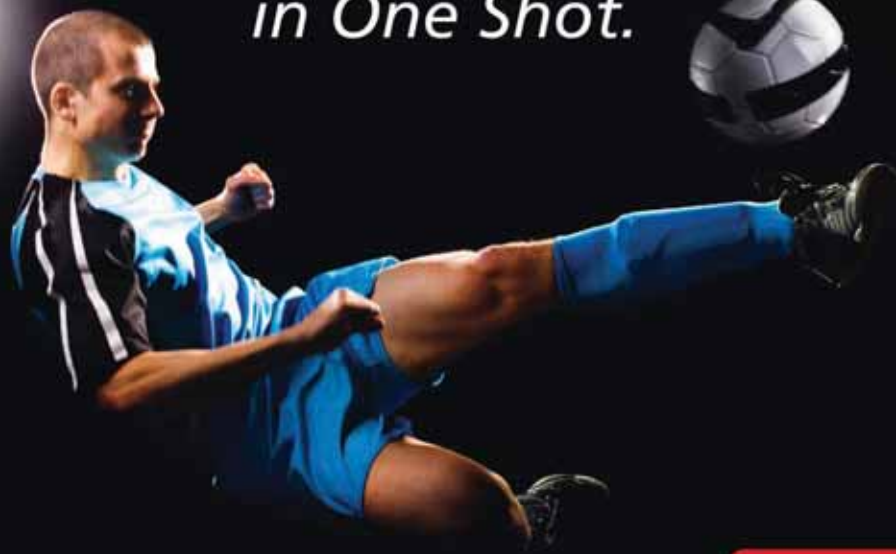
Calibrations Available	^{60}Co ^{192}Ir and/or LDR radionuclides from various manufacturers as requested
Active Volume	240 cm ³
Connector	TNC triax (standard) Other Optional
Range	10 U to 80 MU 0.01 mCi to 20 Ci
Cable	5 ft, 1.5 m
Bias voltage	± 300 volts, typical
Leakage	Less than 25 fA
Stability	0.2% (Reproducibility over 2 years)
Response	± 0.5% over 25 mm at center of axis



Preliminary Data Sheet

127, Bussa Udyog Bhavan T.J Road, Sewri (W) Mumbai - 400 015. INDIA
Tel : 91 22 241 66630, E-mail : support@rosalina.in www.rosalina.in

*True Precision
in One Shot.*



Fully automatic
For all X-ray units

NOMEX[®]

Turnkey Solution for
Absolute Dosimetry and Quality Control

- ▶ Two powerful systems for standalone or combined use
- ▶ RAD/FLU/DENT, DENT-PAN, MAM, CT, CBCT
- ▶ All parameters in one single exposure
- ▶ Autoranging for dose, kV, total filtration
- ▶ Optional tools for image quality assessment and CTDI determination
- ▶ Connection of ionization chambers or semiconductor detectors



PTW THE
DOSIMETRY
COMPANY

PTW DOSIMETRY INDIA PVT. LTD.

ACE Towers, 2nd Floor, 73/75, Dr. Radhakrishnan Road, Mylapore, Chennai - 600004.
Phone: +91 44 4207 9999, 4207 2299 | Email: info@ptw-india.in | Web: www.ptwdosimetry.com

*Stay
flexible.*

NEW Modular
4D Phantom

OCTAVIUS 4D

4D Patient and Machine QA



- ▶ Patient and machine QA with one single system
- ▶ Modular – various detector arrays and phantom tops
- ▶ Truly isotropic 3D dose verification
- ▶ Patient-based DVH analysis, entirely independent of the TPS
- ▶ Fast, independent point dose calculation with optional DIAMOND® software

PTW DOSIMETRY INDIA PVT. LTD.

ACE Towers, 2nd Floor, 73/75, Dr. Radhakrishnan Road, Mylapore, Chennai - 600004.
Phone: +91 44 4207 9999, 4207 2299 | Email: info@ptw-india.in | Web: www.ptwdosimetry.com

LAP A2J LASER SYSTEMS : Patient Marking and Positioning in Radiotherapy

The complete redesigned next generation of our laser systems convince with state-of-the-art technology in a modern look and feel. **HORUS** and **LASERSTAR** are durable, reliable and trusted high precision tools for the daily use in your advanced workflow for virtual simulation and patient positioning.



LAP A2J HORUS Moving Laser System - The re-designed moveable laser System HORUS to bring you even more precision for marking your patients. Available in 1, 3 or mobile axis according to your needs, HOURS and HORUS CS control system are adapted to all work processes.

TECHNICAL DATA HORUS	
HORUS Laser color (wavelength)	Red (638 nm), Green (520 nm)
Line width (up to 4 m distance)	< 1 mm
Line length (at 3 m distance)	> 3 m
Laser class	2
Positioning accuracy	± 0.1 mm
Projection accuracy (up to 4 m distance)	± 0.5 mm
Travel range	700 mm
Power supply	100 –240 V AC
Dimensions (H x W x D) Laser rail	1355 x 155 x 145 mm
Weight Laser rail	20 kg
Configuration.	Horus 1,3,5



Horus Range Set-up



Control Tablet PC

LAP A2J LASERSTAR Fixed Laser System ensures exact and reproducible positioning to the LINAC isocenter. for patient alignment in all three body planes the system consists of at least three LASERSTAR devices. The new version of the LASERSTAR is more compact and fits all configuration.

TECHNICAL DATA LASERSTAR	
Laser color (wavelength)	Red (638 nm), Green (529 nm)
Line width (up to 4 m distance)	< 1nm
Line length (at 3 m distance)	>3 m
Laser class	2
Operating temperature	15 – 30°C
Power supply	100 – 240 V AC
Dimensions (L x W x D)	180 x 112 x 81 mm
Weight	1.4 kg



Radiation Detector Calibration & Services

Our radiation detector calibration service offers a calibration reminder service, industry leading support and speedy turnaround time for recalibrations.

We offer complete service, repairs, recalibration for any kind or brand of Radiation Monitoring Instrument. We are specialized and factory trained to repair Pressurized Ion Chamber survey meters. We have the required plant and machinery to repair these instruments, set the calibration factor and re-calibrate.

Our calibration facility has been recognized by 'Atomic Energy Regulatory Board' in year 2014 and accredited by NABL vide certificate no. CC-3072 dt. 06.11.2019

- Facility to calibrate any brand or type of Radiation Survey Meter, Area (Zone) Monitor and Pocket Dosimeters. Either analogue or digital
- Pick-up and drop can be arranged, if the need arise
- Routine turn-around calibration time is 5-6 days
- Instrument should be in working condition, to avoid delays
- Calibration validity TWO years



NABL Cert. No. CC-3072



Coming Shortly...
Calibration Laboratory for
Nuclear Medicine Dose Calibrators
(AERB Recognised & NABL Accredited)



Radimage Healthcare India Pvt. Ltd.

(An ISO 9001 : 2015 Certified Company)

G-236, Sector-63, Noida - 201 303 (INDIA) Tel.: +91 120 2406096, 4263270 | Fax: +91 120 2406097

• www.radimageindia.com • radimagehealthcare@gmail.com

(A Meditronix Corporation Group Company)

Journal of Medical Physics

(Incorporating AMPI Medical Physics Bulletin)

Editorial Board

Editor-in-Chief:

Dr. A. S. Pradhan, Ex-Bhabha Atomic Research Centre, Mumbai, India

Associate Editors:

Dr. S. D. Sharma, Bhabha Atomic Research Centre, Mumbai, India

Dr. T. Ganesh, Manipal Hospitals Dwarka, New Delhi, India

Members:

Dr. M. M. Aspradakis, Luzerner Kantonsspital, Switzerland

Prof. Bhudatt Paliwal, University of Wisconsin, USA

Dr. D. D. Deshpande, Tata Memorial Hospital, Mumbai, India

Dr. D. Eaton, Mount Vernon Hospital, Northwood, UK

Dr. K. N. Govindarajan, Ex-Bhabha Atomic Research Centre, Mumbai, India

Dr. Hema Vaithianathan, Gippsland Cancer Care Centre, Victoria, Australia

Prof. Indra J. Das, Indiana University School of Medicine, Indianapolis, USA

Dr. C. P. Joshi, Kingston General Hospital, Ontario, Canada

Dr. Kevin Jordan, London Regional Cancer Program, Ontario, Canada

Dr. C. Kirisits, Medical University of Vienna, Austria

Dr. T. Kron, Peter Mac Cancer Centre, Victoria, Australia

Dr. Lalit M. Aggarwal, Banaras Hindu University, Varanasi, India

Dr. Lisa Karam, NIST, Gaithersburg, USA

Dr. R. S. Livingstone, Christian Medical College, Vellore, India

Dr. K. J. Maria Das, SGPGI, Lucknow, India

Dr. B. Paul Ravindran, Christian Medical College, Vellore, India

Dr. Pratik Kumar, AIIMS, New Delhi, India

Dr. B. S. Rao, Ex-Bhabha Atomic Research Centre, Mumbai, India

Dr. R. Ravichandran, Cachar Cancer Hospital & Research Centre, Silchar, India

Dr. M. Ravikumar, Kidwai Memorial Institute of Oncology, Bangalore, India

Dr. S. Rustgi, Radiation Oncology Physics Services, Florida, USA

Prof. Salahuddin Ahmad, University of Oklahoma Health Science Center, USA

Prof. B. Satish Rao, Manipal University, India

Dr. L. J. Schreiner, Queen's University, Ontario, Canada

Dr. S. K. Shrivastava, Apollo Hospitals, Navi Mumbai, India

Dr. A. K. Shukla, SGPGI, Lucknow, India

Dr. P. Tandon, Atomic Energy Regulatory Board, Mumbai, India

Prof. G. A. Zakaria, Kreiskrankenhaus Gummersbach, Germany

Book Review and News Editor:

Dr. Pratik Kumar, AIIMS, New Delhi, India

Former Resident Editors:

Dr. P. S. Iyer (1996-2005), Journal of Medical Physics

Dr. M. S. S. Murthy (1989-95), AMPI Medical Physics Bulletin/Journal of Medical Physics

Dr. K. S. Parthasarathy (1988-89), AMPI Medical Physics Bulletin

Dr. U. Madhvanath (1976-87), AMPI Medical Physics Bulletin



Association of Medical Physicists of India

(Regd. No. 421/1976 GBBSD, Public Trust F 4238)
(An affiliate of the Indian National Science Academy & The International Organization for Medical Physics)
C/o Radiological Physics & Advisory Division, BARC
CT & CRS Building, Anushaktinagar, Mumbai - 400094, ● Website: www.ampi.org.in

The Association of Medical Physicists of India (AMPI) is a professional but a non-profit making / non-governmental organization, devoted to serving the needs of the country in the field of Medical Physics. Its membership is open to science graduates, engineers and physicians interested in the application of physics to medical and biological sciences. Medical Radiation Physicists, Radiation Safety Officers, Radiological and Hospital Physicists, Radiation Oncologists and Radiologists form the main group of the association. It publishes this quarterly journal. The association is having about 1200 active members. The journal is provided to its members and also to the libraries of almost all leading Cancer Centres in the country on a very nominal subscription. Other than publishing Journal of Medical Physics, the association holds a national/ international conference every year to exchange information among its members. The association also supports advanced training of Medical Physicists by offering Travel Fellowships. For public awareness, publication of articles related to medical physics and radiation safety in newspapers and periodicals is encouraged. The association also works towards worldwide exchange of information on medical physics.

The College of Medical Physics of India (CMPI) is an autonomous wing of AMPI which was established to function as the certifying and accreditation body. Membership of AMPI is prerequisite to appear for CMPI certification examination. A member of AMPI can become member of CMPI only by passing the certification examination. CMPI certification indicates that the holder has acquired, demonstrated, and maintained a minimum standard of knowledge in medical physics and the competence to practice as clinical physicist in Diagnostic Radiology, Radiation Oncology and Nuclear Medicine.

Membership Fee Details (w.e.f. February 07, 2015)

Annual Member	
Indian Resident	INR ` 1,280.00
Developing Countries	USD \$ 50.00
Other Countries	USD \$ 165.00
Life Member	
Indian Resident	INR ` 3,615.00
Developing Countries	USD \$ 257.00
Other Countries	USD \$ 970.00
Institution Member (India)	INR ` 4,780.00

AMPI Executive Committee (2018-2021)

President	Dr. Sunil Dutt Sharma
Vice President	Dr. Pratik Kumar
Secretary	Dr. Shobha Jayaprakash
Treasurer	Mr. Sridhar Sahoo
Members	Dr. Anuj Kumar Tyagi Dr. Kovilpillai Joseph Maria Das Dr. Ghanshyam Sahani Dr. Varadharajan Ekambaram Dr. Muthuvelu Kulandaivel Mr. Rajesh Thiyagarajan Mr. Suresh Chaudhari Dr. Godson Henry Finlay Dr. Vinod Kumar Dangwal Mr. Vinod Pandey Prof. Challapalli Srinivas

AMPI Board of Trustees (2018-2021)

Chairman	Mr. Satya Pal Agarwal
Convener	Dr. Pankaj Tandon
Members	Dr. Ramasamy M Nehru Dr. Kamlesh Passi Dr. Arun Chougule

CMPI Board (2018-2021)

Chairman	Dr. Tharmarnadar Ganesh
Vice Chairman	Dr. Ajay Srivastava
Chief Examiner	Dr. Jamema Swamidas
Registrar	Dr. Jagadeesan Velmurugan
Secretary-Treasurer	Dr. Paul Ravindran
Members	Dr. Dayananda Sharma Dr. Raghavendra Holla Dr. M. Ravi Kumar

Journal of Medical Physics

General Information

The journal

The Journal of Medical Physics (earlier known as AMPI Medical Physics Bulletin till 1994) is a quarterly publication of Association of Medical Physicists of India (AMPI). Apart from being the official journal of AMPI, Journal of Medical Physics (JMP) has also been adopted as the official Journal of International Organization for Medical Physics, IOMP (www.iomp.org) with effect from 18th July 2020 and of Asia-Oceania Federation of Organizations for Medical Physics, AFOMP (www.afomp.org) with effect from 4th May 2020. Issues of JMP are published quarterly in January, April, July and October. The main objective of the Journal is to serve as a vehicle of communication to highlight all aspects of medical physics. The scope of this journal covers all aspects of the application of radiation physics to health science, mainly radiation therapy, radiodiagnosis, nuclear medicine, radiation dosimetry, radiation standards, quality assurance, calibration and radiation protection. Papers / manuscripts on radiobiology pertaining to cancer therapy also fall within the scope of the journal. Apart from the original research work, papers which are of practical importance to medical physicists e.g., those dealing with practices (performance and quality assurance tests, clinical investigations and follow-ups with novelty), radiation accidents and emergencies are also published in the journal. Brief manuscripts dealing with the validation of relatively newer concepts may be considered as technical notes or letter to editor. Reviews of publications (e.g., ICRP/ICRU reports and books related to the scope of the journal) may also find a place in the journal. Manuscripts with no or oblique relevance to the scope may not find place.

Abstracting and indexing information

The journal is registered with the following abstracting partners: Baidu Scholar, CNKI (China National Knowledge Infrastructure), EBSCO Publishing's Electronic Databases, Exlibris – Primo Central, Google Scholar, Hinari, Infotrieve, National Science Library, ProQuest, TDNet

The journal is indexed with, or included in, the following: DOAJ, EMBASE/ Excerpta Medica, Emerging Sources Citation Index, Index Copernicus, Indian Science Abstracts, IndMed, Pubmed Central, Scimago Journal Ranking, SCOPUS

Information for Authors

Copies of the journal are provided free of cost to the AMPI members.

There are no page charges for JMP submissions. However, there are charges for color reproduction of photographs. Please check <http://www.jmp.org.in/contributors.asp> for details.

All manuscripts must be submitted online at www.journalonweb.com/jmp.

Subscription Information

A subscription to Journal of Medical Physics comprises 4 issues. Prices include postage. Annual Subscription Rate for non-members-

Annual Subscription Rates

Print	Personal	Institutional
India (INR)	1850.00	3355.00
Abroad (USD)	142.00	308.00
Single Issue		
India (INR)	578.00	1048.00
Abroad (USD)	44.00	96.00

For mode of payment and other details, please visit www.medknow.com/subscribe.asp.

Claims for missing issues will be serviced at no charge if received within 60 days of the cover date for domestic subscribers, and 3 months for subscribers outside India. Duplicate copies cannot be sent to replace issues not delivered because of failure to notify publisher of change of address.

The journal is published and distributed by Wolters Kluwer India Private Limited. Copies are sent to subscribers directly from the publisher's address. It is illegal to acquire copies from any other source. If a copy is received for personal use as a member of the association/society, one cannot resale or give-away the copy for commercial or library use. The copies of the journal to the members of the association are sent by ordinary post. The editorial board, association or publisher will not be responsible for non receipt of copies. If any member/subscriber wishes to receive the copies by registered post or courier, kindly contact the publisher's office. If a copy returns due to incomplete, incorrect or changed address of a member/subscriber on two consecutive occasions, the names of such members will be deleted from the mailing list of the journal. Providing complete, correct and up-to-date address is the responsibility of the member/subscriber.

Please send change of address information to WKHLRPMedknow_subscriptions@wolterskluwer.com.

Advertising policies

The journal accepts display and classified advertising. Frequency discounts and special positions are available. Inquiries about advertising should be sent to Wolters Kluwer India Private Limited, WKHLRPMedknow_advertise@wolterskluwer.com.

The journal reserves the right to reject any advertisement considered unsuitable according to the set policies of the journal.

The appearance of advertising or product information in the various sections in the journal does not constitute an endorsement or approval by the journal and/or its publisher of the quality or value of the said product or of claims made for it by its manufacturer.

Annual Advertisement Tariffs:

Advertising Option	Price Per Issue (GST 5% Extra)
1. Back cover(Color)	INR 84,000
2. Back Inside cover (color)	INR 61,000
3. First Page(Color)	INR 65,000
4. Front Inside cover (color)	INR 65,000
5. Full page color	INR 46,000
6. Art-Card (Back2Back)	INR 96,000
7. Gate Fold Cover	INR 1,20,000

Advertising Option Rate Card Per Month (GST 18% Extra)

1. Static Banner	INR 50,000
2. GIF Banner	INR 70,000

Copyright

The entire contents of the Journal of Medical Physics are protected under Indian and international copyrights. The Journal, however, grants to all users a free, irrevocable, worldwide, perpetual right of access to, and a license to copy, use, distribute, perform and display the work publicly and to make and distribute derivative works in any digital medium for any reasonable non-commercial purpose, subject to proper attribution of authorship and ownership of the rights. The journal also grants the right to make small numbers of printed copies for their personal non-commercial use.

Permissions

For information on how to request permissions to reproduce articles/information from this journal, please visit www.medknow.com.

Disclaimer

The information and opinions presented in the Journal reflect the views of the authors and not of the Journal or its Editorial Board or the Publisher. Publication does not constitute endorsement by the journal. Neither the Journal of Medical Physics nor its publishers nor anyone else involved in creating, producing or delivering the Journal of Medical Physics or the materials contained therein, assumes any liability or responsibility for the accuracy, completeness, or usefulness of any information provided in the Journal of Medical Physics, nor shall they be liable for any direct, indirect, incidental, special, consequential or punitive damages arising out of the use of the Journal of Medical Physics. The Journal of Medical Physics, nor its publishers, nor any other party involved in the preparation of material contained in the Journal of Medical Physics represents or warrants that the information contained herein is in every respect accurate or complete, and they are not responsible for any errors or omissions or for the results obtained from the use of such material. Readers are encouraged to confirm the information contained herein with other sources.

Editorial Office

Dr. A. S. Pradhan
Editor-in-Chief
Journal of Medical Physics,
Association of Medical Physicists of India (AMPI)
C/o Radiological Physics & Advisory Division,
Bhabha Atomic Research Centre,
CTCRS, Anushaktinagar, Mumbai - 400094, India.
E-mail: editor@jmp.org.in / Website: www.jmp.org.in

Published by

Wolters Kluwer India Private Limited,
A-202, 2nd Floor, The Qube,
C.T.S. No.1498A/2 Village Marol, Andheri (East),
Mumbai - 400 059, India.
Phone: 91-22-66491818
Print at Website: www.medknow.com

Printed at

Dhote Offset Technokrafts Pvt. Ltd., Jogeshwari, Mumbai, India

Journal of Medical Physics

Volume 45 - Issue 2 - April-June 2020

Contents

Original Articles

- Characterization and Performance Evaluation of the First-Proton Therapy Facility in India**
Dayananda Sharma Shamurailatpam, A. Manikandan, K. Ganapathy, M. P. Noufal, Kartikeshwar C. Patro, T. Rajesh, R. Jalali 59
- Design, Fabrication, and Validation of a Polymethyl Methacrylate Head Phantom for Dosimetric Verification of Cranial Radiotherapy Treatment Plans**
V. S. Shaiju, Rajesh Kumar, Debjani Phani, K. V. Rajasekhar, George Zacharia, Saju Bhasi, Raghuram K. Nair 66
- Influence of Cleaned-up Commercial Knowledge-Based Treatment Planning on Volumetric-Modulated Arc Therapy of Prostate Cancer**
Mikoto Tamura, Hajime Monzen, Kenji Matsumoto, Kazuki Kubo, Yoshihiro Ueda, Tatsuya Kamima, Masahiro Inada, Hiroshi Doi, Kiyoshi Nakamatsu, Yasumasa Nishimura 71
- Evaluation of Dose Distribution and Normal Tissue Complication Probability of a Combined Dose of Cone-Beam Computed Tomography Imaging with Treatment in Prostate Intensity-Modulated Radiation Therapy**
Tetsuya Tomita, Tomonori Isobe, Yoshinobu Furuyama, Hideyuki Takei, Daisuke Kobayashi, Yutaro Mori, Toshiyuki Terunuma, Eisuke Sato, Hiroshi Yokota, Takeji Sakae 78
- Study of Asymmetric Margins in Prostate Cancer Radiation Therapy Using Fuzzy Logic**
Santosh Kumar Patnaikuni, Sapan Mohan Saini, Rakesh Mohan Chandola, Pradeep Chandrakar, Vivek Chaudhary 88
- Appraisal of Deep-Learning Techniques on Computer-Aided Lung Cancer Diagnosis with Computed Tomography Screening**
S. Akila Agnes, J. Anitha 98
- Assessment of Four Scatter Correction Methods in In-111 SPECT Imaging: A Simulation Study**
Mahsa Noori-Asl 107
- Monte Carlo Calculation of the Energy Spectrum of a 6 MeV Electron Beam using PENetration and Energy Loss of Positrons and Electrons Code**
Danny Giancarlo Apaza Veliz, Jorge Homero Wilches Visbal, Felipe Chen Abrego, José Luis Vega Ramírez 116

Technical Note

- Simultaneous Measurement of *In vivo* and Transit Mid-Plane Doses with Ionization Chambers in Gynecological Malignancy Patients Undergoing Three-Dimensional Conformal Radiotherapy**
Putha Suman Kumar, Challapalli Srinivas, B. M. Vadhiraaja, Sourjya Banerjee, R. Shreyas, PU Prakash Saxena, Ramamoorthy Ravichandran, Dilson Lobo 123

Letter to the Editor

Revision in Standard Operating Procedures of Radiation Oncology Department and Quality Assurance Schedule under COVID-19 Pandemic

Suresh Chaudhari, Sunil Dutt Sharma, Shyam Kishore Shrivastava

130

Book Reviews

Khan's The Physics of Radiation Therapy

Manoj Kumar Semwal

134

Leadership and challenges in medical physics: A strategic and robust approach

Arun Chougule

136

Guidance on the Personal Monitoring Requirements for Personnel Working in Healthcare

K. M. Ganesh

139

Erratum

Erratum: Superparamagnetic Iron Oxide-C595: Potential MR Imaging Contrast Agents for Ovarian Cancer Detection

141

Journal of Medical Physics on Web

<http://www.journalonweb.com/jmp>

The Journal of Medical Physics now accepts articles electronically. It is easy, convenient and fast. Check following steps:

1 Registration

- Register from <http://www.journalonweb.com/jmp> as a new author (Signup as author)
- Two-step self-explanatory process

2 New article submission

- Read instructions on the journal website or download the same from manuscript management site
- Prepare your files (Article file, First page file and Images, Copyright form & Other forms, if any)
- Login as an author
- Click on 'Submit new article' under 'Submissions'
- Follow the steps (guidelines provided while submitting the article)
- On successful submission you will receive an acknowledgement quoting the manuscript ID

3 Tracking the progress

- Login as an author
- The report on the main page gives status of the articles and its due date to move to next phase
- More details can be obtained by clicking on the ManuscriptID
- Comments sent by the editor and reviewer will be available from these pages

4 Submitting a revised article

- Login as an author
- On the main page click on 'Articles for Revision'
- Click on the link "Click here to revise your article" against the required manuscript ID
- Follow the steps (guidelines provided while revising the article)
- Include the reviewers' comments along with the point to point clarifications at the beginning of the revised article file.
- Do not include authors' name in the article file.
- Upload the revised article file against New Article File - Browse, choose your file and then click "Upload" OR Click "Finish"
- On completion of revision process you will be able to check the latest file uploaded from Article Cycle (In Review Articles -> Click on manuscript id -> Latest file will have a number with 'R', for example XXXX_100_15R3.docx)

Facilities

- Submission of new articles with images
- Submission of revised articles
- Checking of proofs
- Track the progress of article until published

Advantages

- Any-time, any-where access
- Faster review
- Cost saving on postage
- No need for hard-copy submission
- Ability to track the progress
- Ease of contacting the journal

Requirements for usage

- Computer and internet connection
- Web-browser (Latest versions - IE, Chrome, Safari, FireFox, Opera)
- Cookies and javascript to be enabled in web-browser

Online submission checklist

- First Page File (rtf/doc/docx file) with title page, covering letter, acknowledgement, etc.
- Article File (rtf/doc/docx file) - text of the article, beginning from Title, Abstract till References (including tables). File size limit 4 MB. Do not include images in this file.
- Images (jpg/jpeg/png/gif/tif/tiff): Submit good quality colour images. Each image should be less than 10 MB) in size
- Upload copyright form in .doc / .docx / .pdf / .jpg / .png / .gif format, duly signed by all authors, during the time mentioned in the instructions.

Help

- Check Frequently Asked Questions (FAQs) on the site
- In case of any difficulty contact the editor

Characterization and Performance Evaluation of the First-Proton Therapy Facility in India

Dayananda Sharma Shamurailatpam, A. Manikandan, K. Ganapathy, M. P. Noufal, Kartikeshwar C. Patro, T. Rajesh, R. Jalali¹

Departments of Medical Physics and ¹Radiation Oncology, Apollo Proton Cancer Centre, Chennai, Tamil Nadu, India

Abstract

Purpose: The purpose of this study is to evaluate the performance characteristic of volumetric image-guided dedicated-nozzle pencil beam-scanning proton therapy (PT) system. **Materials and Methods:** PT system was characterized for electromechanical, image quality, and registration accuracy. Proton beam of 70.2–226.2 MeV was characterized for short- and long-term reproducibility in integrated depth dose; spot profile characteristics at different air gap and gantry angle; positioning accuracy of single and pattern of spot; dose linearity, reproducibility and consistency. All measurements were carried out using various X-ray and proton-beam specific detectors following standard protocols. **Results:** All electro-mechanical, imaging, and safety parameters performed well within the specified tolerance limit. The image registration errors along three translation and three rotational axes were ≤ 0.5 mm and $\leq 0.2^\circ$ for both point-based and intensity-based auto-registration. Distal range (R_{90}) and distal dose fall-off (DDF) of 70.2–226.2 MeV proton beams were within 1 mm of calculated values based on the international commission on radiation units and measurements 49 and $0.0156 \times R_{90}$, respectively. The R_{90} and DDF were reproducible within a standard deviation of 0.05 g/cm^2 during the first 8 months. Dose were linear from 18.5 (0.011 MU/spot) to 8405 (5 MU/spot) MU, reproducible within 0.5% in 5 consecutive days and consistent within 0.8% for full rotation. The cGy/MU for 70.2–226.2 MeV was consistent within 0.5%. In-air X(Y) spot-sigma at isocenter varies from 2.96 (3.00) mm to 6.68 (6.52) mm for 70.2–226.2 MeV. Maximum variation of spot-sigma with air-gap of ± 20 cm was ± 0.36 mm (5.28%) and ± 0.82 mm ($\pm 12.5\%$) along X- and Y-direction and 3.56% for full rotation. Relative spot positions were accurate within ± 0.6 mm. The planned and delivered spot pattern of known complex geometry agreed with ($\gamma^0 \leq 1$) for 1% @ 1 mm >98% for representative five-proton energies at four gantry angle. **Conclusion:** The PT-system performed well within the expected accuracy level and consistent over a period of 8 months. The methodology and data presented here may help upcoming modern PT center during their crucial phase of commissioning.

Keywords: Characterization, commissioning, pencil-beam scanning, proton, validation

Received on: 13-02-2020

Review completed on: 09-05-2020

Accepted on: 10-05-2020

Published on: 20-07-2020

INTRODUCTION

Proton therapy (PT) has shown better sparing of surrounding normal tissue and reduction of integral dose as compare to outcome, improved quality of life, and reduction of second cancer.^[1] Recently, PT with pencil-beam scanning (PBS) technique is increasingly adopted (<https://www.ptcog.ch>) primarily due to its technological advancement as compare to traditional passive-scattering technique, availability of less-expensive single-room compact system, and emergence of promising dosimetric and clinical outcome data.^[1] The first PT facility in India was clinically commissioned at the Apollo Proton Cancer Center (APCC), Chennai. This three room (two gantries and one fix line) PT facility is equipped with the latest

model of Proteus 235 (IBA, Louvain-la-Neuve, Belgium) with dedicated nozzle (DN) and cone-beam computed tomography (CBCT). The DN is a newly developed nozzle exclusively for PBS technique, and it claimed to produce the proton spots of smaller size in comparison to previous universal nozzle.^[2] CBCT is also a new system capability in addition to orthogonal radiograph.

Address for correspondence: Dr. Dayananda Sharma Shamurailatpam, Department of Medical Physics, Apollo Proton Cancer Centre, 100 Feet Road Tharamani, Chennai - 400 053, Tamil Nadu, India.
E-mail: drdayananda_s@apollohospitals.com

This is an open access journal, and articles are distributed under the terms of the Creative Commons Attribution-NonCommercial-ShareAlike 4.0 License, which allows others to remix, tweak, and build upon the work non-commercially, as long as appropriate credit is given and the new creations are licensed under the identical terms.

For reprints contact: WKHLRPMedknow_reprints@wolterskluwer.com

How to cite this article: Shamurailatpam DS, Manikandan A, Ganapathy K, Noufal MP, Patro KC, Rajesh T, *et al.* Characterization and performance evaluation of the first-proton therapy facility in India. *J Med Phys* 2020;45:59-65.

Access this article online

Quick Response Code:



Website:
www.jmp.org.in

DOI:
10.4103/jmp.JMP_12_20

The characterization of a new PT system is of paramount importance to understand its complete behavior and establishing baseline data for subsequent consistency check. Characterization need to be carried out with the highest possible accuracy for precise and safe delivery of dose to patient. Very recently, the American Association of Physicist in Medicine (AAPM) have published the guideline for the quality assurance (QA) of PT system in its task group report no 224 (AAPM-TG 224).^[3] However, consensus guideline for the characterization of PT facility for clinical commissioning is still lacking in the literature. Adopted methodology and test protocols vary from center to center depending on the system configuration, measuring equipment type, and physicist viewpoint. Proton beam characteristic of active scanning PT systems have been reported from few PT centers, equipped with different proton accelerators and beam delivery techniques.^[4-6] However, comprehensive proton-beam characteristics, dosimetric data, electromechanical, image quality, and image registration evaluation results from Proteus 235 PT system with dedicated PBS nozzle is lagging in the literature. In this study, we report the performance characteristics of the first gantry of our multi-room PT facility capable of delivering both single-field uniform dose and intensity-modulated proton therapy. Performance characterization includes (a) electro-mechanical characterization, (b) image quality and image registration accuracy test using different registration algorithms, and (c) characterization, calibration, and consistency of proton beam.

MATERIALS AND METHODS

Overview of the proton therapy facility

Proteus-235 comprises C230 isochronous cyclotron, energy selection system (ESS), beam transport system (BTS), dedicated PBS nozzle, and two pairs of kV X-ray tube (Rad-A and Rad-B) and flat-panel detectors. Leoni robot (Leoni, France) was integrated to Proteus 235 for patient positioning and set-up error correction in six dimensions (6D). The C230 isochronous cyclotron uses an azimuthally varying field to accelerate hydrogen nuclei up to 230 MeV which can be reduced till 70 MeV using beam degrader in ESS. Minimum and maximum extracted beam current ranges from 1 to 350 nA with an average extraction efficiency better than 50%. Average magnetic field at center, valley, and extraction is 1.76, 0.9, and 2.188 Tesla, respectively. The stated range of proton varies from 4 to 32 g/cm² at DN exit. The range of proton beam can be reduced further by 7.5 g/cm² using an add-on Lexan (density = 1.25 g/cm²) Range shifter having water equivalent thickness of 7.5 g/cm² (physical thickness of 6 cm). One spot sigma for the maximum proton energy in air and at isocenter was quoted at 3 mm. The maximum field size was 30 cm × 40 cm at isocenter. Minimum and maximum MUs per spot were limited to 0.01–12 MU by the controller software. The two pairs of kV imaging system driven by Adapt Insight software (IBA, Louvain-la-Neuve, Belgium) enable patient positioning verification in 6D employing orthogonal

planar radiograph and CBCT and the same can be corrected in 6D using Leoni robot.

Electro-mechanical and safety test

Electromechanical test related to translational and rotational movement accuracy of Leoni robot patient positioning system (PPS), gantry rotational and speed accuracy, isocentric accuracy with respect to PPS and gantry movement, congruence of proton isocenter, and imaging isocenter were tested following standard test methods. Safety interlock tests were performed following the manufacturer test protocol. Mechanical and image quality-related tests of IGRT system were carried out in both stereo X-ray imaging and CBCT mode using appropriate test tools and methodology described in AAPM TG179^[7] and acceptance test protocol of IBA. The included test were the congruence of Rad-A and Rad-B isocenter, low and high-contrast resolution in planar radiography and CBCT mode, computed tomography (CT) number accuracy and uniformity test for CBCT in small and large field of view (LFOV). The details of the test methods are describe elsewhere.^[7]

Image registration accuracy test

Image registration accuracy test was carried out using an anthropomorphic head and neck phantom having seven markers implanted at predefined locations. Thin slice (1 mm) CT scan of this phantom acquired on 85 cm bore multislice AcquilonLB (M/S Canon Medical System Corporation, Japan) CT scanner was used to create a four-field treatment plan in RayStation TPS. The approved plan was exported to AdaptInsight through MOSAIQ oncology information system. The phantom was setup on the Leoni PPS and aligned using room laser as if it is done for the patient. An orthogonal radiographs were acquired and subsequently registered with the digitally reconstructed radiograph; first using the point-based automatic registration algorithm and second by automatic matching based on intensity. The procedure was repeated after applying known off-set in all three translational axes and rotation. The measured stereo X-ray correction vectors were compared with the known off-sets. Using the same plan, CBCT were acquired for the same phantom and co-registered with reference planning CT datasets using intensity-based auto-registration and estimated correction vectors were compared against known expected values.

Characterization and calibration of proton beam

Pristine Bragg peak/integrated depth dose measurement

Integrated depth doses (IDD) from 70.2 to 226.2 MeV proton energy were acquired in 10 MeV increment using 3D scanning tank (Blue Phantom2) and large diameter (12 cm) parallel plate ionization chamber (StingRay Sr No 0042; IBA Dosimetry, Germany). The IC23 available in DN exit was used as a reference detector. All the measurements were carried out at gantry 0° and water surface at isocenter following general guideline described in AAPM TG106.^[8] The measured range (R_{90}) from each IDD was compared against calculated range based on the international commission on

radiation units and measurements 49.^[9] The measured distal dose fall-off (DDF), defined as the depth difference between 20% and 80% distal depth dose ($DDF = R_{20\%} - R_{80\%}$), were compared against expected value calculated as 0.0156 times calculated range.^[10] The complete set of IDD measurements was repeated in the next week to check the short-term reproducibility. IDD measurements were also measured from 70.2 to 226.2 MeV in 10 MeV increment using a Zebra multi-layer ionization chamber (MLIC) (IBA Dosimetry, Germany). It contains 180 air-vented parallel plate ionization chambers of 2.5 cm diameter and inter-chamber spacing of 2 mm. It can cover energies ranging from 2 to 33 cm of WET with a resolution of 2 mm. The detail performance characteristics of Zebra MLIC is reported elsewhere.^[11] The R_{90} extracted from the IDD measurements in water phantom using stingray and zebra MLIC was compared to establish the baseline for subsequent QA. The long-term reproducibility of the IDD measurements over the period of 8 months was also assessed from the five repeated measurements of IDD measurements using Zebra MLIC.

Spot profile and position measurement

Spot profiles from a five-spot pattern of mono-energy proton ranging from 70.2 to 226.2 MeV were acquired in 10 MeV increment in air by keeping the active layer of Lynx (IBA Dosimetry, Germany) at air gap of 0 cm (isocenter), ± 10 cm and ± 20 cm, respectively. Lynx is a gadolinium-based two-dimensional-scintillation detector having an effective spatial resolution of 0.5 mm and active surface area of 30 cm \times 30 cm and its detail characteristics are reported elsewhere.^[12] From these five sets of measurements per chosen energy, the central spot profiles were analyzed using Omnipro IMRT software and myQA fast tract software (IBA dosimetry, Germany) and was used as an input data for commissioning RayStation TPS. Spot size represented by one sigma (1σ) of each Gaussian distribution along X and Y direction were estimated for each selected energies at five air gaps. Spot symmetry along X and Y direction were also estimated from the measured profiles for the selected energies and air gaps. The dependence of spot size with gantry angle was investigated by repeating the measurement of spot pattern at different gantry angles of 0°, 60°, 220°, and 270° degree for five proton energies of 70.2, 100, 115, 145, and 226.2 MeV, respectively. The same five spot patterns acquired for 70.2–226.2 MeV in 10 MeV increment at gantry 90° at different air gaps were also used to calculate the relative spot position of the corner spots with respect to the central spot.

Spot pattern accuracy

A complex dose/spot pattern of known geometry was created in PBS layer dose (PLD) file, an IBA specific format. This PLD file was exposed on Lynx at four gantry angles of 0°, 60°, 270°, and 220° for every proton energy of 226.2, 145, 120, 100, and 70.2 MeV, respectively. The agreement between measured and planned dose fluence of the known geometry was compared using gamma ($\gamma\% \leq 1$) values set at 1.0% dose difference at 1 mm.

Absolute dose calibration

Dose (cGy)/monitor unit calibration

The number of spots (1681), spot spacing (2.5 mm), and monitor unit (MU)/spot (1 MU) of every mono-energy scanned field were optimized to deliver a uniform dose to 10 cm \times 10 cm field. Ionization measurement from 33 mono-energy (70.2–226.2 MeV in 5 MeV increment) scanned field of 10 cm \times 10 cm were carried out in water phantom at 2–8 cm depths, using PPC05 parallel plate chamber and Dose-1 electrometer (IBA dosimetry, Germany), following recommendation of RayStation TPS beam physics guide. The absorbed dose to water at the reference depths was calculated following the formalism of International Atomic Energy Agency TRS-398.^[13]

Dose linearity and monitor unit accuracy

The above mono-energy scanned field of 10 cm \times 10 cm were edited with MU/spot ranging from 0.011 to 5 resulting in 12 fields, each delivering total MU ranging from 18.49 to 8405 respectively. Dose measurement from these 12 fields were carried out for proton energy of 226.2, 145 and 70.2 MeV using PPC05 ionization chamber positioned at 2 cm depth in a solid RW3 phantom of 35 cm \times 35 cm \times 35 cm. For each programmed MUs, the corresponding MU readings from primary and secondary monitor chambers were also recorded at the end of the irradiation to check the accuracy of MU counters.

Dose reproducibility and Output constancy with gantry angle

The short and long term dose reproducibility were tested by repeating the measurement 10 times within 15 min, 8 h (1 day) and 5 days (1 week) from any arbitrarily chosen energy of 200 MeV scanned for 10 cm \times 10 cm with 1 MU/spot. Ionization measurement from 150 MeV scan field of 10 cm \times 10 cm were also performed for five times for every gantry angle of 0°, 30°, 90°, 135°, 180°, 270°, 325°.

RESULTS

The results of the electromechanical test related to Leoni PPS, Gantry, isocentricity, congruence of X-ray and proton isocenter are summarized in Table 1. It also shows the results of planar kV and CBCT image quality, scale and distance measurement on CBCT images, CT number accuracy and uniformity in CBCT both for small field of view and LFOV. All the parameters were within the acceptance tolerance limit provided by the manufacturer and recently published AAPM TG224.^[3,7] Also, all the safety features pass the acceptance criteria. The point based image registration errors along translation (X, Y, Z) and rotation (Yaw, pitch, roll) were 0.3, -0.2, 0.5 mm and 0°, 0.2°, 0.1° respectively. The corresponding values for intensity based auto-registration error were 0.4, 0.0, 0.1 mm and -0.1°, 0.0°, 0.1° respectively. The details of the test results will not be discussed in this manuscript.

Characterization and calibration of proton beam

Pristine Bragg peak/integrated depth dose characteristics

Figure 1 represents one set of normalized IDD measurements from 70.2 to 226.2 MeV proton energy in 10 MeV increment. The

Table 1: Results of the electromechanical test and imaging parameters

	Results
Electro-mechanical parameters test related to Leoni PPS and proton gantry	
Accuracy in linear movements of Leoni PPS	Max deviation from programmed position along X=0.3 mm, Y=0.2 mm and Z=0.1 mm
Accuracy in the angular movement of Leoni PPS	Max deviation from programmed position in Pitch=0.1°, roll=0.1° and rotation=0.3°
Isocentricity of Leoni PPS	<1 mm diameter (Max deviation along X=±0.4 mm, Y=±0.7 mm, Z=±0.4 mm)
Isocentricity with respect to gantry rotation	<1 mm diameter (Max deviation along X=±0.2 mm, Y=±0.4 mm, Z=±0.3 mm)
MRD of gantry due to emergency stop	<5° for rotational speed of 6°/S and <1° for rotational speed of 1°/S
Gantry rotation speed	6°/s for gantry speed of 1 RPM, 1°/s for Gantry speed of 0.13 RPM
Rotational accuracy of gantry	±0.1°
X-ray beam and Proton beam co-incidence at different gantry angle	<1.5 mm diameter
Image quality test performed	
High-contrast spatial resolution tested using Digi-13 imaging phantom for planar kV X-rays	3.1 lp/mm for Rad A and 3.4 lp/mm for Rad B
Low-contrast resolution tested using Digi-13 imaging phantom for planar kV X-rays	1.2% for Rad A and 0.8% for Rad B
Scale and distance measurement accuracy in CBCT images	Deviation between expected and measured distance were ≤0.5 mm for both large and small FOV
CT number accuracy and uniformity test for CBCT in small and large FOV	Measured and expected CT number for water, acrylic, air and LDPE agrees within±30 HU and±20 HU for SFOV and LFOV, respectively
High-contrast spatial resolution tested using CatPhan-600 for CBCT	8 lp/cm for LFOV and 7 lp/cm for SFOV
Low contrast sensitivity tested using CatPhan-600 for CBCT	15 mm @ 1%

PPS: Patient positioning system, MRD: Maximum rotational displacement, CT: Computed tomography, CBCT: Cone beam CT, FOV: Field of view, LFOV: Large FOV, SFOV: Small FOV

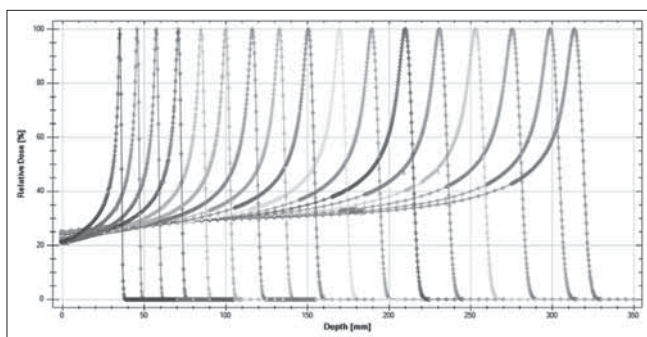


Figure 1: Normalized integrated depth doses from 70.2 to 226.2 MeV proton beam measured using large diameter StingRay parallel plate ionization chamber in water tank

corresponding calculated range (R_{90}) and the absolute difference observed in two separate measurements (inside bar plot) is shown in Figure 2a. The expected range for 70.2–226.2 MeV increases from 4.1 to 32.04 g/cm². The difference between calculated and measured ranges for the entire energy was within ±0.1 g/cm². Furthermore, the first and second sets of measured IDD agree within ±0.1 g/cm². Figure 2b shows the calculated DDF ($DDF = 0.0156 \times \text{calculated range}$) for 70.2–226.2 MeV proton energy in 10 MeV increment. The inside bar plot represents the absolute difference between calculated and measured ($R_{20} - R_{80}$) DDF. The calculated and measured DDF agrees well within ±0.08 g/cm² for all proton energies. The mean values of R_{90} for 70.2–226.2 MeV measured with Zebra MLIC and StingRay agrees within ±0.1 g/cm². The

five sets of IDD measured from 70.2 to 226.2 MeV in 10 MeV increment over the period of 8 months using Zebra MLIC were reproducible within a standard deviation (SD) of 0.05 g/cm² in R_{90} [Figure 3].

Spot Profile and position characteristics

The spot size (1σ) measured at different air gaps of 0 cm (isocenter), ±10 cm and ±20 cm from the isocenter for 70.2–226.2 MeV proton in 10 MeV increment are shown in Figure 4. The Spot sigma along X-direction [Figure 4a] varies from 2.96 mm for 226.2 MeV to 6.68 mm for 70.2 MeV at isocenter. The corresponding values in Y-direction [Figure 4b] were 3.0 mm and 6.52 mm respectively. For the same proton energy, the percentage difference in the spot sigma along X and Y direction varies from ±0.19% (±0.01 mm) up to ±4.5% (±0.15 mm) at isocenter. No correlation was observed between the magnitude of deviation and beam energy. However, the deviation between X and Y sigma increases as the air gap increases primarily due to the changes in Y spot sigma with air gap. In comparison to spot sigma measured at isocenter, the variation in spot sigma with air gap was minimal along X-direction with a maximum deviation of 0.36 mm (5.28%) for 70.2 MeV and more along Y-direction with maximum deviation of ±0.82 mm (±12.5%) for 70.2 MeV, which gradually decreases with increase in energy and attain a minimum value of ±0.21 mm (±7.15%) for 226.2 MeV. The spot sigma measured at isocenter along X and Y direction for five selective energies at four different gantry positions is shown in Table 2. In comparison to median spot size, a

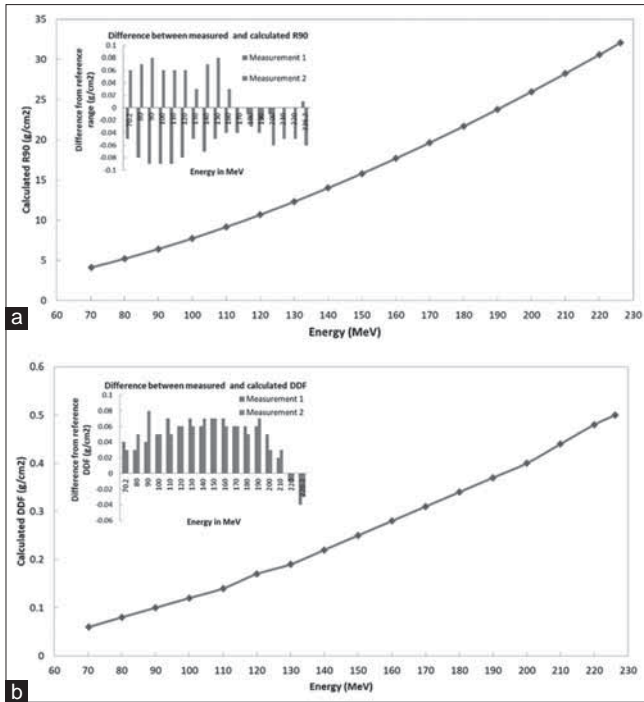


Figure 2: (a) Expected range (R_{90}) in g/cm^2 for proton energies from 70.2-226.2 MeV. Inside bar plot represent the difference in ranges between expected and from two sets of separate measurement. (b) Expected distal dose fall-off in g/cm^2 for proton energies from 70.2 to 226.2 MeV. Inside bar plot represent the difference in distal dose fall-off between expected and from two sets of separate measurement

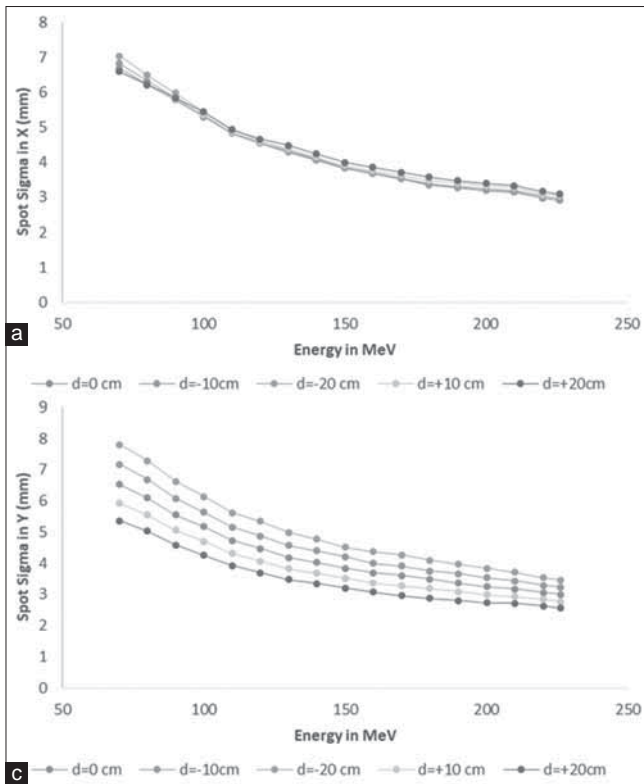


Figure 4: In-air spot size represented by one sigma (1σ) of X profile (a) and Y profile (b) of the central spot at isocenter for various air gap of 0 (isocenter) cm, ± 10 cm and ± 20 cm for proton energies ranging from 70.2–226.2 MeV in 10 MeV increment

maximum deviation of 3.56% was observed for range of 145 MeV at 220 gantry angle. The deviation between planned and measured positions of the four-corner spots with respect to central spot were within ± 0.6 mm as shown in Figure 5a. The central spot profiles of 70.2–226.2 MeV at different air gaps of 0 (isocenter), ± 10 cm and ± 20 cm were symmetric both in X and Y direction within $\pm 10\%$ [Figure 5b]. The comparison of planned and measured spot pattern/dose fluence along with the gamma analysis value for one of the representative proton energy of 226.2 MeV at 0° gantry is shown in Figure 6. In

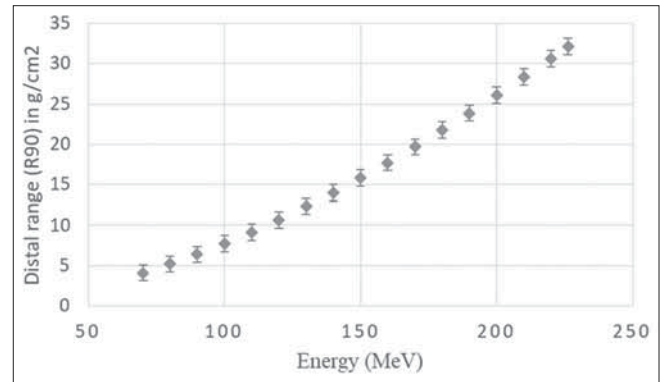


Figure 3: Variation in the distal range (R_{90}) corresponding to proton energy ranging from 70.2 to 226.2 MeV over the period of 8 months. All measurements were performed using Zebra multi-layer ionization chamber

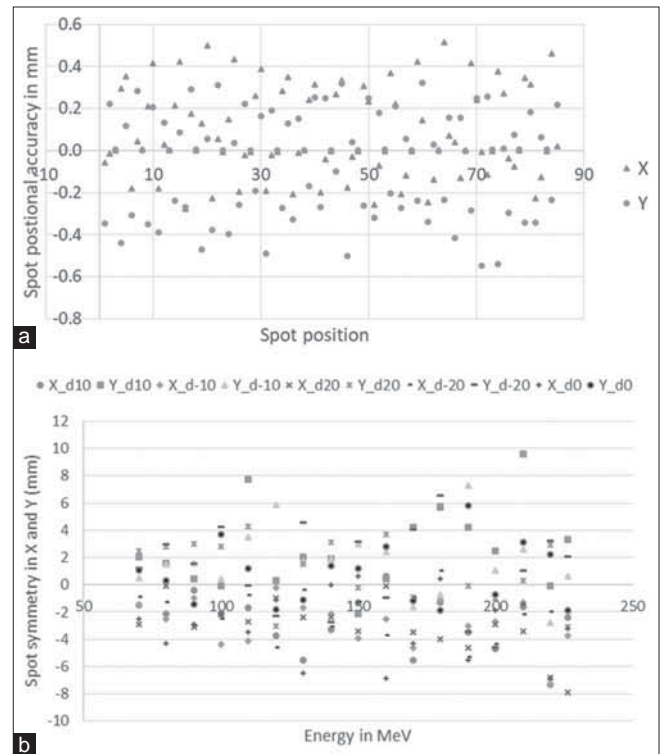


Figure 5: (a) Relative positional deviation of the four corner spots normalized with respect to the central spot for energies from 70.2 to 226.2 MeV at isocenter (air gap = 0) and for gantry 90° . (b) Symmetry in % of the central single spots along X and Y direction measured for 70.2–226.2 MeV at 10 MeV increment for gantry 90° and at different air gaps of 0 (isocenter), ± 10 cm and ± 20 cm

Table 2: The variation in spot sigma in mm along X and Y direction for different energies at different gantry angle

Gantry angle	Spot size (1σ) value in mm along X and Y direction for different energies of									
	226.2 MeV		145 MeV		115 MeV		100 MeV		70.2 MeV	
	X	Y	X	Y	X	Y	X	Y	X	Y
0	3.00	3.08	3.89	4.01	4.55	4.74	5.36	5.23	6.48	6.63
60	3.03	3.02	3.87	4.04	4.51	4.76	5.11	5.40	6.49	6.74
220	3.01	2.97	3.93	3.87	4.54	4.65	5.16	5.32	6.52	6.68
270	3.00	3.00	3.98	4.02	4.60	4.70	5.22	5.37	6.56	6.65
Median spot size	3.01	3.01	3.91	4.02	4.55	4.72	5.19	5.35	6.51	6.67
SD	0.01	0.05	0.05	0.08	0.04	0.05	0.11	0.07	0.04	0.05

SD: Standard deviation

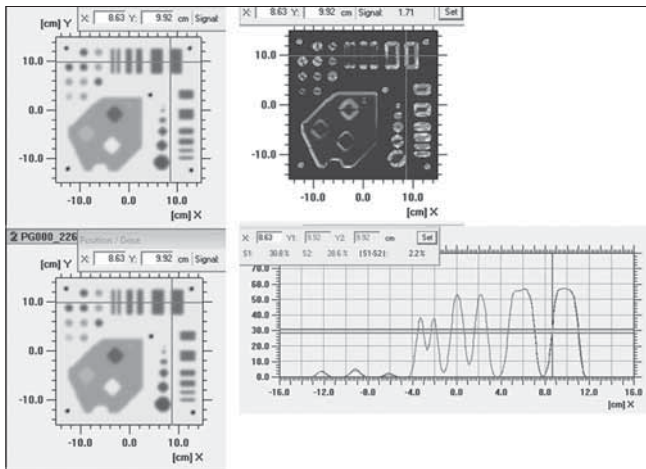


Figure 6: Comparison of planned and measured dose fluence/spot pattern along with the gamma analysis for 226.2 MeV at gantry 0°

all four gantry angles and proton energies studied, planned and measured dose distribution/spot pattern agrees with ($\gamma\% \leq 1$) greater than 97% for evaluation criteria of 1% dose difference at 1 mm distance-to-agreement (1% @ 1 mm). The average \pm SD $\gamma\%$ were $98.0 \pm 0.44\%$ for 226.2 MeV, $98.15\% \pm 0.23\%$ for 145 MeV, $98.85\% \pm 0.05\%$ for 120 MeV, $98.85\% \pm 0.23\%$ for 100 MeV and $99.35\% \pm 0.11\%$ for 70.2 MeV respectively.

Absolute calibration

The variation of output (cGy/MU) with proton energies and their reproducibility in two different days of measurement separated by a week is shown in Figure 7. The output (cGy/MU) decreases sharply in lower energy region and becomes relatively less sensitive in medium to higher energy. The maximum deviation between the two consecutive set of measurement were within $\pm 0.5\%$. The delivered MU versus the measured dose for three select proton energies is shown in Figure 8. The measured dose was linear within MU ranging from 18.5 to 8405 with regression co-efficient (R^2) value of 1.0 for all the three proton energies. The deviation between programed MU and MU monitored by the primary and secondary monitor chambers were within $\pm 0.05\%$ for set $MU \geq 400$. This deviation increases gradually by up to 0.48% for primary and 0.54% for secondary for smaller programed MU of 18.5. However, the

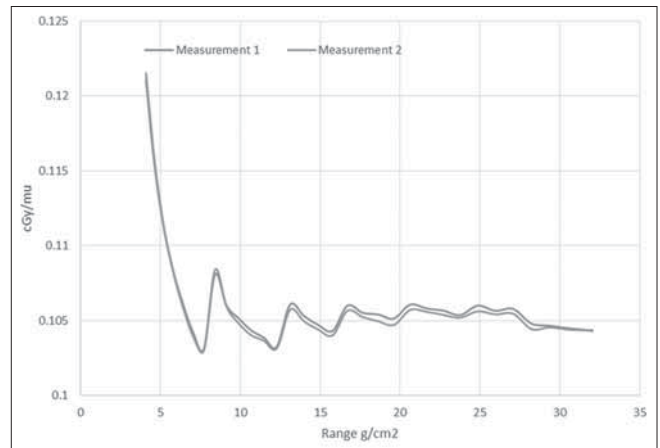


Figure 7: Variation in output (cGy/MU) from 70.2 to 226.2 MeV at 5 MeV increment at gantry 0° and at different depths of measurement in two different days separated by a week

overall absolute difference between the programmed MU and monitor chamber monitored MU were within ± 0.5 MU for both primary and secondary except for the very high programmed MU of 8405 where the secondary MU monitor recorded more by 1.21 MU. The measured dose from the scanned mono-energy field was reproducible with a co-efficient of variation of 0.07% in 15 min, 0.44% in 8 h and 0.45% in 5 consecutive days. The variation of output at different gantry angle as compared to output at gantry 0° were $< 0.8\%$.

DISCUSSION

Although the accelerator (C230 isochronous cyclotron) and beam delivery technique (PBS) used in our study is similar to the one investigated in the study by Pidikiti *et al.*,^[6] the ESS, BTS, nozzle and image guidance system differs largely and hence expect differences in electro-mechanical and proton beam characteristics. Therefore our results are not directly comparable with any of the previous publications.^[4-6] Moreover, almost all PT systems today are designed to deliver proton beam in PBS technique and the number of such installations are increasing worldwide. Thus reporting of characterization, performance, commissioning procedures and results from various PT system and delivery technique will be useful for inter comparison of new or existing PT

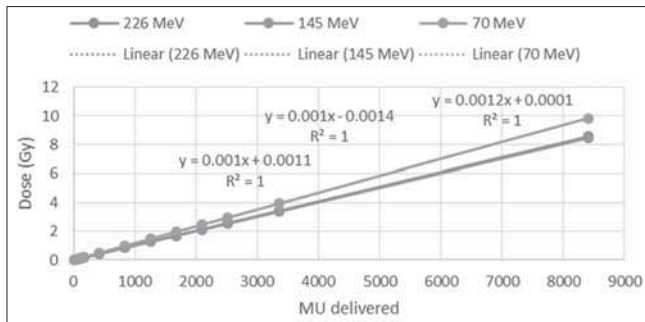


Figure 8: Linearity of the response of the dose monitoring unit over the ranges of 18.49–8405 MU for 226, 145 and 70 MeV

centres, which subsequently may help in developing a common consensus guideline and protocol.

The maximum deviation of calculated and measured R_{90} were within the specified tolerance limit of 1 mm and were comparable to the data reported by previous investigators.^[4-6] However it is slightly higher than ± 0.15 mm between FLUKA MC calculated and measurement reported by Mirandola *et al.*^[5] This could be due to the difference in depth resolution. The deviation between measured and calculated DDF were within the specified tolerance limit of 1 mm.^[6] The increase in spot size with decrease in beam energy is primarily due to the larger wide angle scatter of lower energy proton. However, the larger variation in Y-spot sigma observed at different air gap could be due to the inability of the beam optics to focus all beams at different air gaps. IBA calibrate the beam optics only to make X-and Y spot-sigma similar at isocenter. The variation of spot size with respect to gantry rotation and accuracy of relative spot positions were well within the specified limit of the manufacturer and AAPM TG224.^[3]

The output (cGy/MU) calibration for PBS techniques has been reported mostly based on a single depth (2 cm) of measurement. In our study, we have chosen different depth of measurement based on the recommendation of RayStation beam physics guide. The output (cGy/MU) was consistent for the entire energy with a maximum variation of $\leq 0.5\%$. We found a very small dependence of ion recombination factor of PPC05 with beam energy and hence corrected accordingly. Excellent results of dose linearity, reproducibly, MU accuracy, and output constancy demonstrate the capability of beam management system to deliver any number of MU between 0.01 MU/spot to 5 MU/spot with high accuracy consistently with accurate monitoring by both primary and secondary MU counters.

CONCLUSION

The performance of first gantry of Proteus235 PT facility equipped with PBS DN and CBCT at APCC is well within

the expected accuracy level. The methodology and results presented here might certainly help upcoming modern PT center during its crucial commissioning phase wherein establishing highest possible accuracy of test parameters in time sensitive project is of paramount important.

Financial support and sponsorship

Nil.

Conflicts of interest

There are no conflicts of interest.

REFERENCES

1. Loeffler JS, Durante M. Charged particle therapy--optimization, challenges and future directions. *Nat Rev Clin Oncol* 2013;10:411-24.
2. Lin L, Ainsley CG, Solberg TD, McDonough JE. Experimental characterization of two-dimensional spot profiles for two proton pencil beam scanning nozzles. *Phys Med Biol* 2014;59:493-504.
3. Arjomandy B, Taylor P, Ainsley C, Safai S, Sahoo N, Pankuch M, *et al.* AAPM task group 224: Comprehensive proton therapy machine quality assurance. *Med Phys* 2019;46:e678-e705.
4. Gillin MT, Sahoo N, Bues M, Ciangaru G, Sawakuchi G, Poenisch F, *et al.* Commissioning of the discrete spot scanning proton beam delivery system at the University of Texas M.D. Anderson Cancer Center, Proton Therapy Center, Houston. *Med Phys* 2010;37:154-63.
5. Mirandola A, Molinelli S, Vilches Freixas G, Mairani A, Gallio E, Panizza D, *et al.* Dosimetric commissioning and quality assurance of scanned ion beams at the Italian National Center for Oncological Hadrontherapy. *Med Phys* 2015;42:5287-300.
6. Pidikiti R, Patel BC, Maynard MR, Dugas JP, Syh J, Sahoo N, *et al.* Commissioning of the world's first compact pencil-beam scanning proton therapy system. *J Appl Clin Med Phys* 2018;19:94-105.
7. Bissonnette JP, Balter PA, Dong L, Langen KM, Lovelock DM, Miften M, *et al.* Quality assurance for image-guided radiation therapy utilizing CT-based technologies: A report of the AAPM TG-179. *Med Phys* 2012;39:1946-63.
8. Das IJ, Cheng CW, Watts RJ, Ahnesjö A, Gibbons J, Li XA, *et al.* Accelerator beam data commissioning equipment and procedures: Report of the TG-106 of the Therapy Physics Committee of the AAPM. *Med Phys* 2008;35:4186-215.
9. Berger MJ, Inokuti M, Andersen HH, Bichsel H, Powers D, Seltzer SM, *et al.* Stopping powers and ranges for protons and alpha particles: ICRU (International Commission on Radiation Units and Measurements) Report 49; May, 1993.
10. Arduini G, Cambria R, Canzi C, Gerardi F, Gottschalk B, Leone R, *et al.* Physical specifications of clinical proton beams from a synchrotron. *Med Phys* 1996;23:939-51.
11. Dhanesar S, Sahoo N, Kerr M, Taylor MB, Summers P, Zhu XR, *et al.* Quality assurance of proton beams using a multilayer ionization chamber system. *Med Phys* 2013;40:092102.
12. Russo S, Mirandola A, Molinelli S, Mastella E, Vai A, Magro G, *et al.* Characterization of a commercial scintillation detector for 2-D dosimetry in scanned proton and carbon ion beams. *Phys Med* 2017;34:48-54.
13. Andreo P, Burns DT, Hohlfeld K, Huq MS, Kanai T, Laitano F, *et al.* Absorbed Dose Determination in External Beam Radiotherapy: An International Code of Practice for Dosimetry Based on Standards of Absorbed Dose to Water. IAEA Technical Report Series 398. Vienna: IAEA; 2000.

Design, Fabrication, and Validation of a Polymethyl Methacrylate Head Phantom for Dosimetric Verification of Cranial Radiotherapy Treatment Plans

V. S. Shaiju, Rajesh Kumar¹, Debjani Phani, K. V. Rajasekhar², George Zacharia, Saju Bhasi, Raghuram K. Nair

Department of Radiation Physics, Regional Cancer Centre, Thiruvananthapuram, Kerala, ¹Radiological Physics and Advisory Division, Bhabha Atomic Research Centre, Mumbai, Maharashtra, ²Department of Radio Diagnosis (Head), Meenakshi Academy of Higher Education and Research, Chennai, Tamil Nadu, India

Abstract

Purpose: The present study aims to design and fabricate a novel, versatile, and cost-effective Polymethyl Methacrylate (PMMA) head phantom for the dosimetric pretreatment verification of radiotherapy (RT) treatment plans. **Materials and Methods:** The head phantom designing involves slice-wise modeling of an adult head using PMMA. The phantom has provisions to hold detectors such as ionization chambers of different sizes, Gafchromic films, gel dosimeter, and optically stimulated luminescence dosimeter. For the point dose verification purpose, 15 volumetric modulated arc therapy patient plans were selected, and doses were measured using a CC13 ionization chamber. The percentage gamma passing rate was calculated for acceptance criteria 3%/3 mm and 2%/2 mm using OmniPro I^mRT film QA software, and Gafchromic EBT3 films were used for 2D planar dose verification. **Results:** Treatment planning system calculated, and the measured point doses showed a percentage deviation ranged from 0.26 to 1.92. The planar dose fluence measurements, for set acceptance criteria of 3%/3 mm and 2%/2 mm, percentages of points having gamma value <1 were in the range of 99.17 ± 0.25 to 99.88 ± 0.15 and 93.16 ± 0.38 to 98.89 ± 0.23 , respectively. Measured dose verification indices were within the acceptable limit. **Conclusions:** The dosimetric study reveals that head phantom can be used for routine pretreatment verification for the cranial RT, especially for stereotactic radiosurgery/RT as a part of patient-specific quality assurance. The presently fabricated and validated phantom is novel, versatile, and cost-effective, and many institutes can afford it.

Keywords: Gamma analysis, head phantom, point dose

Received on: 17-03-2020

Review completed on: 12-04-2020

Accepted on: 15-04-2020

Published on: 20-07-2020

INTRODUCTION

External beam radiation therapy is among the most commonly used treatments for various tumors. Advances in radiation therapy have resulted in dose escalation and also a better precision during treatment. Due to the complex nature of the advanced treatment technique using multi-leaf collimators (MLCs), pretreatment verification is an important aspect of the quality assurance (QA) program.^[1,2] Although most treatments are performed accurately, accidents have been reported even in centers with advanced technology and experienced staff.^[3,4] Therefore, patient-specific QA (PSQA) is an essential step to ascertain that the equipment is capable of delivering the plan generated in the treatment planning system (TPS) within the acceptable tolerances.^[5-8] PSQA facilitate the clinical implementation of intensity-modulated radiotherapy (RT) delivered using MLCs. PSQA involves

measuring the point dose and analyzing the planar dose distribution from the TPS on a water-equivalent phantom material before treating a patient.

A number of verification phantoms are available commercially with different types of detectors for advanced RT techniques.^[9-12] A majority of these phantoms are made up of solid/plastic water materials, and most of them are not suitable for QA of cranial RT. Although a few phantoms are suitable like Lucy three-dimensional (3D) stereotactic radiosurgery/RT (SRS/SRT)

Address for correspondence: Ms. Debjani Phani,
Department of Radiation Physics, Regional Cancer Centre,
Thiruvananthapuram - 695 011, Kerala, India.
E-mail: debjaniphani@gmail.com

This is an open access journal, and articles are distributed under the terms of the Creative Commons Attribution-NonCommercial-ShareAlike 4.0 License, which allows others to remix, tweak, and build upon the work non-commercially, as long as appropriate credit is given and the new creations are licensed under the identical terms.

For reprints contact: WKHLRPMedknow_reprints@wolterskluwer.com

How to cite this article: Shaiju VS, Kumar R, Phani D, Rajasekhar KV, Zacharia G, Bhasi S, *et al.* Design, fabrication, and validation of a polymethyl methacrylate head phantom for dosimetric verification of cranial radiotherapy treatment plans. *J Med Phys* 2020;45:66-70.

Access this article online

Quick Response Code:



Website:
www.jmp.org.in

DOI:
10.4103/jmp.JMP_21_20

QA phantom^[13] from Standard Imaging Inc. (Middleton, WI, USA), they are very expensive (unaffordable to many centers) and some have limited measurement options especially for SRS/SRT QA. Therefore, there is a need for a low-cost QA head phantom with tissue equivalent materials, which is suitable for dosimetry QA of cranial RT using advanced RT techniques. Although the dosimetry protocols recommend performing the measurements in water, solid water substitutes are widely used because of their convenience and satisfactory results.^[14,15] For maintaining accuracy and precision in QA procedure, the physical and radiological properties of water and the phantom material should be equivalent.^[16,17]

In this work, the effort is taken to design and fabricate a protruding type novel head phantom that can contribute to PSQA with actual treatment parameters of a plan with noncoplanar beams. As an initial step, we fabricate the phantom with Polymethyl Methacrylate (PMMA) ($C_5O_2H_8$)_n as it is cheap and easily available. Article describes the head phantom design, fabrication, and also the steps involved in its validation and results.

MATERIALS AND METHODS

Head phantom design and fabrication

The phantom was designed using PMMA slabs. Commercially available PMMA slabs have a thickness ranging 10–40 mm were used. The slabs were stacked together and machined such that the external contour of the slabs matches that of an average human head with an inter-pterion distance of 14.5 cm. The average human head dimension was acquired for fabricating the phantom from the computed tomography (CT) data set of head available in our hospital. The model was sectioned in the craniocaudal direction. The inner dimensions of the PMMA slabs were tooled using a 3D Computer Numerical Control (CNC) router (Makino S56), a five-axis vertical machining centre with a spindle speed of 13,000 rpm. Figure 1 shows the phantom design, the machining process, the finished product, and the assembled phantom on the treatment couch for dose measurements. Carefully, the point of measurement was kept at the interface of two selected slices for all the detectors. This will help in identifying the plane to align the phantom using lasers during measurements. To conveniently handle and properly fix the slices, tongue and groove joints were provided on both sides of the slices. Figure 2 shows a slice drawing and the corresponding machined part. The external contour was later machined, stacking the individual slices. In addition, two PMMA cylindrical rods with 2 cm diameter were provided to secure the slices while the phantom is on the treatment couch.

A cavity of size 40 mm × 40 mm × 40 mm was provided in the region of dose measurements for positioning the different dosimetric detectors such as ionization chambers with various active volumes, gel dosimeter, radio-chromic films and optically stimulated luminescence dosimeter (OSLD). Due to the constraints in the machining of internal dimensions, cavity fillets (cuboids) were provided at the internal vertical

edges of the cavity. The cuboid inserts for various types of detectors were modeled with Creo Parametric, a 3D modeling software after physical measurements, and applying required tolerances and were machined individually on the CNC router. The cuboid inserts were machined in symmetric halves owing to the small tolerances applied, which would be subsequently glued together. The point of measurement for all detectors was positioned at the center of the cuboid. Figure 3 shows the drawing of 40 mm × 40 mm × 40 mm cuboid with a detector holder and the corresponding machined part.

Provisions for placing Gafchromic film and gel dosimeter were also included in the design. Figure 4a and b shows the schematic diagram for the gel and film inserts of

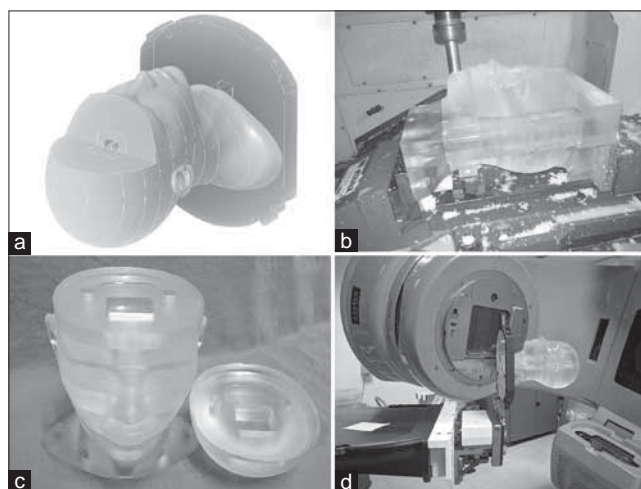


Figure 1: Head phantom concept to reality: (a) designed part (b) machining the outer contour of the phantom using a Computer numerical control machine (c) fabricated head phantom, and (d) phantom mounted on linear accelerator couch for dose measurements

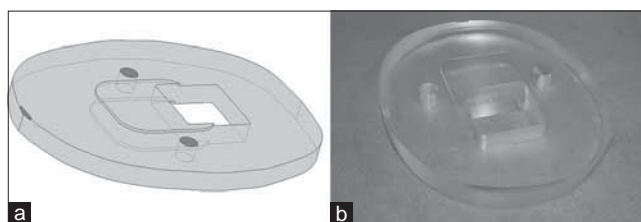


Figure 2: (a) Individually designed slice three dimensional model and (b) the corresponding machined part

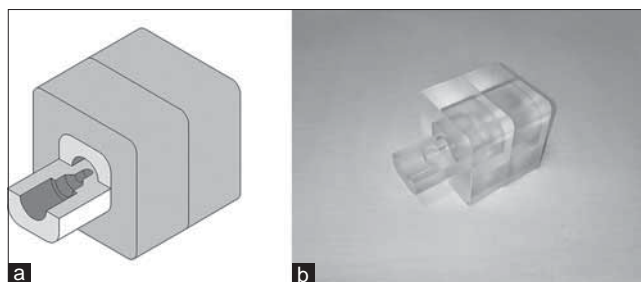


Figure 3: (a) 40 mm × 40 mm × 40 mm cuboid three dimensional model with detector insert and (b) the corresponding machined part

40 mm × 40 mm × 40 mm. Figure 4c shows the fabricated OSLD insert. Gel and OSLD inserts are intended for the future dosimetric works. Care was taken to align the point of measurement of the detectors at the center of the cuboid. The head phantom was mounted on the treatment couch using BrainLab® Stereotactic Frame Interface (BSFI) through a base plate machined out of PMMA. The base plate closely followed the inner contour of the BSFI frame. Slots were provided on this plate for the inserts.

Validation of the phantom

Point dose measurements

For this purpose, CC13 (IBA Dosimetry, Active volume 0.13 cc) ionization chamber with their holders was placed in the head phantom for evaluating the treatment plans. In our institute, CC13 ionization chamber is routinely used for the point dose measurements. CT set of the phantom with detector was taken in CT simulator (GE Optima [580W], GE Healthcare) with a slice thickness of 1.25 mm. These CT sets were imported in the Eclipse V13.7.14 (Varian Medical Systems, Palo Alto, CA, USA) TPS for creating the treatment verification plans. Figure 5 shows the sagittal view of the head phantom with a CC13 detector placed at the isocenter. Volumetric-modulated arc therapy (VMAT) verification plans of 15 patients were created with co-planar arcs. The verification plans were delivered on the head phantom in Varian Clinac iX 6 MV Medical Linear Accelerator.

Planar dose verification

As a part of PSQA, unaltered fluence of the verification plan was analyzed using-EBT3 film (Ashland, NJ, USA). For this purpose, we have selected SRT verification VMAT plans of 5 patients with field size <40 mm × 40 mm. The SRT VMAT plans include co-planar arcs (a combination of full and partial arcs) with a prescribed dose of 3.5 Gy delivered for the QA purpose. A precut 40 mm × 40 mm Gafchromic EBT3 film was placed axially at the isocentric plane that was irradiated with respective verification plans, as shown in Figure 6a. The irradiated films were scanned by a flatbed scanner (EPSON® Expression 10000XL; EPSON, UK), and the images are saved in RGB uncompressed tagged image file format, as shown in Figure 6b. Two-dimensional dosimetric analyses of films were carried out using OmniPro I^mRT (Scanditronix Wellhofer AB, Sweden) film QA software by comparing it with the unaltered planar dose pattern from TPS. To obtain the calibration curve for the External Beam Therapy (EBT) films, a set of 50 mm × 30 mm EBT3 film samples was placed perpendicular to the beam direction in a PMMA slab phantom and irradiated with 6 MV X-rays with known doses of 0, 50, 100, 150, 200, 250, 350, 450, 550, 600, and 650 cGy. A dose-response curve was plotted, and the best fit of these data was used to determine unknown dose values from the knowledge of OD of exposed films using the polynomial equation.^[17]

$$\text{Dose} = a \times \text{OD} + b \times \text{OD}^c$$

Where a, b, and c are the fitting parameters.

RESULTS AND DISCUSSION

The head phantom was designed and fabricated as per the drawings. The phantom setup found to be user friendly and firmly withstand in the cantilever position for the dose

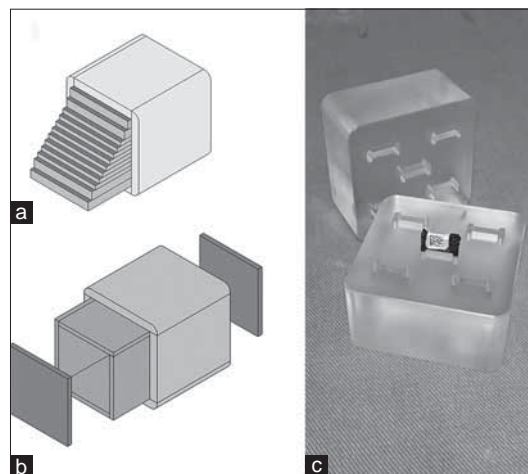


Figure 4: Cavity insert drawing with external dimension 40 mm × 40 mm × 40 mm for (a) Gel dosimetry (b) radio-chromic film and (c) fabricated optically stimulated luminescence dosimeter insert cuboid

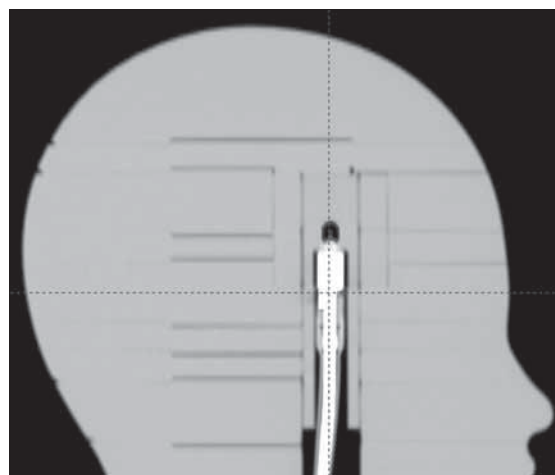


Figure 5: Sagittal computed tomography view of the head phantom with detector CC13



Figure 6: (a) 40 mm × 40 mm Gafchromic EBT3 film placed in the phantom for irradiation and (b) the exposed film with fiducial marks on the films

measurements. Moreover, SRS/SRT QA setups demand such phantoms. The cost of the head phantom is found to be about 6 to 8 times lesser than the cost of Lucy 3D SRS/SRT QA phantom and similar other commercial phantoms with equivalent features. This helps to make it affordable to many institutes. The results of VMAT verification plans of 15 patients are tabulated in Table 1. The table indicates that the relative percentage variation ranges from 0.26 to 1.92 for the head phantom. The mean percentage of deviation of 0.87% was found.

Figure 7 shows the planar dose analysis using the Gafchromic EBT3 film in the transverse plane through the isocenter of the head phantom. The gamma analysis results reveal that for set acceptance criteria of dose difference (3%) and distance to agreement (3 mm); percentages of points having gamma value <1 were in the range of 99.17 ± 0.25 to 99.88 ± 0.15 while for a set acceptance criterion of 2% and 2 mm; percentages of points having gamma value <1 were in the range of 93.16 ± 0.38 to 98.89 ± 0.23 , as shown in Table 2. During the gamma analysis, threshold dose was set to 10% of isocenter dose.

Fabricated head phantom can improve the PSQA procedures, especially for SRS/SRT techniques that need more degrees of freedom during beam delivery. Most of the RT centers use slab phantoms or other expensive commercially available phantoms such as ArcCheck phantom (Sun Nuclear Corporation, Melbourne, FL, USA), Octavius phantom (PTW®-Freiburg, Germany), etc., for the PSQA of SRS/SRT plans. It is typically placed over the couch and difficult to simulate the actual treatment positions while doing QA. Thus it fails to simulate noncoplanar treatment positions. The present head phantom can be used for the collision checks of the gantry and couch prior to the complex non-coplanar beam treatment delivery. The fabricated head phantom holds all the detectors in such a way that the point of measurement of each detector remains the same. This allows the phantom setup easier. In the present phantom, all the ionization chamber detectors are inserted through the rear side of the phantom. This avoids the chamber

connector cables from radiations as it may create noise in the signals. The design can overcome the surface irregularity

Table 1: Validation results of the head phantom using a CC13 ion chamber

Point dose measurements using a CC13 ion chamber for VMAT plans			
Number of patients	TPS dose (cGy)	Measured dose (cGy)	Percentage of variation
1	180.90	183.86	1.61
2	190.70	194.43	1.92
3	186.50	187.14	0.34
4	178.40	178.87	0.26
5	181.40	182.32	0.50
6	188.40	192.03	1.89
7	178.50	179.94	0.80
8	190.00	191.11	0.58
9	172.40	173.87	0.85
10	196.20	197.60	0.71
11	187.30	188.74	0.76
12	184.10	184.90	0.43
13	177.40	179.81	1.34
14	177.70	178.33	0.35
15	186.40	187.67	0.68
Mean percentage of deviation			0.87

VMAT: Volumetric Modulated Arc Therapy, TPS: Treatment Planning System

Table 2: Gamma analysis statistics of stereotactic radiotherapy patients in the transverse plane

Serial number of patients	Gamma Analysis (DTA, DD)	
	3 mm/3% (SD)	2 mm/2% (SD)
1	99.88±0.15	98.89±0.23
2	99.17±0.25	93.16±0.38
3	99.73±0.18	96.50±0.27
4	99.81±0.19	95.38±0.28
5	99.85±0.16	96.23±0.24

SD: Standard deviation, DD: Dose difference, DTA: Distance to agreement

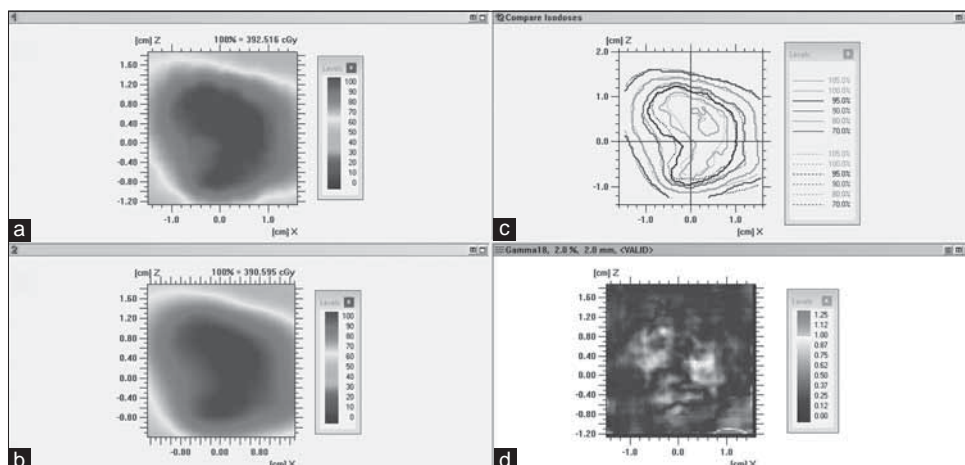


Figure 7: (a) Transverse plane film image, (b) Transverse unaltered planar dose, (c) combined isodose lines and (d) the corresponding gamma analysis

and couch attenuation factor while performing the PSQA compared to commercially available phantoms. This phantom can also be used to measure the dose to the body surface of the critical organs such as lens, thyroid using appropriate surface dosimetry detectors. Phantom measurement results are in better agreement with the TPS calculated values. The dosimetric study results show that the designed head phantom can be used for the routine pretreatment verification for the cranial RT.

CONCLUSIONS

A novel, versatile, cost-effective PMMA head phantom was designed, fabricated validated for the PSQA. Developed head phantom can be used for routine pretreatment verification for the cranial RT, especially for SRS/SRT as a part of PSQA.

Acknowledgments

We extend our sincere thanks to Dr. Thayal Singh Elias, Head, Radiation Physics Division, Regional Cancer Centre, Thiruvananthapuram, India, for his valuable support.

Financial support and sponsorship

This research work has been funded by Kerala State Council for Science, Technology, and Environment (KSCSTE), Kerala, India.

Conflicts of interest

There are no conflicts of interest.

REFERENCES

- Williams PC. IMRT: Delivery techniques and quality assurance. *Br J Radiol* 2003;76:766-76.
- Manning MA, Wu Q, Cardinale RM, Mohan R, Lauve AD, Kavanagh BD, *et al.* The effect of setup uncertainty on normal tissue sparing with IMRT for head-and-neck cancer. *Int J Radiat Oncol* 2001;51:1400-9.
- Yeung TK, Bortolotto K, Cosby S, Hoar M, Lederer E. Quality assurance in radiotherapy: Evaluation of errors and incidents recorded over a 10 year period. *Radiother Oncol* 2005;74:283-91.
- Huang G, Medlam G, Lee J, Billingsley S, Bissonnette JP, Ringash J, *et al.* Error in the delivery of radiation therapy: Results of a quality assurance review. *Int J Radiat Oncol* 2005;61:1590-5.
- Laub W, Thomas CR. Patient-specific quality assurance measurements for VMAT treatments: Do we really catch errors? *J Clin Oncol* 2013;31 Suppl 31:81.
- Polsoni M, Bartolucci F, Fidanze C, Rosica F, Orlandi G. VMAT patient specific QA: Characterization and validation of the compass system. *Phys Medica Eur J Med Phys* 2016;32:55.
- Song Y, Obcemea C, Mueller B, Mychalczak B. A systematic approach to patient specific QA for volumetric modulated arc therapy (VMAT). In: Long M, editor. *World Congress on Medical Physics and Biomedical Engineering May 26-31, 2012, Beijing, China. IFMBE Proceedings. Vol. 39.* Berlin, Heidelberg: Springer; 2013.
- Low C, Toye W, Phung P, Huston C. Patient-specific quality assurance protocol for volumetric modulated arc therapy using dose volume histogram. *J Med Phys* 2018;43:112-8.
- Benchmark™ IMRT QA Phantom. Available from: <http://bionetla.com/images/CIVCOSourcebook.pdf>. [Last accessed on 2020 May 06].
- Norfolk, VA, USA: Computerized Imaging Reference Systems, Inc. Available from: <https://www.cirsinc.com/product-category/radiation-therapy>. [Last accessed 2020 May 06].
- IBA Dosimetry AB. Uppsala, Sweden. Available from: <https://www.iba-dosimetry.com/product/qa-phantoms>. [Last accessed 2020 May 06].
- Standard Imaging. Middleton, WI, USA. Available from: <https://www.standardimaging.com/solutions>. [Last accessed on 2020 May 06].
- Lucy 3D QA Phantom. Available from: <https://www.standardimaging.com/phantoms/lucy-3d-qa-phantom>. [Last accessed on 2020 May 06].
- Constantinou C, Attix FH, Paliwal BR. A solid water phantom material for radiotherapy X-ray and γ -ray beam calibrations. *Med Phys* 1982;9:436-41.
- Arjunan M, Sekaran SC, Sarkar B, Manikandan S. A homogeneous water-equivalent anthropomorphic phantom for dosimetric verification of radiotherapy plans. *J Med Phys* 2018;43:100-5.
- Cameron M, Cornelius I, Cutajar D, Davis J, Rosenfeld A, Lerch M, *et al.* Comparison of phantom materials for use in quality assurance of microbeam radiation therapy. *J Synchrotron Radiat* 2017;24:866-76.
- Kumar R, Sharma SD, Deshpande S, Ghadi Y, Shaiju VS, Amols HI, *et al.* Acrylonitrile butadiene styrene (ABS) plastic-based low cost tissue equivalent phantom for verification dosimetry in IMRT. *J Appl Clin Med Phys* 2010;11:24-32.

Influence of Cleaned-up Commercial Knowledge-Based Treatment Planning on Volumetric-Modulated Arc Therapy of Prostate Cancer

Mikoto Tamura, Hajime Monzen, Kenji Matsumoto, Kazuki Kubo, Yoshihiro Ueda¹, Tatsuya Kamima², Masahiro Inada³, Hiroshi Doi³, Kiyoshi Nakamatsu³, Yasumasa Nishimura³

Department of Medical Physics, Graduate School of Medical Sciences, Kindai University, ¹Department of Radiation Oncology, Osaka International Cancer Institute, ²Department of Radiation Oncology, Faculty of Medicine, Kindai University, Osaka, ³Department of Radiation Oncology, The Cancer Institute Hospital, Japanese Foundation for Cancer Research, Koto, Tokyo, Japan

Abstract

Purpose: This study aimed to investigate the influence of cleaned-up knowledge-based treatment planning (KBP) models on the plan quality for volumetric-modulated arc therapy (VMAT) of prostate cancer. **Materials and Methods:** Thirty prostate cancer VMAT plans were enrolled and evaluated according to four KBP modeling methods as follows: (1) model not cleaned – trained by fifty other clinical plans (KBP_{ORIG}); (2) cases cleaned by removing plans that did not meet all clinical goals of the dosimetric parameters, derived from dose–volume histogram (DVH) (KBP_{C-DVH}); (3) cases cleaned outside the range of ± 1 standard deviation through the principal component analysis regression plots (KBP_{C-REG}); and (4) cases cleaned using both methods (2) and (3) (KBP_{C-ALL}). Rectal and bladder structures in the training models numbered 34 and 48 for KBP_{C-DVH}, 37 and 33 for KBP_{C-REG}, and 26 and 33 for KBP_{C-ALL}, respectively. The dosimetric parameters for each model with one-time auto-optimization were compared. **Results:** All KBP models improved target dose coverage and conformity and provided comparable sparing of organs at risks (rectal and bladder walls). There were no significant differences in plan quality among the KBP models. Nevertheless, only the KBP_{C-ALL} model generated no cases of $>1\%$ $V_{78\text{ Gy}}$ (prescribed dose) to the rectal wall, whereas the KBP_{ORIG}, KBP_{C-DVH}, and KBP_{C-REG} models included two, four, and three cases, respectively, which were difficult to overcome with KBP because the planning target volume (PTV) and rectum regions overlapped. **Conclusions:** The cleaned-up KBP model based on DVH and regression plots improved plan quality in the PTV–rectum overlap region.

Keywords: Cleaned-up model, knowledge-based treatment planning, plan quality, prostate cancer

Received on: 17-12-2019

Review completed on: 02-04-2020

Accepted on: 21-04-2020

Published on: 20-07-2020

INTRODUCTION

Knowledge-based treatment planning (KBP) with a machine-learning technique is an approach used to reduce variations in plan quality in high-precision radiotherapy, thereby improving planning consistency.^[1] A commercial KBP module, RapidPlan® (Varian Medical Systems, Palo Alto, CA, USA), has been released for use with the Eclipse (Varian) treatment planning system. The KBP uses a statistical model generated from a library of clinically accepted, high-quality plans to train dose–volume histograms (DVHs).^[1,2] This model predicts an achievable DVH range and generates dose–volume objectives based on the relationships between geometric and dosimetric features, to optimize intensity-modulated radiation

therapy and volumetric-modulated arc therapy (VMAT) plans.^[1,2]


Many studies have reported that KBP can generate better (or at least comparable) dosimetric results at some anatomical sites.^[1–15] Our previous study showed that KBP with one-time auto-optimization could create an acceptable VMAT plan for prostate cancer that could be used in clinical practice with no major problems concerning dosimetric accuracy or mechanical

Address for correspondence: Dr. Hajime Monzen,
377-2 Onohigashi, Osakasayama, Osaka 589-8511, Japan.
E-mail: hmon@med.kindai.ac.jp

This is an open access journal, and articles are distributed under the terms of the Creative Commons Attribution-NonCommercial-ShareAlike 4.0 License, which allows others to remix, tweak, and build upon the work non-commercially, as long as appropriate credit is given and the new creations are licensed under the identical terms.

For reprints contact: WKHLRPMedknow_reprints@wolterskluwer.com

How to cite this article: Tamura M, Monzen H, Matsumoto K, Kubo K, Ueda Y, Kamima T, *et al.* Influence of cleaned-up commercial knowledge-based treatment planning on volumetric-modulated arc therapy of prostate cancer. *J Med Phys* 2020;45:71–7.

Access this article online	
Quick Response Code: 	Website: www.jmp.org.in
	DOI: 10.4103/jmp.JMP_109_19

performance.^[10,16] Ueda *et al.* suggested that sharing the KBP model could enable other institutions to reproduce the dose distributions, although whether the registered DVH curves match the plan design of the institution required verification.^[17] However, the volumes over which high doses were delivered to organs at risks (OARs) in the KBP were inferior to those of clinical plans (CPs)^[10,16] because the doses applied to any overlapping regions of the target and OARs were not considered in the KBP system.^[18] Some reports described the effects of outliers in the KBP model on the plan quality, or investigated whether a “cleaned-up” KBP model created by removing the outlier plans or structures which have potential of the negative effect on the model could improve the plan’s quality.^[1,19–21] Aviles *et al.* showed that the DVHs estimated using cleaned-up KBP had greater accuracy.^[20] In contrast, Hussein *et al.*^[1] and Delaney *et al.*^[21] reported that statistical outliers had no significant impact on plan quality. Therefore, it remains unclear whether a cleaned-up KBP model can improve plan quality. Additionally, the modeling process itself is not completely understood.

The purpose of this study was to investigate how a cleaned-up KBP model affects the plan quality of VMAT for new prostate cancer patients. For this study, we created a cleaned-up KBP model by excluding outlying items according to the DVH and/or regression plots, and investigated whether the cleaned-up KBP model could improve the plan quality involving the target–OAR overlap region with one-time auto-optimization application, which is easy to install in a clinical situation. The one-time auto-optimization can eliminate the subjectivity and heuristics, which results in the standardization of high VMAT plan quality at many institutions.

MATERIALS AND METHODS

Volumetric-modulated arc therapy planning for prostate cancer

Thirty prostate cancer patients (T1–T2c) who underwent VMAT with CPs during 2016–2017 were selected for the KBP model validation. All VMAT plans for prostate cancer were created using 10-MV photon beams, two full arcs (gantry angles rotating clockwise from 181° to 179° and counterclockwise from 179° to 181°), and collimator angles of 30° and 330°, calculated using the Varian analytic anisotropic algorithm^[22] and the Eclipse treatment planning system (version 13.6; Varian Medical Systems, Palo Alto, CA, USA) of a TrueBeam® radiotherapy system (Varian).^[16] The clinical target volume (CTV) in the present study was defined as the prostate and seminal vesicle. It was delineated by experienced radiation oncologists. The planning target volume (PTV) was defined as a 6-mm posterior margin and a 10-mm margin in all other directions added to the CTV, to reduce the dose at the prostate–rectal interface. The OARs were the rectal and bladder walls. The rectum was delineated as a region up to 1.0 cm above and below the PTV. The rectal and bladder walls were delineated as regions 4.0 mm inside the

outer surface of the rectum and bladder. The prescribed dose was 78 Gy in 39 fractions to 95% of the volume of the PTV minus the rectum (PTV – R).^[16] All patients underwent urine collection for 1–2 h before computed tomography simulation and treatment.

The clinical goals and acceptable criteria for treatment plans in our institution are shown in Table 1.^[16,23] The overlap region between the PTV and rectal wall was covered with a 90% isodose line.

Original knowledge-based treatment planning model library

The KBP model was trained with fifty cases of T1–T2c prostate cancer treated during 2015–2016. This model was defined as the original KBP model (KBP_{ORIG}). Informed consent was obtained from all patients, and our institutional ethics committee approved this study (institutional review board number: 29–133).

The KBP model configuration and training process are well explained in the literature.^[5,7,10] The fifty structures of the PTV – R, rectum, and bladder were registered in the original KBP library. The geometric and dosimetric outliers were not excluded from this KBP_{ORIG} model.

Methods for cleaning-up the knowledge-based treatment planning model

Three cleaned-up KBP models were derived from the KBP_{ORIG} model:

1. Cleaned cases by removing the plans that did not meet the clinical goal of the dosimetric parameters; derived from DVH plots (KBP_{C-DVH} model)
2. Cleaned cases by removing the plans that were outside ±1 standard deviation (SD); derived from principal component analysis (PCA) regression plots (KBP_{C-REG} model)
3. Cleaned cases by removing the plans using the filters (1 and 2) (KBP_{C-ALL} model).

The schema of the cleaned-up KBP modeling methods are shown in Figure 1. The clean-up processes were performed using the above-mentioned methods and a Varian model

Table 1: Clinical goal and acceptable criteria for each structure in our institution

	Parameter	Clinical goal (%)	Acceptable criteria (%)
PTV-R	D _{max}		<110
	D ₉₅		100
	D _{mean}		>99, <103
Rectal wall	V _{40 Gy}	<60	<65
	V _{60 Gy}	<30	<35
	V _{70 Gy}	<20	<25
	V _{78 Gy}		<1
Bladder wall	V _{40 Gy}	<60	<65
	V _{70 Gy}		<35

PTV–R: Planning target volume minus the rectum

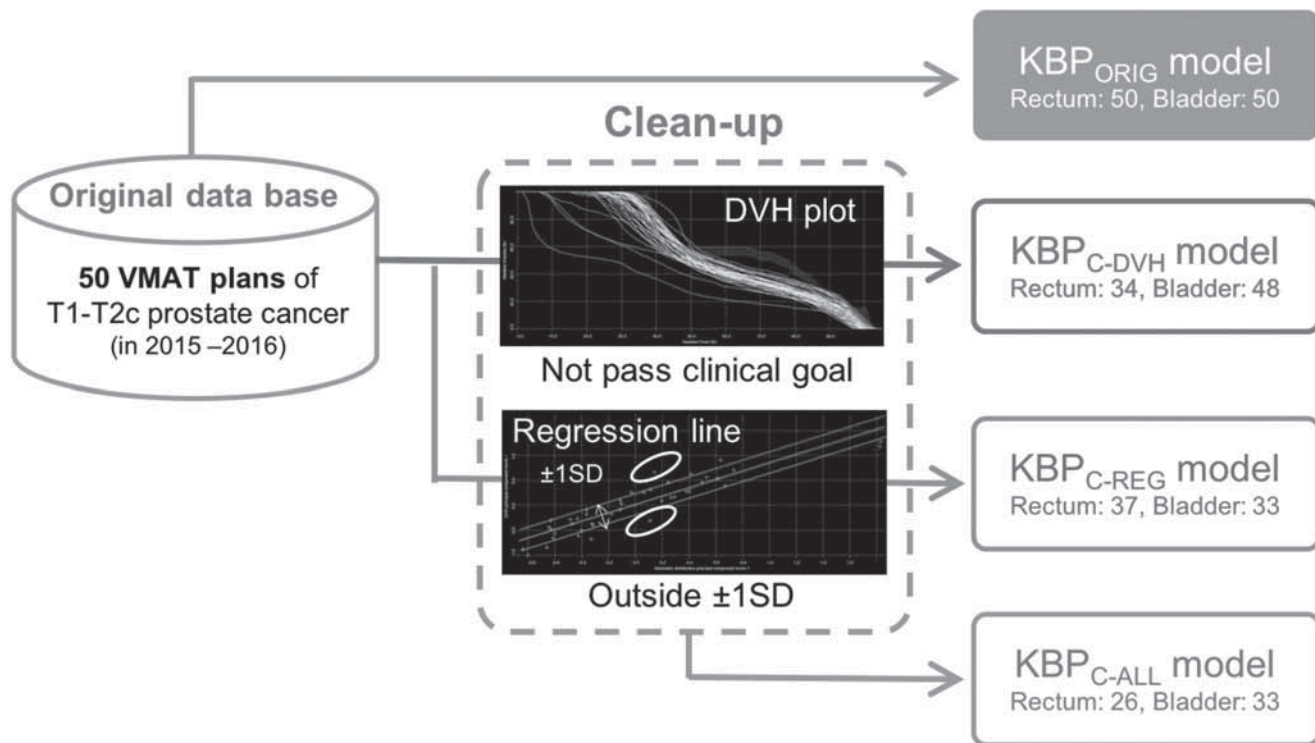


Figure 1: Schema of the cleaned-up KBP modeling methods. The KBP_{C-DVH} model was created by excluding cases that did not meet the clinical goal based on DVH plots. The KBP_{C-REG} model was created by excluding cases outside ± 1 standard deviation from PCA regression plots. Finally, the KBP_{C-ALL} model was created by excluding all cleaned-up cases as in both the KBP_{C-DVH} and KBP_{C-REG} models. KBP: Knowledge-based treatment planning, DVH: Dose–volume histogram, PCA: Principal component analysis

analytical tool.^[21] The number of rectal and bladder structures used to train the model was 34 and 48 for the KBP_{C-DVH} model, 37 and 33 for the KBP_{C-REG} model, and 26 and 33 for the KBP_{C-ALL} model, respectively. The volume of the PTV-R in all KBP models was within the range of 56.28–202.94 cm³. The rectal volume ranges for the KBP_{ORIG} , KBP_{C-DVH} , KBP_{C-REG} , and KBP_{C-ALL} models were 28.39–117.26 cm³, 28.39–116.46 cm³, 33.39–117.26 cm³, and 33.39–116.46 cm³, respectively. The bladder volume ranges for the KBP_{ORIG} , KBP_{C-DVH} , KBP_{C-REG} , and KBP_{C-ALL} models were 49.18–486.52 cm³, 58.08–486.52 cm³, 58.08–486.52 cm³, and 58.08–486.52 cm³, respectively. All objectives for the KBP models were generated automatically.

Plan evaluation

The thirty plans used for the KBP validation were compared across the CPs and four KBPs using the following dosimetric parameters.^[16]

1. Maximum (D_{max}), minimum (D_{min}), and mean (D_{mean}) doses of the PTV–R volume ($D_{95} = 100\%$)
2. Homogeneity index = $100 \times (D_{2\%} - D_{98\%})/D_{50\%}$, where $D_{98\%}$, $D_{2\%}$, and $D_{50\%}$ are doses received by 98%, 2%, and 50% of the PTV – R, respectively^[24]
3. The 95% isodose conformity index (CI_{95}) = $V_{95\%}/V_{PTV-R}$, where $V_{95\%}$ is the volume covered by 95% of the prescribed dose (74.1 Gy), and V_{PTV-R} is the PTV–R volume^[1]

4. Dose–volume parameters of the rectal wall: V_{40Gy} , V_{60Gy} , V_{70Gy} , V_{78Gy}
5. Dose–volume parameters of the bladder wall: V_{40Gy} , V_{70Gy}
6. Modulation complexity scores (MCSs) and monitor unit (MU) values.^[10] The MCS assesses the variability between multi-leaf collimator positions and the aperture opening, and has values ranging from 0 to 1, with lower values indicating greater modulation.^[1]

Statistical analysis

Data were expressed as means and SDs, unless otherwise indicated. The Wilcoxon signed-rank test was used to compare continuous variables and trends between the each KBP model and the CP. All statistical analyses were performed using R version 3.4.2 (The R Foundation for Statistical Computing, Vienna, Austria). $P < 0.05$ was considered to indicate statistical significance.

RESULTS

Table 2 summarizes the results of the dosimetric parameters and plan complexity between the each KBP model and the CP. Figures 2 and 3 compare the dose parameters between each KBP model and its CP for PTV – R and OARs.

The values of D_{min} and D_{mean} for PTV–R were comparable between the CP and all KBPs. Regarding D_{max} for PTV – R, all KBPs were statistically significantly lower than those with

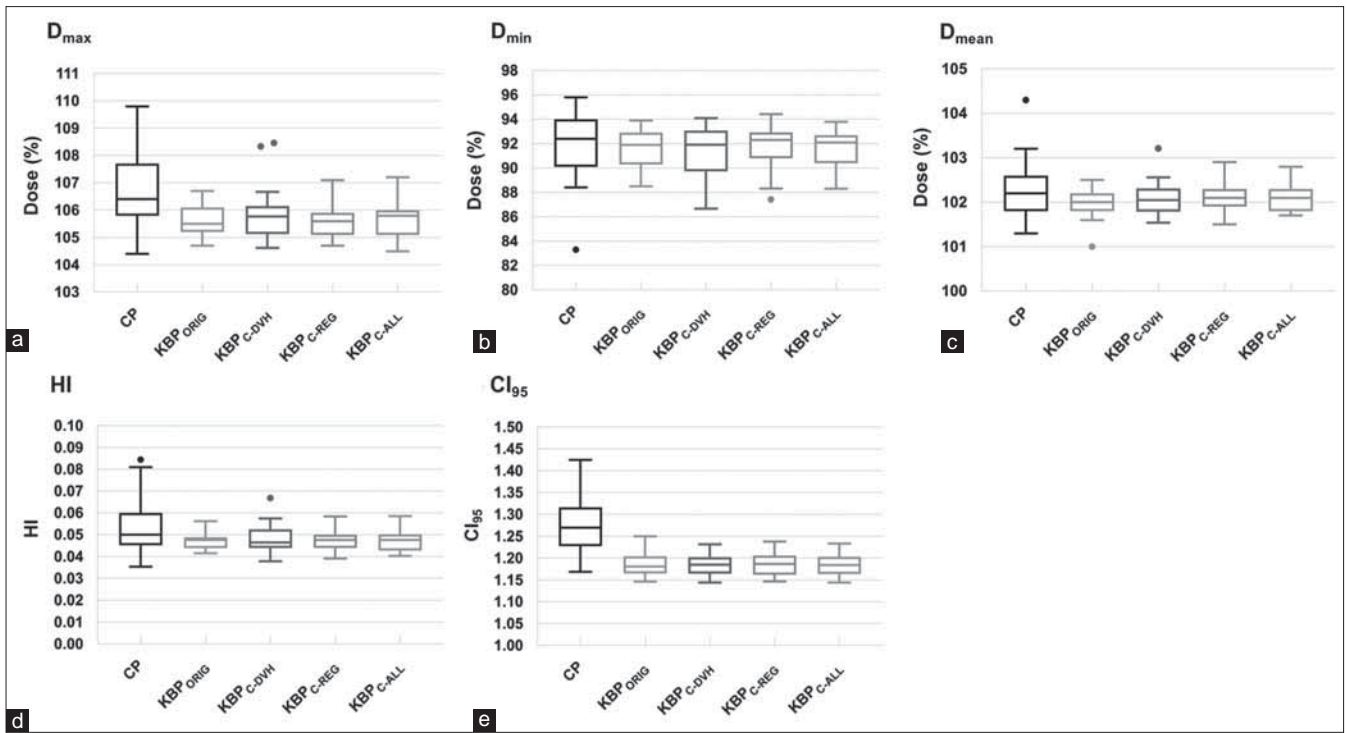


Figure 2: (a) D_{max} , (b) D_{min} , (c) D_{mean} , (d) HI, and (e) CI_{95} . Comparison of dose parameters for the PTV – R among the KBPs and the clinical plans. Middle, lower, and upper lines in each box are the median value, first quartile, and third quartile, respectively. Whisker values do not contain the outliers, which are plotted as individual points. PTV – R: Planning target volume minus the rectum, KBP: Knowledge-based treatment planning

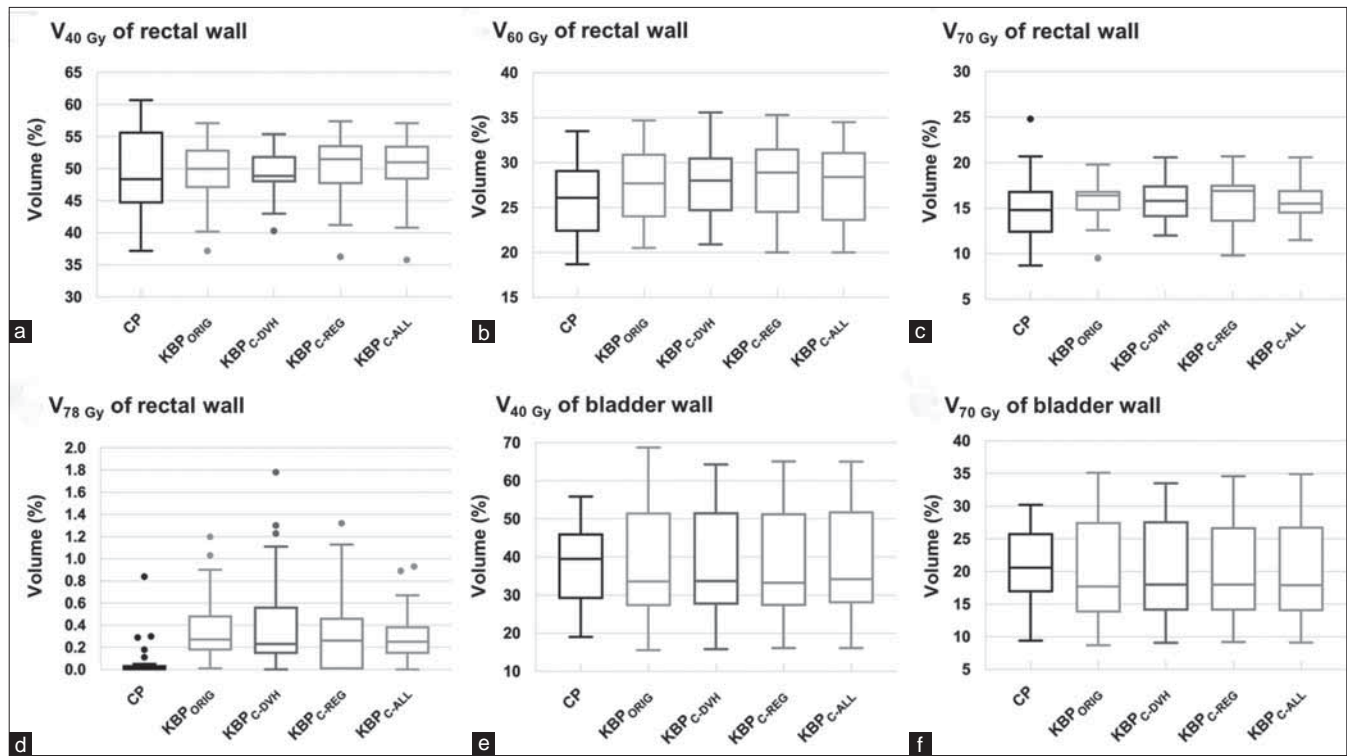


Figure 3: (a) V_{40Gy} of rectal wall, (b) V_{60Gy} of rectal wall, (c) V_{70Gy} of rectal wall, (d) V_{78Gy} of rectal wall, (e) V_{40Gy} of bladder wall, and (f) V_{70Gy} of bladder wall. Comparison of dose parameters for the organs at risks for all knowledge-based treatment plannings and clinical plans. Middle, lower, and upper lines in each box are the median value, first quartile, and third quartile, respectively. Whisker values do not contain the outliers, which are plotted as individual points.

Table 2: Dosimetric parameters and plan complexity for each knowledge-based treatment planning model and clinical plan.

	Parameter	CP	KBP _{ORIG}	KBP _{C-DVH}	KBP _{C-REG}	KBP _{C-ALL}
PTV-R	D _{max} (%)	106.63±1.31	105.61±0.50	105.77±0.93	105.63±0.54	105.66±0.69
	D _{min} (%)	91.90±2.74	91.54±1.67	91.58±1.87	91.76±1.64	91.53±1.60
	D _{mean} (%)	102.30±0.66	102.01±0.31	102.09±0.36	102.08±0.27	102.06±0.29
	HI	0.053±0.013	0.047±0.003	0.048±0.006	0.047±0.004	0.047±0.004
	CI ₉₅	1.28±0.065	1.19±0.025	1.18±0.024	1.19±0.025	1.19±0.023
Rectal wall	V _{40 Gy} (%)	48.95±6.38	49.24±4.94	49.35±3.96	50.51±4.94	50.05±5.28
	V _{60 Gy} (%)	26.90±4.32	27.62±4.32	27.58±3.94	27.85±4.69	27.52±4.54
	V _{70 Gy} (%)	15.00±3.49	15.94±2.25	15.86±2.15	15.69±2.80	15.61±2.33
	V _{78 Gy} (%)	0.07±0.17	0.35±0.29	0.44±0.47	0.33±0.36	0.29±0.24
Bladder wall	V _{40 Gy} (%)	38.56±10.80	38.34±14.38	37.91±13.38	38.36±13.75	38.23±13.71
	V _{70 Gy} (%)	21.00±6.40	20.47±6.19	20.29±7.23	20.39±7.29	20.31±7.38
MU		619.20±60.88	621.26±24.77	625.26±37.90	619.41±30.28	625.11±26.92
MCS		0.27±0.022	0.27±0.015	0.27±0.020	0.27±0.017	0.27±0.018

Results are expressed as means±1 SD. KBP: Knowledge-based treatment planning, CP: Clinical plan, MCSs: Modulation complexity scores, MU: Monitor unit, PTV-R: Planning target volume minus the rectum, SD: Standard deviation

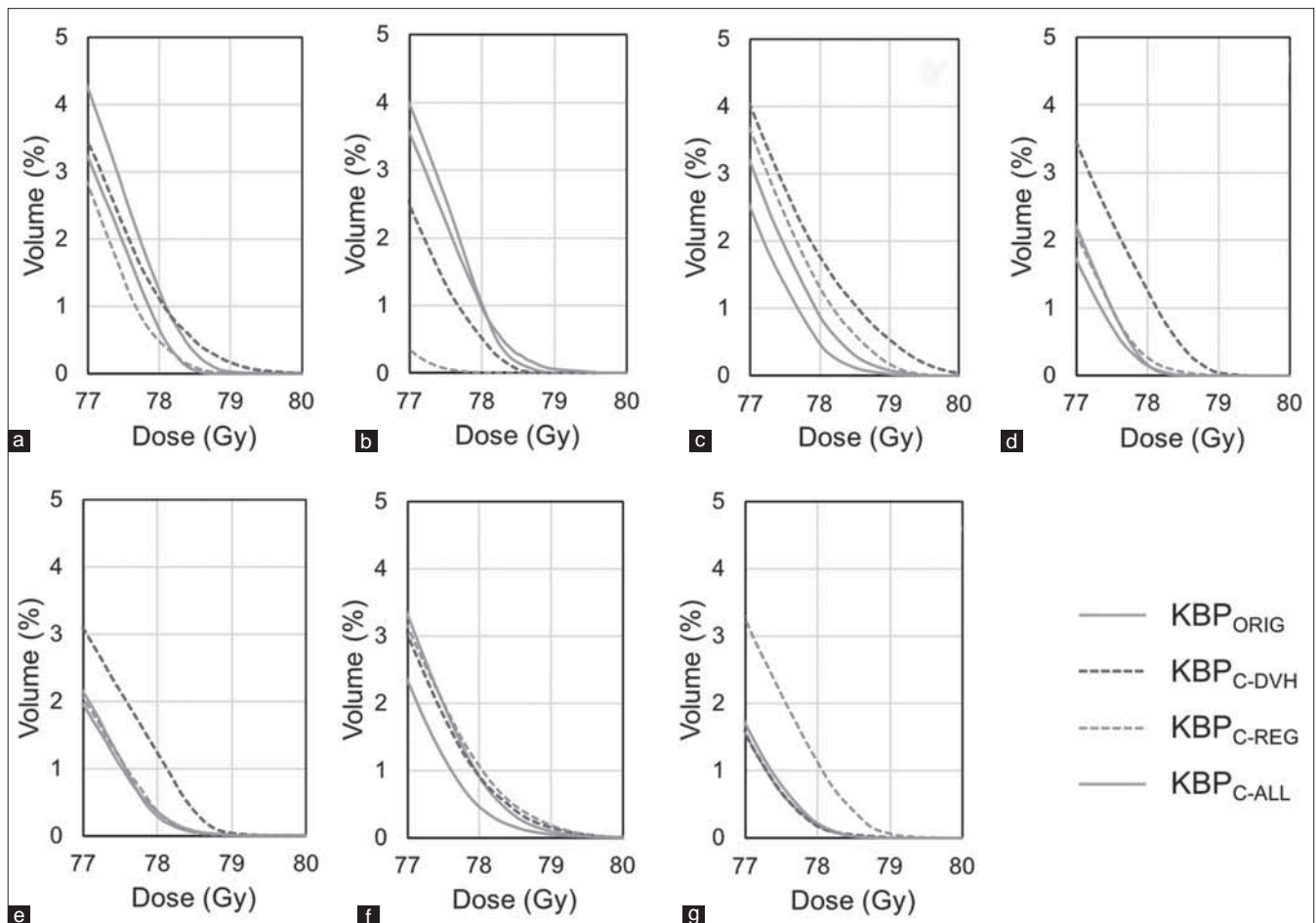


Figure 4: DVH-based curves of the rectal wall for cases that did not pass the criterion of $V_{78 \text{ Gy}} < 1\%$ for any of the four KBP models. The KBP_{ORIG}, KBP_{C-DVH}, and KBP_{C-REG} models had two cases (a and b), four cases (a and c-e), and three cases (c, f and g), respectively, that did not meet the $V_{78 \text{ Gy}} < 1\%$ criterion. The DVH curves for KBP_{ORIG}, KBP_{C-DVH}, and KBP_{C-REG} show a long tail close to the maximum dose in some cases, whereas that for KBP_{C-ALL} had no tail in any case. KBP: Knowledge-based treatment planning, DVH: Dose–volume histogram

the CP ($P < 0.001$). For the homogeneity of PTV – R, all KBPs were better than that found with the CP, although only KBP_{ORIG} showed a statistically significant difference from the CP ($P = 0.04$). Additionally, the PTV – R coverage of all KBPs was more conformal than that of the CP ($P < 0.001$). For the OARs, the dose parameters of all KBPs were comparable to those of the CP, except for the $V_{78\text{ Gy}}$ of the rectal wall. The $V_{78\text{ Gy}}$ of the rectal wall was significantly higher for all KBPs than for the CPs. However, the KBP_{C-ALL} was the only planning whose $V_{78\text{ Gy}}$ of the rectal wall was $<1\%$ for all cases, whereas KBP_{ORIG}, KBP_{C-DVH}, and KBP_{C-REG} resulted in two, four, and three cases, respectively, with a $V_{78\text{ Gy}}$ of the rectal wall $>1\%$.

Figure 4 shows the DVH curves of the cases that did not pass the criterion of $V_{78\text{ Gy}} < 1\%$ for any of the four KBP models. The DVH curves for the KBP_{ORIG}, KBP_{C-DVH}, and KBP_{C-REG} models display a long tail close to the maximum dose in some cases with $V_{78\text{ Gy}} > 1\%$, whereas none of the KBP_{C-ALL} curves show such a tail. KBP_{C-DVH} and KBP_{C-REG} had one case each with $V_{60\text{ Gy}}$ of the rectal wall $>35\%$. KBP_{ORIG} had one case with $V_{40\text{ Gy}}$ of the bladder wall $>65\%$ and one case with $V_{70\text{ Gy}}$ of the bladder wall $>35\%$, whereas KBP_{C-REG} had one case with $V_{40\text{ Gy}}$ of the bladder wall $>65\%$. Hence, only KBP_{C-ALL} fulfilled all the criteria for all cases. For the MU and MCS, there were no significant differences in CP and each KBP model.

DISCUSSION

In this study, we investigated how the cleanup of KBP models affected the quality of a VMAT plan for treating prostate cancer with one-time auto-optimization. The cleaned-up KBPs, based on DVH and regression plots, may overcome one of the characteristics of KBPs that the high-dose delivered volumes of the OARs are inferior to those of the CPs.

Other studies have also investigated the effect of a cleaned-up KBP model on plan quality.^[1,19-21] Delaney *et al.* showed the effect of dosimetric outliers for head-and-neck cancer and concluded that the cleaned-up KBP did not improve the plan quality, although the presence of many outliers deteriorated the plan quality.^[21] Hussein *et al.* established a model in the pelvic region and also noted that the cleaned-up KBP model had no significant impact.^[1] Conversely, Aviles *et al.* concluded that a cleaned-up KBP could improve the accuracy of the estimated DVHs,^[20] although its usefulness in a new patient was unclear. Our study showed that in new patients, a cleaned-up KBP model could address weak points where the PTV overlapped with an organ. The KBP_{C-ALL} model was the only one that did not generate cases with $V_{78\text{ Gy}} > 1\%$, as shown in Figures 3d and 4, although KBP_{ORIG}, KBP_{C-DVH}, and KBP_{C-REG} had two, four, and three such cases, respectively, among the thirty evaluated clinical cases. Additionally, KBP_{C-ALL} was the only model that could meet all the criteria of the dosimetric parameters, as shown in Table 2 and Figures 2 and 3, although only a few structures were used. Thus, cleaned-up KBPs could improve the accuracy of estimated DVHs, especially in regions of high-dose delivery where a long tail appears following a

close-to-maximum dose to the OARs (estimated using DVHs), as shown by Aviles *et al.*^[20]

KBPs were shown to be inferior to clinically accepted plans for the high-dose volumes delivered to OARs^[10,16] because the only priority in the KBP system was the PTV, although the line objectives for the OARs were used during the optimization process. These line objectives for the OARs were placed horizontally in the overlap region between the PTV and OARs to prevent underdosing with the PTV.^[10,18] The KBP model has heuristic factors, one of which may be manual clean-up modeling derived from both DVH and PCA regression plots, although the upgraded version of the KBP software may solve this problem. This KBP modeling method may be helpful for updating the KBP model and for creating a KBP model that could be used in treatment sites with many overlap regions, such as in head-and-neck cancer. The performance of the cleaned-up database has been described; few got some advantages, whereas few did not get any.^[21] Cleaning up the database may be an obvious fact; however, no previous reports described step-wise outlier cleanup of the database. In this study, we showed that the KBP_{C-ALL} model could improve plan quality in the overlap region, while the KBP_{C-DVH} and KBP_{C-REG} models might be inferior to the CP and the plans generated with the original model. Cleaning up of a KBP model must be performed carefully with adequate model validations.

CONCLUSIONS

The cleaned-up KBP model created using both DVH and PCA regression plots could improve plan quality, especially for overlap regions, without causing any deterioration in the coverage of the target with one-time auto-optimization for prostate VMAT.

Acknowledgment

We thank Nancy Schatken, BS, MT (ASCP), from Edanz Group (www.edanzediting.com/ac), for editing a draft of this manuscript.

Financial support and sponsorship

This work was supported by the Japan Society for the Promotion of Science KAKENHI (grant number: 16K10406) and the Japanese Society of Radiological Technology (JSRT) Research Grant (2019, 2020).

Conflicts of interest

There are no conflicts of interest.

REFERENCES

- Hussein M, South CP, Barry MA, Adams EJ, Jordan TJ, Stewart AJ, *et al.* Clinical validation and benchmarking of knowledge-based IMRT and VMAT treatment planning in pelvic anatomy. *Radiother Oncol* 2016;120:473-9.
- Wu H, Jiang F, Yue H, Li S, Zhang Y. A dosimetric evaluation of knowledge-based VMAT planning with simultaneous integrated boosting for rectal cancer patients. *J Appl Clin Med Phys* 2016;17:78-85.
- Tol JP, Delaney AR, Dafele M, Slotman BJ, Verbakel WF. Evaluation of a knowledge-based planning solution for head and neck cancer. *Int J*

- Radiat Oncol Biol Phys 2015;91:612-20.
4. Fogliata A, Wang PM, Belosi F, Clivio A, Nicolini G, Vanetti E, *et al.* Assessment of a model based optimization engine for volumetric modulated arc therapy for patients with advanced hepatocellular cancer. *Radiat Oncol* 2014;9:236.
 5. Fogliata A, Belosi F, Clivio A, Navarria P, Nicolini G, Scorsetti M, *et al.* On the pre-clinical validation of a commercial model-based optimisation engine: Application to volumetric modulated arc therapy for patients with lung or prostate cancer. *Radiother Oncol* 2014;113:385-91.
 6. Fogliata A, Nicolini G, Bourgier C, Clivio A, de Rose F, Fenoglietto P, *et al.* Performance of a Knowledge-Based Model for Optimization of Volumetric Modulated Arc Therapy Plans for Single and Bilateral Breast Irradiation. *PLoS One* 2015;10:e0145137.
 7. Fogliata A, Nicolini G, Clivio A, Vanetti E, Laksar S, Tozzi A, *et al.* A broad scope knowledge based model for optimization of VMAT in esophageal cancer: Validation and assessment of plan quality among different treatment centers. *Radiat Oncol* 2015;10:220.
 8. Chin Snyder K, Kim J, Reding A, Fraser C, Gordon J, Ajlouni M, *et al.* Development and evaluation of a clinical model for lung cancer patients using stereotactic body radiotherapy (SBRT) within a knowledge-based algorithm for treatment planning. *J Appl Clin Med Phys* 2016;17:263-75.
 9. Chang AT, Hung AW, Cheung FW, Lee MC, Chan OS, Philips H, *et al.* Comparison of planning quality and efficiency between conventional and knowledge-based algorithms in nasopharyngeal cancer patients using intensity modulated radiation therapy. *Int J Radiat Oncol Biol Phys* 2016;95:981-90.
 10. Kubo K, Monzen H, Ishii K, Tamura M, Kawamorita R, Sumida I, *et al.* Dosimetric comparison of rapidplan and manually optimized plans in volumetric modulated arc therapy for prostate cancer. *Phys Med* 2017;44:199-204.
 11. Kamima T, Ueda Y, Fukunaga JI, Shimizu Y, Tamura M, Ishikawa K, *et al.* Multi-institutional evaluation of knowledge-based planning performance of volumetric modulated arc therapy (VMAT) for head and neck cancer. *Phys Med* 2019;64:174-81
 12. Kubo K, Monzen H, Ishii K, Tamura M, Nakasaka Y, Kusawake M, *et al.* Inter-planner variation in treatment-plan quality of plans created with a knowledge-based treatment planning system. *Phys Med* 2019;67:132-40.
 13. Ueda Y, Miyazaki M, Sumida I, Ohira S, Tamura M, Monzen H, *et al.* Knowledge-based planning for oesophageal cancers using a model trained with plans from a different treatment planning system. *Acta Oncol* 2020;59:274-83.
 14. Inoue E, Doi H, Monzen H, Tamura M, Inada M, Ishikawa K, *et al.* Dose-volume histogram analysis of knowledge-based volumetric-modulated arc therapy planning in postoperative breast cancer irradiation. *In Vivo* 2020;34:1095-101.
 15. Uehara T, Monzen H, Tamura M, Ishikawa K, Doi H, Nishimura Y. Dose-volume histogram analysis and clinical evaluation of knowledge-based plan with manual objective constraints for pharyngeal cancer. *J Radiat Res* 2020;61:499-505.
 16. Tamura M, Monzen H, Matsumoto K, Kubo K, Otsuka M, Inada M, *et al.* Mechanical performance of a commercial knowledge-based VMAT planning for prostate cancer. *Radiat Oncol* 2018;13:163.
 17. Ueda Y, Fukunaga JI, Kamima T, Adachi Y, Nakamatsu K, Monzen H. Evaluation of multiple institutions' models for knowledge-based planning of volumetric modulated arc therapy (VMAT) for prostate cancer. *Radiat Oncol* 2018;13:46.
 18. Tol JP, Dahele M, Delaney AR, Slotman BJ, Verbakel WF. Can knowledge-based DVH predictions be used for automated, individualized quality assurance of radiotherapy treatment plans? *Radiat Oncol* 2015;10:234.
 19. Fogliata A, Reggiori G, Stravato A, Lobefalo F, Franzese C, Franceschini D, *et al.* RapidPlan head and neck model: The objectives and possible clinical benefit. *Radiat Oncol* 2017;12:73.
 20. Aviles JE, Marcos MI, Sasaki D, Sutherland K, Kane B, Kuusela E. Creation of knowledge-based planning models intended for large scale distribution: Minimizing the effect of outlier plans. *J Appl Clin Med Phys* 2018;19:215-26.
 21. Delaney AR, Tol JP, Dahele M, Cuijpers J, Slotman BJ, Verbakel WF. Effect of dosimetric outliers on the performance of a commercial knowledge-based planning solution. *Int J Radiat Oncol Biol Phys* 2016;94:469-77.
 22. Esch A Van, Tillikainen L, Huyskens DP. Testing of the analytical anisotropic algorithm for photon dose calculation. *Med Phys* 2006;33:4130-48.
 23. Norihisa Y, Mizowaki T, Takayama K, Miyabe Y, Matsugi K, Matsuo Y, *et al.* Detailed dosimetric evaluation of intensity-modulated radiation therapy plans created for stage C prostate cancer based on a planning protocol. *Int J Clin Oncol* 2012;17:505-11.
 24. Wu H, Jiang F, Yue H, Zhang H, Wang K, Zhang Y. Applying a RapidPlan model trained on a technique and orientation to another: A feasibility and dosimetric evaluation. *Radiat Oncol* 2016;11:108.

Evaluation of Dose Distribution and Normal Tissue Complication Probability of a Combined Dose of Cone-Beam Computed Tomography Imaging with Treatment in Prostate Intensity-Modulated Radiation Therapy

Tetsuya Tomita^{1,2}, Tomonori Isobe³, Yoshinobu Furuyama⁴, Hideyuki Takei³, Daisuke Kobayashi^{1,2}, Yutaro Mori³, Toshiyuki Terunuma³, Eisuke Sato⁵, Hiroshi Yokota², Takeji Sakae³

¹Graduate School of Comprehensive Human Sciences, University of Tsukuba, Ibaraki, ²Department of Radiology, University of Tsukuba Hospital, Ibaraki,

³Faculty of Medicine, University of Tsukuba, Ibaraki, ⁴Department of Radiology, Chiba University Hospital, Chiba,

⁵Faculty of Health Sciences, Juntendo University, Tokyo, Japan

Abstract

Purpose: The purpose of this study is to evaluate the effects of cone-beam computed tomography (CBCT) on dose distribution and normal tissue complication probability (NTCP) by constructing a comprehensive dose evaluation system for prostate intensity-modulated radiation therapy (IMRT). **Methods:** A system that could combine CBCT and treatment doses with MATLAB was constructed. Twenty patients treated with prostate IMRT were studied. A mean dose of 78 Gy was prescribed to the prostate region, excluding the rectal volume from the target volume, with margins of 4 mm to the dorsal side of the prostate and 7 mm to the entire circumference. CBCT and treatment doses were combined, and the dose distribution and the NTCP of the rectum and bladder were evaluated. **Results:** The radiation dose delivered to 2% and 98% of the target volume increased by 0.90 and 0.74 Gy on average, respectively, in the half-fan mode and on average 0.76 and 0.72 Gy, respectively, in the full-fan mode. The homogeneity index remained constant. The percent volume of the rectum and bladder irradiated at each dose increased slightly, with a maximum increase of <1%. The rectal NTCP increased by approximately 0.07% from 0.46% to 0.53% with the addition of a CBCT dose, while the maximum NTCP in the bladder was approximately 0.02%. **Conclusions:** This study demonstrated a method to evaluate a combined dose of CBCT and a treatment dose using the constructed system. The combined dose distribution revealed increases of <1% volume in the rectal and bladder doses and approximately 0.07% in the rectal NTCP.

Keywords: Cone-beam computed tomography, image-guided radiation therapy, imaging dose, intensity-modulated radiation therapy, normal tissue complication probability

Received on: 16-01-2020

Review completed on: 02-03-2020

Accepted on: 31-03-2020

Published on: 20-07-2020

INTRODUCTION

In recent years, with the advancement of radiation therapy technology, intensity-modulated radiation therapy (IMRT) has become popular. IMRT is an irradiation method that locally administers a high dose to a tumor while sparing the surrounding normal tissues. For IMRT for prostate cancer, as there are risk organs – particularly the rectum and the bladder – near the prostate, a steep dose distribution is formed at the boundary between the prostate and the risk organs. If there is any deviation from the computed tomography (CT) image in the patient setup during

treatment, not only will the dose delivered to the prostate be insufficient, but also a high dose may be administered to the surrounding normal organs. Therefore, a treatment plan that considers both the patient setup during treatment and anatomical variations is important.

Address for correspondence: Prof. Tomonori Isobe,
1-1-1 Tennodai, Tsukuba, Ibaraki, Japan.
E-mail: tiso@md.tsukuba.ac.jp

This is an open access journal, and articles are distributed under the terms of the Creative Commons Attribution-NonCommercial-ShareAlike 4.0 License, which allows others to remix, tweak, and build upon the work non-commercially, as long as appropriate credit is given and the new creations are licensed under the identical terms.

For reprints contact: WKHLRPMedknow_reprints@wolterskluwer.com

How to cite this article: Tomita T, Isobe T, Furuyama Y, Takei H, Kobayashi D, Mori Y, *et al.* Evaluation of dose distribution and normal tissue complication probability of a combined dose of cone-beam computed tomography imaging with treatment in prostate intensity-modulated radiation therapy. *J Med Phys* 2020;45:78-87.

Access this article online

Quick Response Code:



Website:
www.jmp.org.in

DOI:
10.4103/jmp.JMP_4_20

This challenge has been significantly addressed by the introduction of image-guided radiation therapy (IGRT). IGRT is a reference technology that reproduces the irradiation position determined in the treatment plan by measuring and correcting the patient position displacement during treatment. It is based on the image information obtained immediately before and during irradiation at various frequencies depending on the facility.^[1-4] The images are obtained with on-board kV imagers, oblique X-ray imagers, or cone-beam computed tomography (CBCT). Therefore, IGRT involves radiation exposure, and the absorbed imaging doses measured at the skin surface have been reported as 0.2–0.6 mGy in two-directional imaging with on-board kV imagers, 0.3–0.6 mGy with oblique X-ray imagers, and 30–60 mGy with CBCT.^[5-7] Even if the imaging dose is small, it cannot be ignored when a large number of fractions is required, such as the 30 or more fractions needed for IMRT for prostate cancer. Obtaining images by CBCT after 39 prostate IMRT fractions result in an approximately 1 Gy dose at the isocenter.^[8] Hence, patients are exposed to a considerable CBCT imaging dose.

Ding *et al.* calculated the imaging doses of various devices used in IGRT through Monte Carlo (MC) simulations and showed the imaging dose distribution in a patient's body.^[9-12] However, the total dose, including the imaging dose, was not evaluated in their study. Although some studies reported methods to combine the imaging dose with the treatment dose,^[13-15] none of them have evaluated the combined dose on clinical CT images with contours using MC simulation. According to the American Association of Physicists in Medicine (AAPM) Task Group 180 Report, the imaging dose should be included in the prescription dose if the imaging dose exceeds 5% of the prescription dose.^[16] However, this report did not show how to evaluate the combined dose, which is the sum of the imaging dose and the treatment dose. Furthermore, the radiation treatment planning system (RTPS) currently used in clinical practice cannot determine the imaging dose from IGRT image acquisition and thus cannot comprehensively evaluate the total dose.

Therefore, this study aims to demonstrate a method to evaluate the combined dose of CBCT imaging and the treatment dose in prostate IMRT. For this purpose, we constructed a system that can calculate the CBCT dose and add it to the treatment dose. Furthermore, this system can evaluate changes in dose distribution and normal tissue complication probability (NTCP).

METHODS

Patients and treatment planning

The subjects were 20 patients who underwent prostate IMRT at the University of Tsukuba Hospital from 2015 to 2018. The treatment plan for prostate IMRT was created using Pinnacle v9.10 (Philips Medical Systems, Fitchburg, WI, USA). The clinical target volume included the whole prostate with a seminal vesicle base of approximately 1 cm, plus a 4-mm

margin on the dorsal side and a 7-mm margin in all other directions as the margins of the planning target volume (PTV). The prescription dose was set such that the D_{mean} of the region, excluding the rectal volume from the PTV (PTV–rectum), was 78 Gy with $\pm 1\%$ error. The dose constraints were as follows: <14%, 22%, and 34% of the rectum volume receiving more than 60 Gy (V_{60}), V_{50} , and V_{35} , respectively, and <30% and 50% of the bladder receiving V_{60} and V_{45} , respectively. This study was conducted after obtaining approval from the Clinical Research Ethics Review Committee (H29-076).

Construction of a comprehensive dose evaluation system

A system that could comprehensively evaluate the treatment dose determined using the RTPS and CBCT dose was constructed with MATLAB r2018b. Figure 1 shows an overview of the system. It can perform MC simulations with the CT images used for treatment planning and dose-volume histogram (DVH) analysis after dose summation using organ structures.

The MC code EGSnrc/BEAMnrc was used.^[17-20] An on-board imager v1.6 (OBI; Varian Medical Systems, Palo Alto, CA, USA), X-ray source, inherent filter, aperture, and two types of bowtie (half-bowtie and full-bowtie) filters were simulated. A phase space file with a tube voltage of 125 kV at 50 cm from the X-ray source was created in the simulation. The geometric structure and materials of each component were simulated according to the drawings provided by Varian Medical Systems. Figure 2 shows the constructed simulation system.

To confirm the accuracy of the constructed simulation system, the calculated values of the percent depth dose (*PDD*) and off-center ratio (*OCR*) in water were compared with those measured using an ionization chamber. The simulation was performed by creating a water phantom measuring 30 cm \times 30 cm \times 30 cm (W \times L \times H) using the EGSnrc/DOSXYZnrc code.^[21] The calculated voxel size was set to 1 cm \times 1 cm \times 0.2 cm up to a depth of 1 cm, 1 cm \times 1 cm \times 0.5 cm up to a depth of 2 cm, and 1 cm \times 1 cm \times 1 cm for deeper positions to obtain the *PDD* and 0.5 cm \times 0.5 cm \times 0.5 cm to obtain depths of 1 and 5 cm for the *OCR*. The simulation settings included photoelectron angular sampling, Rayleigh scattering, atomic relaxation, spin effects, and electron impact ionization. The photon and electron cutoff energies were both set to 1 keV. Measurements were performed using a Farmer-type ionization chamber TM30013 (PTW, Freiburg, Germany) in a three-dimensional water phantom, with the *PDD* up to a depth of 20 cm and *OCR* at 1 and 5 cm depths. The field size was 30.3 cm \times 20.6 cm when the half-bowtie filter was installed and 27.2 cm \times 18.4 cm when the full-bowtie filter was installed.

The DOSXYZnrc code was used for the simulation with CT images of the patients. The DICOM format CT volume image of each patient was imported into the MC simulation system using the CTCREATE code.^[21] Each voxel in the DICOM image was converted from the CT value to a specific material such as air, lung, tissue, bone, and density, and the MC simulations were performed.

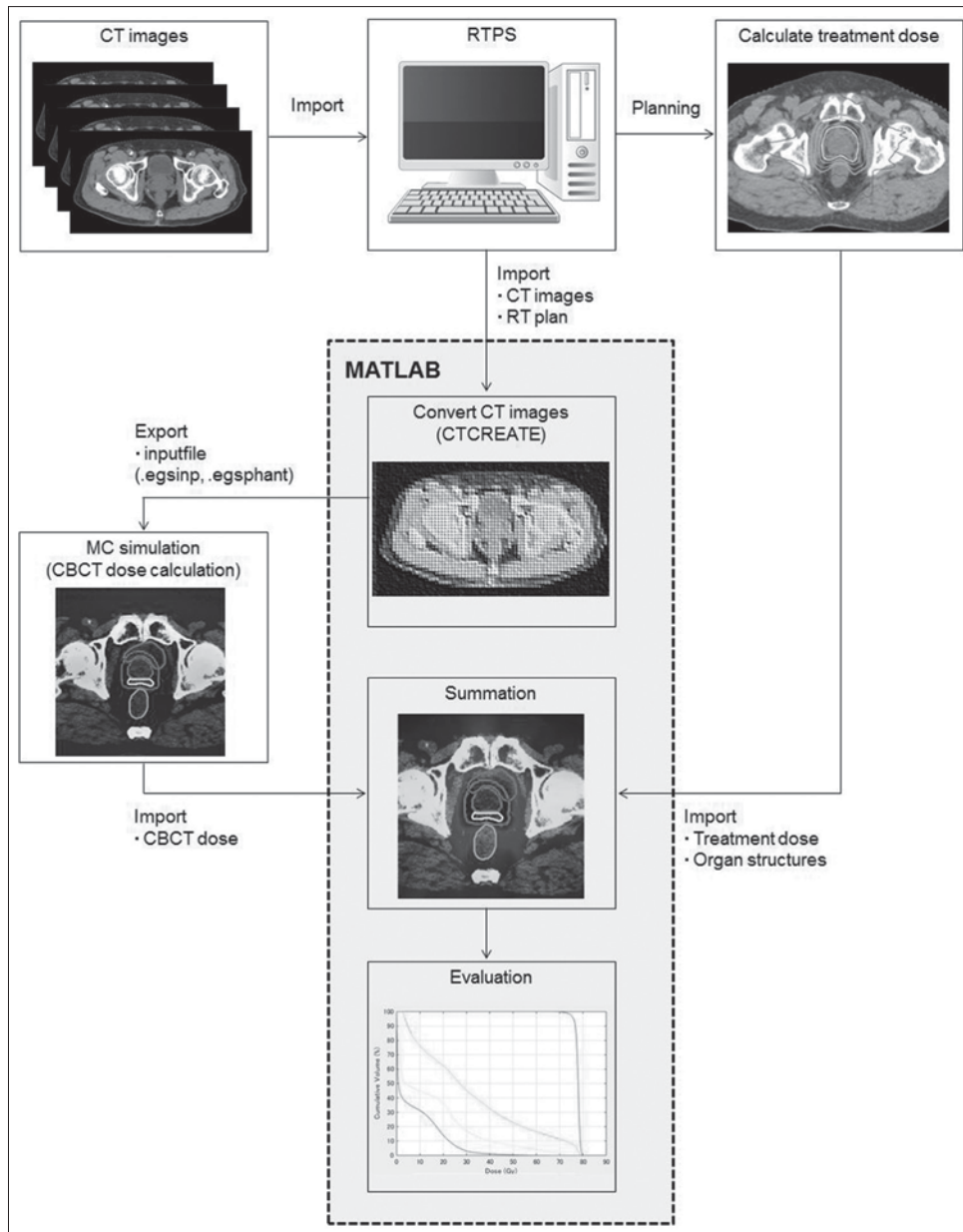


Figure 1: Schematic of our methodology. The computed tomography images used for the treatment plan and the drawn organ structure were imported into the program constructed in MATLAB. The cone-beam computed tomography dose was calculated through Monte Carlo simulation using the isocenter and treatment fractionation set in the treatment plan. Dose-volume histogram can be determined by adding the calculated cone-beam computed tomography and treatment doses calculated using the radiation treatment planning system

Monte Carlo simulation calibration

Using CT images used for treatment planning, the MC calculations were calibrated to accurately obtain the CBCT dose. The MC simulation of the CBCT dose was performed using the planning CT images of a water-equivalent polystyrene elliptical phantom (I^mmRT phantom, IBA Dosimetry, Schwarzenbruck, Germany) with a detector inserted. Using the same geometry, we measured the CBCT dose using a Farmer-type ionization chamber TM30013 and converted it to the absorbed dose as follows:^[22]

$$D_w = MN_k P_{Q, \text{cham}} \left(\frac{\bar{\mu}_{\text{en}}}{\rho} \right)_{\text{air}}^w \quad (1)$$

where D_w is the absorbed dose in water at a point in the water phantom, M is the charge with various corrections, N_k is the air kerma calibration coefficient, $P_{Q, \text{cham}}$ is the correction factor for the change in the chamber response, and $\left(\bar{\mu}_{\text{en}} / \rho \right)_{\text{air}}^w$ is the water-to-air ratio of the mean mass energy absorption coefficient. N_k was measured as the calibration factor from the charge of the Farmer-type ionization chamber TM30013 to the air kerma using the Accu-gold + ionization chamber (Radcal, Monrovia, CA, USA). $P_{Q, \text{cham}}$ and $\left(\bar{\mu}_{\text{en}} / \rho \right)_{\text{air}}^w$ were obtained from the literature.^[22] Calibration was performed by comparing the measured and MC-calculated absorbed doses at the center

of the elliptical phantom, and the doses measured at eight other points were used to validate the MC calculations [Figure 3]. The calibration coefficient f_{MCcal} for converting the calculated MC value into the absorbed dose in the phantom was obtained as:

$$f_{MCcal} = \frac{D_{exp}}{D_{MCcal}} \quad (2)$$

where D_{exp} is the measured absorbed dose at the center of the elliptical phantom and D_{MCcal} is the MC-calculated value at the center of the elliptical phantom. Table 1 presents the CBCT imaging conditions for dose measurements.

Evaluation of organ dose and dose distribution

To evaluate the imaging dose for the pelvic CBCT (half-fan mode and full-fan mode), CBCT was performed 39 times. Subsequently, the doses that were delivered to 2% (D_2) and 50% (D_{50}) of volumes of the prostate, rectum, bladder, and pelvis were calculated. To compare the dose distribution of the prostate IMRT treatment plan alone and the IMRT plan combined with the CBCT dose, we analyzed the DVH of the target and risk organs. The target was evaluated using the D_2 and D_{98} of the PTV–rectum and the homogeneity index (HI), defined as $(D_2 - D_{98})/D_{50}$.^[23] The risk organs were evaluated using D_2 and D_{50} of the rectum, bladder, and pelvic bones; V_{75} , V_{70} , V_{65} , and V_{60} of the rectum; and V_{80} , V_{75} , V_{70} , and V_{40} of the bladder, with and without CBCT.

Table 1: Default cone-beam computed tomography pelvic imaging conditions (pelvis and pelvis spotlight)

	Pelvis (half-fan mode)	Pelvis spotlight (full-fan mode)
Tube voltage (kV)	125	125
Tube current (mA)	80	80
Exposure time (ms)	13	25
Gantry rotation angle (°)	92-88	292-88
Exposure (mAs)	695	740
Filter	Half-bowtie	Full-bowtie

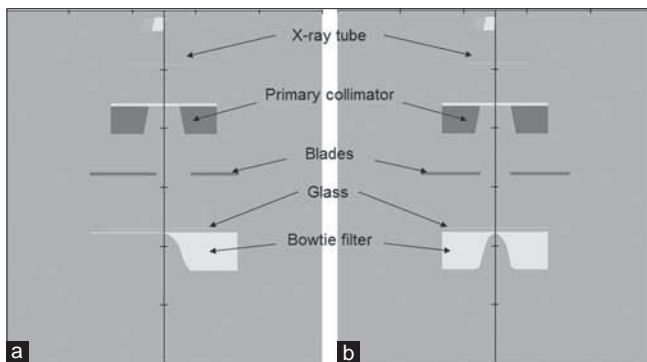


Figure 2: Schematic of the geometry of the on-board imager v1.6 device used for Monte Carlo simulation: (a) half-fan mode uses half-bowtie filter, and (b) full-fan mode uses full-bowtie filter

Normal tissue complication probability calculations for rectum and bladder

We used the formula manipulation software Mathematica 9.0 (Wolfram Research Inc., Champaign, IL, USA) and the Lyman–Kucher–Burman (LKB) model for our calculations.^[24] The NTCP in the LKB model was obtained as follows.

$$NTCP = \frac{1}{\sqrt{2\pi}} \int_{-\infty}^t \exp\left(\frac{-t^2}{2}\right) dt \quad (3)$$

$$v = \frac{V_{eff}}{V_{ref}} \quad (4)$$

$$t = \frac{(D - TD_{50}(v))}{(m \cdot TD_{50}(v))} \quad (5)$$

$$TD_{50}(v) = \frac{TD_{50}(1)}{v^n} \quad (6)$$

Here, V_{eff} is the volume defined by the effective volume method;^[25] if irradiated uniformly, this volume would experience a complication probability similar to that caused by the actual nonuniform dose delivered. Furthermore, V_{ref} is the total volume of the organ, n represents the volume effect dependence, and m represents the slope of the NTCP curve. Organ-specific values were obtained from the literature.^[26] $TD_{50}(v)$ is a dose that causes late adverse events in 50% of patients when a partial volume of normal tissues v is uniformly irradiated, whereas $TD_{50}(1)$ is a dose that causes late adverse events in 50% of patients when overall normal tissues are uniformly irradiated. D is the prescribed dose. There are various reports on the parameters used to calculate NTCP,^[27] however, this study used the classic Burman report. The rectum was evaluated for severe proctitis, necrosis, stenosis, and fistula with $n = 0.12$, $m = 0.15$, and $TD_{50}(1) = 80$ Gy; the bladder was evaluated for symptomatic bladder contracture and volume loss, with $n = 0.15$, $m = 0.11$, and $TD_{50}(1) = 80$ Gy.^[26]

RESULTS

Consistency between simulations and actual measurements

Figure 4 shows the calculated and measured PDD and OCR with 125-kV X-rays using two types of bowtie filters. PDD was normalized to a depth of 10 cm. The simulation using the half-bowtie filter showed a maximum difference of 0.67% lower than the measured value up to 1.0 cm from the water surface. As the depth increased beyond 1.0 cm, the simulated value exhibited a tendency to become lower than the measured value, with a maximum difference of 3.98%. In the simulation using the full-bowtie filter, a maximum difference of 2.84% was observed from the water surface to a depth of 1.0 cm. As the depth increased, a tendency to become lower than the measured value was observed with a maximum difference between the simulated and measured value of 2.51%. The OCR was normalized at the center of the beam axis with a depth of 1.0 cm. The simulated OCR using both bowtie filters

showed disagreement with the measured *OCR* of 15.72% and 2.51%, respectively, at 1.0 cm deep, and 11.95% and 5.18%, respectively, at 5.0 cm deep inside the field. These values were 8.91% and 29.90%, respectively, at 1.0 cm deep, and 5.63% and 11.88%, respectively, at 5.0 cm deep outside the field.

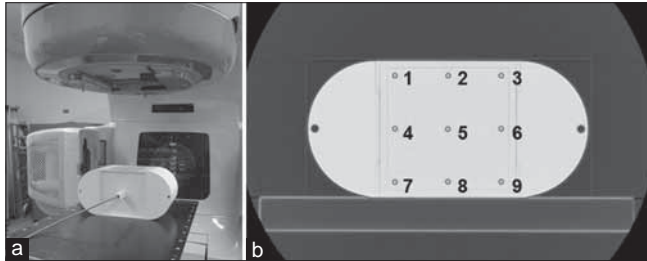


Figure 3: The cone-beam computed tomography dose was measured by inserting a Farmer-type ionization chamber TM30013 into an elliptical phantom. (a) Arrangement of phantom during cone-beam computed tomography dose measurement and (b) measurement points using the Farmer-type ionization chamber TM30013. The calculated Monte Carlo value was calibrated with the absolute dose at measurement point 5

Both bowtie filters showed relatively large errors at the edge of the field where the dose was 50% or less.

The CBCT dose in the elliptical phantom was calculated via the MC simulations for two types of imaging protocols. The calculated MC values in Table 2 were calibrated with the measured values at the center of the elliptical phantom (measurement point 5). The calculations with the half-fan mode showed a deviation of up to 5% from the actual measurements, whereas those values obtained by the full-fan mode showed a deviation of up to 8%. Calculated MC values for both types of imaging protocols tended to be higher on the ceiling side of the elliptical phantom (measurement points 1–3) and lower on the floor side (measurement points 7–9). The values at the middle section of the elliptical phantom (measurement points 4–6) tended to be lower in the half-fan mode and higher in the full-fan mode.

Organ dose and dose distribution

Figure 5 shows an example of a dose distribution map and DVH of the planned, CBCT, and combined doses. Using

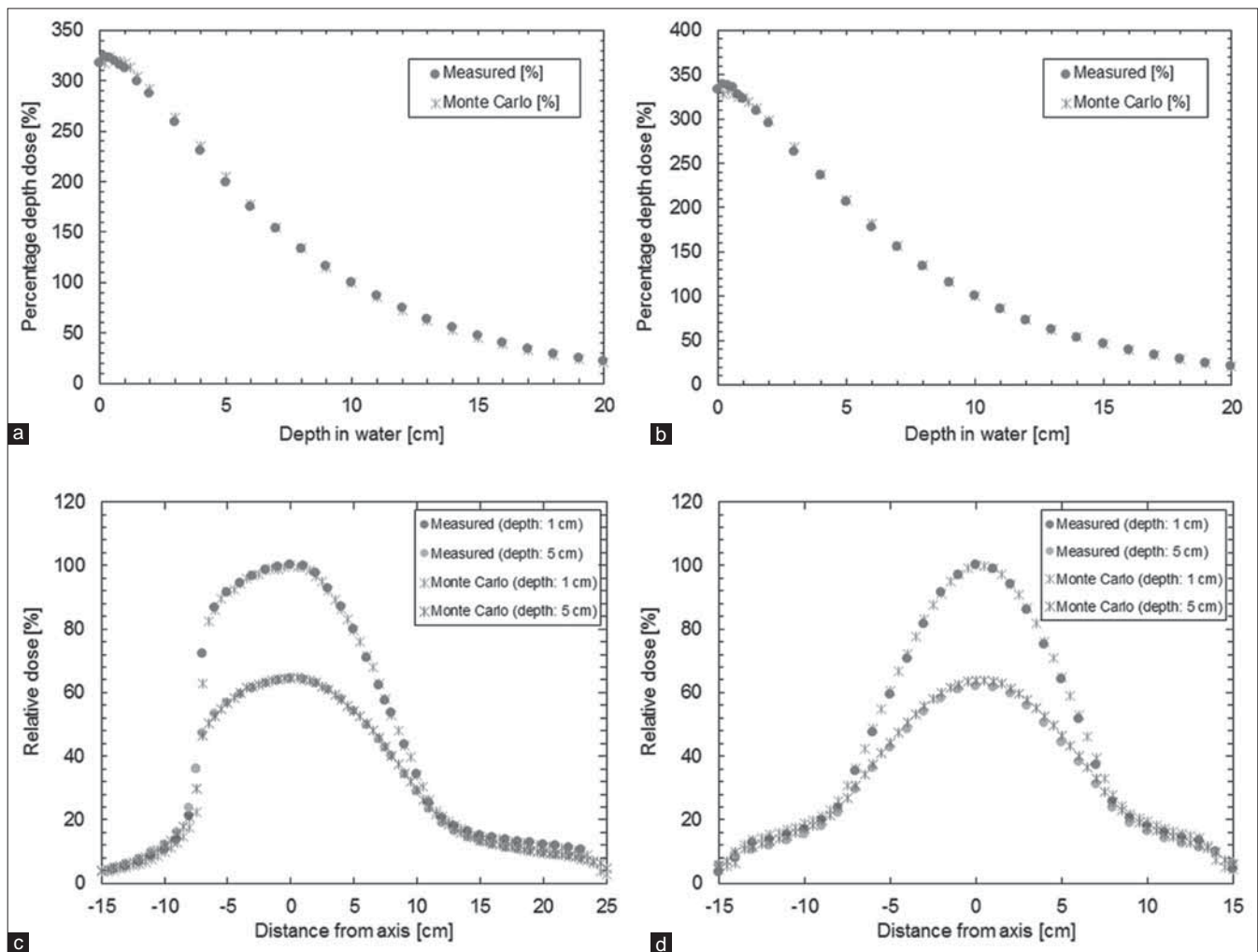


Figure 4: Comparison of 125-kV X-ray percent depth dose and off-center ratio with two bowtie filters obtained by Monte Carlo calculations and ionization chamber measurements: (a) percent depth dose (half-bowtie filter), (b) percent depth dose (full-bowtie filter), (c) off-center ratio (half-bowtie filter), and (d) off-center ratio (full-bowtie filter)

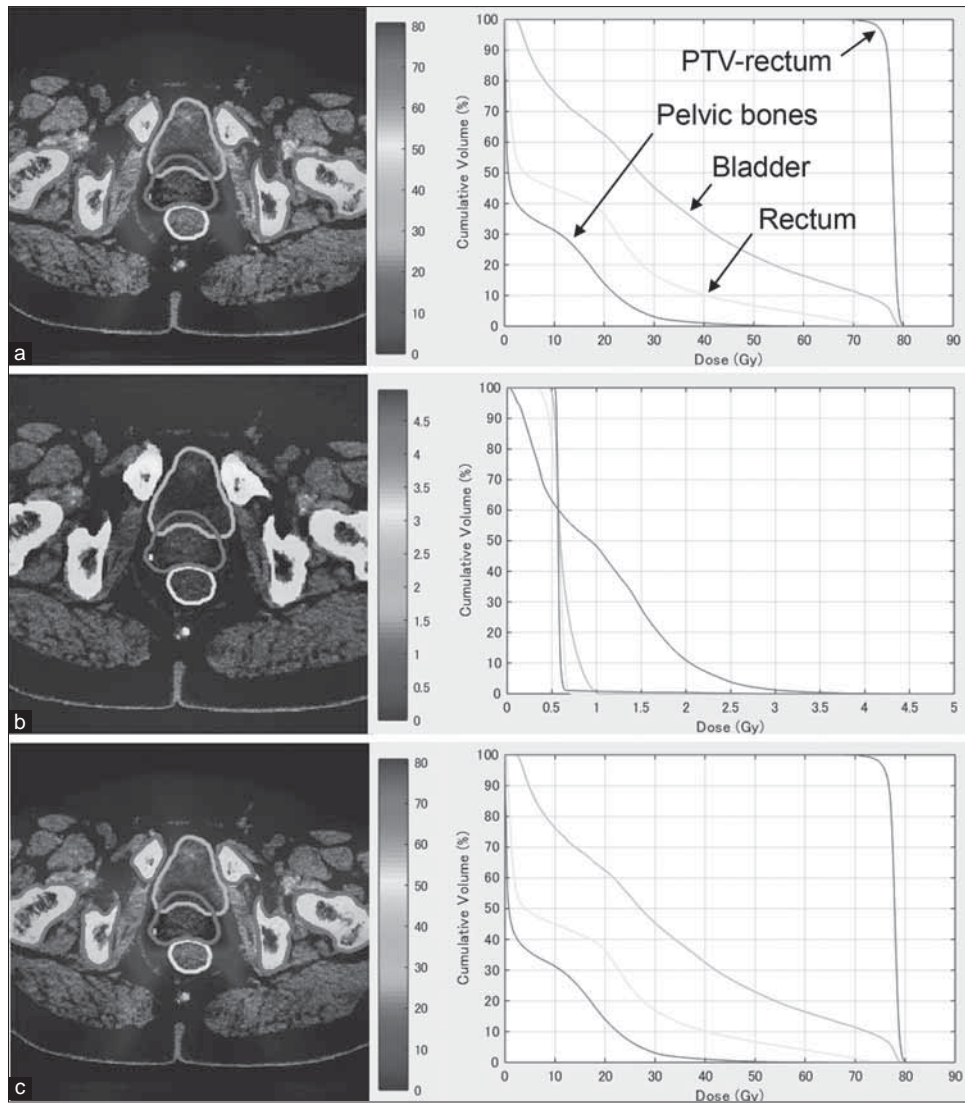


Figure 5: Calculated cone-beam computed tomography doses with the constructed system, combined with the planned treatment dose and dose-volume histogram. (a) Planned treatment dose, (b) cone-beam computed tomography dose, and (c) combined dose

Table 2: Comparison of doses obtained by Monte Carlo calculations and measured doses in an elliptical phantom

Measurement points	Pelvis (half-fan mode)			Pelvis spotlight (full-fan mode)		
	Measured (cGy)	Monte Carlo (cGy)	Difference (%)	Measured (cGy)	Monte Carlo (cGy)	Difference (%)
1	2.88	2.89	0.12	0.93	0.99	6.95
2	4.02	4.09	1.64	0.78	0.83	5.38
3	3.16	3.27	3.33	0.60	0.64	7.23
4	2.53	2.48	-1.93	2.28	2.32	1.83
5	2.67	2.67	-	2.45	2.45	-
6	2.49	2.46	-1.26	1.88	1.91	1.45
7	3.07	3.00	-2.46	4.18	4.12	-1.42
8	3.74	3.70	-1.02	5.32	5.36	0.58
9	2.78	2.66	-4.56	4.12	3.89	-5.55

The values calculated through Monte Carlo simulations were calibrated at the center of the elliptical phantom (measurement point 5)

this map, it was possible to identify only the CBCT dose, for which a dose of 3–4 Gy was observed in the pelvic bones [Figure 5b]. According to the dose distribution in

the planned and combined doses, there was no significant change in both the dose distribution and/or the DVH near the prostate [Figure 5a and c].

Table 3 presents the calculation results of 39 CBCT dose fractions. D_{50} was <1 Gy in the prostate, rectum, and bladder in the half-fan mode but higher in the pelvic bones at 1.76 ± 0.27 Gy. In the full-fan mode, the average D_{50} of the prostate, bladder, and pelvic bones decreased by 17.5%, 46.6%, and 25.0%, respectively, and increased by 25.0% in the rectum, compared to the half-fan mode. In the half-fan mode, the D_2 values for the prostate, bladder, rectum, and the pelvic bones were approximately 1.3 Gy, 1.2 Gy, 0.9 Gy and 4.0 Gy, respectively. The maximum dose was around the pubic bone. In the full-fan mode, the average D_2 of the prostate and bladder decreased by 12.5% and 38.5%, respectively, compared to the half-fan mode. Conversely, the average D_2 for the rectum and pelvic bones increased by 38.7% and 10.2%, respectively, and the maximum dose was around the coccyx.

Table 4 presents the D_2 , D_{98} , and HI of the target, which combines the imaging dose of 39 CBCT fractions and the treatment dose. In 39 CBCT fractions, D_2 and D_{98} increased by 0.90 Gy and 0.74 Gy, respectively, in the half-fan mode and 0.76 Gy and 0.72 Gy, respectively, in the full-fan mode. HI showed no change in either mode.

Tables 5 and 6 present the organ volume percentage for rectal and bladder doses in the combined dose DVH. For the rectum, V_{75} increased by approximately 0.1%, and V_{70} , V_{65} , and V_{60} increased by approximately 0.3%, irrespective of the imaging conditions. For the bladder, in the full-fan mode, V_{80} , V_{75} , and V_{40} increased by approximately 0.4% and V_{70} increased by 0.3%. For the bladder in the half-fan mode, both V_{80} and V_{75} increased by 0.6%, V_{70} increased by 0.4%, and V_{40} increased by 0.8%.

Normal tissue complication probability of the rectum and bladder

Table 7 presents the results of the DVH and the NTCP obtained by adding the planned and CBCT doses. Compared with the

calculated planned dose, rectal NTCP increased due to the addition of the CBCT dose. The rectal NTCP increased from 0.46% to 0.53% when 39 CBCT doses were added in both the half-fan and full-fan modes. The NTCP in the urinary bladder was approximately 0.02% at most, even with the inclusion of the CBCT dose.

DISCUSSION

Consistency between simulations and measurements

Verification of the 125-kV X-ray beam model used in the pelvic CBCT was performed using *PDD* and *OCR*. Modeling of the 125-kV X-ray beam used in the OBIs through MC simulations was reported by Ding *et al.* and Hioki *et al.*^[9,28] Hioki *et al.* examined 125-kV X-rays with a half-bowtie filter similar to the filter used here and found that the difference between *PDD* and *OCR* was within 3%. The differences between the *PDD* and *OCR* obtained using the half-bowtie and the full-bowtie filters were within approximately 3% in our study as well. Hence, the model used in this study at least as accurate as Hioki *et al.*'s model.^[28] However, in our study, the difference between the measured and calculated values was greater at the shallow part of the *PDD* and the irradiation field edge, where the dose at the *OCR* was <50%. The uncertainty near the surface during measurements is large, making evaluation difficult; however, the MC calculation value is considered to have a large systematic error near the surface. As the dose was low at the edge of the irradiation field, the effect on dose distribution and DVH was considered to be small.

The doses in the half-fan and full-fan modes of CBCT were simulated using the modeled beam. The calculated MC dose in the elliptical phantom differed from the dose measured by the ionization chamber up to 5% in the half-fan mode and up to 8% in the full-fan mode. Although the error was relatively large owing to the comparison of numerical values with small

Table 3: Cone-beam computed tomography doses in organs

	Mean±SD (Gy) (range)			
	Pelvis (half-fan mode)		Pelvis spotlight (full-fan mode)	
	D_2	D_{50}	D_2	D_{50}
Prostate	1.28±0.87 (0.73-3.67)	0.80±0.10 (0.55-0.99)	1.12±0.71 (0.57-3.19)	0.66±0.09 (0.47-0.77)
Rectum	0.93±0.12 (0.65-1.10)	0.84±0.11 (0.57-1.00)	1.29±0.18 (0.91-1.59)	1.05±0.16 (0.73-1.35)
Bladder	1.22±0.22 (0.75-1.61)	0.88±0.14 (0.58-1.16)	0.75±0.19 (0.29-1.13)	0.47±0.09 (0.30-0.61)
Pelvic bones	3.92±0.45 (2.70-4.65)	1.76±0.27 (0.90-2.09)	4.32±0.60 (2.83-5.16)	1.32±0.22 (0.66-1.63)

SD: Standard deviation

Table 4: D_2 , D_{98} , and homogeneity index of the target

	Mean±SD (range)			
	Treatment dose	Combined dose (half-fan mode)		Combined dose (full-fan mode)
D_2 (Gy)	79.64±0.52 (78.50-80.68)	80.54±0.50 (79.73-81.67)	$P<0.001$	80.40±0.51 (79.54-81.59) $P<0.001$
D_{98} (Gy)	74.46±0.74 (73.06-75.67)	75.20±0.72 (73.88-76.50)	$P<0.001$	75.18±0.70 (73.90-76.34) $P<0.001$
HI	0.07±0.01 (0.05-0.09)	0.07±0.01 (0.05-0.09)	$P>0.1$	0.07±0.01 (0.05-0.09) $P>0.1$

For D_2 , D_{98} , and HI, the significance of the difference between the two combined doses and planned treatment dose was evaluated using the Wilcoxon signed-rank test. SD: Standard deviation, HI: homogeneity index

Table 5: $V_{75'}$, $V_{70'}$, $V_{65'}$ and V_{60} of the rectum

	Mean±SD (%) (range)				
	Treatment dose	Combined dose (half-fan mode)		Combined dose (full-fan mode)	
V_{75}	0.11±0.19 (0.00-0.67)	0.20±0.29 (0.01-1.04)	$P<0.001$	0.19±0.30 (0.01-1.10)	$P<0.001$
V_{70}	1.55±0.75 (0.12-2.90)	1.89±0.86 (0.16-3.31)	$P<0.001$	1.88±0.86 (0.18-3.32)	$P<0.001$
V_{65}	3.44±1.26 (0.69-5.88)	3.73±1.35 (0.78-6.38)	$P<0.001$	3.73±1.36 (0.78-6.40)	$P<0.001$
V_{60}	5.14±1.67 (1.65-8.71)	5.41±1.76 (1.75-9.22)	$P<0.001$	5.42±1.77 (1.78-9.25)	$P<0.001$

For V_{75} , V_{70} , V_{65} , and V_{60} , the significance of the difference between the two combined doses and planned treatment dose was evaluated using the Wilcoxon signed-rank test. SD: Standard deviation

Table 6: $V_{80'}$, $V_{75'}$, $V_{70'}$ and V_{40} of the bladder

	Mean±SD (%) (range)				
	Treatment dose	Combined dose (half-fan mode)		Combined dose (full-fan mode)	
V_{80}	0.08±0.13 (0.00-0.41)	0.66±0.91 (0.01-3.64)	$P<0.001$	0.48±0.78 (0.00-3.20)	$P<0.001$
V_{75}	8.15±3.80 (3.34-18.14)	8.74±4.01 (3.58-19.27)	$P<0.001$	8.58±3.97 (3.49-19.01)	$P<0.001$
V_{70}	11.07±4.89 (4.44-23.90)	11.47±5.03 (4.64-24.64)	$P<0.001$	11.35±5.01 (4.58-24.43)	$P<0.001$
V_{40}	27.89±8.72 (12.80-46.16)	28.70±8.79 (13.34-46.89)	$P<0.001$	28.32±8.78 (13.06-46.65)	$P<0.001$

For V_{80} , V_{75} , V_{70} , and V_{40} , the significance of the difference between the two combined doses and planned treatment dose was evaluated using the Wilcoxon signed-rank test. SD: Standard deviation

Table 7: Rectal normal tissue complication probability (%) of treatment and combined dose

Patient number	Treatment dose	Combined dose (half-fan mode)	Combined dose (full-fan mode)
1	0.32	0.35	0.35
2	0.28	0.32	0.32
3	0.60	0.69	0.69
4	0.63	0.75	0.74
5	0.62	0.72	0.72
6	0.32	0.38	0.34
7	0.52	0.61	0.60
8	0.29	0.33	0.33
9	0.31	0.33	0.33
10	0.64	0.73	0.73
11	0.87	1.03	1.04
12	0.73	0.82	0.82
13	0.13	0.15	0.15
14	0.30	0.35	0.35
15	0.42	0.49	0.49
16	0.31	0.36	0.36
17	0.43	0.50	0.51
18	0.43	0.51	0.51
19	0.26	0.27	0.27
20	0.75	0.88	0.89
Mean (SD)	0.46 (0.20)	0.53 (0.24), $P<0.001$	0.53 (0.24), $P<0.001$

The significance of the difference between the two combined doses and the planned dose was evaluated using the Wilcoxon signed-rank test. SD: Standard deviation

absolute values, the absolute doses were a maximum of 0.12 and 0.23 cGy in the half-fan and full-fan modes, respectively. Hence, the CBCT dose was reproduced with high accuracy. In both modes, the MC-calculated dose tended to be lower at the measurement points on the floor side (7 and 9). This occurred

because the CT couch was included in the calculation volume as the CT images involved the couch in the MC calculation. In the actual measurement, the CBCT dose was measured by placing an elliptical phantom on a carbon top plate with a width of 14.5 cm and height of 2.0 cm, which has lower X-ray absorption. The calculated MC doses at the measurement points on the ceiling side (1, 2, and 3) were also considered to be higher because the MC calibration and the measured value had different doses due to the different beam absorptions of the couches.

Organ dose and dose distribution combined with treatment dose and cone-beam computed tomography dose

According to the AAPM Task Group 180 Report, when the imaging dose exceeds 5% of the prescription dose, dose distributions, including the imaging dose and evaluation of the organ dose, are required.^[16] With our proposed system, accurate and comprehensive determination of the CBCT dose is achievable.

In the half-fan mode, the average D_{50} values of the prostate, rectum, bladder, and pelvic bones were 0.80 ± 0.10 Gy, 0.84 ± 0.11 Gy, 0.88 ± 0.14 Gy, and 1.76 ± 0.27 Gy, respectively. Nelson *et al.* reported the imaging dose in a patient's body for one CBCT determined through MC simulations. In that study, the D_{50} ranges of the prostate, rectum, bladder, and pelvis in the half-fan mode were 1.19–1.79 Gy, 1.51–1.99 Gy, 1.36–2.20 Gy, and 2.93–3.96 Gy, respectively.^[29] These doses were converted into 39 fractions, yielding 0.46–0.70 Gy, 0.59–0.78 Gy, 0.53–0.86 Gy, and 1.14–1.54 Gy, respectively, which are approximately consistent with or calculated doses. The D_2 values of the prostate, rectum, and bladder are not significantly different from D_{50} , and the dose increased uniformly owing to the small volume. On the other hand, for pelvic bones, the average D_{50} was 1.76 ± 0.27 Gy and the average D_2 was 3.92 ± 0.45 Gy. Ding *et al.* reported that the absorption of 125 kV X-rays is extremely high in bones – approximately

three times higher than in soft tissue.^[9] This MC-calculated dose shows a similar tendency and thus is considered a reasonable result. In addition, D_{50} is smaller than D_2 because the volume with a high dose includes the pelvic bone volume. In the full-fan mode, the rectal dose increased by 25.0% on average, bladder dose decreased by 46.6%, and pelvic bone dose decreased by 25.0% for D_{50} compared to the half-fan mode. The full-fan mode was set such that the X-ray tube passed through the patient's back from a gantry angle of 292° – 88° . Therefore, the decreased dose in the bladder can be attributed to the absence of radiation to the ventral side. The rectal dose increase in the full-fan mode is due to increased exposure time. The same effect was observed for the maximum pubic bone dose in the half-fan mode and the maximum coccyx dose in the full-fan mode.

The D_2 and D_{98} of the target increased by approximately 1 Gy in both modes because of the added CBCT dose. In addition, there was no significant change in the HI. The CBCT dose did not lose the uniformity of the target dose and increased by approximately 1 Gy.

Rectal V_{75} , V_{70} , V_{65} , and V_{60} showed similar results in both modes with increases of 0.08%–0.09%, 0.33%–0.34%, 0.29%, and 0.27%–0.28%, respectively. Despite the fact that the rectal dose exceeded the CBCT dose by approximately 1 Gy, the maximum increases of V_{75} , V_{70} , V_{65} , and V_{60} were 1.10%, 3.32%, 6.40%, and 9.25%, respectively, while they increased only 0.3% in average over all patients. The Radiation Therapy Oncology Group (RTOG) 0415 prostate IMRT dose constraints were 15%, 25%, 35%, and 50% for V_{75} , V_{70} , V_{65} , and V_{60} , respectively.^[30] The treatment plan used in this study was designed considering the PTV–rectum as the target, so the RTOG0415 constraints were satisfied. V_{80} , V_{75} , V_{70} , and V_{40} of the bladder increased by 0.58%, 0.59%, 0.40%, and 0.81%, respectively, in the half-fan mode, and 0.40%, 0.43%, 0.28%, and 0.43%, respectively, in the full-fan mode. In the full-fan mode, the X-ray tube runs around the patient's back; therefore, the dose to the ventral side of the bladder is reduced. The V_{80} , V_{75} , V_{70} , and V_{40} values of the bladder calculated by adding the treatment and CBCT doses were 3.64%, 19.27%, 24.64%, and 46.89%, respectively, at maximum, satisfying the RTOG0415 constraints.^[30] The dose increase due to the addition of the CBCT dose is slight, and it is unlikely that the rectal and bladder complication probability will be significantly increased. However, if the target margin on the rectum or bladder side is enlarged or the prescribed dose is escalated, a safer treatment plan should consider the dose increase of approximately 1 Gy from the 39 CBCT doses. Because the X-ray tube passes through almost half of the patient's body in the full-fan mode, it is necessary to use a revised approach, such as passing the tube through the ventral side of the body, to reduce the rectal dose.

Normal tissue complication probability of the rectum and bladder

The NTCP of $0.46\% \pm 0.20\%$ in average with the treatment dose increased to $0.53\% \pm 0.24\%$ with 39 fractions of CBCT. Maund *et al.* reported that the NTCP of the rectum in prostate IMRT

was 1.9% when target margins of 4 or 5 mm were applied to the rectum and 1.3% when 3 mm margins were applied.^[8] Because we used a rectal margin of 0 mm in the treatment plan, we can assume that our NTCP would be lower than that of Maund *et al.* CBCT can result in unplanned radiation exposure, potentially increasing the rectal NTCP by up to 0.07%. Chung *et al.* reported that IGRT reduced the setup margin and the incidence of RTOG Grade 2 or higher bladder disorders from 60% to 13% and rectal disorders from 80% to 13%.^[2] The increase in rectal NTCP due to the implementation of CBCT is unlikely to have any clinical impact, while the benefits of CBCT are considered to be significant in reducing the complexity by improving the accuracy of location verification. However, unnecessary radiation exposure should be kept to a minimum, and exposure reduction measures, such as using a surface monitor and an ultrasonic monitor without exposure, adjusting imaging conditions, and using full-fan mode, should be applied.

Limitations

In this study, only CBCT doses using 125 kV X-rays were evaluated; however, in clinical practice, images are acquired using various techniques such as kV and MV images and MV CBCT. Furthermore, pelvic organ variations for each treatment were not considered in the evaluation of the treatment plan. To perform more accurate dose evaluations, we recommend considering other imaging doses besides CBCT and devising a method for correcting for internal organ displacement using CBCT images taken for each treatment. The combined dose was evaluated by simply adding the CBCT dose from kV X-rays and the therapeutic dose from MV X-rays. Therefore, biological effects due to the differences in radiation quality were not considered. Future work will include the creation of a dose distribution that considers relative biological effectiveness when accounting for the beam quality, evaluation of the DVH and NTCP when accounting for beam quality, and estimation of secondary cancer risk.

CONCLUSIONS

In this study, we demonstrated a method for evaluating combined dose distribution that has not yet been proposed. The constructed system calculates the CBCT dose of prostate IMRT by MC simulation and enables comprehensive evaluation of the treatment plan by adding the CBCT dose to the treatment dose. The CBCT dose of each organ calculated in our study can be used as a reference value when planning treatment, although some errors may occur depending on the patient's anatomy. The combined dose distribution revealed a slight increase of <1% in the percentage volume for each rectal and bladder dose and a 0.07% increase in the rectal NTCP.

Acknowledgment

We would like to thank Editage (www.editage.com) for English language editing.

Financial support and sponsorship

Nil.

Conflicts of interest

There are no conflicts of interest.

REFERENCES

- Dawson LA, Jaffray DA. Advances in image-guided radiation therapy. *J Clin Oncol* 2007;25:938-46.
- Chung HT, Xia P, Chan LW, Park-Somers E, Roach M 3rd. Does image-guided radiotherapy improve toxicity profile in whole pelvic-treated high-risk prostate cancer? Comparison between IG-IMRT and IMRT. *Int J Radiat Oncol Biol Phys* 2009;73:53-60.
- Bujold A, Craig T, Jaffray D, Dawson LA. Image-guided radiotherapy: has it influenced patient outcomes? *Semin Radiat Oncol* 2012;22:50-61.
- Sveistrup J, af Rosenschöld PM, Deasy JO, Oh JH, Pommer T, Petersen PM, *et al.* Improvement in toxicity in high risk prostate cancer patients treated with image-guided intensity-modulated radiotherapy compared to 3D conformal radiotherapy without daily image guidance. *Radiat Oncol* 2014;9:44.
- Perkins CL, Fox T, Elder E, Kooby DA, Staley CA 3rd, Landry J. Image-guided radiation therapy (IGRT) in gastrointestinal tumors. *JOP* 2006;7:372-81.
- Murphy MJ, Balter J, Balter S, BenComo JA Jr, Das IJ, Jiang SB, *et al.* The management of imaging dose during image-guided radiotherapy: report of the AAPM Task Group 75. *Med Phys* 2007;34:4041-63.
- Wen N, Guan H, Hammoud R, Pradhan D, Nurushev T, Li S, *et al.* Dose delivered from Varian's CBCT to patients receiving IMRT for prostate cancer. *Phys Med Biol* 2007;52:2267-76.
- Maund IF, Benson RJ, Fairfoul J, Cook J, Huddart R, Poynter A. Image-guided radiotherapy of the prostate using daily CBCT: the feasibility and likely benefit of implementing a margin reduction. *Br J Radiol* 2014;87:20140459.
- Ding GX, Duggan DM, Coffey CW. Accurate patient dosimetry of kilovoltage cone-beam CT in radiation therapy. *Med Phys* 2008;35:1135-44.
- Ding GX, Coffey CW. Radiation dose from kilovoltage cone beam computed tomography in an image-guided radiotherapy procedure. *Int J Radiat Oncol Biol Phys* 2009;73:610-7.
- Ding GX, Munro P, Pawlowski J, Malcolm A, Coffey CW. Reducing radiation exposure to patients from kV-CBCT imaging. *Radiother Oncol* 2010;97:585-92.
- Ding GX, Munro P. Radiation exposure to patients from image guidance procedures and techniques to reduce the imaging dose. *Radiother Oncol* 2013;108:91-8.
- Abuhaimed A, Martin CJ, Sankaralingam M. A Monte Carlo study of organ and effective doses of cone beam computed tomography (CBCT) scans in radiotherapy. *J Radiol Prot* 2018;38:61-80.
- Grelewicz Z, Wiersma RD. Combined MV + kV inverse treatment planning for optimal kV dose incorporation in IGRT. *Phys Med Biol* 2014;59:1607-21.
- Alaei P, Spezi E, Reynolds M. Dose calculation and treatment plan optimization including imaging dose from kilovoltage cone beam computed tomography. *Acta Oncol* 2014;53:839-44.
- Ding GX, Alaei P, Curran B, Flynn R, Gossman M, Mackie TR, *et al.* Image guidance doses delivered during radiotherapy: Quantification, management, and reduction: Report of the AAPM Therapy Physics Committee Task Group 180. *Med Phys* 2018;45:e84-e99.
- Kawrakow I. Accurate condensed history Monte Carlo simulation of electron transport. I. EGSnrc, the new EGS4 version. *Med Phys* 2000;27:485-98.
- Kawrakow I, Mainegra-Hing E, Rogers DW, Tessier F, Walters BR. The EGSnrc code system: Monte Carlo Simulation of Electron and Photon Transport National Research Council of Canada Report PIRS-701; 2011.
- Rogers DW, Faddegon BA, Ding GX, Ma CM, We J, Mackie TR. BEAM: a Monte Carlo code to simulate radiotherapy treatment units. *Med Phys* 1995;22:503-24.
- Rogers DWO, Walters B, Kawrakow I. BEAMnrc User's Manual National Research Council of Canada Report PIRS-0509 (A) Rev L; 2018.
- Walters B, Kawrakow I, Rogers DW. DOSXYZnrc User's Manual National Research Council of Canada Report PIRS-794 Rev B; 2018.
- Ma CM, Coffey CW, DeWerd LA, Liu C, Nath R, Seltzer SM, *et al.* AAPM protocol for 40-300 kV x-ray beam dosimetry in radiotherapy and radiobiology. *Med Phys* 2001;28:868-93.
- ICRU. Prescribing, recording, and reporting photon-beam intensity-modulated radiation therapy (IMRT). ICRU Report 83. *J ICRU* 2010;10:1-106.
- Kutcher GJ, Burman C, Brewster L, Goitein M, Mohan R. Histogram reduction method for calculating complication probabilities for three-dimensional treatment planning evaluations. *Int J Radiat Oncol Biol Phys* 1991;21:137-46.
- Kutcher GJ, Burman C. Calculation of complication probability factors for non-uniform normal tissue irradiation: The effective volume method. *Int J Radiat Oncol Biol Phys* 1989;16:1623-30.
- Burman C, Kutcher GJ, Emami B, Goitein M. Fitting of normal tissue tolerance data to an analytic function. *Int J Radiat Oncol Biol Phys* 1991;21:123-35.
- Michalski JM, Gay H, Jackson A, Tucker SL, Deasy JO. Radiation dose-volume effects in radiation-induced rectal injury. *Int J Radiat Oncol Biol Phys* 2010;76:S123-9.
- Hioki K, Araki F, Ohno T, Nakaguchi Y, Tomiyama Y. Absorbed dose measurements for kV-cone beam computed tomography in image-guided radiation therapy. *Phys Med Biol* 2014;59:7297-313.
- Nelson AP, Ding GX. An alternative approach to account for patient organ doses from imaging guidance procedures. *Radiother Oncol* 2014;112:112-8.
- Buckey CR, Swanson GP, Stathakis S, Papanikolaou N. Optimizing prostate intensity-modulated radiation therapy (IMRT): do stricter constraints produce better dosimetric results? *Eur J Clin Med Oncol* 2010;2:139-44.

Study of Asymmetric Margins in Prostate Cancer Radiation Therapy Using Fuzzy Logic

Santosh Kumar Patnaikuni^{1,2}, Sapan Mohan Saini¹, Rakesh Mohan Chandola², Pradeep Chandrakar², Vivek Chaudhary²

¹Department of Physics, National Institute of Technology, ²Department of Radiotherapy, Pt. JNM Medical College, Raipur, Chhattisgarh, India

Abstract

Purpose: The purpose of present study is to estimate asymmetric margins of prostate target volume based on biological limitations with help of knowledge based fuzzy logic considering the effect of organ motion and setup errors. **Materials and Methods:** A novel application of fuzzy logic modelling technique considering radiotherapy uncertainties including setup, delineation and organ motion was used in this study to derive margins. The new margin was applied in prostate cancer treatment planning and the results compared very well to current techniques. Here volumetric modulated arc therapy treatment plans using stepped increments of asymmetric margins of planning target volume (PTV) were performed to calculate the changes in prostate radiobiological indices and results were used to formulate the rule based and membership function for Mamdani-type fuzzy inference system. The optimum fuzzy rules derived from input data, the clinical goals and knowledge-based conditions imposed on the margin limits. The PTV margin obtained using the fuzzy model was compared to the commonly used margin recipe. **Results:** For total displacement standard errors ranging from 0 to 5 mm the fuzzy PTV margin was found to be up to 0.5 mm bigger than the vanHerk derived margin, however taking the modelling uncertainty into account results in a good match between the PTV margin calculated using our model and the one based on van Herk *et al.* formulation for equivalent errors of up to 5 mm standard deviation (s. d.) at this range. When the total displacement standard errors exceed 5 mm s. d., the fuzzy margin remained smaller than the van Herk margin. **Conclusion:** The advantage of using knowledge based fuzzy logic is that a practical limitation on the margin size is included in the model for limiting the dose received by the critical organs. It uses both physical and radiobiological data to optimize the required margin as per clinical requirement in real time or adaptive planning, which is an improvement on most margin models which mainly rely on physical data only.

Keywords: Fuzzy inference system, normal tissue complication probability, planning target volume, tumour control probability, volumetric modulated arc therapy

Received on: 17-12-2019

Review completed on: 18-04-2020

Accepted on: 23-04-2020

Published on: 20-07-2020

INTRODUCTION

The treatment of cancer using radiation therapy is to kill all the cancerous cells whilst sparing the healthy tissues and critical organs. Prior to the treatment the volumes to be irradiated and avoided are outlined. In the treatment planning phase the beam placement and dose optimization is adapted to achieve the overall goal of treatment cure and sparing of normal tissue. There is sufficient evidence that the dose-volume (DV) relationship for the development of complication also exists and this results in the induction of adverse side effects on the normal tissue and critical organs. Optimal treatments thus depend on the selection of the best possible margins due to the inherent complex trade-off between complication and cure. The radiobiological concept of tumour control probability (TCP) describes the probability of killing all tumour cells in a

volume whilst the concept of normal tissue complication probability (NTCP) describes the damage that occurs to normal tissues and critical organs. The radiation effects, in both tumour and surrounding healthy tissue, follow a typical sigmoid shape as function of dose. This relationship is illustrated in Figure 1. A cure without complication can only be achieved if the dose to the tumour is high enough for the destruction of all tumour cells and the tolerance doses of the normal tissues are not to be exceeded. In order to avoid side effects of radiotherapy the dose distribution is spatially conformed to the tumour

Address for correspondence: Dr. Sapan Mohan Saini,
Department of Physics, National Institute of Technology, Raipur - 492 010,
Chhattisgarh, India.
E-mail: smsaini.phy@nitrr.ac.in

This is an open access journal, and articles are distributed under the terms of the Creative Commons Attribution-NonCommercial-ShareAlike 4.0 License, which allows others to remix, tweak, and build upon the work non-commercially, as long as appropriate credit is given and the new creations are licensed under the identical terms.

For reprints contact: WKHLRPMedknow_reprints@wolterskluwer.com

How to cite this article: Patnaikuni SK, Saini SM, Chandola RM, Chandrakar P, Chaudhary V. Study of asymmetric margins in prostate cancer radiation therapy using fuzzy logic. *J Med Phys* 2020;45:88-97.

Access this article online

Quick Response Code:



Website:
www.jmp.org.in

DOI:
10.4103/jmp.JMP_110_19

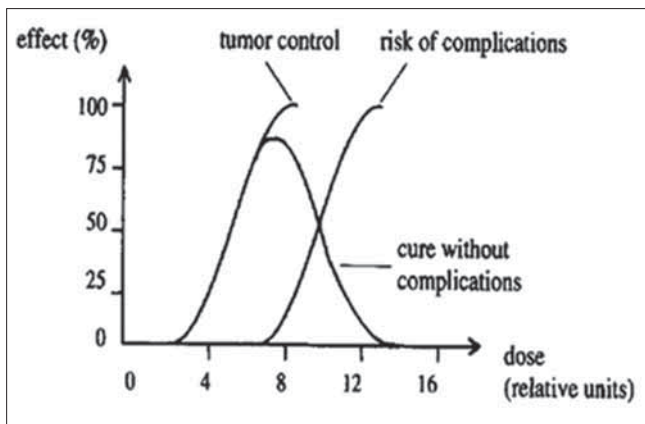


Figure 1: Dependence of the probability of cure without complication on dose, resulting from the probability of tumour control and the risk of complications in the normal tissues (Waschek T *et al.* 1997)

such that the normal tissues are spared as much as possible. Treatment margins have previously been derived based on these radiobiological considerations.^[1-3]

During the actual fractionated patient treatment phase, the presence of organ motion, patient set-up and tumour delineation variations affect the planned treatment and may therefore result in the delivered dose which differs from the intended planned dose. Various recommendations are available for the derivation of margins for the use in radiotherapy treatment planning including the International Commission on Radiation Units and Measurements reports 50,^[4] 62,^[5] 71^[6] and formulation based on probabilistic dose distributions.^[7,8] The published margin formulations tend to assume a linear relationship between tumour margin and radiotherapy errors. This may be varying for all treatment strategies encountered in radiotherapy. New techniques such as dose escalations may be significant challenge which may limit the application of current margins. The rigidity of these formulations to adapt to changing patient condition also limits their applicability to all treatment scenarios.

In the present study we propose the use of fuzzy logic technique to derive asymmetric radiotherapy treatment margins. The use of fuzzy logic technique for the derivation of radiotherapy margins was initially used by Waschek *et al.*^[9] Their technique relied on expert knowledge to derive the clinical target volume (CTV) margins. However they did not consider the effect of organ motion and setup errors in order to derive planning target volume (PTV) margins. Study by Mzenda *et al.*^[10] was based on delineation, set-up and organ motion errors to deduce the treatment margins, but they did not consider the asymmetric nature of motion of PTV and other nearby multiple critical organ effects around target volume whereas these also play significant role and hence they should not be neglected.

In the present study we consider the asymmetric nature of target volume motion and hence effect of nearby critical organs along with the setup-errors and delineation errors to deduce

asymmetric margins based on biological limitations with help of fuzzy logic. The input rules used in fuzzy inference system (FIS) are based on the analytical simulations thus removing the subjective nature of inter-observer variation. In the present study fuzzy logic application is adopted because fuzzy model features make it robust for modelling to derive treatment margins that are too complex to be modelled by means of conventional mathematical techniques. The relationship between radiobiological parameters (TCP and NTCP), radiotherapy margins as well as radiotherapy uncertainties is difficult to quantify mathematically or has a large degree of variability. However fuzzy logic has a distinct advantage in allowing the linkage of these geometrical and radiobiological parameters through use of fuzzy rules and membership functions.^[11-13] In the present study Mamdani-type FIS is used for modelling because it allows to describe the problem in more intuitive manner with suitable environment to correlate target motion estimation which is significant particularly in adaptive radiotherapy planning and treatment. Further the main disadvantage of currently used margin formulations^[4,5,8] is that they do not consider the effects of organ motion and surrounding organ at risk (OAR) when deriving PTV margins. From the clinical cases it was found that fuzziness region to derive exact PTV margin. In the current study the fuzziness region of PTV along with physical and radiobiological factors is considered in determining the asymmetric nature of PTV margins. Complex radiotherapy treatment delivery techniques such as volumetric modulated arc therapy (VMAT) require precise selection of treatment margins for optimization and dose escalation and also the difficulty in treatment planning for prostate cancer varies greatly case by case and hence the application of derived fuzzy margins is assessed in the current study to shape their perspective on clinical decisions.

MATERIALS AND METHODS

Brief description of modelling procedure and modelling input data

The PTV margin modelling procedure using the Mamdani-type knowledge based fuzzy logic system involved a number of steps. The procedure started with the creation of treatment plans using variable PTV margins asymmetrically (LR: 0–12 mm, SI: 0–14, AP: 0–14 mm, PA: 0–12 mm) with the help of pre-and in-treatment image guidance^[14-18] analysis for tighter margins with improved OARs sparing. These plans were used to calculate baseline TCP and NTCP. The above step was followed by simulation technique to displace the prostate and critical organs using typical incremental error magnitude as obtained during radiotherapy treatment. This allowed the recalculation of new TCP and NTCP values after each stepped increment margin. The output obtained provides the basic dosimetric information for use in deriving the fuzzy linguistic rules and membership functions for use in the knowledge based fuzzy logic system. The inputs were then fuzzified using mamdani-type FIS with help of formulated rules and membership functions. The defuzzification stage provided

the initial crisp output. A Gaussian convolution kernel was then applied to optimize the initial fuzzy output. Finally the margin obtained as output from the fuzzy model was compared with currently used margins and applied in current VMAT treatment planning.

The preferred method for treating Prostate cancer patients ($n = 08$) with radiation is VMAT and all VMAT plans were generated with treatment planning system using Eclipse 15.6, Varian Medical Systems with photon optimization with maximum dose rate and dose prescription of 73.5 Gy. All treatment were generated using asymmetric PTV margins as mentioned earlier with 1 mm stepped size to calculate input data for fuzzy model as shown in Figure 2. Most VMAT planning systems apply DV based objective functions^[19] for dose optimization and an acceptable plans can be generated in most cases. For more complex plans, more iteration are required because many Parameters need to be finely tuned. A successful improvement tool-generalized equivalent uniform dose (gEUD) was developed with fewer parameters setting^[20-23] to improve the quality of plans. However gEUD based optimization cannot demonstrate such advantages on first run, more iteration are required to share the dose distribution.^[24] To overcome the disadvantages mentioned above, here treatment planning started with DV-based optimization, and then improved it by adding gEUD-based improvement. Current study based on strategies and choice of volume effect parameters and weightage of cost function by standard recommendations. The superposition dose calculation algorithms were used for plan calculation. The dose distribution of the treatment plans was optimized such that 95% isodose covered the PTV on all slices.

The radiation dose received to prostate target, rectum and bladder was calculated for all plans and output data was used to calculate the radiobiological parameters TCP and NTCP [Appendex-A]. The TCP was calculated with using Matlab

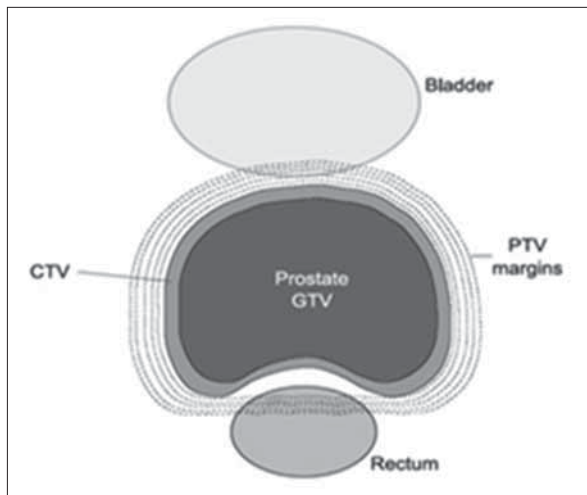


Figure 2: Schematic diagram showing variable planning target volume asymmetric margins used in treatment plans to calculate input data for fuzzy model (B Mzenda *et al.* 2010)

R2018a-based simulation tool based on the concept of EUD modelling.^[25] The concept of EUD is defined as the uniform dose that, if delivered over the same number of fractions as the nonuniform dose distribution of interest, yields the same biological effect. To extend the Concept of EUD, a phenomenological formula referred to as the generalized EUD (DVH-based) or gEUD has been used.

$$gEUD = \left(\sum V_i D_i^a \right)^{\frac{1}{a}} \tag{1}$$

Where V_i is the fractional organ volume receiving a dose D_i and “a” is a tissue-specific parameter that describes the volume effect. For $a \rightarrow -\infty$, gEUD approaches the minimum dose; thus negative values of “a” are used for tumour. For $a \rightarrow +\infty$, gEUD approached the maximum dose. For $a = 1$, gEUD is equal to the arithmetic mean dose, for $a = 0$, gEUD is equal to the geometric mean dose. gEUD objective options can be generally selected in TPS Eclipse 15.6 (VMS) as target EUD selected for the PTV, while max. EUD selected for OARs. The resolution of the dose calculation grid bin size considered unbiased for subsequent computation of various indices. In this way the EUD based TCP and NTCP can be calculated as follows:

$$TCP = \frac{1}{1 + \left(\frac{D_{50}}{EUD} \right)^{4\gamma_{50}}} \tag{2}$$

and

$$NTCP = \frac{1}{1 + \left(\frac{TD_{50}}{EUD} \right)^{4\gamma_{50}}} \tag{3}$$

Where D_{50} is the absorbed dose producing a 50% control rate of the tumour exposed to uniform radiation, γ_{50} is the unit less model parameter for describing the slope of the tumour dose-response curve, and TD_{50} is the tolerance dose producing a 50% complication rate. For radiobiological modelling, the recommended parameters from prostate radiotherapy treatment studies^[26-29] were used in the above equations for the calculation of the tissue control probability and the normal tissue control probability together with the parameters shown in Table 1 were used for calculation according to the relation. Initial TCP and NTCP values were calculated using the above equations for all the treatment plans based on various PTV margins. Subsequent changes in TCP and NTCP due to target volume

Table 1: Parameters used for prostate tumour control probability and for rectum normal tissue complication probability modelling (Mzenda B *et al.* 2010 and AAPM Task Group 166, AAPM)

Structure	D_{50} (Gy)	γ_{50}	a	Dose per fraction	TD_{50} (Gy)
Prostate	46.3	0.95	-10	2.2	-
Rectum	-	-	8.33	2.2	80
Bladder	-	-	2	2.2	80

displacements used these initial TCP and NTCP values to deduce the subsequent loss in TCP and increase in NTCP.

Organ motion, set-up and delineation error effects on radiobiological parameters

With the help of pre-and in-treatment image guidance^[14-18] for tighter margins with improved OARs sparing, the prostate target displacement has been found asymmetrical (LR: 0–12 mm, SI: 0–14, AP: 0–14 mm, PA: 0–12 mm) in all axial views. To avoid interobserver variations in target volumes delineations, the same oncologist outlined all cases. Combined organ motion and setup error with 5 mm added 1 mm step sized asymmetrical margins up to maximum of PTV were used in our study to calculate the changes in radiobiological parameters TCP and NTCP. This was performed using Matlab-based simulation tool,^[30] where translation and rotation followed Gaussian distribution data. A stepwise increase in the combined delineation, set-up and organ motion error was used to shift the organ with respect to the dose distribution and compute the resulting loss of prostate TCP (i.e., Δ TCP) and the increase in rectal NTCP (i.e., Δ NTCP) after each step increment. This procedure was repeated for each of the treatment plans using the different PTV margins. In radiotherapy prostate cancer treatment, an absolute NTCP of 5% is considered to be the maximum acceptable value if rectal complications are to be avoided.^[27] The range of treatment plans and simulated errors in our study produced absolute NTCP values which were all within the 5% absolute limit. In implementing the rules for the fuzzy system for Δ NTCP values above 10%, the PTV margin was not permitted to exceed 5 mm to avoid rectal complications due to margin selection. A further consideration in implementing the fuzzy rules was that for a tubular structure such as the rectum, the irradiated fraction of the circumference is correlated to rectal bleeding.^[31] As such the fraction of irradiated rectal wall was also calculated for each margin as a function of combined errors, and used in the formulation of the fuzzy membership rules.

Implementation of Mamdani Fuzzy Logic System

Mamdani-type fuzzy system was chosen for modelling as shown in Figure 3. It gave results which were consistent with the expected output suited to human input and so widely accepted for capturing expert knowledge which is very significant particularly in real time adaptive treatment. The final number of membership functions and fuzzy rules used in

this study were chosen to fulfil the applied model conditions described below. The system consisted of 2 inputs, namely Δ TCP and Δ NTCP, and 1 output, i.e., PTV margin. Six membership functions i.e., almost zero, very small, small, medium, high and very high were chosen for the input and output terms resulted in the functions shown in Figures 4 and 5. The widths of the functions were based on the gradient of the different sections of the input data. The output membership functions were defined using constants.

The Gaussian type membership functions were chosen for modelling following an assessment of the outputs from triangular, trapezoidal, generalized bell and Gaussian membership functions. The output surfaces from all functions other than the Gaussian function showed steep variations which imply uneven changes in PTV margin with changes in TCP and NTCP, which did not correspond to the known relationships from the input data. The output surface for the Gaussian function however showed relatively continuous and even transitions which correspond well with the input data variation.

The rules of the Mamdani FIS were formulated as shown below:

$$R_i: \text{If } (x_1 \text{ is } f_{i1}) \text{ and } \dots (x_j \text{ is } f_{ij}) \dots \text{ and } (x_m \text{ is } f_{im})$$

$$\text{then } y_i = g_i \tag{4}$$

Where $i = 1, n; j = 1, m;$

m is the number of inputs, n is the number of rules, x_j represents the j th input, f_{ij} the membership function of the i th rule, y_i is the output of rule R_i and g_i represents the analytical function of the inputs x_j , and g_i is a real number. The fuzzy rules were devised based mainly on the condition that the increase in NTCP is compensated for by reducing the PTV margin whilst the loss in TCP is compensated for by increasing the PTV margin size. Preselected Δ NTCP values as well as the irradiated volume of the anterior wall were chosen so as to allow the algorithm to select margins that would avoid rectal complications. Therefore the fraction of irradiated rectal wall was also calculated for each margin as a function of total displacement, and used in the formulation of the fuzzy membership rules. The optimum fuzzy rules^[32,33] derived from input data and using the clinical goals and knowledge-based conditions imposed on the margin limits are as shown in Table 2. The Permutations of the membership functions for Δ TCP, Δ NTCP and PTV margin resulted in 36 fuzzy rules. However these conditions vary from case to

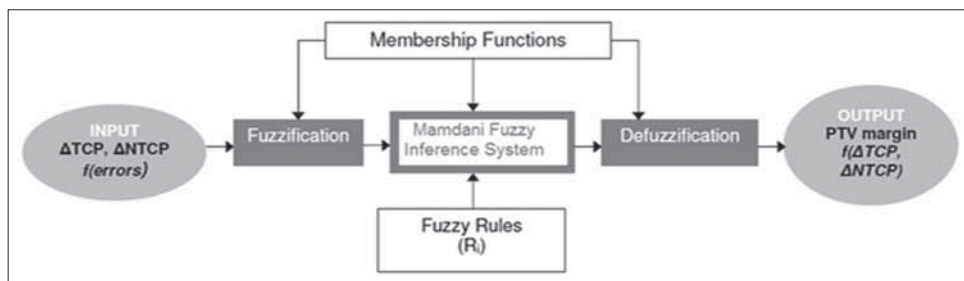


Figure 3: Basic operation principle of the Mamdani type fuzzy inference system used to calculate the planning target volume margin output function

case taking into account organ motion and deformation of target and surrounding normal structures as one of the major confounding factors for prostate tumour site.

RESULTS AND DISCUSSION

Effect of input data on asymmetric margin order of planning target volume and defuzzified output

The effect of magnitude of organ motion and set-up errors on prostate Δ TCP, rectum Δ NTCP and bladder Δ NTCP using

Table 2: Fuzzy rules used in the Mamdani-fuzzy inference system (Mzenda B *et al.* 2010)

Rule	If inputs		Output PTV margin
	Δ TCP	Δ NTCP	
R1	Almost zero	Almost zero	Almost zero
R2	Very small	Almost zero	Small
R3	Very small	Very small	Small
R4	Small	Small	Medium
R5	Small	Medium	Medium
R6	Medium	Medium	Medium
R7	Medium	High	Small
R8	High	High	Very small
R9	High	Very high	Almost zero
R10	Very high	Very high	Almost zero

TCP: Tumour control probability, NTCP: Normal tissue complication probability, PTV: Planning target volume

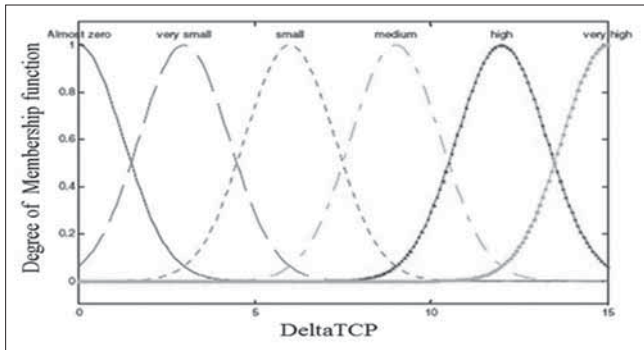


Figure 4: Membership function for Δ tumour control probability

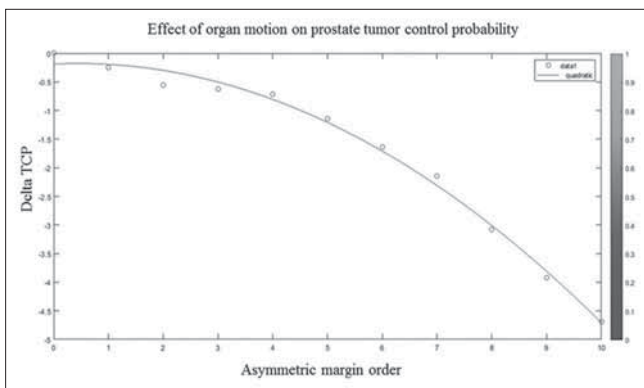


Figure 6: Delta tumour control probability versus asymmetric margin order: Effect of organ motion and setup errors on prostate tumor control probability

CTV only margin, are generated with MatlabR2018a as shown in Figures 6-8, respectively. For the effect on TCP, Increasing the errors resulted in the increased loss of TCP. For combined errors with magnitude of margin order up to 10 used in our study. It was found that increasing the PTV margin resulted in a nonlinear decrease in the loss in TCP. Also for the effect on NTCP, the increase in magnitude of margin order was found to increase the NTCP values. This variation of Δ NTCP with increasing asymmetric margin order from 0 to 10 was found to be approximately nonlinear. This variation may be expected linear or nonlinear depends on organ type and sub volumes overlapping.

Based on the Δ TCP/ Δ NTCP input data, the output function was calculated for the Mamdani-FIS as shown in Figure 9, as a three dimensional surface generated in MatlabR2018a, where each point corresponds to a specific Δ TCP, Δ NTCP and PTV margin value. From this output function it was observed that the increase in the Δ NTCP results in a decrease in the PTV margin. Correspondingly an increase in the Δ TCP results in an increase in the PTV margin. This result satisfies the imposed margin requirements as the increase in the loss in TCP gives rise to an increase in the PTV margin as required. Also, in compensation, an increase in critical organ dose results in

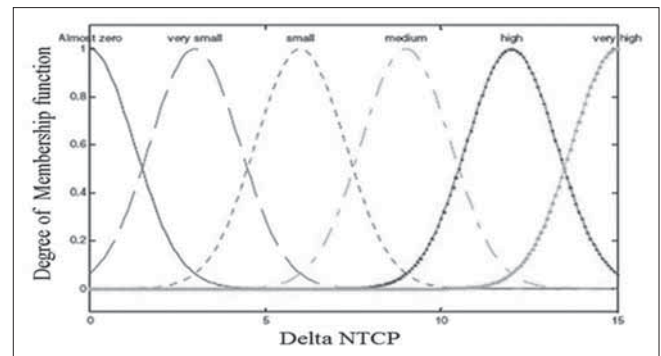


Figure 5: Membership function for Δ normal tissue complication probability

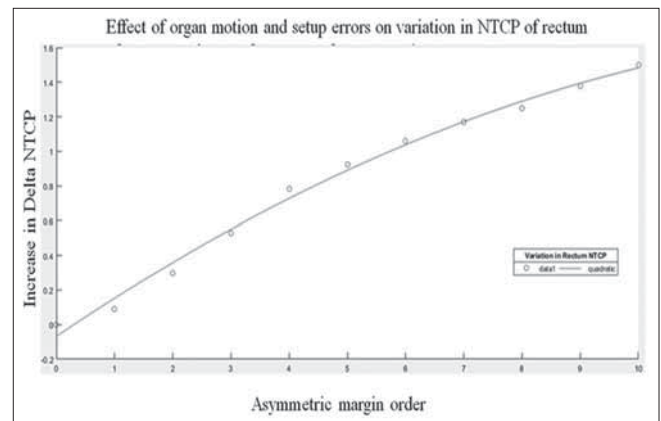


Figure 7: Delta normal tissue complication probability versus asymmetric margin order: Effect of organ motion and setup errors on the variation in normal tissue complication probability of rectum

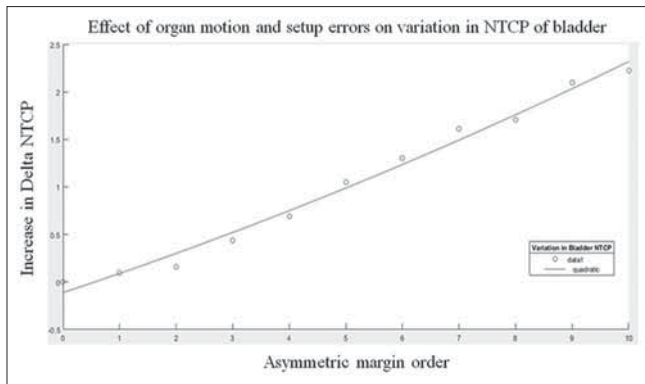


Figure 8: Delta normal tissue complication probability versus asymmetric order: Effect of organ motion and setup errors on the variation in normal tissue complication probability of Bladder

a decrease in the PTV margin. The output function satisfied the applied system rules and also the conditions regarding predefined Δ NTCP tolerance levels on the margin limitations.

Fuzzy margin comparison to current margins

The PTV margin obtained using the fuzzy model was compared to the commonly used margin recipe proposed by van Herk *et al.*^[8] For total displacement standard errors ranging from 0 to 5 mm, the fuzzy PTV margin was found to be up to 0.5 mm bigger than the van Herk derived margin, however taking the modelling uncertainty into account results in a good match between the PTV margin calculated using our model and the one based on van Herk *et al.* formulation for equivalent errors of up to 5 mm standard deviation (s. d.) at this lower range. When the total displacement standard errors exceed 5 mm s. d. the van Herk margin was higher because the van Herk *et al.* theoretical formulation shows a continuous linearly increasing PTV margin. In practice the combined treatment errors encountered in prostate radiotherapy seldom result in PTV margins that exceed 12 mm whilst the fuzzy margin remained below 12 mm. This trend is attributed to the effect of introducing TCP and NTCP in the margin formulation and the dominance of the constraint for rectal sparing in the margin formulation. This variation is dependent on the chosen TCP and NTCP tolerances as well as the proximity between the tumour volume and the OARs. A standard uncertainty of ± 0.5 mm was computed as the error in the PTV margin values obtained using the fuzzy model in this study.

The fuzzy PTV margin was applied in VMAT treatment planning example to assess its performance against current margins. Using the standard deviation of total displacement errors, treatment margins corresponding to 4 mm standard errors were selected. This led to a 9 mm margin for the fuzzy PTV and 8 mm margin for the van Herk PTV. Equivalent treatment plans were produced using these margins, together with a prescription dose of 73.5 Gy. Similar biasing were applied to these plans and the effects on the critical organs were evaluated. The results obtained from the VMAT plans for the prostate PTV are shown in Figure 10a. As it can be

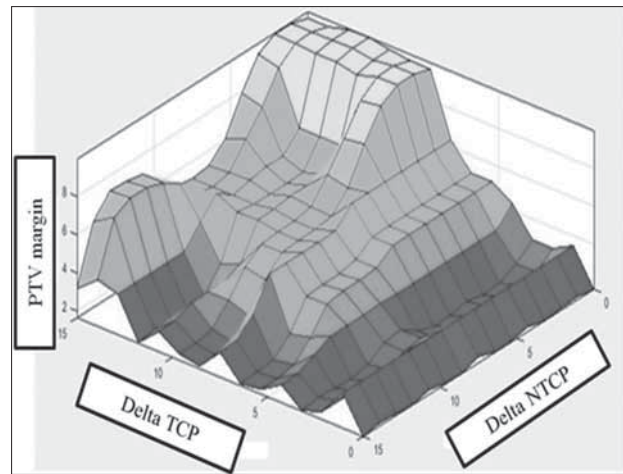


Figure 9: Output function from fuzzy system

seen very small differences were observed between the plans. No significant differences were found in the prostate PTV, rectum, and bladder DVHs between the two plans when equal displacement errors were introduced. This is due to the small differences in these parameters in the original plans and the application of a reduced error magnitude due to the reduction of systematic and random errors from the applied image-guided radiation therapy protocol. Similarly equivalent treatment plans were produced using 12 mm margin for the fuzzy PTV and 14 mm margin for the van Herk PTV for treatment margins corresponding to 6 mm standard errors and the results obtained from the VMAT plans for the prostate PTV are shown in Figure 10b. Noticeable differences were found in the prostate, rectum, and bladder DVHs due to effect of introducing TCP and NTCP in the margin formulation and due to the dominance of the constraints for bladder and rectal sparing embedded in the margin selection procedure. Thus in the region of large errors, the rate of PTV margin increase is seen to decrease significantly for the fuzzy case compared to the conventional method.

The advantage of using mamdani-fuzzy logic is that a practical limitation on the margin size is imposed in the model for limiting the dose received by the critical organs. It uses both physical and radiobiological data to optimize the required margin as per clinical requirement in real time or adaptive planning, which is an improvement on most margin models which mainly rely on physical data only. The fuzzy model is also relatively simple to implement and gives accurate margin sizes and can thus be extended to other treatment sites as required. The main objective of this work was to show the feasibility of the computational methods for deriving patient margins, and this has been supported by the findings. Whilst the proposed methods have been compared together, it is worth pointing out that without a “gold standard,” this comparison is relevant only for the sample of patient data used in this study. The novelty of the method proposed in this study lies more in that they allow for the calculation of individualised patient margins and prospective purpose, which

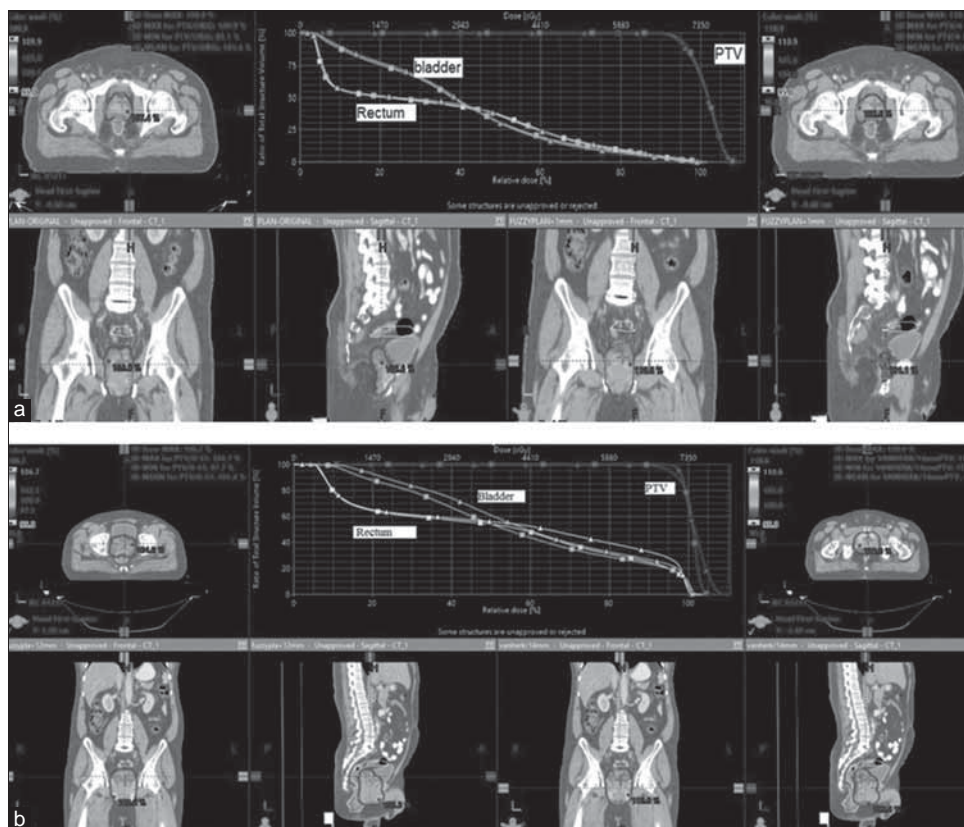


Figure 10: (a) Volumetric modulated arc therapy plan and dose volume histogram for planning target volume, Bladder, Rectum using the van Herk (-▲-▲-▲-▲-) and fuzzy (-■-■-■-■-) derived margins corresponding to 4 mm standard error standard deviation (b) Volumetric modulated arc therapy plan and Dose volume histogram for planning target volume, Bladder, Rectum using the van Herk (-▲-▲-▲-▲-) and fuzzy (-■-■-■-■-) derived margins corresponding to 6 mm standard error standard deviation

is currently very difficult to accomplish with manual setup of current techniques which result in low patient efficiency due to individualised patient setup corrections particularly in busy radiotherapy departments.

CONCLUSION

Fuzzy logic has the potential to be combined with existing algorithms in radiotherapy planning, leading to intelligent solutions to the complexities encountered in current and emerging radiotherapy treatment techniques. New treatment strategies e.g., VMAT and Cyberknife, are capable of delivering highly conformal dose distributions to the tumour volume. This inevitably involves steep dose gradients lying next to the critical organs. Using the same margin size for the same tumour type for all patients as is currently the case will not be ideal in such treatments. This is due to physiological variations from patient to patient. Using the models from this study it is possible to compute margins on a patient-by-patient basis using individual measured errors. This way the most reliable margins will always be used. A Matlab based software tool is in development for the practical implementation of this fuzzy margin in radiotherapy treatment planning.

Financial support and sponsorship

Nil.

Conflicts of interest

There are no conflicts of interest.

REFERENCES

1. Lind BK, Källman P, Sundelin B, Brahme A. Optimal radiation beam profiles considering uncertainties in beam patient alignment. *Acta Oncol* 1993;32:331-42.
2. Lof J, Lind BK, Brahme A. Optimal radiation beam profiles considering the stochastic process of patient positioning in fractionated radiation therapy. *Inverse Probl* 1995;11:1189.
3. Stavrev PV, Stavreva NA, Round WH. A new method for optimum dose distribution determination taking tumour mobility into account. *Phys Med Biol* 1996;41:1679-89.
4. Jones D. ICRU report 50—prescribing, recording and reporting photon beam therapy. *Med Phys* 1994;21:833-4.
5. Wambersie A, Landgerg T. ICRU Report 62: Prescribing, Recording and Reporting Photon Beam Therapy. Bethesda MD: ICRU Published; 1999.
6. Gahbauer R, Landberg T, Chavandra J, Dobbs J, Gupta N, Hanks G, *et al.* Prescribing, recording, and reporting electron beam therapy. *J ICRU* 2004;4:1-2.
7. Stroom JC, de Boer HC, Huizenga H, Visser AG. Inclusion of geometrical uncertainties in radiotherapy treatment planning by means of coverage probability. *Int J Radiat Oncol Biol Phys* 1999;43:905-19.
8. van Herk M, Remeijer P, Rasch C, Lebesque JV. The probability of correct target dosage: Dose-population histograms for deriving treatment margins in radiotherapy. *Int J Radiat Oncol Biol Phys* 2000;47:1121-35.
9. Waschek T, Levegrün S, van Kampen M, Glesner M, Engenhart-Cabillic R, Schlegel W. Determination of target volumes for

- three-dimensional radiotherapy of cancer patients with a fuzzy system. *Fuzzy Sets Syst* 1997;89:361-70.
10. Mzenda B, Hosseini-Ashrafi M, Gegov A, Brown DJ. Implementation of a fuzzy model for computation of margins in cancer treatment. In: IEEE World Congress on Computational Intelligence, Spain (Conference Proceedings: FUZZ-IEEE 2010. p. 1931-1938.
 11. Alcalá R, Cano JR, Cordon O, Herrera F, Villar P, Zwir I. Linguistic modeling with hierarchical systems of weighted linguistic rules. *Int J Approx Reason* 2003;32:187-215.
 12. Baboshin NP, Naryshkin DG. On identification of multidimensional fuzzy systems. *Fuzzy Sets Syst* 1990;35:325-31.
 13. de Oliveira JV, Gomide F. Formal methods for fuzzy modeling and control. *Fuzzy Sets and Systems* 2001;121:1-2.
 14. Yartsev S, Bauman G. Target margins in radiotherapy of prostate cancer. *Br J Radiol* 2016;89:20160312.
 15. Gardner SJ, Wen N, Kim J, Liu C, Pradhan D, Aref I, *et al.* Contouring variability of human- and deformable-generated contours in radiotherapy for prostate cancer. *Phys Med Biol* 2015;60:4429-47.
 16. Zahra N, Monnet C, Bartha E, Courbis M, Le Grévellec M, Bosset M, *et al.* EP-1657: Inter-observer variability study for daily CBCT registration of VMAT prostate treatment. *Radiother Oncol* 2015;115:S908.
 17. Wen N, Kumarasiri A, Nurushev T, Burmeister J, Xing L, Liu D, *et al.* An assessment of PTV margin based on actual accumulated dose for prostate cancer radiotherapy. *Phys Med Biol* 2013;58:7733-44.
 18. Zelefsky MJ, Crean D, Mageras GS, Lyass O, Happersett L, Ling CC, *et al.* Quantification and predictors of prostate position variability in 50 patients evaluated with multiple CT scans during conformal radiotherapy. *Radiother Oncol* 1999;50:225-34.
 19. NCCN. Prostate Cancer. NCCN Practice; 2016. Available from: <http://www.nccn.org/guidelines/inoncology-/projsessional/physician-g/s/f-guidelines.asp.v3>. [Last accessed on 2018 Aug 05].
 20. Niemierko A. Reporting and analyzing dose distributions: A concept of equivalent uniform dose. *Med Phys* 1997;24:103-10.
 21. Choi B, Deasy JO. The generalized equivalent uniform dose function as a basis for intensity-modulated treatment planning. *Phys Med Biol* 2002;47:3579-89.
 22. Ray Search Laboratories AB SS Biological Optimization using the Equivalent Uniform dose in Pinnacle. Ray Search White Paper; 2003.
 23. Wang JE, Mayr NA, Yuh W. Behind EUD *Acta Oncol* 2008;47:971-2.
 24. Wu Q, Mohan R, Niemierko A, Schmidt-Ullrich R. Optimization of intensity-modulated radiotherapy plans based on the equivalent uniform dose. *Int J Radiat Oncol Biol Phys* 2002;52:224-35.
 25. Gay HA, Niemierko A. A free program for calculating EUD-based NTCP and TCP in external beam radiotherapy. *Phys Med* 2007;23:115-25.
 26. Burman C, Kutcher GJ, Emami B, Goitein M. Fitting of normal tissue tolerance data to an analytic function. *Int J Radiat Oncol Biol Phys* 1991;21:123-35.
 27. Agren A, Brahme A, Turesson I. Optimization of uncomplicated control for head and neck tumors. *Int J Radiat Oncol Biol Phys* 1990;19:1077-85.
 28. Fiorino C, Reni M, Bolognesi A, Cattaneo GM, Calandrino R. Intra- and inter-observer variability in contouring prostate and seminal vesicles: Implications for conformal treatment planning. *Radiother Oncol* 1998;47:285-92.
 29. AAPM Task Group. American Association of Physicists in Medicine : The use and QA of Biologically Related Models for Treatment Planning, AAPM Task Group 166. AAPM;2012.
 30. Mzenda B, Hosseini-Ashrafi ME, Palmer A, Hodgson DF, Liu H, Brown DJ. Determination of target volumes in radiotherapy and the implications of technological advances: A literature review. *J Radiother Pract* 2009;8:41-51.
 31. Benk VA, Adams JA, Shipley WU, Urie MM, McManus PL, Efrid JT, *et al.* Late rectal bleeding following combined X-ray and proton high dose irradiation for patients with stages T3-T4 prostate carcinoma. *Int J Radiat Oncol Biol Phys* 1993;26:551-7.
 32. Combs WE, Andrews JE. Combinatorial rule explosion eliminated by a fuzzy rule configuration. *IEEE Trans Fuzzy Syst* 1998;6:1-11.
 33. Dubois D, Prade H, Ughetto L. Checking the coherence and redundancy of fuzzy knowledge bases. *IEEE Trans Fuzzy Syst* 1997;5:398-417.

Appendix-A

The MATLAB based algorithm is to calculate target and OARs EUD-based NTCP and TCP for inputs in our fuzzy model study.

A free program for calculating EUD-based NTCP and TCP in external beam radiotherapy (Reference-25) may be downloaded from <http://www.ecu.edu/radiationonco/gy/downloads.htm>

%Save this file in Matlab as eudmodel.m

% EUDMODEL (DVH), where DVH is a 2 column matrix corresponding to the cumulative, not
 % differential, dose volume histogram. The 1st column corresponds to increasing absolute dose or
 % percentage dose values, and the 2nd column to the corresponding absolute or relative volume value.
 %The matrix must have a minimum of two rows, and both columns must be of equal length.

function probability = eudmodel (dvh)

%user input section

clc; disp('Welcome to the Equivalent Uniform Dose (EUD)-Based Model Program'); disp(' ');

disp('Please note that: 1) the variable dvh should be a CUMULATIVE, not differential, DVH');

disp(' 2) the program assumes that all treatment fractions are equal');

disp(' '); disp(' ');

%end of user input section

%verifying that the **cumulative DVH** has at least 2 rows and columns

```

[nb, N]=size (dvh);
if (nb < 2)
disp('Error: Cumulative dvh must have at least 2 rows. '); return;
end
if (N < 2)
disp('Error: Cumulative dvh must have at least 2 columns. '); return;
end
%converting percentage dose bins into absolute dose bins
for i = 1:nb
dvh (i, 1)=dvh (i, 1)*nf*normalized fraction/100;
end
%if DVH dose data is in cGy it is converted to Gy
%EUD mathematical model parameters input section
clc; disp('Does the DVH correspond to:');
disp(' 1. tumor target');
disp(' 2. normal tissue')
tissue type = input('Enter 1 or 2: '); disp(' ');
if (tissue type==1)
clc
disp ('* = Niemierko'); disp(' ');
a = input ('Enter the value of parameter a: ');
gamma50 = input ('Enter the value of parameter gamma50 (recommend 2 if unknown): ');
tcd50 = input ('Enter the TCD50 (Gy): ');
ab = input ('Enter the tumor alpha/beta ratio (Gy): ');
elseif (tissue type ==2)
clc
disp ('Normal tissue EUD Parameters:'); disp(' ');
td50 = input('Enter the TD50 (Gy): ');
ab = input('Enter the normal tissue alpha/beta ratio (Gy): ');
else
disp ('Error: Invalid choice. Exiting program. '); return;
end
%calculating the biologically equivalent dose and the total volume
%normalizing volume data to 1 (therefore, total volume corresponds to 1)
for I = 1: nb
dvh (i, 2) = dvh (i, 2)/total volume;
bndvh (i, 2) = dvh (i, 2);
end

```

%calculating the EUD

for I = 1: nb

eud = eud+(bndvh (i, 2))*(bndvh (i, 1))^a;

end

%Results section

If (tissue type == 1)

% calculating tumor control probability

tcp = 1/(1+((tcd50/eud)^(4*gamma50)));

tcp = mcp*100;

message = sprintf('The tumor control probability = %10.10f %%', tcp);

% calculating normal tissue complication probability

tcp = 1/(1+((td50/eud)^(4*gamma50)));

ntcp = ntcp*100;

message = sprintf('The normal tissue complication probability = %10.10f %%', ntcp);

% end of Results section.

Appraisal of Deep-Learning Techniques on Computer-Aided Lung Cancer Diagnosis with Computed Tomography Screening

S. Akila Agnes, J. Anitha

Department of CSE, Karunya Institute of Technology and Sciences, Coimbatore, Tamil Nadu, India

Abstract

Aims: Deep-learning methods are becoming versatile in the field of medical image analysis. The hand-operated examination of smaller nodules from computed tomography scans becomes a challenging and time-consuming task due to the limitation of human vision. A standardized computer-aided diagnosis (CAD) framework is required for rapid and accurate lung cancer diagnosis. The National Lung Screening Trial recommends routine screening with low-dose computed tomography among high-risk patients to reduce the risk of dying from lung cancer by early cancer detection. The evolution of clinically acceptable CAD system for lung cancer diagnosis demands perfect prototypes for segmenting lung region, followed by identifying nodules with reduced false positives. Recently, deep-learning methods are increasingly adopted in medical image diagnosis applications. **Subjects and Methods:** In this study, a deep-learning-based CAD framework for lung cancer diagnosis with chest computed tomography (CT) images is built using dilated SegNet and convolutional neural networks (CNNs). A dilated SegNet model is employed to segment lung from chest CT images, and a CNN model with batch normalization is developed to identify the true nodules from all possible nodules. The dilated SegNet and CNN models have been trained on the sample cases taken from the LUNA16 dataset. The performance of the segmentation model is measured in terms of Dice coefficient, and the nodule classifier is evaluated with sensitivity. The discriminant ability of the features learned by a CNN classifier is further confirmed with principal component analysis. **Results:** Experimental results confirm that the dilated SegNet model segments the lung with an average Dice coefficient of 0.89 ± 0.23 and the customized CNN model yields a sensitivity of 94.8 on categorizing cancerous and noncancerous nodules. **Conclusions:** Thus, the proposed CNN models achieve efficient lung segmentation and two-dimensional nodule patch classification in CAD system for lung cancer diagnosis with CT screening.

Keywords: Computer-aided diagnosis system for lung cancer, convolutional neural network, deep learning, false-positive reduction, lung segmentation, pulmonary nodule detection

Received on: 14-11-2019

Review completed on: 03-03-2020

Accepted on: 27-03-2020

Published on: 20-07-2020

INTRODUCTION

Lung cancer is the superior reason of cancer deaths worldwide.^[1] People, who are identified with lung cancer in advanced stages, have a very low survival rate, and this prevents effective treatments. Earlier detection of cancer expands survival and supports people to live a long life by taking proper treatment without necessarily extending life. In the United States, every year approximately \$9.6 billion are spent on lung cancer treatment. This poses a significant financial burden for the people, though they have health insurance. As the newer technologies and treatments increases, the expenditures for cancer-preventive care may increase at a faster rate than overall medical expenditures.^[2] These facts create a demand on cost-effective cancer control and prevention schemes such as computer-aided lung cancer

screening programs. The National Lung Screening Trial confirms that low-dose computed tomography (LDCT) screening reduces the mortality rate by lung cancer.^[3] The American College of Chest Physicians provides guidelines for the successful execution of lung cancer screening program.^[4] Lung cancer screening with LDCT is advised for adults with the age of 55–80 years who have about 30 years of smoking history. Routine screening with CT imaging is suggested to high-risk patients for early cancer detection. However, an extra attention is needed while repeating LDCT screening

Address for correspondence: Dr. J. Anitha,
Department of CSE, Karunya Institute of Technology and Sciences,
Coimbatore, Tamil Nadu, India.
E-mail: anitha_j@karunya.edu

Access this article online

Quick Response Code:



Website:
www.jmp.org.in

DOI:
10.4103/jmp.JMP_101_19

This is an open access journal, and articles are distributed under the terms of the Creative Commons Attribution-NonCommercial-ShareAlike 4.0 License, which allows others to remix, tweak, and build upon the work non-commercially, as long as appropriate credit is given and the new creations are licensed under the identical terms.

For reprints contact: WKHLRPMedknow_reprints@wolterskluwer.com

How to cite this article: Agnes SA, Anitha J. Appraisal of deep-learning techniques on computer-aided lung cancer diagnosis with computed tomography screening. *J Med Phys* 2020;45:98-106.

tests because it accumulates radiation exposure. The recent practice guidelines given by the American College of Chest Physicians recommended longer intervals between CT scans.^[5] The US Preventive Services Task Force has reported that the consequence of radiation exposure is insignificant as compared with the cut-rate of cancer death.

Screening with LDCT helps to diagnose lung cancer, and if lung cancer is diagnosed at an earlier state before spreading to other organs, people might have a better chance of long life. However, false-positive (FP) diagnosis results may lead the people to one more advanced level radiation testing, which may harm their normal health. Hence, cautious screening and accurate diagnosis is very important. Recently, the machine-learning community has developed computerized tools and learning models for computer-aided diagnosis (CAD) systems that demonstrate clinically acceptable performance. At present, the Food and Drug Administration has given premarket approval for two CAD application domains such as breast cancer diagnosis with mammogram images and lung cancer diagnosis with chest radiographs.^[6] Vapnik *et al.* have proposed a new artificial intelligence-based system that could learn hidden and essential information to improve CAD technology for lung cancer diagnosis.^[7] In general, CAD system for lung cancer diagnosis comprises two components such as parenchyma segmentation and classification of candidate nodules. Figure 1 shows the framework of CAD system for lung cancer diagnosis with deep learning.

Parenchyma segmentation is a preliminary procedure for any clinical diagnosis system intended to simplify the early diagnosis of lung diseases. This process obtains the lung parenchyma volume from the unprocessed CT scan image by removing the undesired parts such as image artifacts, heart, spinal cord, trachea, bronchi, bone, and muscle. Classifying the normal and cancerous pulmonary nodules is an essential step in cancer diagnosis process. Pulmonary nodules are small abnormalities existing in the lung region, which are need not be cancer nodules that can be caused by old infections or other causes. On chest CT scans, a lung nodule is described as a small tumor on the lung, which varies in diameter from 3 mm to 3 cm. In general, the malignant nodules have unusual shapes, irregular surfaces, and color mutations. Detectability of cancerous nodules in the lung depends on the contrast between the nodule and the surrounding nonnodule tissue.

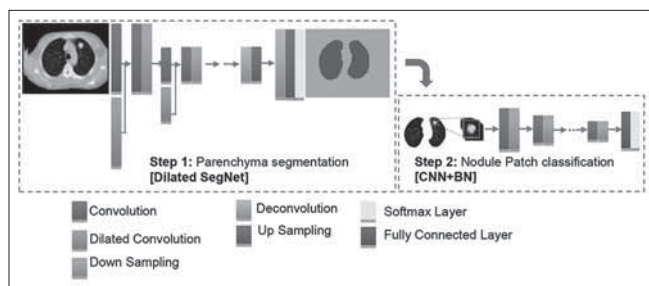


Figure 1: Computer-aided diagnosis system for lung cancer with deep-learning approach

The samples of true and false pulmonary nodule patches are illustrated in Figure 2.

Related work

Deep-learning techniques produced excellent results in various computer vision problems. The reason behind the success of deep learning is the feature learning behavior and least domain expertise effort. This approach finds the solution directly from the target problem by supervised learning method. This attracts the researchers toward deep-learning techniques for medical image analysis. Convolutional neural network (CNN) is the most popular neural network for spatial image (two-dimensional [2D] matrix) analysis.

Quite a few ConvNet architectures have been proposed for semantic segmentation that acquires the spatial features from the annotated datasets and produces a prediction map. Most of the segmentation CNN models are symmetrical architecture consisting of an encoder and an equivalent decoder. These networks demand high memory configuration and difficult to be trained on entire volumetric medical images. However, these deep models have been trained with 2D slices or small 3D crop to learn the global features by accommodating memory limitations without compromising its capability. Nie *et al.* have proposed a multiple fully connected CNN to segment infant brain images by fusing feature data from multiple modalities.^[8] U-Net is an improved CNN that is designed to segment medical images. It is widely employed on a range of medical image analysis tasks such as liver segmentation^[9] and breast segmentation.^[10] SegNet^[11] is a kind of CNN which is also designed for semantic segmentation of outdoor scene. SegNet architecture uses the feature maps computed from max-pooling layers in its decoder section; thus, it produces accurate results by consuming less memory during training phase. Khagi *et al.*^[12] have suggested that the encoder-decoder network of SegNet with certain alterations can be used in medical magnetic resonance imaging image segmentation.

The existing lung parenchyma segmentation methods such as random walk, watershed segmentation, fuzzy logic, and graph search algorithms are the compound of multiple procedures that consume more time and could not afford result at a single step. Recently, few research works have been carried particularly on lung segmentation with deep neural networks that are presented in Table 1. Due to the computational speed and storage capacity limitations, these networks have not been trained on entire 3D data.

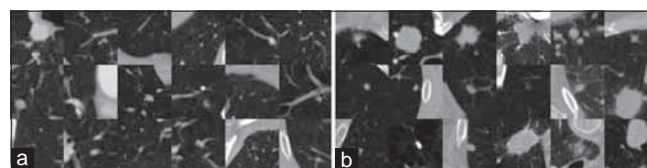


Figure 2: Samples of true positive and false nodules extracted from the Lung Image Database Consortium dataset, (a) False nodules, (b) True nodules. Nodule is located at the center of 64 × 64 mm axial view patch

The pulmonary nodule classification is a critical task in CAD system for lung cancer. This will be done in two steps such as candidate nodule detection and FP reduction. The candidate nodules are detected using thresholding, followed by a morphological opening operation. In FP reduction phase, the false nodules are identified and dropped using classification techniques. Recognizing the suitable features for distinguishing the nodules is more challenging; hence, an automatic feature learning method is required to find more descriptive features from raw data.

The pulmonary nodule classification is done in two ways such as feature-based approach and deep-learning-based approach. In a feature-based approach, the radiological features such as nodule volume, position, appearance, texture, and so forth are extracted from the candidates, and then, a classifier is built to determine the class of the nodule. Here, obtaining and choosing the significant subset of features for an accurate lung nodule classification is a vital task. In deep-learning-based approach, a model is designed to learn the essential features from the candidate nodules for accurate classification. During the last decade, numerous medical image classification tasks have employed deep-learning techniques. Hinton introduced deep learning in 2006,^[16] which is motivated by the working of human neural schema and designed by mimicking the intercommunication of several neurons. Table 2 presents the overview of recent works carried out on pulmonary nodule classification using deep-learning techniques.

Pulmonary nodule classification is a sort of 3D image analysis problem, but most of the present deep models have utilized 2D details for building the convolutional neural networks (CNNs)^[28] or multiview 2D CNN^[27,29] classifier model. Considering only 2D data might skip essential information required for malignancy determination. Hussein *et al.* classify the nodules based on the features extracted by 3D CNN model and fused with six more featured advised by radiologists.^[30] Identifying such high-level nodule attributes based demands the knowledge of experienced radiologists. Zhu *et al.* have proposed a 3D deep model to classify lung nodules using gradient boosting machine with the features extracted for nodule classification.^[17] Qi Dou *et al.*^[26] have proposed a hierarchical 3D CNN to extract contextual features from candidate nodules at various hierarchical levels and filter the high-probability locations as true nodules. Unbalanced data distribution and scarcity problems of medical image dataset can be overcome by incorporating transfer learning technique while designing the classifier model.^[24,27]

Voxel-based machine learning (VML) is a kind of supervised learning technique used to segment the pulmonary nodules directly from the input image without selecting the candidate nodules.^[31] For accurate lung nodule segmentation, the classifier requires both local details about nodule appearance and global contextual details about nodule location. In VML approach, the model is trained in a supervised manner directly from the volumetric features retrieved from voxel values of

Table 1: Deep-learning approaches for lung parenchyma segmentation

Authors	Main methods	Performance metrics
Harrison <i>et al.</i> ^[13]	Progressive and multipath CNN	Dice: 0.985
Agnes <i>et al.</i> ^[14]	Convolutional deep and wide network	Dice: 0.950
Skourt <i>et al.</i> ^[15]	U-Net architecture	Dice: 0.9502

CNN: Convolutional neural network

Table 2: Pulmonary nodule classification using deep-learning techniques

Authors	Main methods	Performance metrics
Zhu <i>et al.</i> ^[17]	2D-CNN	Sensitivity: 0.86
Eun <i>et al.</i> ^[18]	Ensemble 2D CNN	Sensitivity: 0.92
Hamidian <i>et al.</i> ^[19]	3D FCN, 3D CNN	Sensitivity: 0.80
Fu <i>et al.</i> ^[20]	Thresholding, 2D CNN, hand-crafted feature extraction	Accuracy: 0.91
Li <i>et al.</i> ^[21]	2D-CNN	Sensitivity: 0.87
Setio <i>et al.</i> ^[22]	Multistream CNN	Sensitivity: 0.85
Ypsilantis and Montana ^[23]	RNN-CNN	Sensitivity: 0.90
Ciampi <i>et al.</i> ^[24]	Pretrained CNN (OverFeat)	AUC: 0.868
Van Ginneken <i>et al.</i> ^[25]	Pretrained CNN	Sensitivity: 0.71
Dou <i>et al.</i> ^[26]	Multilevel 3D convolutional neural networks	Sensitivity: 0.94
Nibali <i>et al.</i> ^[27]	Deep residual network (ResNet)	Sensitivity :0.9107
Shen <i>et al.</i> ^[28]	MCNN	Accuracy: 86.84

2D: Two-dimensional, 3D: Three-dimensional, CNN: Convolutional neural network, MCNN: Multiscale CNN, FCN: Fully convolutional network, RNN: Recurrent neural network

CT images. Tong *et al.*^[32] have proposed a deep-learning-based pulmonary nodule segmentation algorithm. The algorithm segments the pulmonary nodules from the CT image directly using modified U-Net architecture, and the performance is evaluated with the Dice coefficient.

A number of research works have been carried out on medical image analysis with deep learning, but few works have been contributed for developing an effective lung cancer diagnosis system. Still, the CAD system for lung cancer requires improvement in detecting the cancer case without missing true pulmonary nodules. In this study, an enhanced SegNet model is proposed to segment the lung region and a modified CNN model is implemented to categorize the pulmonary lung nodules.

SUBJECTS AND METHODS

Dataset

Data acquisition is the preliminary act that acquires an input image for an effective diagnosis. CT scanners send radiation

beam to the human body and produce a more detailed CT scan image. CT imaging modality produces the volume data in a Digital Imaging and Communications in Medicine (DICOM) directory where the data are neatly packed with consequent numbering. Commonly, the medical images are preserved in standard DICOM format that helps the physicians to access the images and allows them to diagnosis the disease. Normally, the three-dimensional (3D) CT data are viewed in 2D planes such as axial, sagittal, and coronal, which provide an in-depth look to the radiologists for effective diagnosis. Since the 3D CT images are complex with many anatomical structures, it is reasonable to have a 2D view for better understanding of humans. CT scans enable the physicians to detect lung nodules accurately rather than chest X-ray scans.

The National Cancer Institute has made a collaborative work known as the Lung Image Database Consortium (LIDC) and Image Database Resource Initiative. LIDC- IDRI collection provides thoracic CT images and the marked lesions, and this stimulates the research progress on lung cancer diagnosis from CT images.^[8] The LIDC is a collaborative effort of five educational foundations that are operating collectively to build an image archive that supports universal research for the innovation of the CAD system for lung nodule detection on CT scans. LIDC-IDRI dataset contains nearly a thousand of patient data in DICOM file. Each file includes a series with stacked of axial slices of the chest cavity. The amount of 2D slices for every patient depends on the scanner machine, which takes the scan. Commonly, the thickness of slice in an axial direction is more than 2.5 mm. The identified lesions are categorized into three classes such as nonnodules, nodules smaller than 3 mm, and nodules bigger than 3 mm. Every study in this collection includes thoracic CT scan images and the related eXtensible Markup Language file that specify the coordinates of the nodule and its label. The nodule annotations have been marked by four qualified radiologists.

Convolutional neural network

CNN is a backpropagation neural network that works on multidimensional data. The standard CNN model should have a pile of convolutional and pooling layers tailed by a fully connected layer and a final softmax layer. Piling the convolutional layers enables the model to explore the hidden features and pattern of the input image at hierarchical levels. The basic operation of the convolutional layer is a convolution that recognizes the spatial relationship among pixels. The hierarchical order of convolution filters may extract features directly from the raw input image at different levels. The convolutional filter is called kernel, and the kernel weights are learned during the model training. Pooling is a downsampling process which reduces the dimensionality of the feature map which is obtained from the previous convolutional layer without missing any important information. The fully connected layer consolidates the set of features obtained from multiple convolutional layers into a single feature. Finally, the softmax layer classifies the outputs using the softmax activation function.

Dilated SegNet

SegNet is a kind of CNN that consists of a symmetrical encoder and decoder part. The encoder comprises a sequence of convolutional and downsampling layers. The decoder has a sequence of deconvolutional and upsampling layers and ended with a softmax layer that does pixel-wise classification. SegNet model does not contain a fully connected layer; therefore, this is faster than other segmentation neural networks such as fully convolutional network and DeconvNet. The proposed dilated SegNet model for lung segmentation is illustrated in Figure 3. The dilated SegNet model contains an improved encoder that produces fused convolved feature sets extracted at different dilation rates. Dilation rate specifies the gaps between the kernels and fills the empty positions with zeroes. A 3 × 3 kernel with a dilation rate of 2 will have the wider field view of 5 × 5 kernel. The dilated convolutional operations help the segmentation CNN model to sustain minimum computation time even higher field views are used. The encoder part consists of 2 convolutional layers, and each of them is followed by max-pooling layers. At convolutional layer, 32 kernels of size 3 × 3 with dilation rate of 1 and another 32 kernels of size 3 × 3 with dilation rate of 2 are applied. The convolved features obtained by both dilated and nondilated convolutional layers are fused and forwarded to the next pooling layer. Max-pooling operation with 2 × 2 window size (nonoverlapping) and a stride of two is applied at pooling layer to downsample the feature set by skipping the redundant details.

Convolution operation convolves two matrixes such as input image I and kernel filter H and produces the convolved matrix using Eq. 1, where $*$ indicates the convolution operation.

$$C[x, y] = [I[x, y] * H[x, y]] \tag{Eq. 1}$$

Convolution is a process of summing each pixel $I[i, j]$ of the image to its neighbors, weighted by the kernel filter $H[x-l, y-j]$

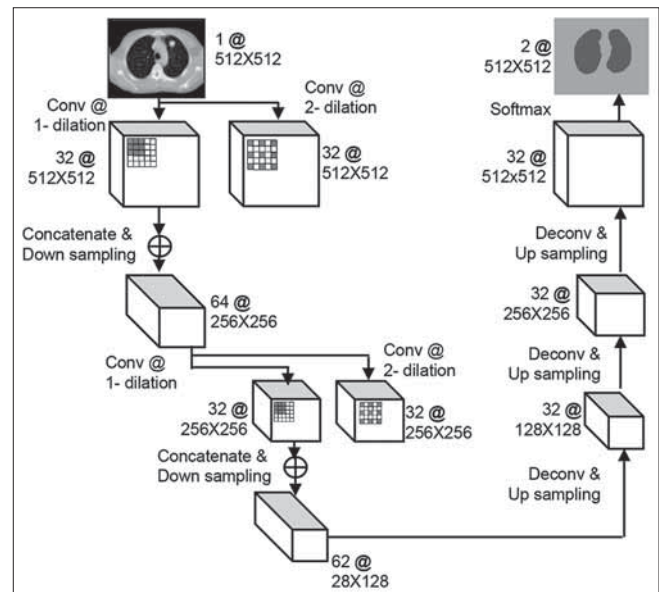


Figure 3: Illustration of the proposed dilated SegNet for lung segmentation

$$C[x, y] = \sum_j \sum_i I[i, j] H[x-i, y-j] \quad \text{Eq. 2}$$

Dilated convolution requires an additional parameter called dilation rate, which describes the gap between pixels. It enlarges the receptive field by introducing the gap between the cells in a kernel. Figure 4 illustrates an example of convolution operation on 6×6 input data with 3×3 filter at different dilation rates.

The decoder part contains deconvolutional layers, followed by upsampling layer. Upsampling operation helps the network to get back the original image dimension. In the proposed model, hidden convolution layers use ReLU activation function $ReLU(x) = \max(0, x)$ and the output layer uses softmax activation function. A softmax function is a type of squeezing function which confines the output vector into the range of 0–1. The softmax function takes an N-dimensional input vector with float values and produces another N-dimensional vector with real values in the range (0, 1) using Eq. 3.

$$Softmax(X): (x_1, x_2, \dots, x_n) \rightarrow S: (s_1, s_2, \dots, s_n), \text{ where } S_i = e^{x_i} / \sum_{j=1, \dots, n} e^{x_j} \quad \text{Eq. 3}$$

The objective function of the dilated SegNet aims to minimize the Dice loss that is calculated simply as:

$$DiceLoss = 1 - DiceCoeff \quad \text{Eq. 4}$$

Dice coefficient is computed using Eq. 5, where R is the segmented region mask image and G is the ground truth mask image.

$$DiceCoef(R, G) = \frac{2|R \cap G|}{|R| + |G|} \quad \text{Eq. 5}$$

Convolutional neural network with batch normalization

The CNN is a backpropagation neural network that comprises a series of convolutional and pooling layers, followed by a final classification layer. The 2D CNN model with batch normalization (BN) is developed to classify the nodule patches with a size of 64×64 . The learning process should not dilute the discriminant features between true and false nodule patches. Hence, a BN layer is attached after every

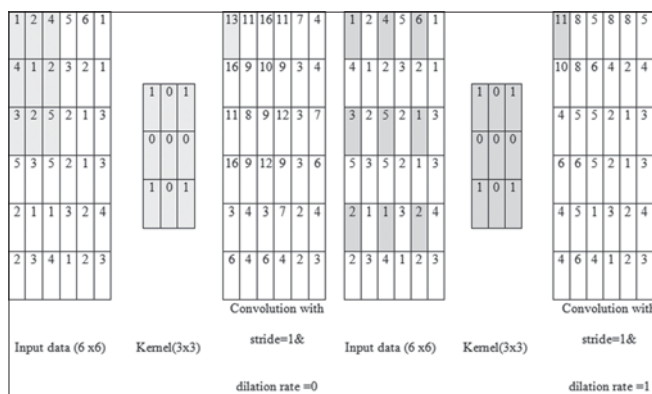


Figure 4: Illustration of convolution on 6×6 input data with 3×3 filter at different dilation rates

convolutional layer to standardize data throughout the network. BN technique helps to avoid network overfitting problem and improve the stability of the network. BN layer is used before the activation layer that normalizes the input by applying a linear scale and shift to the mini-batch.^[33] During training time, a BN layer calculates the batch mean μ_{batch} and variance σ_{batch} of the layer input $X: (x_1, x_2, \dots, x_m)$.

$$\mu_{batch} = \frac{1}{m} \sum_{i=1, \dots, m} x_i \quad \text{Eq. 5}$$

$$\sigma_{batch} = \frac{1}{m} \sum_{i=1, \dots, m} (x_i - \mu_{batch})^2 \quad \text{Eq. 6}$$

normalize the layer inputs using the calculated batch mean and variance. Output $Y: (y_1, y_2, \dots, y_m)$ is obtained by scaling and shifting the normalized inputs \bar{x}_i with the learned parameters γ and β .

$$\bar{X}_i = \frac{X_i - \mu_{batch}}{\sqrt{\sigma_{batch} + \xi}} \quad \text{Eq. 7}$$

$$y_i = \gamma \bar{x}_i + \beta \quad \text{Eq. 8}$$

2D CNN framework for lung nodule patch classification is shown in Figure 5. The CNN model consists of convolutional layer, followed by BN and max-pooling layer. Finally, a softmax layer classifies the nodule patches using the features extracted by the network. Every convolution layer in the model uses increasing number of kernels such as 16, 32 and 64 with the size of 3×3 and ReLU activation function. ReLU activation is a nonlinear activation function which does not suppress the effect of backpropagation and helps faster convergence of the network. The deep neural network efficiently works on normalized data so that the network can converge steadily without oscillations. The BN layer controls the magnitude and mean of the activations independent of all other layers. Max-pooling layer helps to eliminate the redundant details by choosing the maximum value within the block of size 2×2 . The softmax classifier implements classification by fitting the data classification boundaries, using gradient descent optimization technique. The softmax activation function maps the output vector into categorical probability vector

DISCUSSION

Lung segmentation with dilated SegNet

Dilated SegNet is modified SegNet model for separating lung region from chest CT images. The model has been trained with a subset of 1000 2D axial images obtained from LIDC dataset. The center axial slice is obtained from each volumetric CT scan images, and the slice is rescaled into 512×512 resolutions. The network weights are initialized randomly and fixed during training by backpropagation method. The first-order gradient optimizer “Adam” is used for tuning the model. Dice coefficient loss is used as the cost function, and a fixed learning rate of 1×10^{-3} is set for all iterations. The segmented result of the dilated SegNet is compared with the segmented results

obtained by Fuzzy C-means (FCM) clustering and SegNet models. Figure 6 shows the segmentation results of all models. The output images confirm that the proposed dilated SegNet model could segment the lung region accurately than FCM and SegNet algorithms. From the results, it is apparent that the intensity of the lung and scanner regions is similar, but the lung region has a clear boundary and different texture details as compared with the surrounding region. This helps the CNN to learn the abstract level features from the raw image and segment lung region accurately.

The performance of segmentation algorithms is quantitatively evaluated by the Dice coefficient that calculates the spatial overlay between the segmentation results and the ground truth results. In Dice coefficient measure, a value of one indicates the perfect spatial intersection between the ground truth result and the segmented result and a value of zero represents no spatial overlap. The performance of the dilated SegNet model in terms of Dice coefficient during network training is shown in Figure 7. The performance graph shows that the model has converged after 90 epochs. During the training phase, the dilated SegNet model attains the maximum Dice coefficient of 0.9745 with dice loss of 0.0255.

The models have been tested with 50 images, and an average Dice coefficient and accuracy of various lung segmentation methods are shown in Table 3. The quantitative performance analysis states that dilated SegNet shows improved performance in terms of both Dice coefficient and accuracy as compared with FCM and SegNet models. The dilated

convolution increases the receptive area without increasing the computation load and helps to learn global features. The proposed dilated SegNet model learns both the local and global features by the different receptive areas using dilated convolution operation. The features obtained by the dilated convolutional layers are combined, and the fused feature set obtained by dilated SegNet is used for segmenting the lung region. The experiment results confirm that the incorporation of global features enhances the performance of the SegNet.

Patch-level nodule classification with convolutional neural network + batch normalization

Based on the annotations given by the radiologists, the nodule patches are extracted from the LUNA16 data set. The 2D nodule patches in axial view with the dimension of 64×64 are sliced from the CT images. The number of true nodules is very low than false nodules; this imbalance dataset made the classifier bias toward the majority class. Data augmentation technique makes the dataset balanced by augmenting the minority class samples and also prevents the CNN model for overfitting issue. Data augmentation techniques such as rotation, horizontal flipping, and vertical flipping are adapted to augment the nodule patches. Random 5000 patches from each category are used to build the model. The CNN + BN model is trained from scratch, and the weights are adjusted at the learning rate of 0.001. The model is trained with Adamax optimizer and a weight decay of $1e-5$ for 100 epochs. The metric accuracy is used as a cost function for tuning the network.

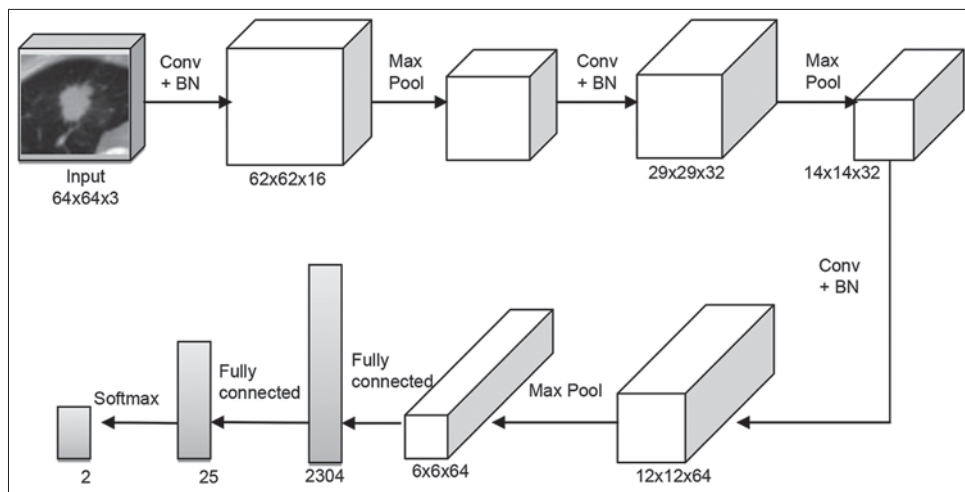


Figure 5: Illustration of the proposed convolutional neural network + batch normalization model for lung nodule patch classification

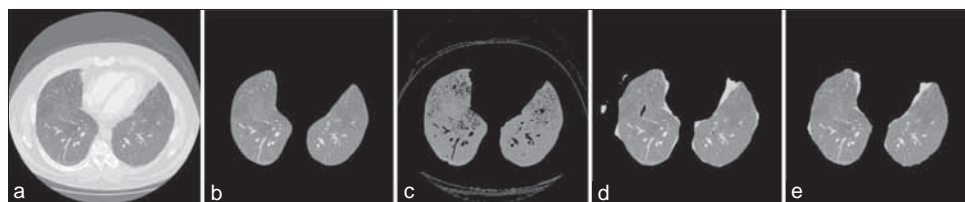


Figure 6: Lung segmentation results of various models (from left to right), (a) Chest computed tomography image in axial view, (b) Lung obtained from ground truth mask, (c) Lung segmented from Fuzzy C-means, (d) Lung segmented by SegNet, (e) Lung segmented by dilated SegNet

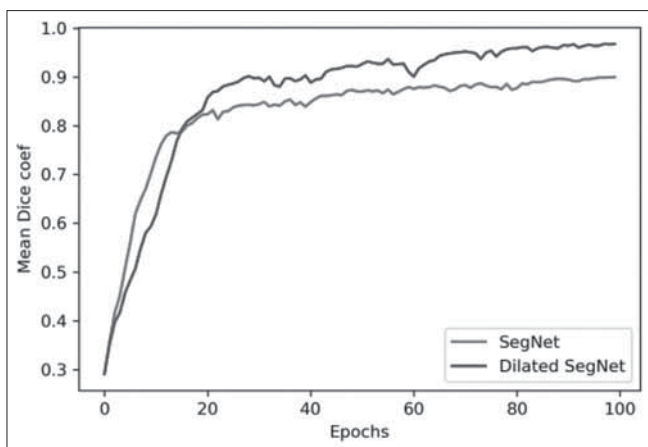


Figure 7: The performance analysis graphs of dilated SegNet model for lung segmentation during training phase

Table 3: Performance comparisons of dilated SegNet with other methods

Method	Dice coefficient	Accuracy
FCM	0.75±0.19	0.87±0.11
SegNet	0.84±0.69	0.92±0.04
Dilated SegNet	0.89±0.23	0.94±0.07

FCM: Fuzzy C-means

The performance of the CNN + BN model is qualitatively examined by visualizing the learned features. Figure 8 shows the abstract feature maps learned at various convolutional layers. The essential features activated by the convolutional layers during the feedforward operation are highlighted. Figure 9 shows the precisely classified nodule patches from the test dataset. This result confirms that the CNN model with BN could classify the true nodules that are smaller in size and complex structures with a probability of higher than 0.60.

The performance of the pulmonary nodule classification model is quantitatively assessed with accuracy and sensitivity. In medical image classification, true positive (TP) denotes the exact classification rate of positive units, and true negative denotes the exact classification rate of negative units. FP indicates the wrong classification rate of negative units and false negative (FN) refers to the wrong classification rate of positive units. The sensitivity (or recall) represents the ratio between TPs and TPs plus FNs. Higher accuracy and sensitivity indicate better classification performance. Confusion matrix results for CNN model with and without BN are shown in Figure 10. These results show that CNN + BN model has fewer FPs compared to CNN model without BN and maintains a high sensitivity of 94.8.

Table 4 presents the performance of CNN model with BN in comparison with CNN model without BN in nodule classification. BN layer is injected after every convolution layer in the CNN model to regulate the features derived by a convolutional layer. This feature normalization assures that the model could retain the required discriminant features across

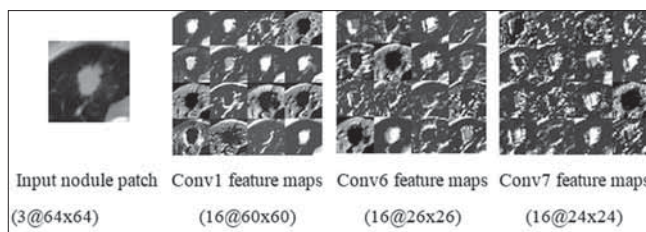


Figure 8: Visualization of the activations (feature maps) of the consecutive convolutional layers such as conv1, conv2, and conv3 for a nodule patch

multiple iterations. The CNN + BN achieves the accuracy of 93.8, which is higher than the CNN model without BN. The test results confirm that the BN improves the efficiency of the CNN model by discovering generalized features for classifying the true and false nodules.

Both CNN models achieved good results in classifying the 2D nodule patches. Further, the impact of BN in CNN is examined using the principal component analysis method. Although the CNN model without BN classifies the nodule patches with satisfying accuracy, the discriminative capability of the features learned by the CNN model without BN is poor as compared with CNN with BN layer.

Figure 11 illustrates the discriminant ability of the features learned by both CNN model with and without BN. The first two principal components obtained from the 256 features learned by CNN models are visualized with a scatter plot to analyze its discriminative ability. From this plot, it is observed that the CNN + BN model learns generalized features that help to discriminate true nodules from the false nodules precisely.

CONCLUSIONS

A perfect CAD system is required to avoid the unnecessarily repeated CT scans. The enhancement of CAD for lung cancer is the most required assignment in the current market scenario. In this study, deep-learning models such as dilated SegNet for lung segmentation and CNN model with BN layer for 2D nodule patch classification have been implemented for lung cancer detection. The obtained results of these proposed models demonstrate satisfied performance in the lung cancer diagnosis. The dilated SegNet shows the improved results of 0.89 ± 0.23 Dice coefficient as compared with FCM and SegNet models. Furthermore, the CNN with BN layer extracted features with the high discriminant ability and classifies the nodule patches with a sensitivity of 94.8. The visual results confirm that the CNN model with BN classifies the true nodules that are smaller in size and complex structures with a satisfied probability value. However, certain aspects still require attention in the development of CAD tools for lung cancer detection such as the inclusion of 3D data in lung parenchyma segmentation and nodule detection. It is recommended that the better utilization of 3D data along with deep-learning techniques may boost the performance of the current CAD system.

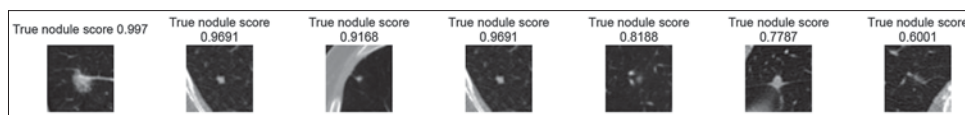


Figure 9: Examples of correctly classified true (cancerous) nodule patches (Score: 1 corresponds to a 100% probability of representing a true nodule)

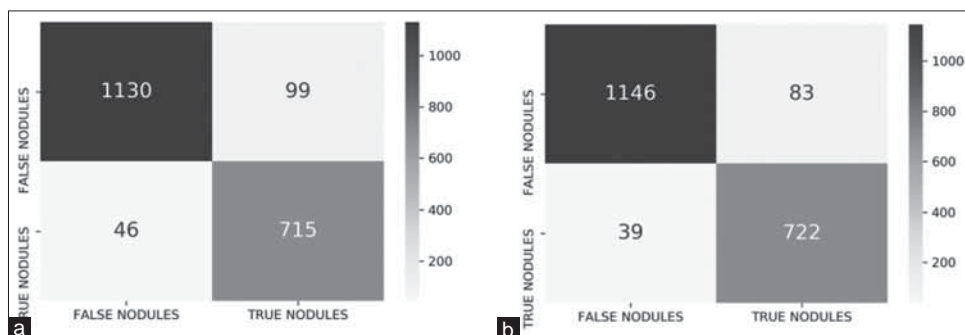


Figure 10: (a) Confusion matrix for convolutional neural network without batch normalization, (b) Confusion matrix for convolutional neural network + batch normalization

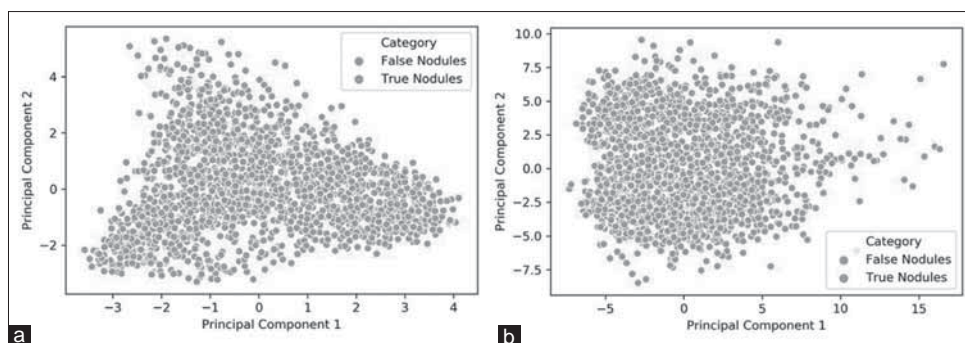


Figure 11: Discrimination capability analysis between convolutional neural network with and without batch normalization for two-dimensional nodule patch classification by visualizing the features extracted. (a) Convolutional neural network without batch normalization. (b) Convolutional neural network with batch normalization

Table 4: Performance comparison of pulmonary nodule classification model

Model variants	Accuracy	Sensitivity
CNN without batch normalization	92.7	93.9
CNN with batch normalization (CNN+BN)	93.8	94.8

BN: Batch normalization, CNN: Convolutional neural network

Financial support and sponsorship

Nil.

Conflicts of interest

There are no conflicts of interest.

REFERENCES

1. American Lung Association and others, Lung Cancer Fact Sheet. Available from: <https://www.lung.org/lung-health-diseases/lung-disease-lookup/lung-cancer/resource-library/lung-cancer-fact-sheet>. [Last accessed on 2014 Aug 12].
2. National Cancer Institute, NIH, DHHS, Bethesda, MD. Cancer Trends Progress Report. Available from: <https://progressreport.cancer.gov/>. [Last accessed on 2017 Jan].

3. Nasim F, Sabath BF, Eapen GA. Lung Cancer. Med Clin North Am 2019;103:463-73.
4. Wiener RS, Gould MK, Arenberg DA, Au DH, Fennig K, Lamb CR, et al. An official American Thoracic Society/American College of Chest Physicians policy statement: Implementation of low-dose computed tomography lung cancer screening programs in clinical practice. Am J Respir Crit Care Med 2015;192:881-91.
5. Detterbeck FC, Mazzone PJ, Naidich DP, Bach PB. Screening for lung cancer: Diagnosis and management of lung cancer, 3rd ed: American College of Chest Physicians evidence-based clinical practice guidelines. Chest 2013;143:e78S-92S.
6. Rao RB, Bi J, Fung G, Salganicoff M, Obuchowski N, Naidich D. LungCAD: A Clinically Approved, Machine Learning System for Lung Cancer Detection, in Proceedings of the 13th ACM SIGKDD International Conference on Knowledge Discovery and Data Mining; 2007. p. 1033-7.
7. Vapnik V, Vashist A, Pavlovitch N. Learning Using Hidden Information (learning with teacher), in 2009 International Joint Conference on Neural Networks; 2009. p. 3188-95.
8. Nie D, Wang L, Adeli E, Lao C, Lin W, Shen D. 3-D fully convolutional networks for multimodal isointense infant brain image segmentation. IEEE Trans Cybern 2019;49:1123-36.
9. Christ PF, Elshaer MEA, Ettlinger F, Tatavarty S, Bickel M, Bilic P, et al. Automatic Liver and Lesion Segmentation in CT Using Cascaded Fully Convolutional Neural Networks and 3D Conditional Random

- Fields,” in International Conference on Medical Image Computing and Computer-Assisted Intervention; 2016. p. 415-23.
10. Dalmics MU, Gubern-Mérida A, Vreemann S, Karssemeijer N, Mann R, Platel B. A computer-aided diagnosis system for breast DCE-MRI at high spatiotemporal resolution. *Med Phys* 2016;43:84-94.
 11. Badrinarayanan V, Kendall A, Cipolla R. Segnet: A deep convolutional encoder-decoder architecture for image segmentation. *IEEE Trans Pattern Anal Mach Intell* 2017;39:2481-95.
 12. Khagi B, Kwon GR. Pixel-label-based segmentation of cross-sectional brain MRI using simplified SegNet architecture-based CNN. *J Healthc Eng* 2018;2018. <https://doi.org/10.1155/2018/3640705>.
 13. Harrison AP, Xu Z, George K, Lu L, Summers RM, Mollura DJ. Progressive and Multi-Path Holistically Nested Neural Networks for Pathological Lung Segmentation from CT Images,” in International Conference on Medical Image Computing and Computer-Assisted Intervention; 2017. p. 621-9.
 14. Agnes SA, Anitha J, Peter JD. Automatic lung segmentation in low-dose chest CT scans using convolutional deep and wide network (CDWN). *Neural Comput Appl* 2018;1-11. <https://doi.org/10.1007/s00521-018-3877-3>.
 15. Skourt BA, El Hassani A, Majda A. Lung CT image segmentation using deep neural networks. *Procedia Comput Sci* 2018;127:109-13.
 16. Hinton GE, Salakhutdinov RR. Reducing the dimensionality of data with neural networks. *Science* 2006;313:504-7.
 17. Zhu W, Liu C, Fan W, Xie X. Deeplung: 3d Deep Convolutional Nets for Automated Pulmonary Nodule Detection and Classification. *arXiv Prepr. arXiv1709.05538*; 2017.
 18. Eun H, Kim D, Jung C, Kim C. Single-view 2D CNNs with fully automatic non-nodule categorization for false positive reduction in pulmonary nodule detection. *Comput Methods Programs Biomed* 2018;165:215-24.
 19. Hamidian S, Sahiner B, Petrick N, Pezeshk A. 3D convolutional neural network for automatic detection of lung nodules in chest CT. in *Proc. SPIE*, vol. 10134, Mar. 2017, Art. no. 1013409.
 20. Fu L, Ma J, Ren Y, Han YS, Zhao J. Automatic detection of lung nodules: False positive reduction using convolution neural networks and handcrafted features,” in *Med Imaging* 2017;10134:101340A.
 21. Li W, Cao P, Zhao D, Wang J. Pulmonary nodule classification with deep convolutional neural networks on computed tomography images. *Comput Math Methods Med* 2016;Article ID 6215085. <https://doi.org/10.1155/2016/6215085>.
 22. Setio AA, Ciompi F, Litjens G, Gerke P, Jacobs C, van Riel SJ, *et al.* Pulmonary Nodule Detection in CT Images: False Positive Reduction Using Multi-View Convolutional Networks. *IEEE Trans Med Imaging* 2016;35:1160-9.
 23. Ypsilantis PP, Montana G. Recurrent Convolutional Networks for Pulmonary Nodule Detection in CT Imaging. *arXiv Prepr. arXiv1609.09143*; 2016.
 24. Ciompi F, de Hoop B, van Riel SJ, Chung K, Scholten ET, Oudkerk M, *et al.* Automatic classification of pulmonary peri-fissural nodules in computed tomography using an ensemble of 2D views and a convolutional neural network out-of-the-box. *Med Image Anal* 2015;26:195-202.
 25. van Ginneken B, Setio AA, Jacobs C, Ciompi F. Off-the-Shelf Convolutional Neural Network Features for Pulmonary Nodule Detection in Computed Tomography Scans,” in *Biomedical Imaging (ISBI), 2015 IEEE 12th International Symposium on*; 2015. p. 286-9.
 26. Dou Q, Chen H, Yu L, Qin J, Heng PA. Multilevel contextual 3-D CNNs for false positive reduction in pulmonary nodule detection. *IEEE Trans Biomed Eng* 2017;64:1558-67.
 27. Nibali A, He Z, Wollersheim D. Pulmonary nodule classification with deep residual networks. *Int J Comput Assist Radiol Surg* 2017;12:1799-808.
 28. Shen W, Zhou M, Yang F, Yang C, Tian J. Multi-scale convolutional neural networks for lung nodule classification. *Inf Process Med Imaging* 2015;24:588-99.
 29. Liu X, Hou F, Qin H, Hao A. Multi-view multi-scale CNNs for lung nodule type classification from CT images. *Pattern Recognit* 2018;77:262-75.
 30. Hussein S, Cao K, Song Q, Bagci U. Risk Stratification of Lung Nodules Using 3d cnn-Based Multi-Task Learning,” in *International Conference on Information Processing in Medical Imaging*; 2017. p. 249-60.
 31. Gerard SE, Patton TJ, Christensen GE, Bayouth JE, Reinhardt JM. FissureNet: A Deep learning approach for pulmonary fissure detection in CT images. *IEEE Trans Med Imaging* 2019;38:156-66.
 32. Tong G, Li Y, Chen H, Zhang Q, Jiang H. Improved U-NET network for pulmonary nodules segmentation. *Optik (Stuttg)* 2018;174:460-9.
 33. Ioffe S, Szegedy C. Batch normalization: Accelerating Deep Network Training by Reducing Internal Covariate Shift,” *arXiv Prepr. arXiv1502.03167*; 2015.

Assessment of Four Scatter Correction Methods in In-111 SPECT Imaging: A Simulation Study

Mahsa Noori-Asl

Department of Physics, Faculty of Science, University of Mohaghegh Ardabili, Ardabil, Iran

Abstract

Introduction: Detection of Compton scattered photons is one of the most important factors affecting the quality of single-photon emission computed tomography (SPECT) images. In most cases, the multiple-energy window acquisition methods are used for estimation of the scatter contribution into the main energy window(s) used in imaging. **Aims and Objectives:** The purpose of this study is to evaluate and compare the performance of four different scatter correction methods in In-111 SPECT imaging. Due to the lack of sufficient studies in this field, it can be useful to perform a more detailed and comparative study. **Materials and Methods:** Four approximations for scatter correction of In-111 SPECT images are evaluated by using the Monte Carlo simulation. These methods are firstly applied on each of photopeak windows, separately. Then, the effect of the correction methods is investigated by considering both the photopeak windows. The images obtained from a simulated multiple-spheres phantom are used for the evaluation of the correction methods by using three assessment criteria, including the image contrast, relative noise, and the recovery coefficient. **Results:** The results of this study show that the correction methods, when using the single photopeak windows, result in increase in image contrast with a significant level of noise. In return, when both the photopeak energy windows are used for imaging, it is possible to achieve the better image characteristics. **Conclusion:** The use of the proposed correction methods, by considering both the photopeak windows, leads to improve the image contrast with a reasonable level of image noise.

Keywords: Energy spectrum, indium-111, scatter correction, single-photon emission computed tomography

Received on: 30-01-2020

Review completed on: 12-04-2020

Accepted on: 29-04-2020

Published on: 20-07-2020

INTRODUCTION

The quality of images obtained from single-photon emission computed tomography (SPECT) imaging systems can be influenced by several factors; two most important of them are attenuation and scatter of photons emitted from the radionuclide used in the imaging. Whereas the attenuated photons do not arrive to the detector, and therefore, they have not any contribution in the final image, the scattered photons may arrive to the detector and be detected. Because these scattered photons have lower energy than the primary photons emitted from the radionuclide, they are often detected at energies lower than the photopeak energy. However, because of the limited energy resolution of the detection material used in gamma cameras (conventionally NaI (TI) scintillation crystal), a number of scattered photons are always detected into the main energy window used in imaging, for example,

in Tc-99m SPECT imaging, about 30%–40% of photons detected in the main energy window are scattered photons.^[1] These scattered photons are added to the final image, resulting in image blurring and decreased image contrast. Therefore, for improvement of the diagnostic accuracy, it is necessary to find a suitable approach for reduction of the scattered photons included in the main energy window.

So far, many studies have been performed in the field of scatter correction in SPECT imaging. Most of these studies are related to the imaging with the radioisotope of technetium-99m.^[2-18] There are a few studies for other radioisotopes. In this study,

Address for correspondence: Dr. Mahsa Noori-Asl,
Department of Physics, Faculty of Science, University of Mohaghegh
Ardabili, Ardabil, Iran.
E-mail: nooriasl.mahsa@gmail.com

Access this article online

Quick Response Code:



Website:
www.jmp.org.in

DOI:
10.4103/jmp.JMP_5_20

This is an open access journal, and articles are distributed under the terms of the Creative Commons Attribution-NonCommercial-ShareAlike 4.0 License, which allows others to remix, tweak, and build upon the work non-commercially, as long as appropriate credit is given and the new creations are licensed under the identical terms.

For reprints contact: WKHLRPMedknow_reprints@wolterskluwer.com

How to cite this article: Noori-Asl M. Assessment of four scatter correction methods in in-111 SPECT imaging: A simulation study. J Med Phys 2020;45:107-15.

we intend to investigate and compare the influence of four scatter correction approximations on the quality of In-111 SPECT images. The indium-111 radioisotope decays by electron capture (EC) process to cadmium-111 with a half-life 67.9 h (2.8 days) that is suitable to use in SPECT imaging. During this decay, two gamma rays are emitted with energies 171 keV and 245 keV, both in high abundance [Figure 1].^[19] Hence, dual-energy window settings are often used in In-111 SPECT imaging. In this study, first, the effect of interested scatter correction approximations on the each of photopeak energy windows is evaluated separately. Then, the scatter correction is performed by considering both photopeak windows.

In this study, we use the SIMulation of Imaging Nuclear Detectors (SIMIND) Monte Carlo simulation to generate the projection images. As, by using the simulation, it is possible to access the scattered and primary counts and also their spectra, independently, the simulation can be a suitable way for the investigation of the problem of scattering and the evaluation of performance of the scatter correction techniques. To evaluate the scatter correction methods, we used the simulated Jaszczak phantom including six spheres with different diameters placed into a cylindrical phantom. Two assessment criteria, image contrast and relative noise of background (RNB) together with the recovery coefficient (RC), are used for investigation of the effect of different scatter correction methods.

MATERIALS AND METHODS

Scatter correction methods

Four methods for scatter correction of In-111 SPECT images are evaluated. First, this scatter correction methods are applied on each photopeak energy window, separately. In the next step, scatter correction is performed by considering both photopeak windows. The photopeak energy windows used in this study are including two 20% energy windows centered at energies 171 keV (154–188 keV) and 245 keV (221–269 keV), respectively.

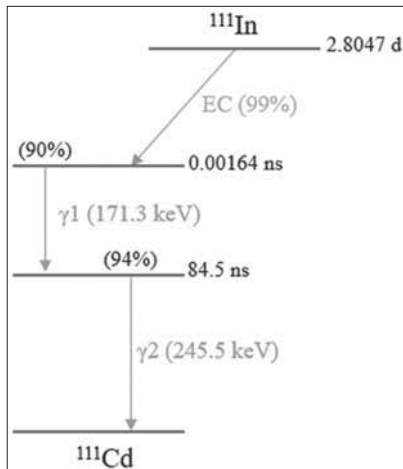


Figure 1: The decay scheme of In-111^[19]

The scatter correction for each photopeaks window

Triple-energy window method for the first photopeak energy window (TEW-PK1)

In this approximation, the scatter counts detected into the first photopeak energy window (154–188 keV) are estimated by using a trapezoidal area. Total counts included into two narrow energy windows centered at energies 154 keV (T_{nw1}) and 188 keV (T_{nw2}) are used to estimate two heights of this trapezoid [Figure 2]. Therefore, the scatter counts of first photopeak window (S_{pk1}) can be estimated by the following equation (Eq. 1):^[7]

$$S_{pk1}^{TEW}(i, j) = \left(\frac{T_{nw1}(i, j)}{w_{nw1}} + \frac{T_{nw2}(i, j)}{w_{nw2}} \right) \times \frac{W_{pk1}}{2} \quad (1)$$

Where w_{nw1} and w_{nw2} are the widths of narrow energy windows centered at energies 154 and 188 keV, respectively, and W_{pk1} is the width of the first photopeak window. (i, j) indicates the location of given pixel in the projection image matrix. In this approximation, two 8% and 6% narrow energy windows centered at the lower and upper energy limits of the first photopeak window are used.

Triple-energy window method for the second photopeak energy window (TEW-PK2)

In this approximation, it is assumed that there is no counts into the narrow energy window centered at the upper energy limit of the second photopeak window (i.e., energy 269 keV). Therefore, the scatter counts included into the second photopeak energy window (221–269 keV) can be estimated by using a triangular area that its height is determined by the total counts into a narrow window centered at energy 221 keV [Figure 3], as shown in the following equation (Eq. 2):

$$S_{pk2}^{TEW}(i, j) = \left(\frac{T_{nw3}(i, j)}{w_{nw3}} \right) \times \frac{W_{pk2}}{2} \quad (2)$$

Where w_{nw3} is the width of narrow energy window centered at energy 221 keV, and W_{pk2} is the width of the second photopeak energy window. In this approximation, a 6% narrow energy window centered at the lower energy limit of second photopeak window is used.

Dual-energy window method for the first photopeak energy window (DEW-PK1)

This scatter correction method is based on the dual-energy window method proposed by Jaszczak *et al.*^[3,6] The essential assumption in this correction method is that the scatter counts into the photopeak window can be estimated as “ k ” times of the total counts acquired into a second energy window (T_1) placed in the left side of the first photopeak window [Figure 4a]. Because almost all of the counts into this second energy window are the scatter counts, it is called as the “scatter window.” Therefore, the scatter counts of the first photopeak window can be estimated as follows:

$$S_{pk1}^{DEW}(i, j) = k_{i71} \times T_1(i, j) \quad (3)$$

According to the above equation (Eq. 3), the value of k factor can change pixel to pixel. Thus, a mean value of k is calculated and used in this scatter correction method. In this study, a scatter window with 20% width is used for the scatter correction.

Dual-energy window method for the second photopeak energy window (DEW-PK2)

Similar to the pervious method, the total counts into a 20% energy window (T_2) placed in the left side of second photopeak window [Figure 4b] are used to estimate the scatter counts into this photopeak window:

$$S_{pk2}^{DEW}(i, j) = k_{245} \times T_2(i, j) \tag{4}$$

Scatter correction methods by considering both photopeak windows

Six-energy window method

This correction method is in fact a combination of triple-energy window (TEW) approximations used for two photopeak energy windows [Figure 5]. Therefore, the total number of scatter photons included into the both photopeak windows can be estimated by summing Eqs. (1) and (2), as follows:

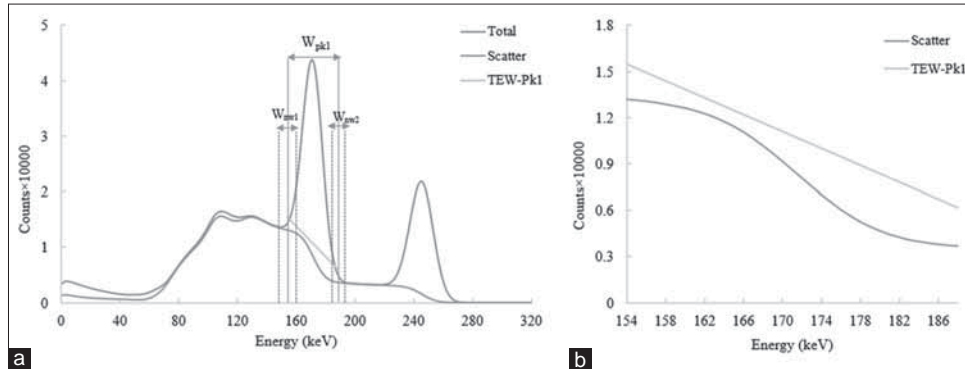


Figure 2: (a) The energy windows used in triple-energy window method by the trapezoidal approximation for the first photopeak window (154–188 keV). (b) The estimation of scatter area of the first photopeak window by the trapezoidal approximation along with the spectrum of true scatter counts into this energy window

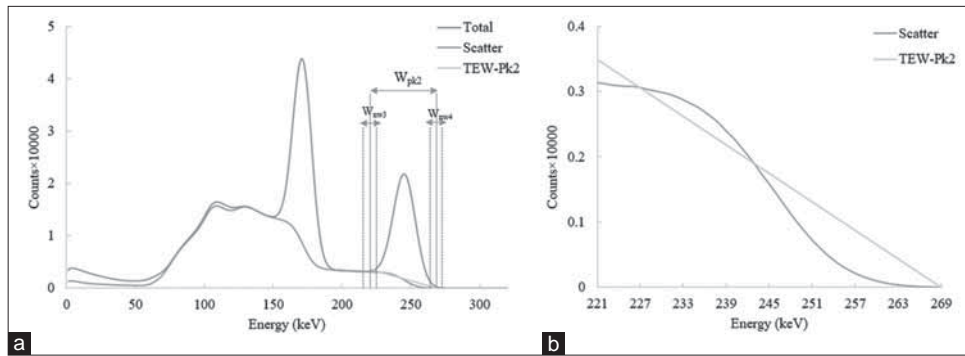


Figure 3: (a) The energy windows used in triple-energy window method by the trapezoidal approximation for the second photopeak window (221–269 keV). (b) The estimation of scatter area of the second photopeak window by the triangular approximation along with the spectrum of true scatter counts into this energy window

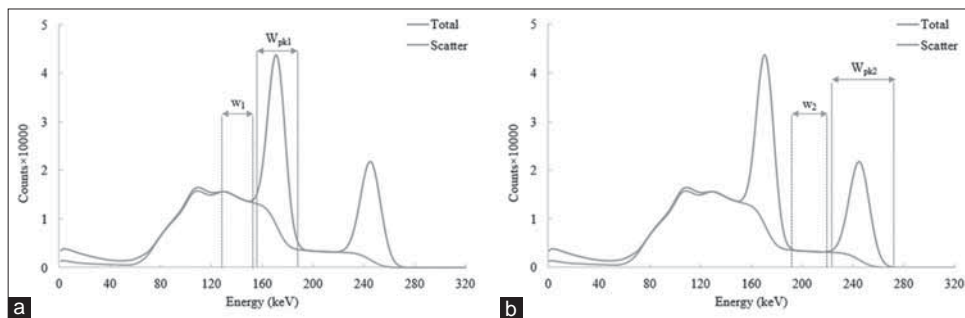


Figure 4: The energy windows used in dual-energy window method for (a) the first photopeak energy window and (b) the second photopeak window

$$S_{pk}^{SEW}(i, j) = S_{pk1}^{TEW}(i, j) + S_{pk2}^{TEW}(i, j) \quad (5)$$

Four-energy window method

This correction method is in fact a combination of dual-energy window approximations used for two photopeak energy windows [Figure 6]. Therefore, the total scattered counts can be estimated as follows:

$$S_{pk}^{FEW}(i, j) = S_{pk1}^{DEW}(i, j) + S_{pk2}^{DEW}(i, j) \quad (6)$$

Simulation

The SIMIND Monte Carlo program^[20] (V.6.1.2 version), a MC code dedicated to simulate SPECT imaging, is used to produce the projection images from two photopeak energy windows and also, the narrow energy windows required to the scatter correction approximations. The simulated SPECT system is including a cylindrical NaI (Tl) crystal with radius 25 cm and thickness 0.95 cm, equipped to a general electric (GE) low-energy high-resolution parallel-hole collimator with the hexagonal holes. The system energy and intrinsic resolutions are 10% (FWHM) and 0.36 cm, respectively, for 140 keV. The projection images (128 × 128 matrices with a pixel size 0.3 cm) are acquired by a 360° rotation of camera with a radius of rotation 20 cm in 128 views. The image reconstruction is performed by using the filtered back-projection method with “Hann” filter in MATLAB (7.5.0 version) environment.

Simulated phantoms and assessment criteria

The phantom used in this study is a simulated model from the Deluxe Jaszczak phantom [Figure 7a] including six spheres with different diameters (3.2, 2.6, 2, 1.6, 1.3, and 1 cm) placed into a water-filled cylindrical phantom [Figure 7b]. This phantom can be simulated as both cold spheres in hot background phantom and hot spheres in cold background phantom, where “hot” and “cold” refer to the presence and absence of In-111 activity, respectively. This phantom is a basic phantom that has been used in many studies in the field of scatter and attenuation compensation.

Two mathematical criteria, including the image contrast and the RNB, are used to evaluate the images obtained from the cold spheres in hot background phantom. For calculation of these parameters, it is firstly necessary to define the regions of interest (ROIs) into each of the spheres and also into the background. These regions for largest to smallest spheres consist of 56, 30, 12, 10, 8, and 2 pixels, and for the background is a 16 × 16 matrix (256 pixels) defined in space between six spheres, as shown in Figure 7b. Accordingly, the assessment criteria are defined by the following equations (Eqs. 7 and 8):^[14]

$$\text{Contrast} = \frac{\bar{N}_{CS} - \bar{N}_{BG}}{\bar{N}_{BG}} \quad (7)$$

$$\text{RNB} = \frac{\delta_{BG}}{\bar{N}_{BG}} \quad (8)$$

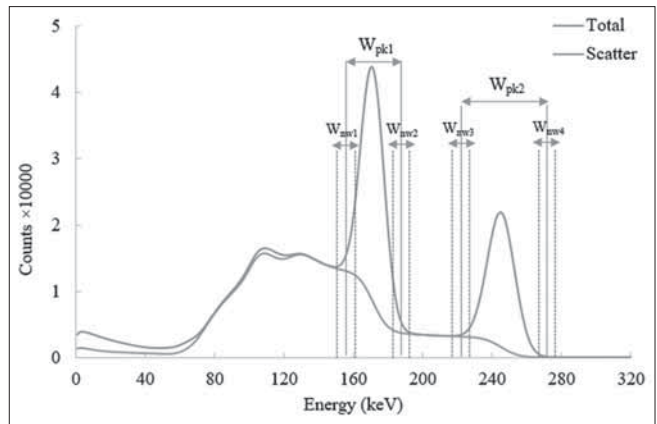


Figure 5: The energy windows used in six-energy window method defined as a combination of triple-energy window approximations used for two photopeak energy windows

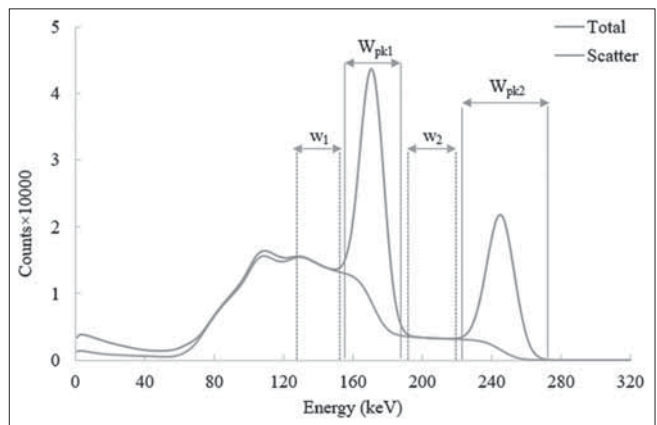


Figure 6: The energy windows used in four-energy window method defined as a combination of dual-energy window approximations used for two photopeak energy windows

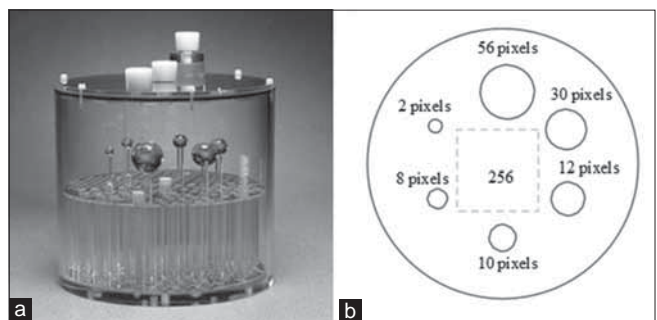


Figure 7: (a) The Deluxe Jaszczak phantom and (b) the cross section of simulated phantom including six spheres with different diameters (3.2, 2.6, 2, 1.6, 1.3, and 1 cm) placed into a water-filled cylindrical phantom together with the ROIs defined for the spheres and the background

Where \bar{N}_{CS} and \bar{N}_{BG} are the average of counts in ROIs defined for the spheres and the background, respectively, and δ_{BG} is standard deviation of the counts in ROI of the background.

On the other hand, the criterion used to evaluate the images results from the hot spheres in cold background phantom is recovery coefficient (RC) that is defined as follows:^[15]

$$RC = \frac{\bar{N}_{HS}^{Corrected}}{\bar{N}_{HS}^{Primary}} \times 100 \quad (9)$$

Where $\bar{N}_{BG}^{Corrected}$ and $\bar{N}_{BG}^{Primary}$ are the average of counts in ROIs of the hot spheres corrected and primary images, respectively.

RESULTS

The results of the simulation for cold spheres in hot background phantom show that about 32.5% of the photons acquired in the first photopeak energy window (154–188 keV) are the scattered photons, in which 72.6% undergo the first-order scattering, 22.0% the second-order scattering, and 5.4% the third-order scattering. On the other hand, for the second photopeak energy window (221–269 keV), 15.7% of the detected photons are the scattered photons, in which 91.8% undergo the first-order scattering, 7.7% the second-order scattering, and 0.4% the third-order scattering. These results indicate that most of the scattered photons in the second photopeak window are the first-order scattered photons. While for the first photopeak window, a significant number of scattered photons undergo the multiple scattering. The reason for this can be explained by using the relation of between energy and angle of Compton scattered photons as follows:^[21]

$$E = \frac{E_0}{1 + (1 - \cos \theta) \frac{E_0}{m_e c^2}} \quad (10)$$

According to this equation (Eq 10), the 245 keV photons that undergo the first-order scattering with angle between 68.43° and 103.44° can be detected into the first photopeak window. It is clear that there is a chance for the multiple-scattered photons to fall into the first energy window in addition to the first-order scattered photons [Figure 8].

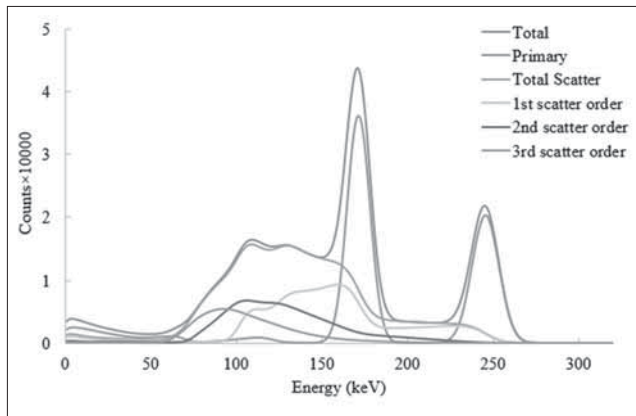


Figure 8: The spectra related to total (scatter + primary), primary (nonscattered), and total scatter (the sum of three scatter orders) counts along with the spectra of the first three scatter orders

The results for TEW correction method

The results obtained from the simulation of cold spheres in hot background phantom indicate that the true number of scattered photons included into the first and second photopeak energy windows are equal to 290,000 and 74,800, respectively. While the number of scattered photons estimated by the trapezoidal and triangular areas are about 371,308 and 84,685, respectively. From these results, the scatter correction by using the TEW method results in an overestimation of about 28% for the first photopeak window (Pk1) and 13.2% for the second photopeak window (Pk2). On the other hand, from Table 1, for both the photopeak windows, the use of the TEW correction method leads to improve the image contrasts of all of the cold spheres compared to before the correction (due to the low number of pixels included into the sphere with smallest diameter [sphere 6] and a lot of change in its contrast in different simulations, we discard from that). The relative increase of the image contrasts for largest to smallest spheres was about 41.46%, 38.20%, 22.50%, 11.71%, and 9.96% for the first photopeak window and 18.07%, 15.50%, 11.21%, 6.00%, and 3.15% for the second photopeak window. These results show that the relative increase of image contrasts for the first photopeak window is more than that of the second photopeak window. In addition, although the RNB obtained for the first photopeak window before correction (0.35) is about twice lower than the RNB for the second photopeak window (0.61), after scatter correction, the deference of these two values is low. This shows that the scatter correction by TEW method results in more increase of the level of noise in images obtained from the first photopeak window compared to the second photopeak window. A slice (slice 64) of the reconstructed images of cold-spheres for both the photopeak windows is shown in Figure 9. In addition, a similar slice of the reconstructed images of hot spheres along with a line profile through the center of spheres 1 and 4 are shown in Figures 10 and 11. From data given in Table 2, the RCs for the images of hot spheres corrected by TEW-Pk1 and TEW-Pk2 approximations are in the range of 10% lower and 2% higher than 100%, respectively, which indicate the corrected images of the second photopeak window have a

Table 1: The image contrast and the relative noise of background obtained from the reconstructed images of cold spheres in hot background phantom for two photopeak windows separately

Situation (RNB)	Spheres				
	S1	S2	S3	S4	S5
NC-Pk1 (0.035)	53.18	43.12	26.45	11.19	6.052
NC-Pk2 (0.061)	72.11	50.44	42.54	15.15	9.016
Primary-Pk1 (0.060)	83.39	68.64	47.05	20.53	9.128
Primary-Pk2 (0.070)	84.63	63.36	49.65	21.56	12.80
TEW-Pk1 (0.072)	91.84	77.99	48.37	22.28	16.01
TEW-Pk2 (0.078)	88.89	64.76	53.18	20.64	12.16
DEW-Pk1 (0.059)	87.12	71.49	45.96	18.52	12.42
DEW-Pk2 (0.076)	88.22	62.57	52.87	19.34	12.20

RNB: Relative noise of background, NC: No correction, TEW: Triple-energy window, DEW: Dual-energy window

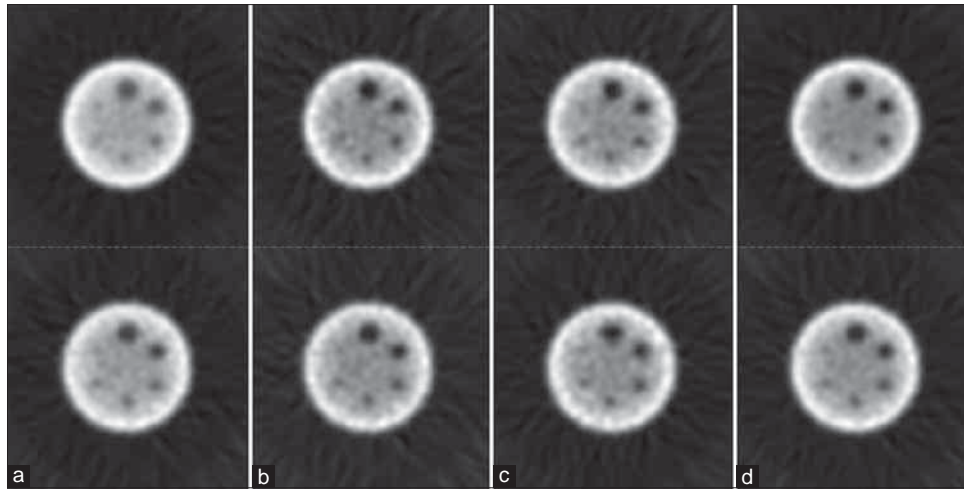


Figure 9: The reconstructed images of cold spheres in hot background phantom in four situations: (a) before correction, (b) corrected by triple-energy window method, and (c) corrected by dual-energy window method together with (d) the image obtained from the primary photons. The first and second rows are related to the first and second photopeak window, respectively

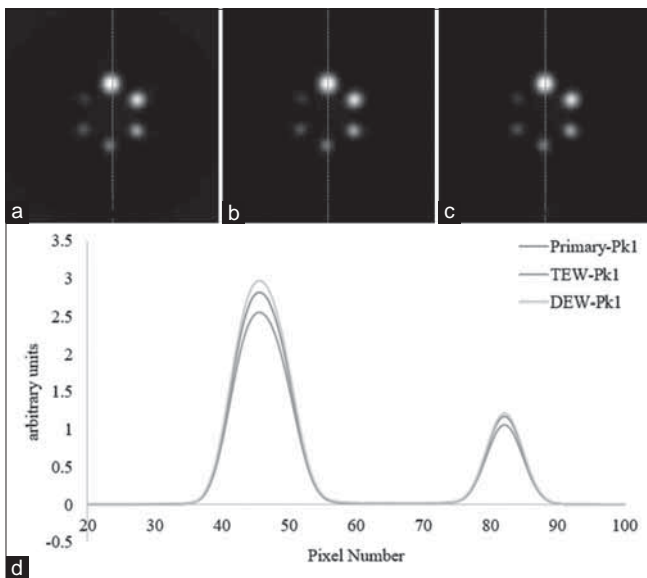


Figure 10: The reconstructed images of hot spheres in cold background phantom for the first photopeak windows in three situations: (a) the image result of the primary counts, (b) the image corrected by triple-energy window method, and (c) the image corrected by dual-energy window method together with (d) the line profiles obtained from a given row through the image of spheres 1 and 4

closer agreement with the primary images than that for the first photopeak window. These results are obvious from the profiles given in Figures 10d and 11d.

The results for DEW correction method

The first step in using the dual-energy window (DEW) correction method is to calculate the *k* factor for each of the photopeak windows. This factor is calculated by considering a 20% energy window in the vicinity of each of the photopeak windows so that the upper energy limit of these 20% windows is located on the lower energy limit of the photopeak windows. From the results of the simulation,

the mean *k* values obtained for the first and second photopeak window are about 0.69 (with a minimum value 0.4232, maximum value 1.1585 and a standard deviation 0.0857) and 0.48 (with a minimum value 0.0596, maximum value of 1.2622, and a standard deviation of 0.1302), respectively. By using the calculated mean *k* values, the DEW correction method results in the relative increase of the cold sphere contrasts of about 36.45%, 30.48%, 20.61%, 7.29%, and 6.36% for the first photopeak window and about 17.47%, 13.07%, 10.74%, 4.21%, and 3.19% for the second photopeak window. Similar to TEW correction method, the use of this scatter correction method for the first photopeak window leads to a more relative increase of the cold sphere contrasts than that for second photopeak window. In addition, from the RNB values given in Table 1 for the first photopeak window, DEW correction method (DEW-Pk1) results in the lower level of image noise compared to TEW correction method (TEW-Pk2). On the other hand, from Table 2, the RCs of hot spheres by using both the DEW-Pk1 and DEW-Pk2 approximations are in a range of 6% higher than 100%, showing a similar agreement between the corrected and primary data for both photopeak windows [Figures 10d and 11d].

Results for SEW and FEW correction methods

Table 3 shows the results obtained from the six-energy window (SEW) and four-energy window (FEW) correction approximations. As expected, the RNB values obtained from these two correction approximations are significantly lower than the values result from approximations used for the single photopeak windows (the RNB value for the FEW correction approximation [0.049] is somewhat lower than that for the SEW correction approximation [0.0536]). Moreover, from the data of Table 3, the relative increase of the image contrasts for the largest to smallest cold spheres is about 33.35%, 29.04%, 19.19%, 9.56%, and 7.28% for the SEW correction approximation and

30.08%, 23.83%, 17.66%, 6.25%, and 5.26% for the FEW correction approximation, showing a more increase of image contrasts by using the SEW approximation than the FEW approximation. Figure 12 shows a slice of reconstructed images of cold spheres corrected by these

Table 2: The recovery coefficients obtained from the reconstructed images of the hot spheres

Situation	Spheres				
	S1	S2	S3	S4	S5
TEW-Pk1	91.03	90.74	90.67	90.58	90.93
TEW-Pk2	101.78	101.48	101.16	101.26	101.14
DEW-Pk1	105.48	104.67	103.86	103.51	103.35
DEW-Pk2	105.46	104.53	103.56	103.08	103.10
SEW	95.37	95.06	94.86	94.84	94.97
FEW	105.46	104.53	103.56	103.08	103.10

TEW: Triple-energy window, DEW: Dual-energy window, SEW: Six-energy window, FEW: Four-energy window

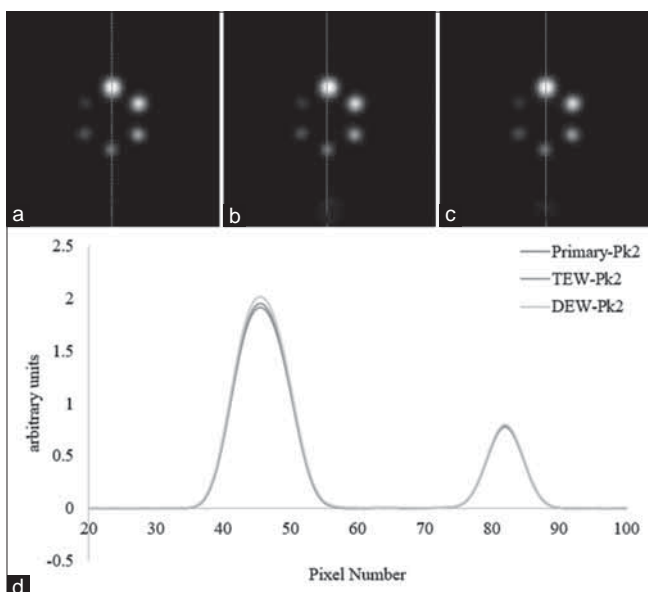


Figure 11: The reconstructed images of hot spheres in cold background phantom for the first photopeak windows in three situations: (a) the image result of the primary counts, (b) the image corrected by triple-energy window method, and (c) the image corrected by dual-energy window method together with (d) the line profiles obtained from a given row through the image of spheres 1 and 4

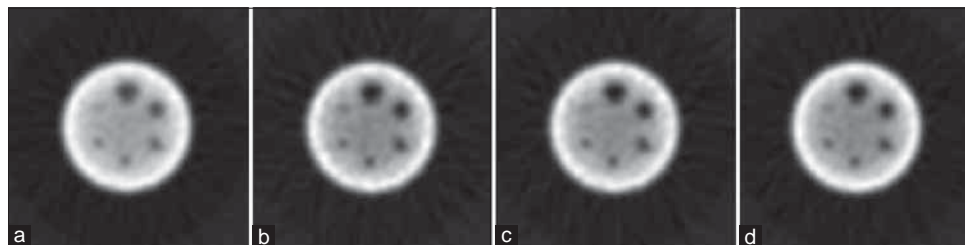


Figure 12: The reconstructed images of cold spheres in hot background phantom in four situations: (a) before correction, (b) corrected by six-energy window method, and (c) corrected by four-energy window method together with (d) the image obtained from the primary photons, by considering both the photopeak windows

two approximations. On the other hand, the RC values obtained from these two correction approximations show a range 6% lower and 6% higher than 100%, for SEW and FEW approximations, respectively. A slice of reconstructed images of hot spheres along with the line profiles through sphere 1 and 4 is shown in Figure 13.

DISCUSSION AND CONCLUSION

Due to the importance of the problem of scattering and its effect on the quality of SPECT images, many studies have been conducted on the scatter correction techniques. Most of these studies are based on setting one or more additional energy windows in the spectrum of radioisotope used in imaging. Because Tc-99m is the most commonly used radioisotope in SPECT imaging, most of the proposed correction methods are based on the energy spectrum of this radioisotope. The correction approximations used for other radioisotopes are usually the modified methods used firstly in Tc-99m SPECT imaging.

In the present study, we investigated the effect of scatter correction on the SPECT images resulting from detection of the gamma rays emitted from the indium-111 radioisotope. It is important to note that the presence of two gamma photopeaks in the energy spectrum of indium-111 radioisotope results in the increase of the scatter contribution into the first photopeak window. This increase is due to fall down a number of scattered photons of the second photopeak window within the first photopeak window. This is why the scatter correction for the multiple-photopeak radioisotopes is more complicated than the single-photopeak radioisotopes.

There are a few studies in the field of the scatter correction in imaging with In-111 radioisotope. In an initial study performed by Gilland *et al.*,^[22] the effect of the nonuniform attenuation correction using the transmission scan method (with a Tc-99m transmission source and a three-head camera) was compared to the uniform attenuation correction using the Chang method. In this study, in addition to two 20% photopeak windows, the other two energy windows positioned below each of the photopeak windows were used to estimate the scatter component into the corresponding photopeak windows. Based on the results of this study, the use of combined correction method (nonuniform attenuation correction + scatter correction) results in the

Table 3: The image contrasts and the relative noise of background obtained from the reconstructed images of cold spheres in hot background phantom by considering both the photopeak windows

Situation (RNB)	Spheres				
	S1	S2	S3	S4	S5
NC (0.033)	59.56	45.59	31.88	12.53	7.052
Primary (0.050)	83.90	66.49	48.11	20.95	10.62
SEW (0.053)	90.55	72.21	50.48	21.56	14.33
FEW (0.049)	87.46	67.77	48.71	18.83	12.31

RNB: Relative noise of background, NC: No correction, SEW: Six-energy window, FEW: Four-energy window

improvement of the qualitative and quantitative accuracy of In-111 SPECT images. (These results are obtained in conditions where the combined projection data of two photopeak windows are used to produce the final image.) In another study, Penny *et al.*^[23] used the dual-photopeak window (DPW) technique^[9] for the scatter correction of the projection data of each of the photopeak windows. Moreover, they used a fifth energy window between two photopeak windows ($W_5 = 195\text{--}225\text{ keV}$) to estimate the scatter spill down from the second photopeak window into the first photopeak window. According to the results obtained from the point source imaging, this scatter correction approximation leads to reduction in the scatter fraction magnitude for both the photopeak windows. In another study, Choi *et al.*^[24] investigated the effect of scatter correction on the projection data acquired from the second photopeak window by a 10% scatter window placed between two photopeaks at an energy of 205 keV using two ways: (1) the standard DEW correction method^[3] and (2) a modified DEW method for accounting the contribution of the scattering into the detector crystal. The results of this study showed that except in cases that the scattering in the patient's body is very low, method 1 results in an accuracy equivalent to that for method 2. Finally, in the study performed by Holstenson *et al.*,^[25] the optimal energy window settings for a camera with ability of the data acquisition in three energy windows were investigated. This study is only a comparative study performed in the field of scatter correction in In-111 SPECT imaging. In this study, first, the effect of scatter correction on each of the 20% photopeak windows was evaluated by using the TEW method.^[7] In the next step, the effect of scatter correction on the combined data of the two photopeak windows was investigated by setting a third energy window in two different positions into the In-111 energy spectrum: (1) a 6% narrow energy window at 149 keV and (2) a 10% broad energy window at 209 keV. The results obtained from the experimental and simulation studies showed that the scatter correction of the combined data of two 20% photopeak windows using a 10% broad energy window at 209 keV can be an optimal energy window setting for In-111 SPECT imaging.

In the present study, an attempt has been made to investigate the scattering problem and also, the efficiency of scatter correction

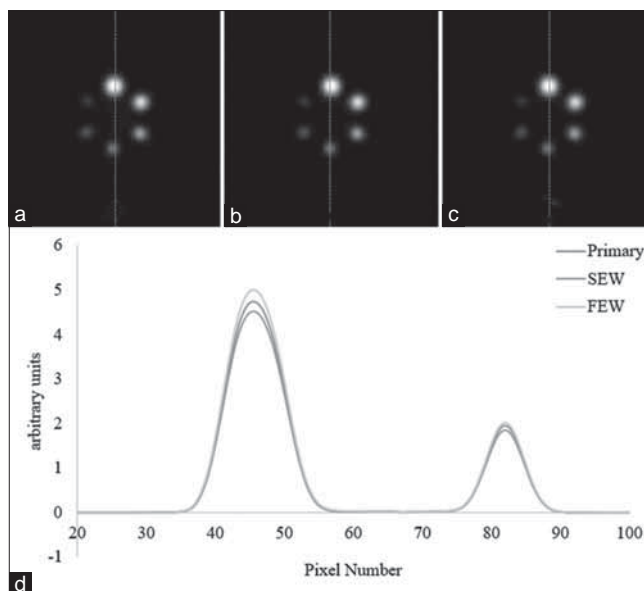


Figure 13: The reconstructed images of hot spheres in cold background phantom by considering both photopeak windows in three situations: (a) the image result of the primary counts, (b) the image corrected by six-energy window method, and (c) the image corrected by four-energy window method together with (d) the line profiles obtained from a given row through the image of spheres 1 and 4

techniques in In-111 SPECT imaging in more detail. For this purpose, in the first stage, we considered two photopeak windows independently and in the next stage, as combined together. The results obtained from the first stage indicate that the use of TEW and DEW correction methods results in the improvement of the cold sphere contrasts for the images from both photopeak windows, with a greater mean relative increase for the first photopeak window (24.76% for the TEW method and 20.24% for the DEW method) compared to the second photopeak window (10.78% for the TEW method and 9.37% for the DEW method). On the other hand, the relative increase of level of noise in the corrected images from the first photopeak window (51.4% for the TEW method and 40.7% for the DEW method) is significantly higher than that from the second photopeak window (21.8% for the TEW method and 19.7% for the DEW method), with a lower level for the DEW correction method compared to the TEW correction method. Furthermore, the RCs obtained from the hot sphere images show that contrary to the TEW method, the images corrected by the DEW method from two photopeak windows show a similar agreement with their primary images. Furthermore, the results obtained from the second stage indicate that the use of SEW and FEW correction approximations leads to an average of relative increase of about 19.68% and 16.61% for cold sphere contrasts and 37.7% and 32.6% for the level of image noise that is comparable to 34% for primary image.

As expected, the use of the collective photopeak window instead of the single photopeak windows led to decrease in the level of noise in In-111 SPECT images. Therefore, according to the results obtained from this study, we can introduce the

SEW and FEW approximations as two suitable methods for the scatter correction of In-111 SPECT imaging, with a greater mean relative increase of the cold sphere contrasts for the SEW approximation and a lower relative increase of level of noise for the FEW approximation. Therefore, the SEW correction approximation is preferred when the image contrast is an important parameter in imaging, and the FEW correction approximation is recommended when the low level of noise in SPECT images is desirable. In addition, because of the need of up to three energy windows for each photopeak energy, the proposed approximations are applicable in the clinical imaging systems.

Financial support and sponsorship

Nil.

Conflicts of interest

There are no conflicts of interest.

REFERENCES

- Hutton BF, Buvat I, Beekman FJ. Review and current status of SPECT scatter correction. *Phys Med Biol* 2011;56:R85-112.
- Rydén T. Development of methods for analysis and reconstruction of nuclear medicine images. *IEEE Trans Nucl Sci* 1991;38:761-6.
- Jaszczak RJ, Greer KL, Floyd CE Jr., Harris CC, Coleman RE. Improved SPECT quantification using compensation for scattered photons. *J Nucl Med* 1984;25:893-900.
- Axelsson B, Msaki P, Israelsson A. Subtraction of Compton-scattered photons in single-photon emission computerized tomography. *J Nucl Med* 1984;25:490-4.
- Floyd CE, Jaszczak RJ, Greer KL, Coleman RE. Deconvolution of Compton scatter in SPECT. *J Nucl Med* 1985;26:403-8.
- Yanch JC, Flower MA, Webb S. A comparison of deconvolution and windowed subtraction techniques for scatter compensation in SPECT. *IEEE Trans Med Imaging* 1988;7:13-20.
- Ogawa K, Harata Y, Ichihara T, Kubo A, Hashimoto S. A practical method for position-dependent Compton-scatter correction in single photon emission CT. *IEEE Trans Med Imaging* 1991;10:408-12.
- Logan KW, McFarland WD. Single photon scatter compensation by photopeak energy distribution analysis. *IEEE Trans Med Imaging* 1992;11:161-4.
- King MA, Hademenos GJ, Glick SJ. A dual-photopeak window method for scatter correction. *J Nucl Med* 1992;33:605-12.
- Pretoris PH, van Rensburg AJ, van Aswegen A, Lötter MG, Serfontein DE, Herbst CP. The channel ratio method of scatter correction for radionuclide image quantification. *J Nucl Med* 1993;34:330-5.
- Buvat I, Rodriguez-Villafuerte M, Todd-Pokropek A, Benali H, Di Paola R. Comparative assessment of nine scatter correction methods based on spectral analysis using Monte Carlo simulations. *J Nucl Med* 1995;36:1476-88.
- Changizi V, Takavar A, Babakhani A, Sohrabi M. Scatter correction for heart SPECT images using TEW Method. *J Appli Clinical Med Phy* 2008;9:136-40.
- Islamian JP, Bahreyni Toossi MT, Momenzhad M, Zakavi SR, Sadeghi R. Monte Carlo study of the effect of backscatter material thickness on 99mTc source response in single photon emission computed tomography. *Iran J Med Phys* 2013;10:69-77.
- Noori-Asl M, Sadremomtaz A, Bitarafan-Rajabi A. Evaluation of six scatter correction methods based on spectral analysis in 99mTc SPECT imaging using SIMIND Monte Carlo simulation. *J Med Phys* 2013;38:189.
- Noori-Asl M, Sadremomtaz A, Bitarafan-Rajabi A. Evaluation of three scatter correction methods based on estimation of photopeak scatter spectrum in SPECT imaging: A simulation study. *Phys Med* 2014;30:947-53.
- Ghaly M, Links JM, Frey E. Optimization of energy window and evaluation of scatter compensation methods in myocardial perfusion SPECT using the ideal observer with and without model mismatch and an anthropomorphic model observer. *J Med Imaging (Bellingham)* 2015;2. pii: 015502.
- Knoll P, Rahmim A, Gültekin S, Šámal M, Ljungberg M, Mirzaei S, *et al.* Improved scatter correction with factor analysis for planar and SPECT imaging. *Rev Sci Instrum* 2017;88:094303.
- Rafati M, Rouhani H, Bitarafan-Rajabi A, Noori-Asl M, Farhood B, Ahangari HT. Assessment of the scatter correction procedures in single photon emission computed tomography imaging using simulation and clinical study. *J Cancer Res Ther* 2017;13:936-42.
- Chiang C, Lin H, Lin C, Jan M, Chuang K. Simulation of Multi-Photon Emission Isotopes using Time-Resolved SimSET Multiple Photon History Generator. 4th International Conference on Advancements in Nuclear Instrumentation Measurement Methods and their Applications (ANIMMA), Lisbon; 2015. p. 1-5.
- Ljungberg M, Strand SE. A Monte Carlo program simulating scintillation camera imaging. *Comput Methods Programs Biomed* 1989;29:257-72.
- Knoll GF. *Detection and Measurement of Radiation*. New York: John Wiley and Sons; 1999.
- Gilland DR, Jaszczak RJ, Turkington TG, Greer KL, Coleman RE. Quantitative SPECT Imaging with Indium-111. *IEEE Trans Nucl Sci* 1991;38:761-6.
- Penney BC, Rajeevan N, Bushe HS, Hademenos G, King A. A Scatter Reduction Method for In-111 Scintigrams using Five Energy Windows. *IEEE Nuclear Science Symposium and Medical Imaging Conference*, 2-9 November, Santa Fe, New Mexico, USA; 1991.
- Choi CW, Barker WC, Buvat I, Carrasquillo JA, Bacharach SL. Implications of dual-energy-window (DEW) scatter correction inaccuracies for 111In quantitative geometric mean imaging. *Nucl Med Commun* 1997;18:79-86.
- Holstensson M, Hindorf C, Ljungberg M, Partridge M, Flux GD. Optimization of energy-window settings for scatter correction in quantitative ¹¹¹In imaging: Comparison of measurements and Monte Carlo simulations. *Cancer Biother Radiopharm* 2007;22:136-42.

Monte Carlo Calculation of the Energy Spectrum of a 6 MeV Electron Beam using PENetration and Energy Loss of Positrons and Electrons Code

Danny Giancarlo Apaza Veliz^{1,2}, Jorge Homero Wilches Visbal³, Felipe Chen Abrego⁴, José Luis Vega Ramírez²

¹Department of Physics, Faculty of Philosophy, Sciences and Letters, University of São Paulo, ⁴Center for Natural and Human Sciences, Federal University of ABC, Brazil, ²Department of Physics, National University of San Agustín, Arequipa, Peru, ³Department of Basic Biomedical Sciences, Faculty of Health Sciences, University of Magdalena, Santa Marta, Colombia

Abstract

Background: The limited bibliographic existence of research works on the use of Monte Carlo simulation to determine the energy spectra of electron beams compared to the information available regarding photon beams is a scientific task that should be resolved. **Aims:** In this work, Monte Carlo simulation was performed through the PENELOPE code of the Sinergy Elekta accelerator head to obtain the spectrum of a 6 MeV electron beam and its characteristic dosimetric parameters. **Materials and Methods:** The central-axis energy spectrum and the percentage depth dose curve of a 6 MeV electron beam of an Elekta Synergy linear accelerator were obtained by using Monte Carlo PENELOPE code v2014. For this, the linear accelerator head geometry, electron applicators, and water phantom were simplified. Subsequently, the interaction process between the electron beam and head components was simulated in a time of 86.4×10^4 s. **Results:** From this simulation, the energy spectrum at the linear accelerator exit window and the surface of the phantom was obtained, as well as the associated percentage depth dose curves. The validation of the Monte Carlo simulation was performed by comparing the simulated and the measured percentage depth dose curves via the gamma index criterion. Measured percentage depth-dose was determined by using a Markus electron ionization chamber, type T23343. Characteristic parameters of the beam related with the PDD curves such as the maximum dose depth (R_{100}), 90% dose depth (R_{90}), 90% dose depth or therapeutic range (R_{85}), half dose depth (R_{50}), practical range (R_p), maximum range (R_{max}), surface dose (D_s), normalized dose gradient (G_0) and photon contamination dose (D_x) were determined. Parameters related with the energy spectrum, namely, the most probable energy of electrons at the surface ($E_{p,0}$) and electron average energy (\bar{E}_0) were also determined. **Conclusion:** It was demonstrated that PENELOPE is an attractive and accurate tool for the obtaining of dosimetric parameters of a medical linear accelerator since it can reliably reproduce important clinical data such as the energy spectrum, depth dose, and dose profile.

Keywords: Dose profile, electron spectrum, Monte Carlo simulation, PENetration and Energy LOSS of Positrons and Electrons, percentage depth-dose

Received on: 27-11-2019

Review completed on: 19-03-2020

Accepted on: 27-03-2020

Published on: 20-07-2020

INTRODUCTION

Radiation therapy is one of the most used treatment modalities of cancer. Its objective is to maximize the dose delivered to cancer while minimizing the delivery in healthy tissues. The choice of the type of radiation (electrons, photons, protons, or heavy ions) and the availability of advanced tools for treatment are crucial to the success of radiotherapy.^[1,2] Electron beams^[3,4] are specially used for the treatment of superficial tumors because of the fast energy loss of the electrons in the first layers of the material.^[5-7] Many efforts have been done both in order to achieve better planning and dosimetry in the

electron treatments and to assess the risks and benefits of this procedure.^[1,8,9] Computational simulations are one of the most common and effective ways used to bring us as close as possible to the conditions and characteristics of the clinical setting. Monte Carlo method (MMC) is a powerful tool to simulate the interaction of ionizing radiation with matter. It

Address for correspondence: Prof. Danny Giancarlo Apaza Veliz, Department of Physics, Faculty of Philosophy, Sciences and Letters, University of São Paulo, Brazil. E-mail: dgav02@gmail.com

This is an open access journal, and articles are distributed under the terms of the Creative Commons Attribution-NonCommercial-ShareAlike 4.0 License, which allows others to remix, tweak, and build upon the work non-commercially, as long as appropriate credit is given and the new creations are licensed under the identical terms.

For reprints contact: WKHLRPMedknow_reprints@wolterskluwer.com

How to cite this article: Apaza Veliz DG, Wilches Visbal JH, Abrego FC, Vega Ramirez JL. Monte carlo calculation of the energy spectrum of a 6 MeV electron beam using PENetration and energy loss of positrons and electrons code. J Med Phys 2020;45:116-22.

Access this article online

Quick Response Code:



Website:
www.jmp.org.in

DOI:
10.4103/jmp.JMP_104_19

also allows to model radiation beams (electrons, photons, positrons, neutrons, and protons) produced in clinical linear accelerators.^[10-14] With this, Monte Carlo simulation (MCS) can be used to obtain and analyze different clinical parameters such as energy spectrum, angular distribution, percentage depth dose (PDD), and other clinical parameters.^[15]

The MCS validation is done by comparing the dose distribution obtained from the simulation with the experimental measurements. To perform this validation, the gamma-index can be used. Gamma-index is a mathematical parameter that evaluates the degree of agreement between two dose distributions considering spatial and dose distances under predefined tolerance limits.^[16-19] The report 42 of the International Commission on Radiation Units and Measurements (ICRU)^[20] states that, in order to have a high level of precision in the MCS of a beam, there should be no discrepancy between dose distributions $>\pm 2\%$ or ± 2 mm.^[21] In addition to the considerations given in the report 42, the accuracy of the simulation depends directly on the choice and how well the parameters or input information, the characteristics of the materials immersed in the constructed geometries, and the nominal energies can be represented.^[15,21]

The choice of the Monte Carlo code for the simulation marks a differential in obtaining satisfactory results. Currently, there are several radiation transport simulation codes based on the MMC, some free and others sold. For example, there is the EGSnrc system which is a Monte Carlo code to simulate the transport of electrons and photons in various geometries,^[12,22,23] and whose valid energy range is between 1 keV and 100 GeV. Geometry ANd Tracking (GEANT4) is a code that simulates the transport of all kinds of particles in the energy range between 250 eV and about 10 TeV.^[24] It is mainly used in high-energy physics as well as in medical physics. FLUKtuierendeKAskade is used in high-energy physics and medical physics. It is a general-purpose code that reproduces the interaction of ionizing radiation with the matter of up to 60 different particles at the same time, electrons and photons (from 1 keV to 1000 TeV), hadrons (up to 20 TeV), neutrons (including thermal), and heavy ions. Like GEANT4, it presents various applications in high-energy physics and medical physics.^[25] Monte Carlo N-Particle is another general-purpose code for the transport of neutrons, photons, and electrons.^[26-28] In this work, the PENetration and Energy LOss of Positrons and Electrons (PENELOPE) code is used. It has extensive information on various applications for radiotherapy and radiodiagnosis.^[4,29-34] Since its first version launched in 1996, the MCS PENELOPE code has become a flexible and reliable tool to describe the coupled transport of photons and electrons in complex material structures,^[35,36] presenting simplicity and versatility to be used in the two most used programming platforms such as Windows and Linux without the necessity of the usage of an intermediary interface. Moreover, the results obtained are presented in *.dat* extension which is easy to read in any code for statistical analysis such as Origin, Matlab, and Gnuplot.

The main motivation of this work is related to there are few research papers about the use of MCS to determine energy spectra of electron beams^[21,31,37,38] and its characteristic dosimetric parameters in comparison to those existent for photon beam,^[11,31,33,39-46] especially for linear accelerators still used in developing countries. Thus, in this work, an Elekta Synergy Platform linear accelerator was used as a reference, since the Synergy is still one of the most used accelerators in the Latin-American market and other developing regions of the world. The novelty of the present work consists of a complete description of how to simulate the Synergy Elekta linear accelerator head using PENELOPE. It was also demonstrated that PENELOPE is a cheap and powerful computational tool for the radiation external source modeling in radiotherapy since it reliably reproduced the relevant dosimetric data of the electron beam studied.

MATERIALS AND METHODS

Monte Carlo simulation codes

MMC is any probabilistic method that is based on random sampling and provides numerical results. This method is widely applied for simulations in physics, biology, chemistry, and mathematics^[12,22,36,47] since it can give numerical solutions of very complex functions. One of the many Monte Carlo versions utilized for studying the radiation transport in a material is the PENetration and Energy LOss of Positrons and Electrons code. Thus, PENELOPE is a general-purpose open code for the transport of electrons, photons, and positrons with a range of energies between 50 eV and 1 GeV. Because of this, its main fields of use are applications in medical physics, namely external radiotherapy, radiodiagnostic, nuclear medicine, and brachytherapy.

The several geometries used are constructed from quadratic surfaces, and variance reduction techniques are incorporated to have better adaptability and greater precision.^[30,33,36,47,48] PENELOPE allows creating materials with a single component, alloys, or mixed materials that are present in the constitution of a clinical linear accelerator. All these help to make better reproductions and representations of experimental conditions. PENELOPE's stop simulation criteria depend on the real time of the simulation or the events/simulated shower number. In this work, the PENELOPE version 2014 was used.

Modeling of the electron radiation source using PENetration and Energy LOss of Positrons and Electrons

PENELOPE code was used to reproduce the physical, geometrical, and material characteristics that make up the head of an Elekta Synergy Platform linear accelerator. The technical detail of each of the mentioned characteristics is described in the phase spaces extracted from the manual provided by the manufacturer, and for commercial reasons, this information is omitted. Based on the geometric information and composition of the elements and components of the linear accelerator head provided in the manufacturer's manual, the virtual simulation was performed in PENELOPE. Both materials of the primary

and secondary collimators and those of the scattering foils used in the virtual geometry are composed of the same alloys and densities as the actual accelerator materials. The precision in the replication of these details allowed determining the characteristics of the energy spectrum of the electron beam both in the exit window after interacting with the head components as well as the spectrum on the surface of the phantom.

Figure 1 shows the virtual geometry of the Elekta linear accelerator built-in PENELOPE. To do this, three-dimensional gview software was used since it is the graphic display extension of PENELOPE. Figure 1a details the locations of the radiation source, the scattering foils, and the collimators inside the accelerator head. The geometry configuration shown in Figure 1b was used to simulate the interaction of the electron beam with the surface of the water phantom: gantry angle of 0°, nominal energy of 6 MeV, field size of 10 cm × 10 cm, 100 cm of source-skin distance (SSD), applicators of 10 cm × 10 cm, and a phantom water of 40 cm × 40 cm × 40 cm. The simulation time employed was 86.4 × 10⁴ s, number of simulated showers of 3.5 × 10⁹, and a confidence level of 99%. To carry out the simulations, the Educational Cluster of the University of São Paulo-Ribeirão Preto was used. All simulations were performed with respect to the central axis of the electron beam. For the experimental dosimetric measurements, the accelerator position was configured as follows: 0° gantry angle, 6 MeV nominal energy, 10 cm × 10 cm field size, 100 cm SSD with 10 cm × 10 cm applicators, and an automated tank, and a parallel flat ionization chamber was used Markus model with 3.05 mm detector radius. Throughout all the work, we will call the PENELOPE simulation as MCS.

Relationships between beam characteristics and depth-dose distribution

There are several dosimetric parameters to fully characterize an electron beam from the PDD curve recommended by ICRU. These parameters are: maximum dose depth (R_{100}), 90% dose depth (R_{90}), 85% dose depth (R_{85}), 50% dose depth (R_{50}), practical range (R_p), maximum range (R_{max}), the most probable energy of electrons on the surface ($E_{p,0}$), average energy of electrons (\bar{E}_0) on the surface, the dose gradient (G_0), percentage of doses of contaminating photons (D_x), and percentage of surface dose (D_s). In the Technical Report Series No. 381 reports of IAEA^[49] and the report 32 of the AAPM,^[6] empirical relationships between the parameters and the PDD curve are shown. The two best known relationships between E_0 and R_{50} are:

$$\bar{E}_0 = 0.656 + 2.059R_{50} + 0.022R_{50}^2 \tag{1}$$

$$\bar{E}_0 = 2.33R_{50} \tag{2}$$

Eq. (1) is recommended in the technical report 381 of the IAEA (1997)^[49] while Eq. (2) is recommended in report 32 of the AAPM.^[6] Both allow calculating the average energy of the electrons from R_{50} .

A very useful relationship is $E_{p,0}$ and R_p , which has the same form of Eq. (1) but with different constants and in relation to R_p .^[6,49]

$$E_{p,0} = 0.22 + 1.98R_p + 0.0025R_p^2 \tag{3}$$

Another characteristic parameter that can be calculated is the standardized dose gradient (G_0), which describes the slope of

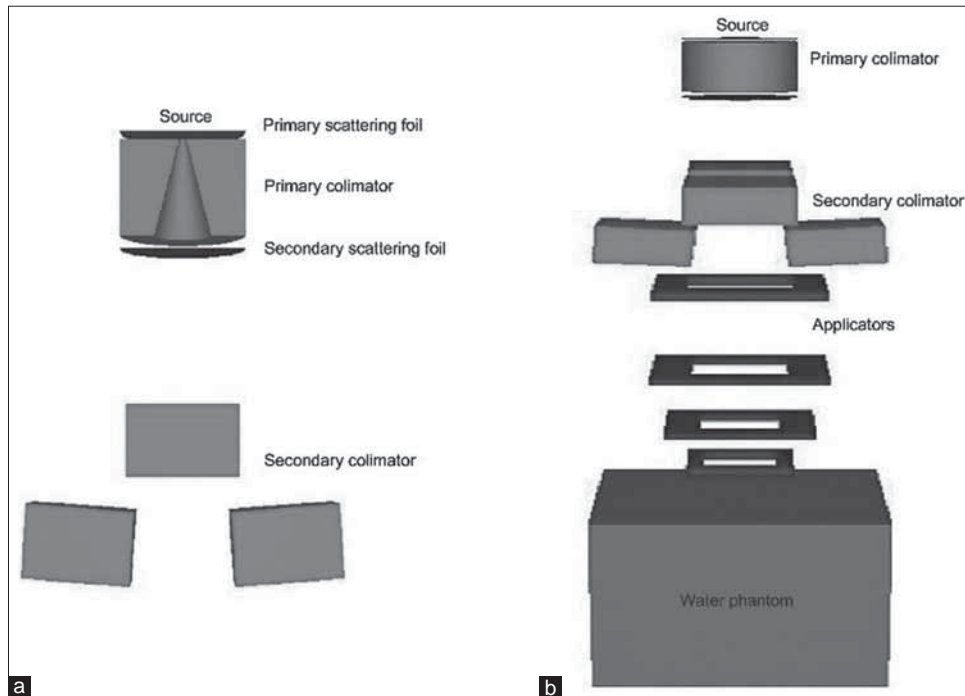


Figure 1: Representation of the virtual geometry simulated of the linear accelerator used to simulate the electron beam. Simulation of the accelerator head geometry (a) and the complete geometry of the linear accelerator (b)

the fall region of the PDD curve. This gradient is related to R_q and R_p ,

$$G_0 = \frac{R_p}{R_p - R_q} \quad (4)$$

All parameters R_{100} , R_{90} , R_{85} , R_{50} , R_q , R_p , R_{max} , $E_{p,0}$, \bar{E}_0 and G_0 were obtained for the measured depth-dose distribution curve and also for the one generated by simulation with PENELOPE code, in order to validate the simulation and have a comparison between both curves.

In order to validate the PDD curve obtained from the simulation, it is compared to the measured PDD which was previously determined by employing an ionization chamber. The comparing method utilized was the gamma-index since it is widely known and used criterion in radiotherapy. The gamma-index (Γ) is determined by:

$$\Gamma(\vec{r}_s, \vec{r}_m) = \sqrt{\frac{|\vec{r}_s - \vec{r}_m|^2}{DTA^2} + \frac{|D_{\vec{r}_s} - D_{\vec{r}_m}|^2}{DD^2}} \quad (5)$$

where $|\vec{r}_s - \vec{r}_m|$ is the distance between the analyzed points, being \vec{r}_s the obtained from simulation and \vec{r}_m the experimentally measured, and $|D_{\vec{r}_s} - D_{\vec{r}_m}|$ represents the dose difference (DD) between the simulated and measured PDD curves at \vec{r}_s and \vec{r}_m respectively. The distance-to-agreement and DD values are scale values that adjust the gamma-index to the acceptance level required, i.e., they are the predefined tolerance values.^[16,18]

RESULTS AND DISCUSSIONS

Electron energy spectrum derived from Monte Carlo simulation

The simulated energy spectra at the linear accelerator exit

window and at the water phantom surface are shown in Figure 2. The spectrum at the exit window was measured after the second scattering foil. The spectra were normalized to its most probable maximum energy value.

Figure 2a is observed the energy spectrum at the exit window with a narrow central peak and the presence of an additional small peak to its left. The narrowness of the central peak is because the electron beam has not interacted with most of the accelerator head structures and the entire air column. The small peak is generated as the beam passing through the first linear accelerator head metal structures (collimator and scattering foils) and interacting with them for producing this secondary radiation. Figure 2b shows the energy spectrum at phantom surface whose shape resembles a slightly asymmetric Gaussian distribution and with a width central peak. There is also observed a small peak to the left of the central peak in the energy range of 0–0.250 MeV which may be due to the contaminating photons that reach the water phantom surface. From Figure 2, two important spectral parameters can be obtained: the most probable energy, E_0 , and the full width at half maximum (FWHM) of the central peak, γ_0 . Not to be confused E_0 with $E_{p,0}$, since while both mean the same, E_0 is the most probable energy obtained from the analysis of the spectrum, while $E_{p,0}$ represents the most probable energy from R_{50} in the PDD curve.

Table 1 shows the values of E_0 and γ_0 for the spectra at the exit window and at the phantom surface. The value of γ_0 , as well as its value respect to E_0 , is shown as well. From Table 1 data, it is noted that as the beam approaches, the surface of the water phantom decreases the most probable energy and increases the FWHM of the spectrum. This is because of the low-energy electrons, generated by the interaction among the beam and the accelerator structures and air, reduce the hardness of the beam and they are more easily scattered.^[21]

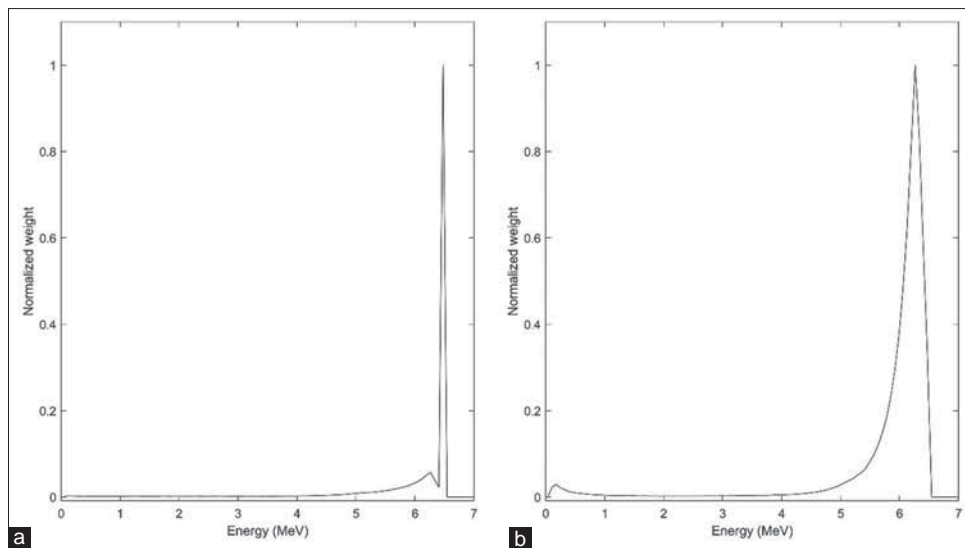


Figure 2: Energy spectra of the electron beam of 6 MeV at the exit window (a) and the phantom surface (b) obtained by PENetration and Energy LOSS of Positrons and Electrons

Comparison of depth-dose distribution curves and dose profiles

Figure 3 shows the simulated and measured PDD curves for the electron beam of 6 MeV nominal energy. Vertical open circle lines are the values of the gamma-index in each depth.

At the build-up region (0–1 cm depth), a noticeable discrepancy in terms of DD is observed. The contribution of contamination photons is noted at the final part of PDD curves, specifically, from the 3.2 cm depth. Contamination photons are generated by the deflection of primary and secondary electrons passing through accelerator structures.^[50] It was found that the contribution of contamination photon dose in the measured PDD curve is greater than the simulated one because of the inefficiency of the simulation to calculate the contamination photons amount. It is possible that such inefficiency obeys to the discrepancies in the constitution of the alloys of the accelerator materials simulated in PENELOPE and those of the real accelerator. ICRU recommendation is that the differences between the treatment (measured) and planning (simulated) PDD curves were within $\pm 2\%/ \pm 2$ mm.^[21] Keeping this in mind, the DDs between the measured and simulated PDD curves were analyzed using the gamma-index. The largest differences are found at the shallow region of the water phantom. In fact, the DD between the PDD curves reached up to 3% in that region, while for the rest, it was not $>1\%$. The acceptance percentage of the simulated PDD curve was 100% and 98% according to the gamma-index criterion of $>95\%$ of simulated curve within $2\%/2$ mm and $1\%/1$ mm, respectively.

Figure 4a displays the measured and simulated PDD curves in the build-up region. In this region, DDs are ranged from 1% to 3%. The largest difference occurs in the depth of the surface dose. This indicates that the simulated spectrum could not reproduce the dose data in this region with high accuracy. However, this is a really hard task since the experimental measurements of the dose at the build-up region are highly

probabilistic due to here occur the first interaction of beam electrons with the water surface.

In Figure 4b, the measured and simulated dose profiles are compared. Dose profiles allow detailing the off-axis DDs between the dose profiles at a reference depth. The reference depth was stated in 1.3 cm. Moreover, from Figure 4b, A good agreement between measured and simulated dose profiles is observed, except in the field edge region. In the edge region, the differences are higher than the other regions of dose profiles because the incident electrons possess a greater angular spread.

Beam characteristics derived from the percentage depth-dose curves

An additional way to evaluate the accuracy of the simulated electron energy spectrum is comparing the values of dosimetric parameters obtained from the measured and simulated PDD curves. The values of dosimetric parameters found are shown in Table 2.

From Table 2, a good approximation between the values of the measured and simulated characteristic parameter is observed. The highest deviations were found for G_0 and D_x .

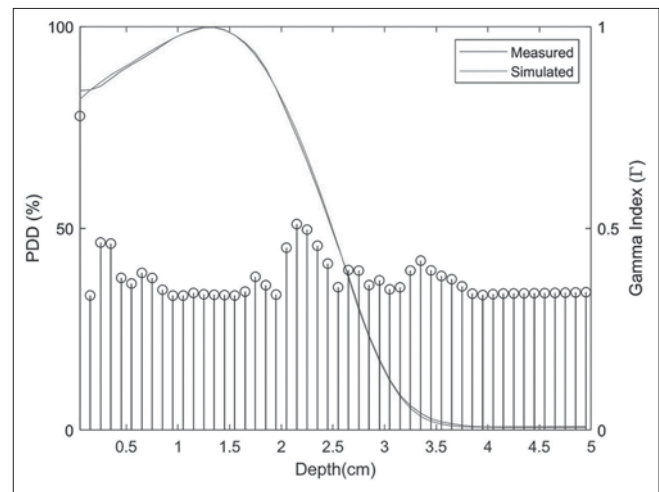


Figure 3: Comparison between the measured and simulated percentage depth-dose curves. Vertical lines (open circles) are the values of the gamma-index in each depth of percentage depth-dose curves. It can be observed that all gamma-index values are lower than 1, which indicates that the simulated percentage depth-dose curve meets with the imposed criterion of $>95\%$ of its points being within a $2\%/2$ mm radius with respect to the measured peak percentage depth-dose curve

Table 1: Relevant dosimetric parameters of the spectrum according to its registration location

Spectrum registration location	E_0 (MeV)	γ_0 (MeV)	γ_0/E_0 (%)
Exit window	6.46	0.04	0.62
Phantom surface	6.26	0.40	6.39

FWHM: Full width at half maximum, E_0 : Most probable energy, γ_0 : FWHM of the spectrum central peak

Table 2: Values of the dosimetric parameters found from the measured and simulated percentage depth-dose curves

PDD curve	R_{100}	R_{90}	R_{85}	R_{50}	R_p	R_{max}	G_0	$E_{p,0}$	\bar{E}_0	D_s	D_x
Measured	1.30	1.84	1.94	2.48	3.20	3.78	0.45	6.58	5.78	84.10	0.58
Simulated	1.31	1.82	1.93	2.48	3.17	3.75	0.43	6.52	5.79	82.29	0.51
Deviation	0.76	1.1	0.52	0	0.95	0.79	4.4	0.91	0.17	2.2	12

Deviation is the percentage relative error between the measured and calculated data. R_{100} : Maximum dose depth, R_{90} : 90% dose depth, R_{85} : 85% dose depth or therapeutic range, R_{50} : Half-dose depth, R_p : Practical range, R_{max} : Maximum range, D_s : surface dose, G_0 : Normalized dose gradient, D_x : Photon contamination dose, PDD: Percentage depth dose

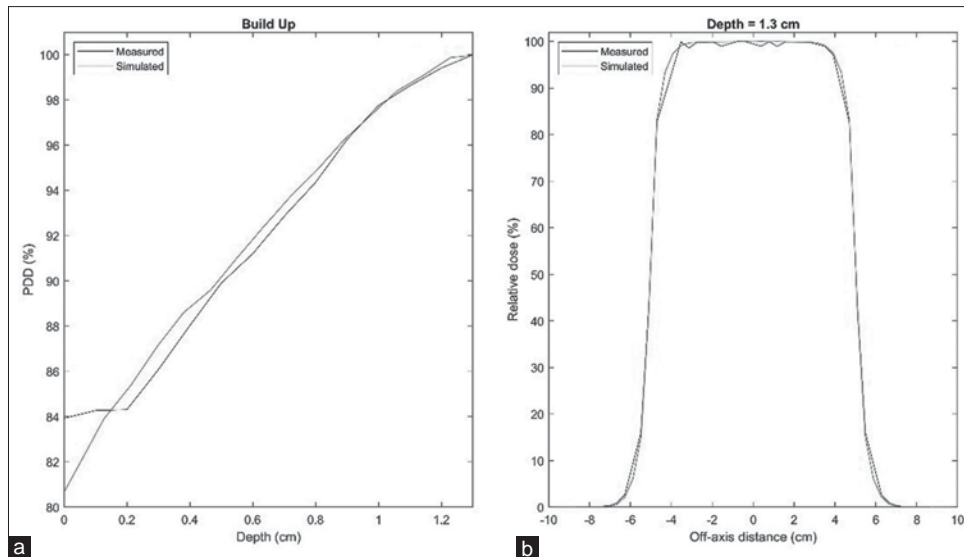


Figure 4: Comparison between the measured and simulated percentage depth-dose curves at the build-up region (a) and between the measured and simulated dose profiles at the reference depth of 1.3 cm (b)

CONCLUSIONS

Monte Carlo PENELOPE code represents a powerful tool to study the effects and characteristics of a medical electron beam. A good agreement between the measured and simulated depth-dose distributions was observed according to the gamma passing rate criterion. It was also seen a good agreement between the measured and simulated dose profiles excepting the field edge region. The small discrepancies found are related to the limited representation of the geometrical and the composition of accelerator head structures as well as the behavior of the simulated energy beam as it traverses such structures and the air. Most of the characteristic parameters of the simulated PDD relative are in accordance with those of the measured PDD. The dose gradient and the photon contamination dose were the characteristic parameters of PDD curves with the highest discrepancies. Therefore, it can be concluded that PENELOPE v2014 is an accurate tool to obtain the electron energy spectrum and other important dosimetric characteristics of an electron beam.

Financial support and sponsorship

Nil.

Conflicts of interest

There are no conflicts of interest.

REFERENCES

1. AAPM AA of P in M. Radiation treatment planning. Vol. 74, American Institute of Physics. New York: American Institute of Physics; 1995. p. 2118.
2. Fraass B, Doppke K, Hunt M, Kutcher G, Starkschall G, Stern R, et al. American Association of Physicists in Medicine Radiation Therapy Committee Task Group 53: Quality assurance for clinical radiotherapy treatment planning. *Med Phys* 1998;25:1773-829.
3. Blomquist M, Karlsson MG, Zackrisson B, Karlsson M. Multi leaf collimation of electrons – Clinical effects on electron energy modulation and mixed beam therapy depending on treatment head design. *Phys Med Biol* 2002;47:1013-24.
4. Brualla L, Zamora RP, Wittig A, Sempau J, Sauerwein W. Comparison between PENELOPE and electron Monte Carlo simulations of electron fields used in the treatment of conjunctival lymphoma. *Phys Med Biol* 2009;54:5469-81.
5. American Association of Physicists in Medicine. A protocol for the determination of absorbed dose from high energy photon and electron beams. *Med Phys* 1983;10:741-71.
6. Khan FM, Doppke KP, Hogstrom KR, Kutcher GJ, Nath R, Prasad SC, et al. Clinical electron-beam dosimetry: Report of AAPM Radiation Therapy Committee Task Group No. 25. *Med Phys* 1991;18:73-109.
7. Almond PR, Biggs PJ, Coursey BM, Hanson WF, Huq MS, Nath R, et al. AAPM's TG-51 protocol for clinical reference dosimetry of high-energy photon and electron beams. *Med Phys* 1999;26:1847-70.
8. Al-Yahya K, Verhaegen F, Seuntjens J. Design and dosimetry of a few leaf electron collimator for energy modulated electron therapy. *Med Phys* 2007;34:4782-91.
9. Strydom W, Parker W, Olivares M. Electron Beams: Physical and Clinical Aspects. In: Radiation oncology physics: A handbook for teachers and students (E.B. Podgorsak Edt). International Atomic Energy Agency (IAEA), Vienna 2005;1:273-299.
10. Durán-Nava OE, Torres-García E, Oros-Pantoja R, Hernández-Oviedo JO. Monte Carlo simulation and experimental evaluation of dose distributions produced by a 6 MV medical linear accelerator. *J Phys Conf Ser, Ciudad de México, México* 2018;1221:1-6.
11. Samir D, Zerfaoui M, Moussa A, Benkhoyou Y, El Quartiti M. Grid Monte Carlo Simulation of a medical linear accelerator. *Eur J Eng Res Sci* 2018;3:40-3.
12. Doucet R, Olivares M, DeBlois F, Podgorsak EB, Kawrakow I, Seuntjens J. Comparison of measured and Monte Carlo calculated dose distributions in inhomogeneous phantoms in clinical electron beams. *Phys Med Biol* 2003;48:2339-54.
13. Siantar CL, Moses EI. The peregrine TM program: Using physics and computer simulation to improve radiation therapy for cancer. *Eur J Phys* 1998;19:513-21.
14. Lux I, Koblinger L, editors. Monte Carlo Particle Transport Methods: Neutron and Photon Calculations. Boca Raton: CRC Press; 2018. p. 513.
15. Björk P, Knöös T, Nilsson P, Larsson K. Design and dosimetry characteristics of a soft-docking system for intraoperative radiation therapy. *Int J Radiat Oncol Biol Phys* 2000;47:527-33.
16. Hussein M, Clark CH, Nisbet A. Challenges in calculation of the gamma index in radiotherapy – Towards good practice. *Phys Medica* 2017;36:1-11.

17. Hussein M, Clementel E, Eaton DJ, Greer PB, Haworth A, Ishikura S, *et al.* A virtual dosimetry audit – Towards transferability of gamma index analysis between clinical trial QA groups. *Radiother Oncol* 2017;125:398-404.
18. Low DA, Dempsey JF. Evaluation of the gamma dose distribution comparison method. *Med Phys* 2003;30:2455-64.
19. Sumida I, Yamaguchi H, Kizaki H, Aboshi K, Tsujii M, Yoshikawa N, *et al.* Novel radiobiological gamma index for evaluation of 3-dimensional predicted dose distribution. *Int J Radiat Oncol Biol Phys* 2015;92:779-86.
20. ICRU. Use of computers in external beam radiotherapy procedures with high-energy photons and electrons. Thirteenth. Measurements International Commission on Radiation Units and Measurements, editor. Maryland; 1987. p. 70. Available from: <https://icru.org/link-index>. [Last accessed on 2020 Apr 09].
21. Björk P, Knöös T, Nilsson P. Influence of initial electron beam characteristics on Monte Carlo calculated absorbed dose distributions for linear accelerator electron beams. *Phys Med Biol* 2002;47:4019-41.
22. Kawrakow I, Mainegra-Hing E, Rogers DWO, Tessier F, Walters BR. EGSnrc: The EGSnrc code system: Monte Carlo simulation of electron and photon transport. NRCC Report. 2015. Ottawa, National Research Council Canada.
23. Sahoo S, Selvam T, Sharma SD, Das T, Dey AC, Patil BN, *et al.* Dosimetry of indigenously developed 192Ir high-dose rate brachytherapy source: An EGSnrc Monte Carlo study. *J Med Phys* 2016;41:115-22.
24. Agostinelli S, Allison J, Amako K, Apostolakis J, Araujo H, Arce P, *et al.* GEANT4 – A simulation toolkit. *Nucl Instrum Methods Phys Res A* 2003;506:250-303.
25. Ferrari A, Sala PR, Fasso A, Ranft J. FLUKA: A Multi-Particle Transport Code. 2014th ed. European Organization for Nuclear Research, editor. Vol. 773, Geneva; 2005. p. 406. Available from: <https://www.researchgate.net/publication/258832731>. [Last accessed 2020 Apr 01].
26. Waters LS, McKinney GW, Durkee JW, Fensin ML, Hendricks JS, James MR, *et al.* The MCNPX Monte Carlo radiation transport code. *AIP Conf Proc* 2007;896:81-90.
27. Jabbari K, Seuntjens J. A fast Monte Carlo code for proton transport in radiation therapy based on MCNPX. *J Med Phys* 2014;39:156-63.
28. Jabbari I, Monadi S. Development and validation of MCNPX-based Monte Carlo treatment plan verification system. *J Med Phys* 2015;40:80-9.
29. Sánchez MS, Pianoschi TA. Study of the distribution of doses in tumors with hypoxia through the PENELOPE code. *Radiat Phys Chem* 2020;167:22-5.
30. Merk R, Kröger H, Hornung LE, Hoffmann B. PENELOPE-2008 Monte Carlo simulation of gamma exposure induced by ⁶⁰Co and NORM-radionuclides in closed geometries. *Appl Radiat Isot* 2013;82:20-7.
31. Brualla L, Rodriguez M, Sempau J, Andreo P. PENELOPE/ primo-calculated photon and electron spectra from clinical accelerators. *Radiat Oncol* 2019;14:6.
32. Sheikh-bagheri D, Rogers DWO. Monte Carlo calculation of nine megavoltage photon beam spectra using the BEAM code. *Med Phys* 2002;29:391-402.
33. Gallardo S, Querol A, Pozuelo F, Verdú G, Ródenas J. Application of the Monte Carlo codes PENELOPE and MCNP5 to unfold X-ray spectra in the diagnostic energy range. *Radiat Phys Chem* 2014;95:166-9.
34. Merk R, Mielcarek J, Döring J, Lange B, Lucks C. Estimating contamination monitor efficiency for beta radiation by means of PENELOPE-2008 Monte Carlo simulation. *Appl Radiat Isot* 2017;127:87-91.
35. Salvat F, Varea JM, Sempau J. PENELOPE 2011: A Code System for Monte Carlo Simulation of Electron and Photon Transport. Nuclear Energy Agency; 2011.
36. Salvat F. The PENELOPE code system. Specific features and recent improvements. *Ann Nucl Energy* 2014;82:98-109.
37. Pimpinella M, Mihailescu D, Guerra AS, Laitano RF. Dosimetric characteristics of electron beams produced by a mobile accelerator for IORT. *Phys Med Biol* 2007;52:6197-214.
38. Björk P, Nilsson P, Knöös T. Dosimetry characteristics of degraded electron beams investigated by Monte Carlo calculations in a setup for intraoperative radiation therapy. *Phys Med Biol* 2002;47:239-56.
39. Jiménez JS, Lagos MD, Martínez-Ovalle SA. A Monte Carlo study of the photon spectrum due to the different materials used in the construction of flattening filters of LINAC. *Comput Math Methods Med* 2017;2017:3621631.
40. Qomariyah N, Wirawan R, Mardiana L, Hadi K Al. Distributions dose analysis for 6 MV photon beams using Monte Carlo-GEANT4 simulation. *AIP Conf Proc* 2019;2169:1-6.
41. Sheikh-bagheri D, Rogers DWO. Monte Carlo calculation of nine megavoltage photon beam spectra using the BEAM code. *Med Phys* 2002;29:391-402.
42. Lin SY, Chu TC, Lin JP. Monte Carlo simulation of a clinical linear accelerator. *Appl Radiat Isot* 2001;55:759-65.
43. Serrano B, Hachem A, Franchisseur E, Héroult J, Marcié S, Costa A, *et al.* Monte Carlo simulation of a medical linear accelerator for radiotherapy use. *Radiat Prot Dosimetry* 2006;119:506-9.
44. Jabbari K, Anvar H, Tavakoli M, Amouheidari A. Monte carlo simulation of siemens oncor linear accelerator with beamnrc and dosxyznrc code. *J Med Signals Sens* 2013;3:172-9.
45. Sadrollahi A, Nuesken F, Licht N, Rube C, Dzierma Y. Monte-Carlo simulation of the Siemens Artiste linear accelerator flat 6 MV and flattening-filter-free 7 MV beam line. *PLoS One* 2019;14:e0210069.
46. Anderson R, Lamey M, MacPherson M, Carlone M. Simulation of a medical linear accelerator for teaching purposes. *J Appl Clin Med Phys* 2015;16:5139.
47. Chin MP, Böhlen TT, Fassò A, Ferrari A, Ortega PG, Sala PR. FLUKA and PENELOPE simulations of 10keV to 10MeV photons in LYSO and soft tissue. *Radiat Phys Chem*. 2014;95:170-3.
48. Almansa JF, Guerrero R, Al-Dweri FM, Anguiano M, Lallena AM. Dose distribution in water for monoenergetic photon point sources in the energy range of interest in brachytherapy: Monte Carlo simulations with PENELOPE and GEANT4. *Radiat Phys Chem* 2007;76:766-73.
49. International Atomic Energy Agency. The Use of Plane Parallel Ionization Chambers in High Energy Electron and Photon Beams: An International Code of Practice for Dosimetry. Technical Reports Series No. 381. Vienna, 1997.
50. Zhengming L, Jette D. On the possibility of determining an effective energy spectrum of clinical electron beams from percentage depth dose (PDD) data of broad beams. *Phys Med Biol* 1999;44:N177-82.

Simultaneous Measurement of *In vivo* and Transit Mid-Plane Doses with Ionization Chambers in Gynecological Malignancy Patients Undergoing Three-Dimensional Conformal Radiotherapy

Putha Suman Kumar, Challapalli Srinivas, B. M. Vadhira¹, Sourjya Banerjee, R. Shreyas, PU Prakash Saxena, Ramamoorthy Ravichandran, Dilson Lobo
Department of Radiation Oncology, Kasturba Medical College (A constituent institution of Manipal Academy of Higher Education, Manipal), Mangalore, ¹Department of Radiation Oncology, Manipal Hospitals, Bengaluru, Karnataka, India

Abstract

Purpose: The aim of this study is to estimate delivered radiation doses inside planning tumor volume (PTV) using the *in vivo* (mid-plane dose) measurement and transit measurement methods in gynecological malignancy patients undergoing three-dimensional conformal radiotherapy (3DCRT) using calibrated ionization chambers. **Materials and Methods:** Six patients with histopathologically proven carcinoma of the cervix or endometrium were planned with four-field 3DCRT to the pelvic site. Isocenter was at the geometric mid-plane of PTV with a dose prescription of 50 Gy in 25 fractions. Clinical mid-plane dose ($D_{iso, Transit}$) estimates were done in one method (transit) using the FC-65 positioned at electronic portal imaging device level. In another method, a repeat computerized tomography scan was performed (at the 11th fraction) using CC-13 having a protective cap in the vaginal cavity for *in vivo* measurements ($D_{in vivo}$). Simultaneous measurements were performed with the two chambers from the 11th fraction onward at least 3–4 times during the remaining course of treatment. **Results:** The agreement of mean doses from these two described methods and treatment planning system reference doses was in the range of $-4.4 \pm 1.1\%$ (minimum) to $-0.3 \pm 2.0\%$ (maximum) and $-4.0 \pm 1.7\%$ (minimum) to $1.9 \pm 2.4\%$ for $D_{in vivo}$ and $D_{iso, Transit}$, respectively, which are an acceptable range of daily radiation dose delivery. **Conclusion:** The fundamental importance of this study lies in simultaneous validation of delivered dose in real time with two methods. A study in this small number of patients has given the confidence to apply transit measurements for quality assurance on a routine basis as an accepted clinical dosimetry for the selected patients.

Keywords: *In vivo* dosimetry, quality assurance, real-time dose estimate, transit dosimetry

Received on: 14-01-2020

Review completed on: 05-05-2020

Accepted on: 05-05-2020

Published on: 20-07-2020

INTRODUCTION

In vivo dosimetry in external-beam radiotherapy plays a vital role in ensuring the delivery of prescribed dose to the patient at the treatment site. In the individual departments, regular quality assurance (QA) checks such as beam output and quality, isocenter, field congruence, and reproducibility in treatment executions are performed in the treatment machines on a routine basis. Apart from these, however, errors are known to occur during the course of treatment (both inter- and intra-treatments) (e.g., setup positions, source to the skin distance, and morphological changes resulting in variations in patient contour), necessitating the implementation of *in vivo* dosimetry.^[1]

An effective way of checking the status of the entire dosimetric procedures, starting from the performance of the treatment machine to accurate positioning of the patient, is to make absorbed dose measurements in the patient and when possible, in body cavities. Several studies have demonstrated

Address for correspondence: Dr. Challapalli Srinivas,
Department of Radiation Oncology, Kasturba Medical College,
(A constituent Institution of Manipal Academy of Higher Education, Manipal),
Mangalore - 575 001, Karnataka, India.
E-mail: challapalli.srinivas@manipal.edu

This is an open access journal, and articles are distributed under the terms of the Creative Commons Attribution-NonCommercial-ShareAlike 4.0 License, which allows others to remix, tweak, and build upon the work non-commercially, as long as appropriate credit is given and the new creations are licensed under the identical terms.

For reprints contact: WKHLRPMedknow_reprints@wolterskluwer.com

How to cite this article: Kumar PS, Srinivas C, Vadhira¹ BM, Banerjee S, Shreyas R, Prakash Saxena PU, *et al.* Simultaneous measurement of *in vivo* and transit mid-plane doses with ionization chambers in gynecological malignancy patients undergoing three-dimensional conformal radiotherapy. *J Med Phys* 2020;45:123-9.

Access this article online

Quick Response Code:



Website:
www.jmp.org.in

DOI:
10.4103/jmp.JMP_3_20

quantification of mid-plane dose during real-time treatment deliveries (e.g., entrance, exit and transit dose measurements) with different detectors (e.g., thermoluminescence detectors, diodes, metal–oxide–semiconductor field-effect transistor, ionization chambers, chemical dosimetry, and/or electronic portal imaging device [EPID]).^[2-5] Ionization chambers have always been the gold standard for reference dosimetry in radiation therapy; several documents, textbook chapters, and clinical studies have demonstrated their important role in *in vivo* dosimetry in patients treated by megavoltage radiotherapy with different techniques, for example, parallel-opposed three-dimensional conformal radiotherapy (3DCRT) and intensity-modulated radiotherapy (IMRT).^[6-12]

Typically, these chambers are placed in a central region of a phantom or in a region corresponding to the uniform high-dose area, which is then irradiated by all of the treatment beams. Ionization chambers are limited by the fact that they can only report dose to a point or averaged over a small area. In some of the studies, the *in vivo* dose was measured by inserting an ionization chamber directly into the natural body cavity (e.g., esophagus, rectum, or vagina) with a protective cap which comes in the region of the treatment portals.^[13-16] The temperature of the cavity (which is the surrogate of the body temperature) where the chamber is placed is taken into account for temperature correction factor that needs to be applied to the charge collected by the chamber. The dose is then calculated by application of all chamber-related correction factors (e.g., calibration factor, temperature, pressure, and beam quality) to the collected charge. The estimated dose is compared to the planned dose by the computerized treatment planning system (TPS). Few studies described methods to assess *in vivo* mid-plane dose in patients through transit signal measured by an ionization chamber positioned at the EPID level while actual treatment is going on.^[3,13,14,16-19]

Angelo Piermattei *et al.*^[18] reported the results of the application of a practical method to determine the *in vivo* dose at the isocenter point of the brain, thorax, and pelvic treatments using a transit signal “ S_t ” (X-ray beam transmitted through the patient) measured with an ionization chamber which is positioned at the EPID level. By this method, the disadvantages associated with the use of solid-state detectors positioned on the patient and their positioning time are minimized. Simultaneous measurements of *in vivo* and mid-plane dose through transit method were performed using two ionization chambers, one placed intraluminally in patients who are undergoing esophagus treatment and the other one kept at a transit level, which was reported in the literature.^[13] A method was described to estimate mid-plane dose by measuring transit signal ($D_{\text{iso-transit}}$) in pelvic and thorax patients which was correlated with TPS-calculated values.^[3,20] In these studies, simultaneous measurements of *in vivo* and mid-plane dose were also carried out on pelvic and thorax phantoms using two ionization chambers, one kept at the mid-plane level and the another one at EPID level which were compared with the TPS-calculated values. In such new treatment plans in the

department, there is a need for documentation of daily dose delivered to the planning target volume (PTV). To confirm delivered doses in a protocol group of pelvic radiotherapy, we need to standardize a method and we investigated simultaneous measurement with *in vivo* and transit dosimetry.

MATERIALS AND METHODS

Subjects of study

A medical linear accelerator (Model: Compact, Elekta Ltd, Crawley, UK) with 6 MV photons, equipped with motorized wedge, 40 pairs multileaf collimator (MLCi2) having leaf thickness of 1 cm at 100 cm isocenter, and camera-based portal imaging was used for 3DCRT treatments. The machine was calibrated to deliver 1cGy/MU with a dose rate of 350MU/min under the calibration conditions stated in the International Atomic Energy Agency (IAEA) dosimetry code of practice (TRS-398).^[21] In this study, online *in vivo* mid-plane dose estimates are made using two calibrated ionization chambers (Models: CC13 and FC65, IBA Dosimetry, Germany) simultaneously in patients with gynecological malignancy (endometrium and cervix), who have received the 3DCRT course schedule. Both the chambers are connected to dual-channel electrometer (Dose2, IBA Dosimetry, Germany) for charge collection, and the absolute dose measurements are arrived in a water phantom using TRS-398 protocol and the doses accepted within 0.2%. Estimates of online *in vivo* mid-plane doses were correlated with the TPS-calculated values at reference point inside the PTV. We got approval from a small number of gynecological malignant patients from institutional ethics committee (approval letter number: IEC KMC MLR 11-14/224) to conduct this *in vivo* dosimetric study. Six patients had participated in this study. After the explanation of the nature of procedure, informed consent was obtained from all patients before the treatment process began.

Treatment planning (immobilization, simulation, and contouring)

All patients were immobilized in the supine treatment position using “Vacloc” device keeping their hands above the head; institution-specific bladder and rectal protocol was followed during simulation and treatment. Transverse images of 5 mm slice thickness acquired from computerized tomography (CT) scanner (Wipro GE, Model: High Speed) were exported to a contouring station (Focal Sim, M/s Elekta Ltd., Crawley, UK) for the generation of the clinical target volume (CTV) and marking organs at risk (OAR). A 5 mm margin was created around the CTV which forms PTV, to account for inter-fractional and geometric positional uncertainties. The contoured image data set was exported to the TPS (CMS XiO[®], version 5.0, Elekta Ltd, Crawley, UK) for dose calculations using a superposition algorithm.

Four-field box technique treatment plans were used in all patients with beams directed through gantry angles of 0°, 90°, 180°, and 270°. The isocenter of all beams coincides with the intersecting point of anterior–posterior and lateral portals,

along with the central axis corresponding to the center of PTV. The generated 3DCRT treatment plan with MLC covers PTV along with an additional margin of 5 mm. Depending on the requirement, either field-in-field (subfields) and/or wedge technique was used, for better homogeneity of the dose around the target region. A dose prescription of 50 Gy in 25 fractions (at 2.0 Gy per fraction) was normalized to 100% isodose line covered to PTV. It was ensured that the dose at the isocenter (i.e., $D_{iso, TPS}$) is identical to the homogeneous prescribed dose in 3DCRT plan. This “template” treatment plan was saved to locate the detector location *in vivo*, in future fractions. Plan evaluation, approval, scheduling, and patient treatment verification before the execution of the first fraction were carried out in a similar way as followed by Putha *et al.*^[3]

Dosimetric measurements

Transit dose estimates

At the EPID level, a 0.65 cc ionization chamber (Model FC65-G from IBA Dosimetry, Germany) with vendor provided acrylic buildup cap (for 6 MV photon beam) of thickness 3.0 cm diameter was placed on the mounting assembly along the central axis. Source to chamber center distance was maintained approximately 1.463 m. The chamber was connected to the channel 1 of Dose2 electrometer for the measurement of transit signals for all conformal fields during “real-time” treatment for all patients. The mid-plane dose at isocenter by transit signal (i.e., $D_{iso, Transit}$) was calculated using the method described by Putha *et al.*^[3] and was compared with the values of “ $D_{iso, TPS}$ ” of all the respective patients’ conformal fields.

Transit and *in vivo* dose estimates

After 10 fractions were done, a repeat CT scan was performed in all patients by placing a CC13 ionization chamber (which is covered with a custom made acrylic cylindrical cap, extending to the stem level) in the vaginal cavity without changing immobilization device and patient orientation. In addition, a removable latex rubber sleeve is used to overcome the risk of fluid intrusion into the cap. As per the technical manual of CC13 ion chamber, the outer electrode is at earth potential along with the cable. Therefore, along with a rubber sleeve, it was confirmed that there is no risk to the patient during the collection of signals in nano Coulombs (nC). In this way, *in vivo* detector positioning was performed in all patients after 10 fractions. Three fiducial markers (one marker representing the anterior entry beam and the other two at left and right lateral sides indicating lateral beam entry) were placed along the patient’s ongoing transverse iso-center plane. Repeat serial CT images were imported to the contouring station for chamber localization and exported them to TPS for dose calculations. Confirmation of CTV and treatment area has been reconfirmed by the radiation oncologist using the first collection of CT images in the repeat CT images. The point of calculation corresponds to the point of intersection of all three “fiducial” markers (visualized on the repeated transverse CT slice). Chamber location was ensured in all conformal

treatment portals. The mean dose of the chamber (i.e., $D_{in vivo, TPS}$) to the location of the sensitive volume is noted from the dose–volume histogram of TPS.

At the 11th fraction of the treatment, *in vivo* detector was positioned into the vaginal cavity of the patient for real-time *in vivo* dose measurements. The temperature of the patient’s body is recorded. Verification of patient’s treatment setup under Linac was checked with camera-based EPID (iViewC). A 3 mm margin of translational (x, y, and z) errors was permitted and appropriate couch changes were applied as needed. Once the treatment setup is verified, the transit stand is fixed at the level of EPID. The fixation of the stand (with FC65 ionization chamber in transit position) at the level of EPID of the Linac is well explained in our earlier work by Putha *et al.*^[3]

Both the chambers (i.e., FC65 [*transit*] and CC13 [*in vivo*]) were connected to the Dose2 electrometer in channel 1 and 2, respectively. The scheduled treatment plan was executed on the patient. With this measurement setup, chamber readings in nano Coulombs were recorded simultaneously during real-time treatment delivery. The readings of the detector (CC13) are converted to absorbed dose by incorporating necessary correction factors (calibration factor, body temperature, pressure, polarity, beam quality, and saturation) at chamber location, designated as *in vivo* dose (i.e., “ $D_{in vivo}$ ”). The chamber reading obtained from FC65 (transit signal) is used to estimate the mid-plane dose at isocenter (i.e., $D_{iso, Transit}$) using the method described by Putha *et al.*^[3] This procedure was repeated at least 3–4 times with a gap of 3–4 fractions during the remaining course of treatment. The measured value of *in vivo* dose, i.e., $D_{in vivo}$, is correlated with the value obtained from TPS i.e., $D_{in vivo, TPS}$. Figure 1 shows the position of CC13 ionization chamber with contour inside the patient’s body in transverse, coronal, and sagittal sections of CMS XiO TPS. The Figure 2a and 2b shows the anterior conformal RT field in a patient (in supine position) with Coronal and Transverse planes where the estimates of mid-plane dose through transit signal with FC65

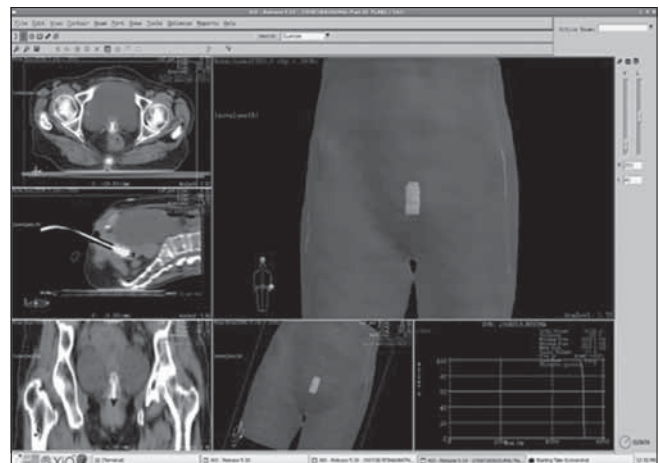


Figure 1: Position of CC13 ionization chamber with contour inside the patient’s body in transverse, coronal, and sagittal sections of CMS XiO TPS

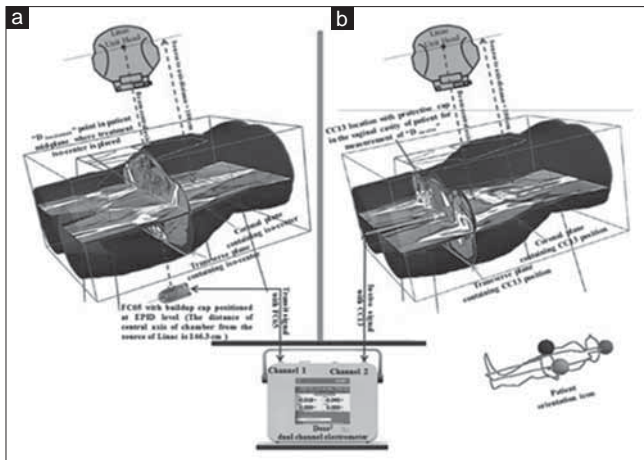


Figure 2: (a and b) Represents the perspective views of anterior field of three-dimensional conformal radiotherapy treatment to the pelvic site of a patient under linac, showing the transverse and coronal planes containing (a) the treatment isocenter for estimation of transit mid-plane dose ($D_{iso, transit}$) through transit signal obtained from FC65 chamber with buildup cap, which was kept at EPID level, and (b) the location of CC13 chamber (with protective cap) in vaginal cavity for measurement of " $D_{in vivo}$ ". Both the measurements were done simultaneously with chambers during real-time treatment delivery, for all four conformal fields (0° , 90° , 180° , and 270°) on at least 3–5 occasions (after having taken the repeat computerized tomography) during the course of treatment. Chambers' signals were measured with "Dose2" dual channel electrometer. The lower right side of the figure represents the patient orientation icon for treatment

(i.e., *Diso*, Transit) and *in vivo* dose measurement with CC13 (i.e., *Din vivo*), respectively, by dual-channel electrometer is obtained.

RESULTS

Table 1 outlines the TPS reference doses correlated to the measured doses by the both (*in vivo* [$D_{in vivo}$] and transit [$D_{iso, Transit}$]) methods. Last four columns compare the agreement of delivered dose, confirmed by these two methods. In Figure 3a-d, the percentage deviations of measured *in vivo* and estimated mid-plane dose through transit signal as against TPS planned dose for 6 patients can be seen. The variations in *in vivo* measurements from these two described methods differed with TPS doses with a mean deviation in the range $-4.4 \pm 1.1\%$ (min) to $-0.3 \pm 2.0\%$ (max) and $-4.0 \pm 1.7\%$ (min) to $1.9 \pm 2.4\%$ (max) for $D_{in vivo}$ and $D_{iso, Transit}$, respectively. Transit dose estimates appear to give more nearer estimates than *in situ* doses, as not much variation due to tissue involuntary motion encountered with dosimeter placed outside.

DISCUSSION

It is easier to implement the *in vivo* dosimetry in sites with regular body contours such as the pelvis and for simple techniques not involving high-dose gradients. In a coordinated research project initiated by IAEA, the importance of exit/transit dosimetry is highlighted, though the entrance dose measurements detect most of the human errors in treatment

setup and error in the treatment equipment, but they could not account for inaccuracies taking place owing to morphological changes in the patients.^[1]

Srinivas *et al.*^[4,16] studied the *in vivo* dose measurements in the vaginal cavity by inserting the different detectors. An ion chamber (0.6 cc Farmer type with protective cap) in 12 cervical carcinoma patients undergoing 3DCRT^[16] treatment to the pelvic site demonstrated good agreement between planned vs prescribed dose which was within 3%.

Wertz *et al.*^[14] showed the feasibility to verify the actual dose measured with a small ionization chamber directly inserted in the rectum of eight patients, during the treatment for prostate with IMRT technique, and compared with TPS calculated values. In one patient, undergoing full pelvic treatment, the dose measurements in a homogeneous high-dose area resulted in a very small dose deviation between the measured and calculated doses. The mean deviation (\pm standard deviation) of $0.1\% \pm 2.1\%$ relative to isocenter was reported in their study.

Goldenberg *et al.*^[13] has compared the *in vivo* dose (in the esophageal region) measured with an ionization chamber (the signal was corrected with the temperature of the body) with transit dose in the same patients and found it to be within 3%. In a clinical application of *in vivo* dosimetry system used for transmission dosimetry, applied on 11 patients who were treated for the pelvic site, with and without bone correction done in TPS,^[22] the mean errors were between -5.20% and $+2.20\%$ for anteroposterior–posteroanterior without bone correction and between -0.62% and $+3.32\%$ with bone correction. For lateral fields, the mean errors were between -10.80% and $+3.46\%$ without bone correction and between -0.55% and $+3.50\%$ with bone correction. It was brought out that the transmission method is a useful form of *in vivo* dosimetry because of non-invasiveness and simplicity with no additional efforts. The above authors emphasized that if bone corrections are not applied, the variation in transmission measurement can be as much as 10%. Even without any patient involved, their dosimetry variation of output was 2% over the course of patient treatments. The algorithm used in our study takes care of the in-homogeneity corrections in TPS.

In two recent publications, dealing with 24 pelvic^[16] and 13 thorax^[20] patients undergoing 3DCRT, the role of transit dosimetry was highlighted in estimating the mid-plane doses using ionization chamber kept at EPID level. The percentage deviation in estimated doses against TPS values was $-1.37\% \pm 2.03$ and $-0.73\% \pm 2.09$, respectively. They also conducted simultaneous measurements with two ionization chambers (one kept at the mid-plane level and other one kept at EPID level) on locally fabricated pelvic and thorax phantoms: Measured/estimated values correlated well with TPS values. The mean percentage deviation of $D_{iso, Transit}$ with $D_{iso, TPS}$ and $D_{iso, mid}$ combined from all fields treated was 0.9 and 0.4% 2.7 and -2.6% , with the pelvic and thorax phantom, respectively.

In this study, we have reported only six patients' data. Our earlier work^[16] brought out the efficacy of on-line collection of

Table 1: Comparison of estimated transit mid-plane and in-vivo doses for treatment planning system reference dose

Patient ID	Measurement number	Fraction number	In-vivo method			Transit method			% Deviation		
			D _{In-vivo, TPS} in cGy	D _{In-vivo} in cGy	D _{In-vivo, TPS} in cGy	D _{Iso, TPS} in cGy	D _{Iso, Transit} in cGy	D _{In-vivo} versus D _{Iso, TPS}	D _{Iso, Transit} versus D _{Iso, TPS}	Mean±SD	Mean±SD
278/18	1	18	136.6	140.8	143.9	145.5	143.9	-3.1	-2.6±0.6	1.1	0.2±1.2
	2	21		139.2	144.7		144.7	-1.8		0.6	
	3	23		140.6	147.4		147.4	-2.8		-1.2	
286/18	1	11	203.4	200.9	201.0	203.6	201.0	1.3	-2.2±2.5	1.3	0.1±0.9
	2	14		208.8	203.1		203.1	-2.6		0.3	
	3	16		212.9	204.7		204.7	-4.4		-0.5	
	4	22		209.9	204.7		204.7	-3.1		-0.5	
292/18	1	11	207.0	204.9	192.4	202.0	192.4	1.0	-0.3±2.0	5.0	1.9±2.4
	2	14		203.8	196.9		196.9	1.6		2.6	
	3	17		212.7	203.4		203.4	-2.7		-0.7	
	4	21		209.5	200.3		200.3	-1.2		0.8	
312/18	1	6	200.9	-	204.5	204.1	204.5	-	-2.0±1.2	-0.2	-1.8±2.0
	2	8		-	204.9		204.9	-		-0.4	
	3	11		203.1	206.0		206.0	-1.1		-0.9	
	4	16		202.4	204.5		204.5	-0.8		-0.2	
334/18	5	20		206.6	214.1		214.1	-2.8		-4.7	
	6	23		207.7	207.0		207.0	-3.3		-1.4	
	1	3	208.8	-	210.6	204.8	210.6	-	-1.5±1.4	-2.7	-4.0±1.7
	2	5		-	210.4		210.4	-		-2.7	
	3	8		-	208.7		208.7	-		-1.9	
	4	13		209.9	209.2		209.2	-0.5		-2.1	
348/18	5	18		215.4	214.6		214.6	-3.1		-4.6	
	6	22		210.5	216.5		216.5	-0.8		-5.4	
	1	3	151.1		164.2	163.1	164.2	-	-4.4±1.1	-0.6	-1.7±1.1
	2	5			168.0		168.0	-		-2.9	
	3	8			167.1		167.1	-		-2.4	
	4	12		158.1	166.8		166.8	-4.4		-2.2	
	5	15		160.7	167.7		167.7	-6.0*		-2.7	
	6	18		157.0	164.2		164.2	-3.8		-0.6	
	7	21		156.7	164.0		164.0	-3.6		-0.5	

*Slightly excess deviation was due to setup error in lateral fields. Following are the abbreviations used in the table: "D_{In-vivo}"=Dose (in cGy) measured through CC13 chamber while actual 3DCRT treatment is going on, "D_{Iso, TPS}"=Mean dose (in cGy) to the chamber volume obtained from DVH of 3DCRT plan of particular patient from TPS, "D_{Iso, Transit}"=Estimated dose (in cGy) at iso-center through transit signal obtained from FC65 chamber while actual 3DCRT treatment is going on, "D_{Iso, TPS}"=Dose (in cGy) calculated by TPS at isocenter. SD: Standard deviation, DVH: Dose-volume histogram

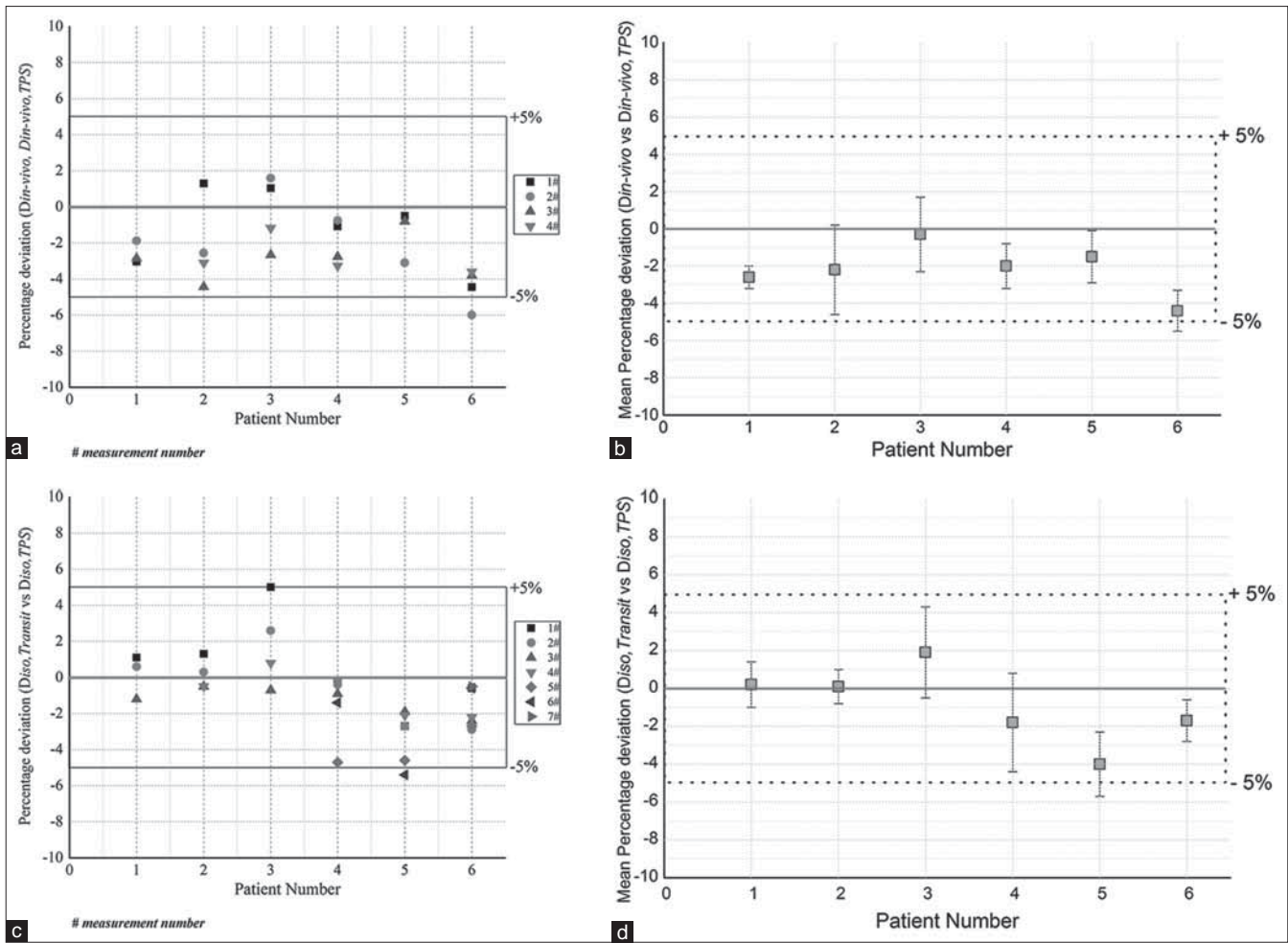


Figure 3: (a) Percentage deviation $D_{in\ vivo}$ vs $D_{in\ vivo, TPS}$ of six patients taken through *in vivo* measurements. (b) Mean percentage deviation of $D_{in\ vivo}$ vs $D_{in\ vivo, TPS}$ of six patients taken through *in vivo* measurements. (c) Percentage deviation $D_{Iso-Transit}$ vs $D_{Iso, TPS}$ of six patients taken through transit signal. (d) Mean percentage deviation of $D_{Iso-Transit}$ vs $D_{Iso, TPS}$ of six patients taken through transit signal measurements

signal during the actual treatment delivery. In our department, we treat more number of cancer cervix patients with radical treatment plans. As we knew the accuracy of our method, we wanted to correlate to *in vivo* dose estimates in the PTV region. Therefore, our physician co-authors felt that six patients are a sufficient number to validate the accuracy of this method. A beam therapy dosimeter based on “ion chamber measurement” gives more confidence to the inference. The measurement of *in vivo* dose and estimation of mid-plane dose simultaneously by means of two ionization chambers may be possible in busy departments as a QA measure at least in protocol patients.

CONCLUSION

The efficacy of this transit dose estimation method is simultaneous validation of the delivered dose in real time. This will enable any corrective actions (if any) that may be applied during subsequent fraction of radiotherapy. Our presentation correlated the confidence limit on the transit dosimetry, with a simultaneous estimate of true dose “*in situ*” of the tumor. The

transit dosimetry method can be routinely applied in clinical dosimetry because the present work has validated the estimated patient dose “*in situ*” simultaneously with “transit method with dosimeter outside.” As the patient does not have any detector, there is no inconvenience to the patients.

Acknowledgments

The authors would like to acknowledge all patients who participated and cooperated in this study. Authors thankfully acknowledge and appreciate the support & involvement of Mr. Prastuth and Ms. Sneha Abraham (Intern students of BSC RTT) during this study.

Financial support and sponsorship

Nil.

Conflicts of interest

There are no conflicts of interest.

REFERENCES

1. Human I, Series H. Development of procedures for *in vivo* dosimetry in radiotherapy. IAEA Human Health Reports 2013;8:1-195.

2. Nijsten SM, Mijnheer BJ, Dekker AL, Lambin P, Mincken AW. Routine individualised patient dosimetry using electronic portal imaging devices. *Radiother Oncol* 2007;83:65-75.
3. Putha SK, Saxena PU, Banerjee S, Srinivas C, Vadhiraja BM, Ravichandran R, *et al.* On-line estimations of delivered radiation doses in three-dimensional conformal radiotherapy treatments of carcinoma uterine cervix patients in linear accelerator. *J Med Phys* 2016;41:224-33.
4. Srinivas C, Shenoy KK, Dinesh M, Savitha KS, Kasturi DP, Supe S, *et al.* *In vivo* dosimetric study of carcinoma of uterine cervix with FBX solution in external beam therapy. *J Med Phys* 1999;24:47-50.
5. Mans A, Wendling M, McDermott LN, Sonke JJ, Tielenburg R, Vijlbrief R, *et al.* Catching errors with *in vivo* EPID dosimetry. *Med Phys* 2010;37:2638-44.
6. Galvin JM, Ezzell G, Eisbrauch A, Yu C, Butler B, Xiao Y, *et al.* Implementing IMRT in clinical practice: A joint document of the American Society for Therapeutic Radiology and Oncology and the American Association of Physicists in Medicine. *Int J Radiat Oncol Biol Phys* 2004;58:1616-34.
7. Mijnheer B. State of the art of *in vivo* dosimetry. *Radiat Prot Dosimetry* 2008;131:117-22.
8. Low DA, Moran JM, Dempsey JF, Dong L, Oldham M. Dosimetry tools and techniques for IMRT. *Med Phys* 2011;38:1313-38.
9. Dong L, Antolak J, Salehpour M, Forster K, O'Neill L, Kendall R, *et al.* Patient-specific point dose measurement for IMRT monitor unit verification. *Int J Radiat Oncol Biol Phys* 2003;56:867-77.
10. Srinivas C, Shenoy KK, Shetty J, Solomon JGR, Ravichandran R, Supe S, *et al.* *In vivo* dosimetry: Confirmation of dose delivery through transit dose measurements in carcinoma of uterine cervix patients undergoing teletherapy. *J Med Phys* 2004;29:177-78.
11. Mijnheer B, Georg D. Guidelines for the Verification of IMRT, ESTRO Booklet 9, Brussels: ESTRO; 2008.
12. Xia P, Verhey LJ. "Intensity modulated radiation therapy," *The Modern Technology of Radiation Oncology: A Compendium for Medical Physicists and Radiation Oncologists*. 2nd ed. Madison, WI: Medical Physics Publishing; 2005.
13. Goldenberg DB, Rao UV, Lott S, Digel J. Dosimetric considerations in cobalt 60 rotational therapy for esophageal lesions. A comparison of transit and intraluminal dose measurement. *Am J Roentgenol Radium Ther Nucl Med* 1969;105:518-22.
14. Wertz H, Boda-Heggemann J, Walter C, Dobler B, Mai S, Wenz F, *et al.* Image-guided *in vivo* dosimetry for quality assurance of IMRT treatment for prostate cancer. *Int J Radiat Oncol Biol Phys* 2007;67:288-95.
15. Walter C, Boda-Heggemann J, Wertz H, Loeb I, Rahn A, Lohr F, *et al.* Phantom and *in-vivo* measurements of dose exposure by image-guided radiotherapy (IGRT): MV portal images vs. kV portal images vs. cone-beam CT. *Radiother Oncol* 2007;85:418-23.
16. Srinivas C, Kumar PS, Ravichandran R, Banerjee S, Saxena PU, Kumar ES, *et al.* Dose verification in carcinoma of uterine cervix patients undergoing 3D conformal radiotherapy with Farmer type ion chamber. *J Med Phys* 2014;39:247-50.
17. Piermattei A, Grimaldi L, D'Onofrio G, Cilla S, Viola P, Craus M, *et al.* *In-vivo* portal dosimetry by an ionization chamber. *Phys Med* 2005;21:143-52.
18. Piermattei A, Fidanzio A, Stimato G, Azario L, Grimaldi L, D'Onofrio G, *et al.* *In vivo* dosimetry by an aSi-based EPID. *Med Phys* 2006;33:4414-22.
19. Piermattei A, Fidanzio A, Azario L, Grimaldi L, D'Onofrio G, Cilla S, *et al.* Application of a practical method for the isocenter point *in vivo* dosimetry by a transit signal. *Phys Med Biol* 2007;52:5101-17.
20. Kumar PS, Banerjee S, Arun Kumar ES, Srinivas C, Vadhiraja BM, Saxena PU, *et al.* *In vivo* dose estimations through transit signal measured with thimble chamber positioned along the central axis at electronic portal imaging device level in medical linear accelerator in carcinoma of the middle-third esophagus patients undergoing three-dimensional conformal radiotherapy. *J Cancer Res Ther* 2018;14:300-7.
21. IAEA. Absorbed Dose Determination in External Beam Radiotherapy. Technical Report Series TRS 398. Vienna: International Atomic Energy Agency; 2000.
22. Kim BK, Chie EK, Huh SN, Lee HK, Ha SW. Clinical application of *in vivo* dosimetry system in radiotherapy of pelvis. *J Radiat Prot Res* 2002;27:37-49.

Revision in Standard Operating Procedures of Radiation Oncology Department and Quality Assurance Schedule under COVID-19 Pandemic

Sir,

Epidemic diseases affecting substantial population of the world is not new and the list of epidemics and pandemics are reported as early as 429 BC.^[1] A pandemic is defined as “an epidemic occurring worldwide, or over a wide area, crossing international boundaries and usually affecting a large population.” In late December 2019, China reported cases of patients with pneumonia of unknown etiology which was classified as epidemic and later upgraded as pandemic. The virus was previously known as “2019 novel coronavirus” and the disease it caused is named as coronavirus disease (COVID-19) which appears to be of zoonotic origin.^[2] The World Health Organization (WHO) raised a global alert on the need of containment, surveillance, detection, isolation, and contact tracing.^[3] Countries across the world responded to this unprecedented pandemic by harsh containment measures. The Indian government responded with the invocation of Disaster Management Act and Epidemic Diseases Act; closing the entire establishment except essential services on March 24, 2020, which was termed as lockdown.

The outbreak of COVID-19 has provided many fold challenges for Radiation Oncology Department worldwide as the treatment is scheduled over weeks (typically 5–7 weeks). It was interesting to study the reported radiotherapy precautions from the Chinese experience,^[4,5] where the outbreak was severe. Personnel-protective equipment (PPE) was provided to the selected staffs of Radiation Oncology Department according to hospital infection control policy for droplet precautions as recommended by the WHO.^[6] Patients were required to wear a surgical mask for the entire duration of the radiation oncology procedure, and the mask was especially required for head and neck patients. Italian experiences have also been reported where the prevention of infection spread has been given sufficient weightage, but infection control measures for radiotherapy accessories have not been discussed.^[7] The impacts of corona pandemic have also been reported from the USA and Europe.^[8,9] The USA report discussed the various measures adopted for controlling the infection while the report of Europe is summary of a questionnaire-based survey conducted to know the influence of the pandemic on the practice of radiotherapy. However, the specific information pertaining to change in the practice for quality assurance (QA), treatment planning, dosimetry, overall workflow for existing and new patients, and policy for managing the gap in the treatment are missing from these publications. It is true that the overall philosophy of radiotherapy practice will remain the same, but

technical and operational aspects of the Radiation Oncology Department need to be revised for controlling the infection to patient, public, staff, equipment, and the environment.

The unfolding events warranted our hospital administration to respond to any eventual emergency. Since many cancer patients are already immunocompromised, the radiation oncology department required to revise the standard operating procedure (SOP) for the continuation of treatment under the COVID-19 situation. Being an international and national accredited hospital, the protocols and guidelines are in place with regard to general infection control in our hospital. However, the unprecedented situation of this pandemic warranted formulation of specific operational guidelines for radiation oncology practice based on the principle of the prevention of COVID-19 infection and lockdown situation. A committee of the radiation oncology department discussed the issue in detail and consensus was arrived to formulate the guidelines covering complete workflow, including technical and administrative aspects for the inclusion in SOP. Specifically, it was decided to revise the SOP of the radiation oncology department by including components on (i) Staff education and safety, (ii) Patient education and safety, (iii) Safe handling of radiotherapy accessories, and (iv) QA/quality control (QC) schedules. As the revision in SOP is linked with equipment, personnel and practices, a brief introduction of the infrastructure of radiation oncology department of the hospital will add clarity in subsequent discussions.

Our radiation oncology department is equipped with flattening filter free (FFF) TrueBeam STx Linear accelerator (Varian Medical System, USA) having photon energies of 6, 10, 15, 6FFF, and 10FFF MV and electron energies of 6, 9, 12, and 15 MeV. The department has active stereotactic treatment program aided by HD120 multileaf collimator (MLC) and ExacTrac X-ray monitoring system (BrainLab AG, Germany) for noncoplanar imaging. Brachytherapy treatments are performed with 18 channel microSelectron high-dose rate (HDR) (Elekta AB, Sweden). On an average, 50–55 patients receive treatment daily. Staffs of radiation oncology department includes 3 full-time radiation oncologists, 2 medical physicists (MPs), 4 radiation therapy technologists (RTTs), 2 nurses, and 2 patient attenders. While formulating the guidelines for inclusion in SOP, the recommendations of individual, institutional, and professional societies were given due considerations.^[4-11] Following are the brief descriptions of the

additional components included in the SOP of the radiation oncology department and their implementation aspects:

Since COVID-19 has incubation period of 5–14 days,^[12] it was recommended to use PPE while treating patients who may or may not be symptomatic. National and international recommendations are followed regarding the use of mask and PPE during the treatment and disposal thereafter.^[13–15] As the primary mode of COVID-19 transmission is through droplets, universal precaution for droplet transmission was identified and the staffs of the department were educated accordingly (hand hygiene; respiratory hygiene; avoid touching eyes, nose and mouth; and judicious use of PPE). In addition, staffs were specially advised to have minimal interaction with the patients. Grouping and rotation of staffs without affecting the efficiency of the department were also incorporated in the SOP. For example, in place of 2 MPs and 4 RTTs, 1 MP, and 2 RTTs will only be available at a time. Further as a matter of policy, treatment by hypofractionation in case of new patients, wherever clinically applicable, is given preference over long duration fractionated treatments. Unless otherwise necessary, brachytherapy treatments (both low and HDRs; temporary or permanent implants) should not be prescribed as it requires long duration dealing with the patients.

The patients were educated for COVID-19 infection mode and infection control measures. Seating arrangement in the waiting area was made to have at least 1 m distance between two patients. The chairs are frequently cleaned with 5% sodium hypochlorite solution. The major source of infection for patients or staff is through contact with radiotherapy accessories. Since most of the accessories are reused for patients over treatment period, frequent cleaning and disinfection were important to control cross contamination. In general, thermoplastic masks are used for the treatment site of brain and head and neck cancers. The masks in use are equipped with nonstick surface coating with antibacterial properties. Guidelines from manufacturer were considered and suggestions from infection control team of the hospital were incorporated (e.g., disinfect the masks before use with alcohol-based disinfectant, wipe the inner and outer surface with sufficient amount of solution, and disinfect the mask after use with 0.5% sodium hypochlorite solution). Head and neck patients or patients having excess mucous secretion were required to wear either a surgical or N95 mask for the entire duration of the radiation oncology procedure (starting from imaging to treatment delivery).

Head support, base plate, armrest, breast board, and any other accessory are wiped after every use with 70% alcohol-based disinfectant. Vacuum cushions were used for the treatment site of thorax, breast, abdomen, and pelvis treatment sites. Each cushion contains small polystyrene spheres surrounded by a durable polyurethane coated nylon fabric. Since these cushions may not directly come into droplet contact, large size paper towel were placed over the cushions. The treatment couch was disinfected after each use with 0.5% sodium hypochlorite solution.

QA/QC of the radiotherapy equipment and accessories is an important component of quality radiotherapy practice. Our QC programme for the accelerator is based on AAPM TG142^[16] and IAEA TRS398^[17] recommendations. However, the list of QA test parameters recommended by AAPM TG142 is quite long requiring revision in existing QA schedule for this period without compromising the quality of performance. This revision in QA schedule is required because of the reduction in human resources due to grouping and rotation. A thorough study of the past performance of the accelerator was carried out and performance results of last 600 measurements were analyzed. Table 1 presents the list of test parameters and their maximum deviation from the baseline value in the last 600 measurements.

It is observed from this table that the deviations are well within the limit all the time which provided us the confidence that even if these tests were eliminated from the QA schedule for a limited period, it will not affect the performance of the accelerator. Accordingly, QA schedule of the accelerator was revised [Table 2] to minimize the resources required for conducting QA/QC on periodic basis.

Some of the monthly tests recommended in AAPM TG142 report were skipped as most of our treatments are IMRT/VMAT. The tolerance levels for laser and optical distance indicator are relaxed because majority of patients were treated under image guidance. MLC QA has been reduced because pretreatment QA for IMRT/VMAT patients is the mandatory requirement as quality service policy of the department. The pretreatment QA is staggered over a week and any failure is considered as potential deterioration of MLC performance. Image quality tests were skipped till the images are suitable for localization. The method of quadratic summation to set the tolerance values to achieve an overall uncertainty of 5% and 5 mm was further refined in AAPM TG142 report. We hope to achieve the tolerance of 5% and 5 mm with recommended tests and frequency. AAPM TG142 allows flexibility in the QA/QC program considering the quality, costs, equipment condition, available test equipment, and institutional needs. Daily/weekly tests can affect dose to the patient and were

Table 1: Test parameters of medical electron linear accelerator and their maximum deviation in last 600 measurements

Test parameters	Maximum deviation from baseline
Output constancy (X-rays) (%)	3.0
Beam uniformity (%)	2.8
Jaw position indicators (mm)	0.1
MLC leaf position accuracy (mm)	0.14
Gantry/collimator indicator (degree)	0.1
Shift in isocenter (mm)	0.37
kV/MV isocenter displacement (mm)	0.16
Couch displacement in lateral/longitudinal/vertical (mm)	0.30

MLC: Multileaf collimator

Table 2: Revised quality assurance/quality control schedule for medical electron linear accelerator along with recommended tolerance, test frequency, and personnel required

Test parameters	Method/instrument	Prescribed tolerance	Recommended tolerance	Test frequency	Personnel required
Dosimetry					
X-ray output constancy	MPC ^[18]	3%	3% (5% AL)	Daily	1
Electron output constancy	MPC	3%	3% (5% AL)	Daily	1
Reference dosimetry	Ion chamber and water phantom	3%	3%	Weekly	2
X-ray profile constancy	MPC	3%	3% (5% AL)	Monthly	1
Electron profile constancy	MPC	3%	3% (5% AL)	Monthly	1
Mechanical					
Laser localization	MPC phantom and couch value	1.5 mm	2 mm (3 mm AL)	Daily	1
ODI	Couch value indicator (vertical=0)	2 mm	2 mm (3 mm AL)	Daily	1
Collimator size indicator	Radiological image based	2 mm	4 mm	Daily	1
Safety					
Door interlock	During MPC	Functional	Functional	Daily	1
Door closing safety	During MPC	Functional	Functional	Daily	1
Audiovisual monitors	During MPC	Functional	Functional	Daily	1
Beam on indicator	During MPC	Functional	Functional	Daily	1
Laser guard interlock test	MPC Phantom	Functional	Functional	Weekly	1
Respiratory gating	-	Functional	Functional	Patient based	1
MLC	Skip, if patient specific QA is carried out (5%/5 mm AL)				1
Imaging					
Collision test	Software restriction	Functional	Functional	Daily/skip	1
Image quality	Perform calibration if image quality is degraded				1

ODI: Optical distance indicator, MPC: Machine performance check, which is an automated and integrated image-based tool for the verification of beam and geometric performance of the TrueBeam, AL: Action level, QA: Quality assurance

carefully tested maintaining minimum standard. Monthly tests include those parameters that have lower likelihood of changing over a month, hence were carefully chosen considering likelihood that this pandemic may be over in next few months. The reference dose measurement and patient specific QA are directly linked with precision and accuracy of treatment delivery (may affect treatment outcome drastically) and hence their measurement frequency were left unchanged. However, care should be taken that minimum personnel are involved, and the safe infection control policy is adhered to. Action levels are specifically mentioned keeping in mind that rectification of the fault may not be possible immediately as engineer movements are also restricted. Hence, we may need to continue treatment even though specific test breaches threshold tolerance and would be mitigated by increasing planning target volume and planning risk volume margins. We have tried to balance minimum standards of QA with infection control aspects. Notable limitation in the QA schedule is the MPC^[18] based tests which is exclusive feature of TrueBeam accelerator.

Since our hospital is a multi-specialty healthcare unit with national and international accreditation, we have infection control policy in place. This provision may not be available in stand-alone centers, and hence, the operational procedures outlined here may serve the purpose to mitigate the operational challenges faced with continuation of radiotherapy treatment in such centers. Further, the operational procedures and QA schedules discussed in this letter are consistent with

droplet precautions policy which has been discussed in various reports.^[4-11] However, we have made an effort to make COVID-19 specific guidelines following the radiation protection principle of time, distance, and shielding. Accordingly, the message is spend minimum time by cutting down nonessential physical meetings/interactions, adhere to social distancing, and use PPE judiciously.

Financial support and sponsorship

Nil.

Conflicts of interest

There are no conflicts of interest.

Suresh Chaudhari, Sunil Dutt Sharma¹, Shyam Kishore Shrivastava

Department of Radiation Oncology, Apollo Hospitals, Navi Mumbai,

¹Radiological Physics and Advisory Division, Bhabha Atomic Research Centre, Mumbai, Maharashtra, India

Address for correspondence: Mr. Suresh Chaudhari, Department of Radiation Oncology, Apollo Hospitals, Plot #13, Parsik Hill Road, Off Uran Road, Sector - 23, CBD Belapur, Opp. Nerul Wonders Park, Navi Mumbai - 400 614, Maharashtra, India.
E-mail: chaudhari_suresh@yahoo.com

Received on: 18-05-2020 Review completed on: 23-05-2020

Accepted on: 06-06-2020 Published on: 20-07-2020

REFERENCES

1. List of Pandemics. Available from: https://en.wikipedia.org/wiki/List_of_epidemics_and_pandemics. [Last accessed on 2020 May 10].

2. Lu H, Stratton CW, Tang YW. Outbreak of pneumonia of unknown etiology in Wuhan, China: The mystery and the miracle. *J Med Virol* 2020;92:401-2.
3. Sohrabi C, Alsaf Z, O'Neill N, Khan M, Kerwan A, Al-Jabir A, *et al.* *International Journal of Surgery* 2020;76:71-6.
4. Tarentino AL, Maley F. A comparison of the substrate specificities of endo-beta-N-acetylglucosaminidases from *Streptomyces griseus* and *Diplococcus Pneumoniae*. *Biochem Biophys Res Commun* 1975;67:455-62.
5. Wei W, Zheng D, Lei Y, Wu S, Verma V, Liu Y, *et al.* Radiotherapy Workflow and Protection Procedures During the Coronavirus Disease 2019 (COVID-19) Outbreak: Experience of the Hubei Cancer Hospital in Wuhan, China, Radiotherapy and Oncology 2020; doi: <https://doi.org/10.1016/j.radonc.2020.03.029>.
6. World Health Organization. Advice on the use of Masks in the Context of COVID-19 Interim Guidance. World Health Organization; 2020. Available from: https://apps.who.int/iris/bitstream/handle/10665/331693/WHO-2019-nCov-IPC_Masks-2020.3-eng.pdf?sequence=1&isAllowed=y. [Last accessed on 2020 May 11].
7. Krengli M, Ferrara E, Mastroleo F, Brambilla M, Ricardi U. Running a radiation oncology department at the time of coronavirus: an Italian experience. [doi: <https://doi.org/10.1016/j.adro.2020.03.003>].
8. Reuter-Oppermann M, Muller-Polyzou R, Wirtz H, Georgiadis A. Influence of the pandemic dissemination of COVID-19 on radiotherapy practice: A flash survey in Germany, Austria and Switzerland. *PLoS One* 2020;15:e0233330.
9. Rivera A, Ohri N, Thomas E, Miller R, Knoll MA. The impact of COVID-19 on radiation oncology clinics and cancer patients in the US. *Adv Radiat Oncol* 2020. [doi: <https://doi.org/10.1016/j.adro.2020.03.006>].
10. Asia-Oceania Federation of Organizations for Medical Physics. Guidelines on Radiation Oncology Operation During COVID-19; 2020. Available from: <http://afomp.org/wp-content/uploads/2020/05/AFOMP-RT-Guidelines-COVID-19.pdf>. [Last accessed on 2020 May 15].
11. Thomson DJ, Palma D, Guckenberger M. Practice recommendations for risk-adapted head and neck cancer radiation therapy during the COVID-19 pandemic: An ASTRO-ESTRO consensus statement. *Int J Radiat Oncol Biol Phys* 2020. [doi: <https://doi.org/10.1016/j.ijrobp.2020.04.016>].
12. Lauer SA, Grantz KH, Bi Q, Jones FK, Zheng Q, Meredith HR, *et al.* The incubation period of corona virus disease 2019 (COVID-19) from publicly reported confirmed cases: estimation and application. *Ann Intern Med* 2020;172:577-82.
13. Government of India, Ministry of Health and Family Welfare. Guidelines on use of Masks for Health Care Workers, Patients and Members of Public 2020; 2020. Available from: <http://pbhealth.gov.in/Guidelines%20on%20use%20of%20masks%20for%20health%20care%20workers,%20patients%20and%20member%20of%20Public.pdf>. [Last accessed on 2020 May 10].
14. Centers for Disease Control and Prevention. Guideline for Disinfection and Sterilization in Healthcare Facilities. USA: Centers for Disease Control and Prevention; 2008. Available from: <https://www.cdc.gov/infectioncontrol/guidelines/disinfection/index.html>. [Last accessed on 2020 May 10].
15. WHO. Decontamination and Reprocessing of Medical Devices for Healthcare Facilities. WHO; 2020. Available from: <https://www.who.int/infection-prevention/publications/decontamination/en/>. [Last accessed on 2020 May 15].
16. Klein EE, Hanley J, Bayouth J, Yin FF, Simon W, Dresser S, *et al.* Task Group 142 report: Quality assurance of medical accelerators. *Med Phys* 2009;36:4197-212.
17. International Atomic Energy Agency. Absorbed dose Determination in External Beam Radiotherapy. Technical Reports Series 398. Vienna, Austria: IAEA; 2000.
18. Barnes MP, Greer PB. Evaluation of the TrueBeam machine performance check (MPC) beam constancy checks for flattened and flattening filter-free (FFF) photon beams. *J Appl Clin Med Phys* 2017;18:139-50.

This is an open access journal, and articles are distributed under the terms of the Creative Commons Attribution-NonCommercial-ShareAlike 4.0 License, which allows others to remix, tweak, and build upon the work non-commercially, as long as appropriate credit is given and the new creations are licensed under the identical terms.

Access this article online

Quick Response Code:



Website:
www.jmp.org.in

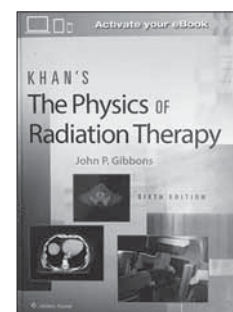
DOI:
10.4103/jmp.JMP_37_20

How to cite this article: Chaudhari S, Sharma SD, Shrivastava SK. Revision in standard operating procedures of radiation oncology department and quality assurance schedule under COVID-19 pandemic. *J Med Phys* 2020;45:130-3.

© 2020 Journal of Medical Physics | Published by Wolters Kluwer - Medknow

Khan's The Physics of Radiation Therapy

Title:	Khan's The Physics of Radiation Therapy
Edition:	Sixth
Editor(s):	
Acquisitions Editor:	Nicole Dernoski
Development Editor:	Sean McGuire
Editorial Coordination:	David Murphy
Author:	Dr. John P. Gibbons
Series Editor (if applicable):	NA
Publisher:	Wolters Kluwer Health
Local Publisher (if applicable):	Wolters Kluwer (India) Pvt. Ltd., New Delhi
Pages:	598
ISBN No (Indian Reprint):	978-93-89335-92-7
Price:	Rs. 11,000/- (Online)
Year:	2019



The Sixth Edition of this classic book entitled, “Khan’s The Physics of Radiation Therapy” was recently published in India by Wolters Kluwer (India) Pvt. Ltd., New Delhi. For the first time since its First Edition in 1984, Dr. Faiz M. Khan, the Principal Author of the Book till the Fifth Edition, is not an active author for the Sixth Edition. Dr. John P. Gibbons, Chief of Physics, Ochsner Health System, New Orleans, Louisiana, USA, who was a coauthor with Dr. Khan for the Fifth Edition of the book published in 2014, is the sole author for the present updated edition.

The book, over three decades of its existence, has established itself as one of the most sought after books among students, as well as seasoned practitioners, of Clinical Medical Physics and Radiation Oncology. In the own words of Dr. Khan, the book, when initially conceptualized, was aimed at fulfilling the needs for a dedicated book on Radiation Therapy Physics with emphasis on practical details. The popularity of the book is evidence enough that it has succeeded in keeping the promise. In the present edition, Dr. Gibbons has updated the content of the book by incorporating newer aspects in dosimetry, Image Guided Radiotherapy (IGRT), Quality Assurance (QA), calculation algorithms, treatment planning, and delivery technology, in addition to minor revision of almost all the chapters. However, the structure of the book has remained similar to the preceding editions.

There are a total of 28 chapters (598 pages) in the book divided into three parts. The first part including eight chapters deals with basic physics; the second part (10 chapters) deals with classical radiation therapy; and the third part (10 chapters) deals with modern radiation therapy techniques. Similar to the preceding editions, the titles of the first eight chapters of this book read as (1) structure of matter, (2) nuclear transformations, (3) production of X-rays, (4) clinical radiation generators, (5) interactions of ionizing radiation,

(6) measurement of ionizing radiation, (7) quality of X-ray beams, and (8) measurement of absorbed dose. All these chapters, understandably, are retained with their original content, except some additions in the eighth chapter dealing with the measurement of absorbed dose. In this Chapter, the addendum to TG-51 dealing with flattening filter-free photon beam dosimetry involving new-quality conversion factors has been discussed. Surprisingly, like the earlier editions of the book, the description of Optically Stimulated Luminescence (OSL) and Metal Oxide Semiconductor Field Effect Transistor (MOSFET) dosimetry continues to be missing in the eighth chapter, despite the fact that most of the other dosimeters, namely calorimeter, chemical dosimeter, Thermoluminescence dosimetry (TLD), silicon diodes, and films, have been discussed in the chapter. Some other chapters in which additional details have been incorporated are as follows: in Chapter 10, the recommendations of TG-71 on normalization depth for Tissue Phantom Ratio (TPR), Tissue Maximum Ratio (TMR), and other dosimetric quantities needed for Monitor Unit (MU) calculations have been included (Section C of the Chapter); in Chapter 17, some additional information related to the failure mode and effects analysis described in TG-100 report has been included in the section describing risk assessment; in Chapter 19, a section (B.3) has been added on discrete ordinates method in the model-based algorithms; in Chapter 26, sections (G and H) dealing with Magnetic Resonance Imaging (MRI) guidance and optical surface imaging technologies that are increasingly coming into clinics have been added. Further, a new chapter, Chapter 28, addressing the issue of knowledge-based planning has been added. This is one of the most evolving fields in Radiotherapy. As a result of the additions, the number of pages in the present edition has gone up slightly from 572 to 598.

The remaining chapters are retained with their original structure and content with minor revisions at some places. These chapters

are as follows: (11) treatment planning I (isodose distributions), (12) treatment planning II (patient data acquisition, treatment verification, and inhomogeneity corrections), (13) treatment planning III (field shaping, skin dose, and field separation), (14) electron beam therapy, (15) Low Dose Rate (LDR) brachytherapy (rules of implantation and dose specifications), (16) radiation protection, (17) quality assurance, (18) total body irradiation, (19) three-dimensional conformal radiotherapy, (20) intensity-modulated radiation therapy, (21) stereotactic radiotherapy and radiosurgery, (22) stereotactic body radiotherapy, (23) High Dose Rate (HDR) brachytherapy, (24) prostate implants: technique, dosimetry, and treatment planning, (25) intravascular brachytherapy, (26) image-guided radiation therapy, and (27) proton beam therapy. In addition, the book continues to provide useful data for ready reference in the Appendix Section for medical physics practitioners and researchers in the form of tables. The Index Section at the end has a list of topics/subtopics in the alphabetical order for ready referencing of the reader.

Overall, the Sixth Edition of this remarkable book is updated thoughtfully to remain as contemporary as ever in a field that is technologically evolving at a rapid pace. At the same time, the book retains its old charm for students and practitioners of Medical Physics and Radiation Oncology. It is printed on a glossy high-quality paper with colorful diagrams and figures that further enhance the reading experience. I believe all students and practicing medical physicists and other


professionals working in the field of Radiotherapy should have a ready access to this seminal book. The online price of the book is Rs 11,000/-.

Manoj Kumar Semwal

Radiation Oncology Centre, Army Hospital (R&R), New Delhi, India

Address for correspondence: Dr. Manoj Kumar Semwal,
Radiation Oncology Centre, Army Hospital (Research and Referral),
Delhi Cantonment, New Delhi, India.
E-mail: manojsemwal@yahoo.co.in

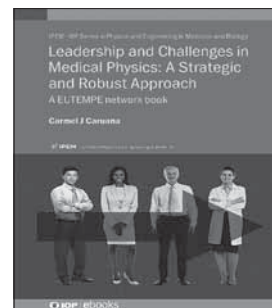
This is an open access journal, and articles are distributed under the terms of the Creative Commons Attribution-NonCommercial-ShareAlike 4.0 License, which allows others to remix, tweak, and build upon the work non-commercially, as long as appropriate credit is given and the new creations are licensed under the identical terms.

Access this article online	
Quick Response Code: 	Website: www.jmp.org.in
	DOI: 10.4103/jmp.JMP_17_20

How to cite this article: Semwal MK. Khan's the physics of radiation therapy. J Med Phys 2020;45:134-5.

Leadership and challenges in medical physics: A strategic and robust approach

Author:	Carmel J Caruana
Edition:	First Edition
Publisher:	Institute of Physics Publishing
ISBN:	978-0-7503-1395-7 (ebook)
ISBN:	978-0-7503-1396-4 (print)
Year of Publication:	2020
DOI:	10.1088 / 978-0-7503-1395-7
Book type:	Educational and Professional
Language:	English
Number of chapters:	10



Medical physics is one of the most challenging and rewarding applications of physics to human health care program and is mainly concerned with the use of ionizing radiation in the diagnosis, therapy, and research in healthcare. Medical physicists working in the clinical environment are health professions as per the International Labor Organization and World Health Organization classification. The environment surrounding healthcare is rapidly evolving, and the technological innovation in the application of radiation in medicine is in fast progress. Medical physicists working in the clinical environment are expected to keep track with the exploding technological development and should have required competency, and therefore, undergo a structured education program and residency. Our exceptional education and training in physics, mathematics, medical devices, radiation, and other physical agents, and information technology has made us what we are today – a highly successful profession that has changed the face of healthcare. As a group, medical physicists are excellent scientists and health-care professionals. On the other hand, our education and training programs provide a little experience in how to deal with the real-world issues facing us when we move from the relative security of our academic physics departments to the realities of modern, large, complex health-care organizations. Therefore, in today's world, being a good medical physicist as health professional is simply not enough to survive and thrive in a multi-professional health-care system where in doctors, nurses, paramedics, administrators, and managers are part of the system; interprofessional teamwork has been reduced from a richly stimulating, intellectually satisfying multiprofessional environment to a battleground where a relatively hostile environment exists, and hence, the strategic and robust leaders are important for all professions, which is true for medical physics profession as well. Conventionally, as a profession we have, and rightly so, given major importance to science and science leadership. Leadership in medical physics is important because without good leadership, clinical or research teams fail to deliver, and

the profession as a group would not develop locally, nationally, regionally, or internationally. On account of the unique services provided by medical physicists, such failures would ultimately result in a degradation of the effectiveness, safety, and efficiency of the patient services. Being in this profession for more than three decades, I have realized how important professional leadership is.

In the past years, we have given greater attention to education and training issues, and one will find many books devoted to education and training of medical physics. The result of low importance given to the professional issues is that we did not have a single book which addresses the issues of leadership or the challenges we face in the profession due to lack of leadership grooming.

It gives me a great pleasure to review the first-ever book on leadership and challenges in medical physics, and I share the author's desire that "the book will stimulate much needed discussion regarding current professional issues and help develop strong strategic leaders for our profession." There is much wisdom in this book, and I am sure many of us who have been involved in the leadership of the profession will recognize many of it as forming part of our own thinking and experience. Being involved in professional activities at various positions in professional organizations, I confess that if such a book would have been available earlier, it would have helped me much more to deliver as a professional leader; nonetheless, it will help in future tasks.

This comprehensive book on leadership in medical physics is compiled by Prof. Carmel J. Caruana and published by the Institute of Physics (IOP) Publishing as a part of "Institute of Physics and Engineering in Medicine–Institute of Physics (IPEM-IOP) Series" in Physics and Engineering in Medicine and Biology. The book very empathetically stresses the difference in leadership and management. According to the authors, the leadership is the process of influencing and motivating others to agree on and work toward an exciting

shared future vision, there is a focus on inspiring others and creating shared organizational culture and values. Managers are employed to get things done by making sure administrative tasks such as planning, organizing, budgeting, quality controlling, staffing, and problem-solving are carried out effectively and without unnecessary waste of resources – the role of a manager is closer to that of an executive officer. The two roles of leadership and management are essential, but they are not the same. According to the author, it is very important to keep in mind that leadership is not administration, and certainly, leadership is not about being a boss. To do this, we need strategic and robust leaders who are well prepared to take on these tasks, which do not only aim to preserve the gains of the past but can push the profession to new heights. However, such leaders need to be educated and trained, and the resources for this simply do not exist. I am hoping that this book will be a first solid attempt at addressing this lacuna in our education and training as a health professional.

In the book, the author has classified four types of intelligence relevant to medical physics leadership, such as analytical, creative, practical, and emotional intelligences.

The book has been divided into ten chapters to deal with various aspects of leadership and strategic planning:

1. Chapter 1: What is strategic and robust leadership, and why is it critical for medical physics in the present environment?
In this chapter, strategic and robust leadership is defined, and its importance for medical physics in a world dominated by austerity economics and interprofessional issues has been discussed. The chapter includes advice on how one can prepare oneself for leadership roles while highlighting that leadership is ultimately a personal journey.
2. Chapter 2: A strategic planning primer for medical physics leaders
In this chapter, strategic planning is described in detail and applied to medical physics. The steps involved in developing, implementing, and evaluating a strategic plan are described. Furthermore, the various types of medical physics groups and teams that one could lead are described in detail and in a very effective manner.
3. Chapter 3: Internal STRENGTHS of medical physics
In this chapter, one finds an inventory of the main strengths of medical physics and their importance for strategic planning. The chapter deals advantages to be a clinical medical physicist, the environment he/she works in, and how he/she can use the situation to strengthen and portray the contribution and importance of medical physics to health-care delivery system.
4. Chapter 4: Internal WEAKNESSES of medical physics
This chapter presents a detailed discussion of the main weaknesses of medical physics and emphasizes on identifying, understanding, and rectifying. The author discusses the medical physics profession and compares the number of medical physicists with the number of nurses and doctors in the hospital/institute. Medical physicist's number is very small as compared to others.
5. Chapter 5: External environmental OPPORTUNITIES for medical physics
In this chapter, there is a detailed discussion of the main opportunities available for the further development of medical physics, and it explains that the key opportunities are those opportunities with a higher benefit value.
6. Chapter 6: External environmental THREATS for medical physics
This chapter presents the main threats and challenges to the development of medical physics. The author emphasizes that such threats should be countered in the same manner that physicists counter all other problems: they should be acknowledged, researched, analyzed, addressed, and eliminated. In a hospital environment, there are attempts of dominance by other professionals and due to their number, powerful union, and influence the management, which can be detrimental to medical physics professionals.
7. Chapter 7: Healthy leadership and leadership styles
This chapter presents the current view of what in the long run makes a leader successful. The various leadership styles are presented, and the application of their use in the different stages of the development of a project team is discussed in this chapter.
8. Chapter 8: Organizational psychology (also known as occupational psychology)
This chapter discusses organizational psychology and its usefulness for the organization's success by improved performance, job satisfaction, motivation, and well-being and emphasizes that in the health-care system, the medical physics leader needs the knowledge of organizational psychology.
9. Chapter 9: Organizational politics – Learning to play the political game
This chapter discusses organizational politics, and according to the author, organizational politics is inevitable and trying to avoid, it is bad for the group but learn how to survive, it is the best strategy.
10. Chapter 10: Negotiating skills for the medical physics leader
This chapter distinguishes between distributive and integrative negotiation and reminds the reader that negotiation is the part of the problem-solving, part of controlling the egoistic tendencies of others, part of game, and part of luck.

The book narrates the importance of leadership in a multidisciplinary competitive health profession, its influence on growth and recognition of the profession. The book guides a professional medical physicist to prepare oneself for leadership with a quote “leadership is a personal journey.” This book is not a textbook, but a useful and unique reference book designed to guide to develop leadership skills. However, the book lacks in illustrations, flowcharts for quick understanding, and the language is bit tricky to understand.

Arun Chougule

Senior Professor and Head, Department of Radiological Physics,
SMS Medical College, Rajasthan, India

I recommend this book a must read for postgraduate students, medical physicists, and educators in this profession.

About the author: Prof. Carmel Caruana.

The author is well known both in Europe and internationally and well placed to write about the topic. At present, Prof. Carmel J. Caruana is heading the Medical Physics Department at the Faculty of Health Sciences, University of Malta. In Malta, he has guided the development of the medical physics profession from a situation when it was totally unknown. As chair of the EFOMP Education and Training Committee, he has contributed to the development of European Guidelines on the Medical Physics Expert and policy documents. As EFOMP representative, he contributed to EU projects such as MEDRAPET, EUTEMPE, and ENETRAP. His experience has helped the development of International Medical Physics Certification Board guidelines. He has set up, under the auspices of EUTEMPE and EFOMP, the first-ever comprehensive module for leadership in medical physics, which has now been running for over 6 years, a module which has been described as a “Mini-MBA for Medical Physicists.” His vast experience and expertise in medical physics education and training has reflected in the text of the book.

Address for correspondence: Prof. Arun Chougule,

A-1405 SKY Terrace, Shipra Path, Mansarovar, Jaipur - 302 020, Rajasthan, India.

E-mail: arunchougule11@gmail.com

This is an open access journal, and articles are distributed under the terms of the Creative Commons Attribution-NonCommercial-ShareAlike 4.0 License, which allows others to remix, tweak, and build upon the work non-commercially, as long as appropriate credit is given and the new creations are licensed under the identical terms.

Access this article online

Quick Response Code:



Website:

www.jmp.org.in

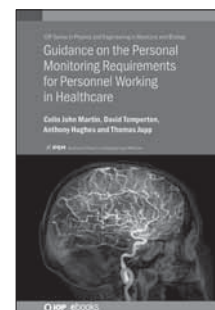
DOI:

10.4103/jmp.JMP_34_20

How to cite this article: Chougule A. Leadership and challenges in medical physics: A strategic and robust approach. J Med Phys 2020;45:136-8.

Guidance on the Personal Monitoring Requirements for Personnel Working in Healthcare

Authors: Colin John Martin, David Temperton, Anthony Hughes, Thomas Jupp
Edition: 20181101
Publisher: IOP Publishing, Bristol, UK
ISBN: ISBN 978-0-7503-2197-6 (print)
 ISBN 978-0-7503-2199-0 (ebook)
Number of Pages: 128
Year of Publication: 2018



This book addresses the needs of radiation workers irrespective of different groups of health professionals working with medical applications of radiation such as in radiodiagnosis, nuclear medicine, and radiation therapy practices. These practices involve exposure to the individual working in the field who need to be monitored periodically to verify their personal doses. Although radiation professionals are well aware of the personal monitoring, they should know how to manage the personal monitoring devices and maintain relevant documents. This book discusses in detail the practice of personal monitoring and the generalized method for predicting dose levels from the workload the facility is handling.

CHAPTER 1: REQUIREMENTS FOR MONITORING RADIATION DOSE

In this chapter, the authors have presented a detailed literature review of various international protocols and guidelines related to monitoring of doses including ICRP and ICRU. As these protocols (ICRP 60 and ICRP 103) do not address in depth about the risk assessment and management, the authors have brought out a detailed procedure for the radiation monitoring of personnel and environment and have explained its relevancy. In addition, the authors have also emphasized on key reasons for carrying out individual personal monitoring.

CHAPTER 2: DOSEMETERS AVAILABLE

This chapter discusses the external and internal dose monitoring in detail. Monitoring of both charged and uncharged particles has been discussed in depth with appropriate detectors of choice. The uses of electronic monitors have been well explained by the authors, and they have also presented few important international standards such as IEC 62387, IEC 61526, and the European Commission Technical Recommendations available for personal monitoring in this chapter.

CHAPTER 3: NUCLEAR MEDICINE

Although the topic of the chapter is a generalized one, it is well written in a structured manner, briefly describing the

dose-monitoring aspects of nuclear medicine applications. Dose monitoring of extremities, eye, and whole body is explained well along with the details of appropriate dosimeters of choice. The authors re-insist that small sources of radiation such as syringe and vial containing radioactive liquid are potential contributors of radiation dose to the fingers. The authors also suggest adopting some principles to draw the radiopharmaceuticals in order to reduce the dose to finger. This chapter gives some useful key points for adopting such protocol. It is important to note the authors' observation that the ring dosimeter underestimates the dose due to high-dose gradient, and hence requires dose correction. The authors explained the dose correction methods, substantiating their observations based on the literature.

CHAPTER 4: DOSIMETRY FOR PERSONNEL WORKING WITH X-RAY EQUIPMENT

This chapter discusses the problems involved in dose monitoring for staff practicing with diagnostic X-rays. The authors had explicitly explained the double dosimeter for body monitoring system. As recommended in the ICRP 2000; 2003, the authors have advised to wear two dosimeters ideally, one either adjacent to the eye or at the collar above the lead aprons, and another underneath the apron, which will be the best option for assessment of the effective dose for highly exposed workers. A number of algorithms have been developed to combine reading from collar and under-apron dosimeter over the years to give a better estimation of effective dose. The authors reported the different algorithms for calculating the effective dose with expression $(E = aH_{ub} + bH_{on})$, where H_{ub} and H_{on} are the personal dose equivalents $H_p(10)$ measured on the body under the apron and at the neck outside the apron, respectively. This chapter attracts more interest of the readers as it deals with the monitoring of the radiation dose to body and eye.

CHAPTER 5: USE OF X-RAYS IN DIAGNOSTIC AND INTERVENTIONAL RADIOLOGY

In this chapter, the authors describe dose-monitoring techniques for a wide range of X-ray units such as X-ray, mammography,

dental, dual-energy X-ray absorptiometry, interventional radiology, cardiology, and computed tomography. In addition, the authors have also explained the recommendation for dose monitoring in orthopedic medicine, endoscopy, and urology applications. This chapter also highlights the importance of training and education regarding personal monitoring to all the health-care professionals involved in the field.

CHAPTER 6: RADIOTHERAPY

This chapter deals with the requirements of personal monitoring in a variety of radiotherapy units such as external beam radiotherapy, brachytherapy (manual and remote after-loading), permanent iodine seed implants, and intraoperative radiotherapy. The authors' simple way of explaining the risk of exposure, such as a nursing staff coming into close contact with the patient for 1 h/day who could receive an effective dose of $\sim 10 \mu\text{Sv}$ per patient over a 48 h period which would translate into an annual dose of 0.5 mSv for a workload of 50 patients/year, is highly appreciable. The authors stress many such situations explaining the seriousness of the requirements of personal monitoring for all individuals.

CHAPTER 7: RISK ASSESSMENTS TO PREDICT LIKELY PERSONAL DOSES

In general dose monitoring, the requirements are based on the risk assessment. This chapter provides detailed information on good practice that needs to be followed to fulfill the requirements of the regulations for ionizing radiation. The authors have tabulated different recommendations regarding various approaches to monitor the dose at different dose levels by quoting the references available in the literature. In this chapter, the authors have referred quite a large number of publications relevant to risk assessment, which deserves wider appreciation. This chapter explains a generalized method for predicting dose levels from workload in detail with a mathematical expression. For all the risk assessment procedures, the authors have described several mathematical expressions in a simple manner.

CHAPTER 8: MANAGING PERSONAL MONITORING

It is very difficult to manage personal monitoring issues in any hospital. Most of the problems arise due to poor cooperation of staff in safe handling and timely return of the monitoring devices, which results in uncertainty in dose evaluation. In

this chapter, the authors have dealt with the management of the missing dosimeter, incidences of unusual dose reading, and overexposures. This chapter will benefit radiation safety officers working in medical institutions, especially the one who is handling the personal monitoring-related issues.

CONCLUDING REMARKS

In general, the book showers in-depth knowledge and is very appropriate for the professionals involved in radiation safety in medical institutions. The importance and safe use of personal monitoring and available choices for health professionals have been explained in detail. This book gives overall information on the available international protocols in a nutshell along with a brief description of personal monitoring procedures in detail. This book will widely attract the attention of radiation professionals for its simplicity and easy-to-understand way of presentation. Overall, the book is well structured with the presentation of chapters in an organized manner. The entire radiation professional will appreciate the authors' efforts in bringing out this excellent document.

K. M. Ganesh

Department of Radiation Physics, Kidwai Memorial Institute of Oncology, Bengaluru, Karnataka, India

Address for correspondence: Dr. K.M. Ganesh,
Department of Radiation Physics, Kidwai Memorial Institute of Oncology,
Bengaluru - 560 029, Karnataka, India.
E-mail: kmganesh1@gmail.com

This is an open access journal, and articles are distributed under the terms of the Creative Commons Attribution-NonCommercial-ShareAlike 4.0 License, which allows others to remix, tweak, and build upon the work non-commercially, as long as appropriate credit is given and the new creations are licensed under the identical terms.

Access this article online	
Quick Response Code: 	Website: www.jmp.org.in
	DOI: 10.4103/jmp.JMP_35_20

How to cite this article: Ganesh KM. Guidance on the personal monitoring requirements for personnel working in healthcare. *J Med Phys* 2020;45:139-40.

Erratum: Superparamagnetic Iron Oxide-C595: Potential MR Imaging Contrast Agents for Ovarian Cancer Detection

The article titled “Superparamagnetic iron oxide-C595: Potential MR imaging contrast agents for ovarian cancer detection”, published in *Journal of Medical Physics* on pages 198-204, Issue 4, Volume 38, 2013 (<https://doi.org/10.4103/0971-6203.121198>).^[1] This article was received on May 21, 2013, accepted for publication on August 20, 2013 and published on Nov 11, 2013.

It was noted that another publication titled ‘Detection of MUC1-Expressing Ovarian Cancer by C595 Monoclonal Antibody-Conjugated SPIONs Using MR Imaging’ was published in *The Scientific World Journal*, Hindawi, Volume 2013 (Article ID 609151, <https://doi.org/10.1155/2013/609151>)^[2] wherein the article is shown to have been received on Aug 5, 2013, accepted for publication on September 1, 2013 and published on Sept 30, 2013. The article in Hindawi is known to have been published under CC-BY license which makes it free to be re-published under allowable modification.

Both articles have been submitted to both journal by same authors. They first submitted their research in *Journal of Medical Physics* and as per their claim, the extension of the same research was published in *The Scientific World Journal*, Hindawi, under CC-BY license.

Thus, this erratum notice is being published to notify the readers about the above.

REFERENCES

1. Shahbazi-Gahrouei D, Abdolahi M. Superparamagnetic iron oxide-C595: Potential MR imaging contrast agents for ovarian cancer detection. *J Med Phys* 2013;38:198-204.
2. Shahbazi-Gahrouei D, Abdolahi M. ‘Detection of MUC1-Expressing Ovarian Cancer by C595 Monoclonal Antibody-Conjugated SPIONs Using MR Imaging. *The Scientific World Journal*, Volume 2013. Article ID 609151 <https://doi.org/10.1155/2013/609151>.

DOI: 10.4103/0971-6203.290236



Reject

Accept

**To IMPROVE your chance of
publication in high-quality journals,
turn to wkauthorservices.editage.com**

The English-language editing and publication support service
trusted by more than 72,000 authors worldwide
is now available from Wolters Kluwer.

Get a quote for your manuscript today!



Academic Editing • Translation • Plagiarism Check • Artwork Preparation

Film is ~~a hassle.~~

S N A P

GafChromic introduces **FilmQA-PRO** Verification Software for **IMRT QA.**

You know that film gives you a more complete picture than electronic arrays. What's more, emerging techniques like SRS and RapidArc™ are better suited to film because film lets you shoot from any angle. But film may feel hard to work with and time-consuming. ■ All that changes. Now FilmQAPro™ 3.0 is taking full advantage of what we've built into GafChromic™ film. ■ One-scan analysis lets you do calibration and plan verification simultaneously. So you eliminate variables, and post-exposure growth no longer gets between you and your results. You get answers in minutes. And multi-channel dosimetry ensures the integrity of your measurement. ■ Finally, software that makes film easy. With help from FilmQAPro 3.0, **the future is film.**

GAFCHROMIC® Films for Radiotherapy:

(1) Gafchromic® EBT3 and EBT3-1417 (2) Gafchromic® RTQA2-1010 (3) Gafchromic® RTQA2-111



Let's take care.

Exclusively distributed in India by:

LATESTECH INTERNATIONAL

17-G/319, Vasundhara, Ghaziabad-201012, INDIA
Telephone: 0120-2881252 Fax: 91-120-2881179

Mob: 09873278842 Email: latestech@rediffmail.com





Journal of Medical Physics

Home | Search | Ahead of print | Current Issue | Archives | Instructions | Subscription | Login
Users online: 113
The official journal of Association of Medical Physicists of India

We are pleased to announce that all PDF downloads pertaining to Journal of Medical Physics are now available free of cost.



Submit Articles ONLINE

Email Alerts
A free & easy way to keep up to date



Highlights of Current Issue

April-June 2020 | Vol 45 | Issue 2

Original Article

Characterization and performance evaluation of the first-proton-therapy facility in India



Dayananda Sharma Shamuralipam, A Manikandan, K Ganapathy, MP Noufal, Kartikeyhar C Paloo, T Rajesh, R Jothi

Purpose: The purpose of this study is to evaluate the performance characteristic of volumetric image-guided dedicated-nozzle pencil beam-scanning proton therapy (PT) system. **Materials and ...**
[Abstract] [HTML Full text] [PDF] [Mobile HTML Full text] [EPub]

Original Article

Design, fabrication, and validation of a polymethyl methacrylate head phantom for dosimetric verification of cranial radiotherapy treatment plans



VS Shashi, Rajesh Kumar, Debjani Phani, KV Rajasekhar, George Zacharia, Saju Bhaskar, Raghuram K Nar

Purpose: The present study aims to design and fabricate a novel, versatile, and cost-effective Polymethyl Methacrylate (PMMA) head phantom for the dosimetric pretreatment verification of rad...
[Abstract] [HTML Full text] [PDF] [Mobile HTML Full text] [EPub]

Original Article

Influence of cleaned-up commercial knowledge-based treatment planning on volumetric-modulated arc therapy of prostate cancer



Mikoto Tamura, Hajime Morzen, Kenji Matsumoto, Kazuki Kubo, Yoshihiro Ueda, Tatsuya Kamima, Masahiro Inada, Hiroshi Doi, Kiyoshi Nakamitsu, Yasunaka Hishimura

Purpose: This study aimed to investigate the influence of cleaned-up knowledge-based treatment

- + Editorial Board
- + The Journal
- + The Association
- + Advertise
- + Contact us

Search this journal

Advance Search

Article Access Statistics

Table of Contents

RSS

RADIATION ONCOLOGY

MEDITRONIX

PRODUCTS & SERVICES

Having representing the best technologies for over 35 years, we have understood the treatment needs which changes with the newer challenges everyday. Today, we represent world's premium brands for different modalities of cancer diagnosis and treatment.



Klarity Solo Align AIO Baseplate with SBRT



Klarity 'O' Type AIO Baseplate for Elekta HexaPOD™ evo RT System



Klarity SRS Base Plate



Thermoplastics Masks



Fluke Survey Meter



Rexon TLD Reader System



RIT QA Software



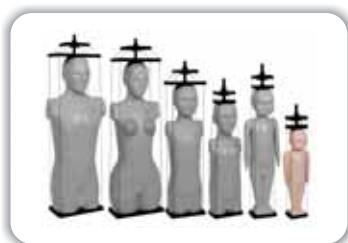
Ludlum Area Monitor & Pocket Dosimeter



Ludlum Neutron Survey Meter



CIRS Dynamic Thorax Phantom



CIRS Atom Dosimetry Verification Phantom (Whole Body Phantom)



QUARTZ dido Easy Series QA Tools



Radimage Healthcare India Pvt. Ltd.

(An ISO 9001 : 2015 Certified Company)

G-236, Sector-63, Noida - 201 303 (INDIA)

Tel.: +91 120 4263270 Fax: +91 120 2406097

www.radimageindia.com; radimagehealthcare@gmail.com

(A Meditronix Corporation Group Company)

DAILYQA

Finished before your first cup of coffee

MONTHLYQA

Never re-learn workflow again

ANNUALQA

Confidence with fewer gray hairs

STEREOTACTIC

When millimeters matter most

ABSOLUTE DOSIMETRY

"Pinpoint" is our margin of error

PATIENT DOSIMETRY

Pre-treatment is just the beginning



QA Solutions.

Our expertise is at your service.

STANDARDIMAGING



MORE THAN JUST QA PRODUCTS , FIND QA SOLUTIONS AT

www.standardimaging.com

INDIAN DISTRIBUTOR

MEDITRONIX CORPORATION

(An ISO 9001 : 2015 Certified Company)

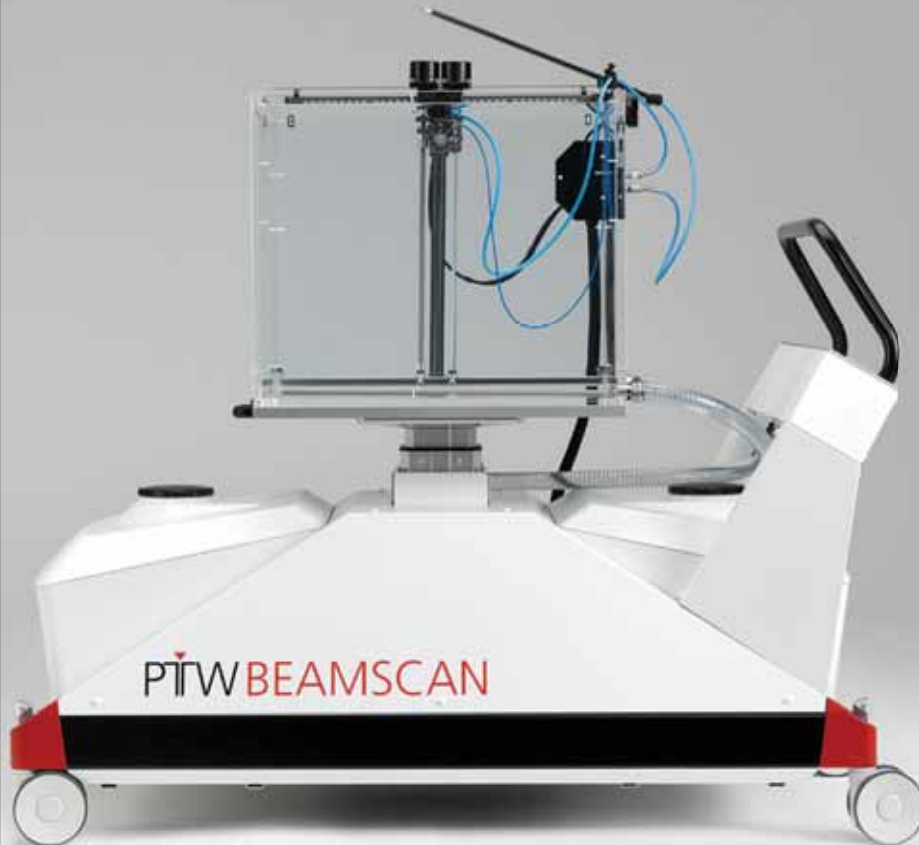
G-236, Sector-63, Noida-201 303 (INDIA)

Tel.: 0120-2406096 Fax: 0120-2406097

info@meditronixindia.com | www.meditronixindia.com



Beams You Up to a New Era in 3D Water Scanning.



PRECISION



SIMPLICITY



SPEED



QUALITY



The future in 3D water scanning starts now.

BEAMSCAN™ – The New Water Phantom.

Automated • Wireless • Fast

Explorers wanted.

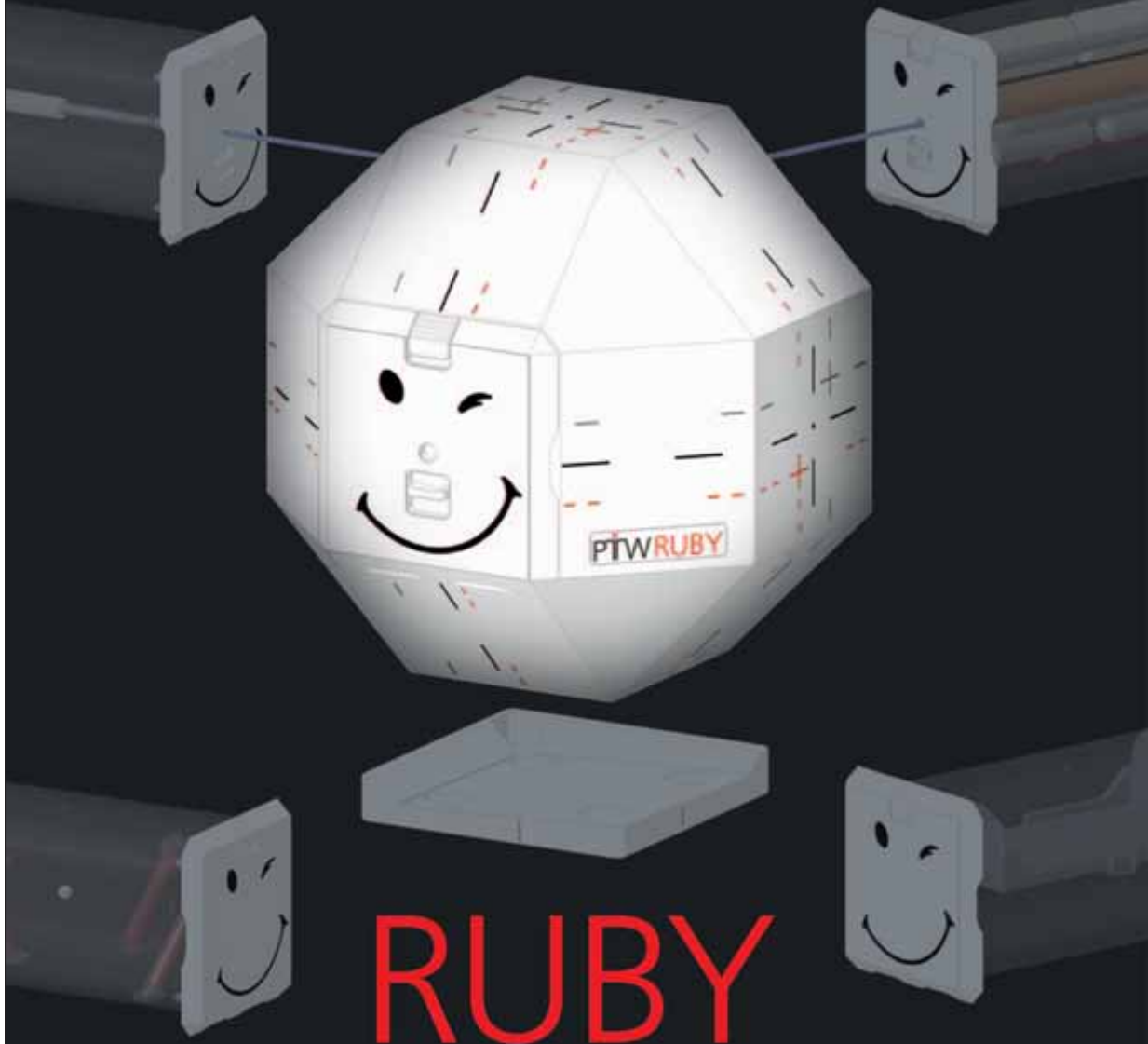
PTW THE
DOSIMETRY
COMPANY

PTW DOSIMETRY INDIA PVT. LTD.

ACE Towers, 2nd Floor, 73/75, Dr. Radhakrishnan Road, Mylapore, Chennai - 600004.

Phone: +91 44 4207 9999, 4207 2299 | Email: info@ptw-india.in | Web: www.ptwdosimetry.com

PTW THE
DOSIMETRY
COMPANY



RUBY

SYSTEM QA • LINAC QA • PATIENT QA

**The Modular QA Phantom Platform for High-Precision
Radiotherapy and SRS/SBRT QA**

PTW DOSIMETRY INDIA PVT. LTD.

ACE Towers, 2nd Floor, 73/75, Dr. Radhakrishnan Road, Mylapore, Chennai - 600004.
Phone: +91 44 4207 9999, 4207 2299 | Email: info@ptw-india.in | Web: www.ptwdosimetry.com



QUALITY GLOBAL CALIBRATION AND INSPECTION SERVICES



Certification No. : CC 3107

AERB RECOGNISED CALIBRATION LABORATORY FOR RADIATION MONITORING INSTRUMENTS
NABL ACCREDITED CALIBRATION LABORATORY AS PER ISO/IEC 17025:2017

Quality Global calibrates all models of radiation monitoring instruments at our in-house calibration facility. Our fixed range offers consistent and high quality calibration.



Quality Global Calibration team ensures that calibration of your instrument is completed within 3 business days and the instrument is packed securely for insured shipment back to you. In situations where you need your radiation survey meter returned to you quickly, 1-day turnaround and overnight shipping available.



CONTACT US

Bhousaheb Pangare (8600100700 | 8600331234)

Tanmay Pangare (8600100704 | 8600100699)

bkp_qndt@yahoo.in | bhousaheb@qualityndt.org

tanmaypangare@gmail.com

Plot NO. B.G.A.-1/4, Bhosari General Block MIDC, Bhosari, Pune - 411026. Maharashtra

(020) 27121843, 27119490, 8600100704

ROSALINA
INSTRUMENTS

ROSALINA INSTRUMENTS
127 BUSSA UDYOG BHAVAN
T.J. ROAD
SEWRI, MUMBAI 400015 INDIA
+919820627499
www.ROSALINA.in



MR3T LASER SYSTEMS IN RT PRECISE PATIENT ALIGNMENT

DORADOnova MR3T
ESSENTIAL AND COMFORTABLE

APOLLO MR3T
ESSENTIAL AND ELEMENTARY



**REMOTE
CONTROLLED
LASER
ADJUSTMENT**



www.LAP-LASER.com



Universal Radiation
Dosimeter



We Make The Things
That Make Indian Medical Physicist Proud



Cutting edge Indian technology, high calibre engineering expertise,
decades of experience, devotion and total commitment to the nation.

Innovative Leadership in Radiation Oncology and Medical Physics

Farmer type ionisation chambers

Electro Meters

Specialized phantoms

IGRT Dosimetry

Absolute Dosimetry

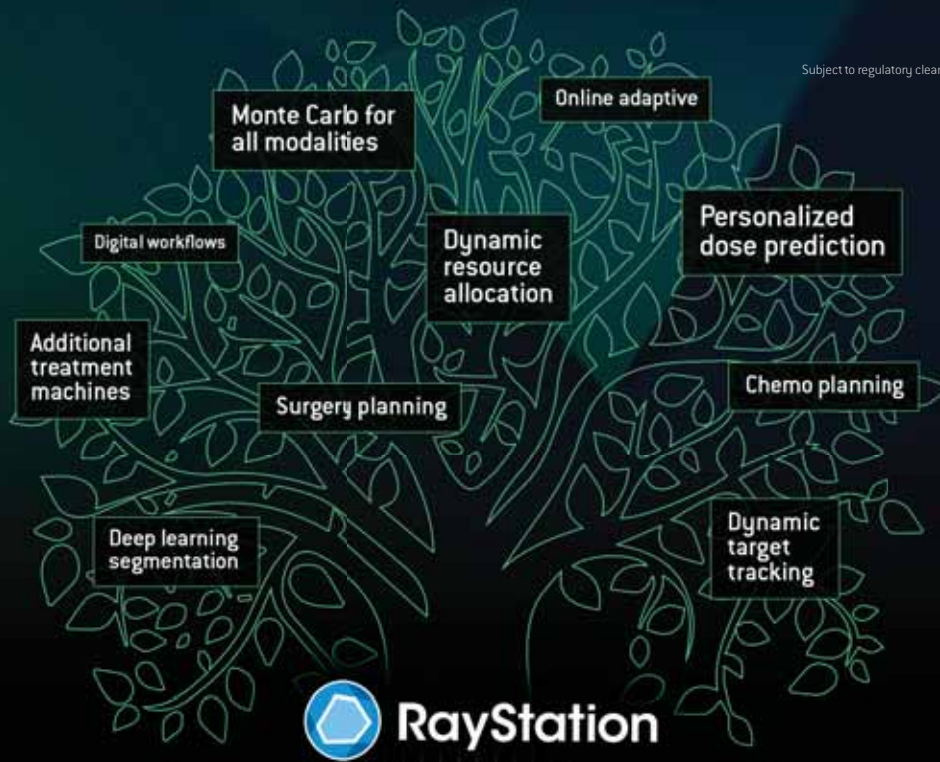
Relative Dosimetry

VMAT Dosimetry

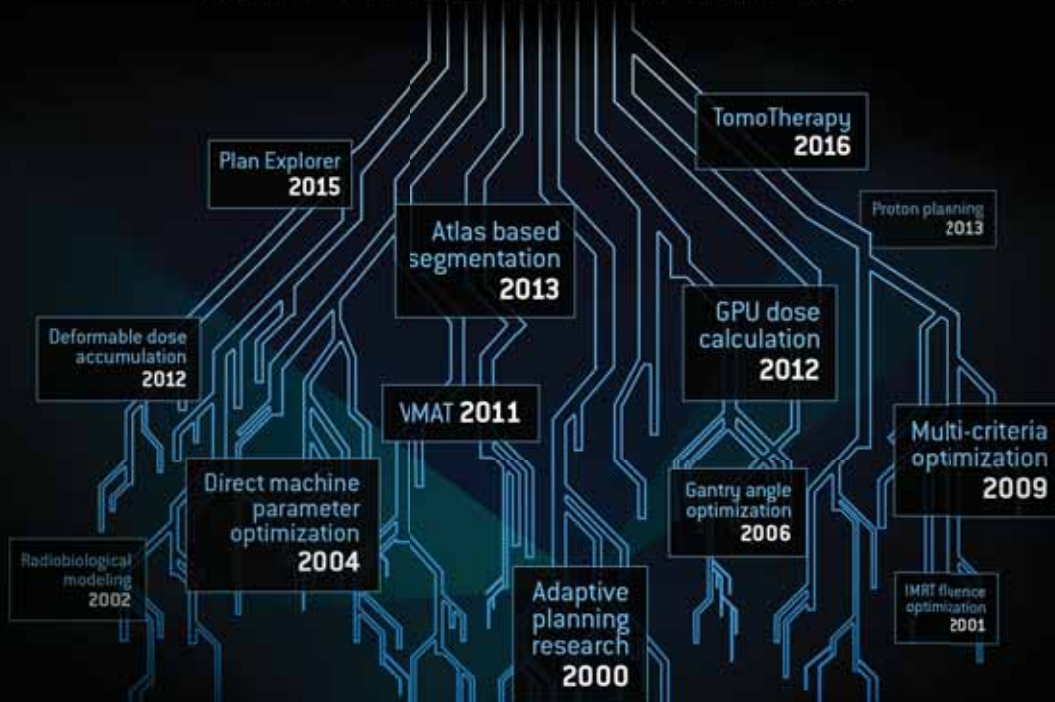
INVIVO Dosimetry

www.rosalina.in

Subject to regulatory clearance in some markets



DEEPLY ROOTED AND FUTURE PROOF



**ADVANCING
CANCER
TREATMENT**

**RaySearch
Laboratories** 

Perfect choice for patient dose QA

- ✓ Absolute Dose
- ✓ Profile Match
- ✓ DTA
- ✓ Gamma Index
- ✓ DVH Anatomy

ScandiDos

Delta⁴[®] Phantom +

TRUE VOLUMETRIC
PRE-TREATMENT VERIFICATION

Wi-Fi

Efficiency, accuracy and clinical relevance at the same time

Cornerstones of ScandiDos

**INSTANTLY ANALYZE AND
APPROVE PLANS**

The analysis starts with the Dose - Picture.

**QUICKLY AND EASILY FIND
THE CAUSE OF DEVIATIONS**

If a deviation is noted, the user can easily zoom in on the details.

**VERIFY THE DOSE DELIVERY
WITHOUT COMPROMISES IN 3D**

Reliable QA must be highly accurate and comprehensive. Delta 4[®]PT measures the dose with high density in the high gradient region with the resolution of 50nGy.

**ANALYZE THE CLINICAL
RELEVANCE OF A DEVIATION**

The level of importance in discrepancy between delivered and planned dose is determined using patient anatomy (e.g. target and risk structures) to gauge the clinical relevance.

THE DIFFERENCE CLEAR

ROSALINA
INSTRUMENTS

The first step in advancing cancer care is to make advancements that are miles ahead.✱

A cancer care ecosystem that's creating a world
free from the fear of cancer.

Staying ahead in the cancer fight calls for being on the forefront of evolving cancer care. That's why we're singularly focused on advancing care through the integration of a full spectrum of oncology solutions—providing actionable insights and innovative treatment delivery so you can improve patient outcomes. Because when everything works together, your cancer care can work wonders.

See how we can help you move cancer care forward at: varian.com/victories

© 2018 Varian Medical Systems, Inc. Varian is a registered trademark of Varian Medical Systems, Inc.



varian